

RL-TR-97-224
In-House Report
June 1998



SMART PIXELS FOR OPTICAL PROCESSING AND COMMUNICATIONS: DESIGN, MODELS, FABRICATION AND TEST

Michael A. Parker and James S. Kimmet, Capt., USAF

APPROVED FOR PUBLIC RELEASE; DISTRIBUTION UNLIMITED.

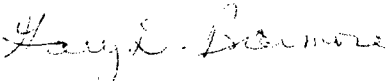
19980727 182

AIR FORCE RESEARCH LABORATORY
ROME RESEARCH SITE
ROME, NEW YORK

Although this report references a limited document (*), listed on page 231, no limited information has been extracted.

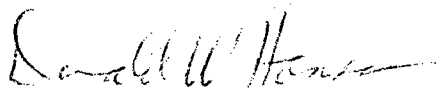
This report has been reviewed by the Air Force Research Laboratory, Information Directorate, Public Affairs Office (IFOIPA) and is releasable to the National Technical Information Service (NTIS). At NTIS it will be releasable to the general public, including foreign nations.

RL-TR-97-224 has been reviewed and is approved for publication.

APPROVED: 

GARY D. BARMORE, Maj., USAF
Chief, Photonics Division
Surveillance & Photonics Directorate

FOR THE DIRECTOR:



DONALD W. HANSON, Director
Surveillance & Photonics Directorate

If your address has changed or if you wish to be removed from the Air Force Research Laboratory mailing list, or if the addressee is no longer employed by your organization, please notify AFRL/SNDP, 25 Electronic Pky, Rome, NY 13441-4515. This will assist us in maintaining a current mailing list.

Do not return copies of this report unless contractual obligations or notices on a specific document require that it be returned.

ALTHOUGH THIS REPORT IS BEING PUBLISHED BY AFRL, THE RESEARCH WAS ACCOMPLISHED BY THE FORMER ROME LABORATORY AND, AS SUCH, APPROVAL SIGNATURES/TITLES REFLECT APPROPRIATE AUTHORITY FOR PUBLICATION AT THAT TIME.

REPORT DOCUMENTATION PAGE			Form Approved OMB No. 0704-0188	
<small>Public reporting burden for this collection of information is estimated to average 1 hour per response, including the time for reviewing instructions, searching existing data sources, gathering and maintaining the data needed, and completing and reviewing the collection of information. Send comments regarding this burden estimate or any other aspect of this collection of information, including suggestions for reducing this burden, to Washington Headquarters Services, Directorate for Information Operations and Reports, 1215 Jefferson Davis Highway, Suite 1204, Arlington, VA 22202-4302, and to the Office of Management and Budget, Paperwork Reduction Project (0704-0188), Washington, DC 20503.</small>				
1. AGENCY USE ONLY (Leave blank)		2. REPORT DATE June 1998	3. REPORT TYPE AND DATES COVERED In House, Oct 94 - Sep 96	
4. TITLE AND SUBTITLE SMART PIXELS FOR OPTICAL PROCESSING AND COMMUNICATIONS: DESIGN, MODELS, FABRICATION AND TEST			5. FUNDING NUMBERS PE - 62702F PR - 4600 TA - P3 WU - 28	
6. AUTHOR(S) Michael A. Parker and James S. Kimmet, Capt., USAF				
7. PERFORMING ORGANIZATION NAME(S) AND ADDRESS(ES) Air Force Research Laboratory/SNDP 25 Electronic Pky Rome, NY 13441-4515			8. PERFORMING ORGANIZATION REPORT NUMBER RL-TR-97-224	
9. SPONSORING/MONITORING AGENCY NAME(S) AND ADDRESS(ES) Air Force Research Laboratory/SNDP 25 Electronic Pky Rome, NY 13441-4515			10. SPONSORING/MONITORING AGENCY REPORT NUMBER RL-TR-97-224	
11. SUPPLEMENTARY NOTES Air Force Research Laboratory Project Engineer: Michael A. Parker/SNDP/(315)330-4918				
12a. DISTRIBUTION AVAILABILITY STATEMENT Approved for public release; distribution unlimited.			12b. DISTRIBUTION CODE	
13. ABSTRACT (Maximum 200 words) The smart pixel is an opto-electronic device that functions both as an optical interconnect and as a logic element (analog or digital). Elementary issues in the design, modeling, fabrication and testing of smart pixels are examined. In particular, the report investigates the monolithic integration of field effect transistors with lasers, optical quenched lasers, vertical cavity lasers, edge-emitting lasers with intracavity modulators. The report starts with self electro-optic effect devices since they are one of the first smart pixels. Details are included on fabrication and on the use of an in-situ reflectometer for wet and dry etching. The report also covers the basic software for the design and test of laser heterostructure and DBR mirror stacks.				
14. SUBJECT TERMS semiconductor lasers, gain quenched lasers, fabrication, transistors, monolithically integrated, optoelectronic integrated circuits (OEICs)			15. NUMBER OF PAGES 254	
			16. PRICE CODE	
17. SECURITY CLASSIFICATION OF REPORT UNCLASSIFIED	18. SECURITY CLASSIFICATION OF THIS PAGE UNCLASSIFIED	19. SECURITY CLASSIFICATION OF ABSTRACT UNCLASSIFIED	20. LIMITATION OF ABSTRACT UL	

ACKNOWLEDGMENTS

This technical report covers in-house work performed at the USAF Photonics Center during the time Oct. 93 to Sept. 96. The authors acknowledge the contributions of others. During a trip to LA in 1992, B. Kaminsky discussed aspects of neural nets as an application for the integrated amorphous silicon memory elements. Capt. W. A. Davis significantly contributed to the fabrication of these memory elements during the first several months of his tour of duty at Rome Laboratory. A. R. Pirich provided many useful discussions along with a working environment conducive to in-house work. D. Hanson, G. Barmore, J. Cusack, J. L. Rossi, and I. Fouse have provided significant financial and administrative support. In addition, H. Burstyn, Esq., provided assistance with patent issues.

The authors acknowledge the helpful collaboration of C. L. Tang (and his group) and D. B. Shire in the School of Electrical Engineering at Cornell University; they fabricated and tested some of the Vertical Lasers with Optical Gain Control (V-LOGiC). The fabrication of other devices was performed by Photonics Center Personnel at the Cornell Nanofabrication Facility (CNF), Cornell University. The authors appreciate the assistance given by the staff of the CNF, especially J. Drumheller, G. Bordinaro and D. Buttinger.

Dr. M. A. Parker was responsible for this technical report and its content including the design, modeling, fabrication and testing. Capt. J. S. Kimmet assisted with the investigation of the monolithic integration of FETs and Lasers. Capt. Kimmet advanced many of the fabrication procedures. The information found in several of the chapters of this report are edited versions of those in his MS Thesis titled "Monolithic GaAs Opto-Electronics: A Fabrication Method for Integrating Field-Effect Transistors with Edge-Emitting Lasers." Captain Kimmet earned the MSEE degree from Syracuse University in conjunction with his in-house work at the USAF Photonics Center. Although Dr. R. J. Michalak spent the majority of his time on the growth of

GaAsN on Si, he still found time to work with some of the reported devices. In addition to providing advice on administrative matters, he assisted with the fabrication of the coupled waveguide detectors, the experimental aspects of surface roughness due to etching, and the initial testing of the coupled waveguide detectors.

ABSTRACT

The smart pixel is an opto-electronic device that functions both as an optical interconnect and as a logic element (analog or digital). Elementary issues in the design, modeling, fabrication and testing of smart pixels are examined. In particular, the report investigates the monolithic integration of field effect transistors with lasers, optically quenched lasers, vertical cavity lasers, edge-emitting lasers with intracavity modulators. The report starts with self electro-optic effect devices since they are one of the first smart pixels. Details are included on fabrication and on the use of an in-situ reflectometer for wet and dry etching. The report also covers the basic software for the design and test of laser heterostructure and DBR mirror stacks.

CONTENTS

Part 1: Devices	1
1. Introduction to the Smart Pixel	2
2. Review of SEEDs, CELLS and DOES Smart Pixels	4
2.A Introduction to SEEDs	4
2.B R-SEEDs	12
2.C S-SEEDs	14
2.D F-SEEDs	16
2.E Surface Emitting Laser Logic Devices	19
2.F DOES Smart Pixels	25
2.G A SEED Smart Pixel Cross Bar	28
2.H A SEED Smart Pixel Neuron	29
2.I Summary Discussion	31
3. Brief History of Quenched Laser Devices	37
4. A Model for Optically Quenched Lasers	40
4.A Introduction	40
4.B Approximate Closed Form Solution	42
4.C The RF Modulation Bandwidth	48
4.D Summary	51
5. V-LOGiC Devices	52
5.A The Basic V-LOGiC Switch	52
5.B A V-LOGiC Memory Element	55
5.C The Spontaneous Emission Filter	56
5.D The Signal Router for ATM Switching	57
6. Diode Laser Logic	58
6.A The Logic Family	58
6.B A Simple Model	64
6.C Fabrication	69
6.D Experimental Results	70
6.E Summary	74
7. Coupled Waveguide Detectors	75
7.A Introduction	75
7.B Description of the Coupled-Waveguide Detectors	77
7.C Fabrication	80
7.D Experimental Results	81
7.E Discussion	83
8. Introduction to Opto-Electronic Technology	85
9. The Design of Monolithically Integrated FETs and Lasers	91
9.A FET Design	91
9.B Laser Design	99
9.C Heterostructure for the Monolithically Integrated FETs and Lasers	103
10. Preliminary Tests of Monolithically Integrated FETs and Lasers	107
11. Amorphous Silicon Memory Elements for Optical Neurons	112
11.A Introduction	112
11.B Description and Use of the Memory Elements	115
11.C Summary Discussion	119

Part 2: Fabrication	121
12. Developing a Reliable Etch -----	122
12.A Selective Wet Etching	124
12.B Selective Reactive Ion Etching	127
12.C Electron Cyclotron Resonance Etching	132
13. High Quality Gas Etching Using a Cyclotron Resonance Etcher (ECR) -----	139
14. Using a Laser Reflectometer as an In-Situ Monitor During a Gas Etch -----	144
15. Etched-Surface Roughness Measurements from a Laser Reflectometer -----	151
16. Fabrication Methodology -----	161
16.A Layout Design and Mask Generation	161
16.B Wafer Cleaning	162
16.C Photolithographic Image Reversal	163
16.D Opto-Electronic Fabrication Sequence	164
Part 3: Software	177
17. Wavelength Dependent Reflectivity for Multiple Layers of GaAs-AlGaAs ----	178
18. Software for the Laser Reflectometer -----	195
19. Software for the Tencor Instruments Alpha Step 200 -----	216
20. Software for Complex Number Arithmetic -----	219
21. Software and Hardware for an 8 Bit Analogue to Digital Converter -----	224
References	228

LIST OF FIGURES

Chapter 2: Review of SEEDs, CELLS and DOES Smart Pixels

2.1 MQW Reflection Modulator and Reflectivity Spectrum	5
2.2 Energy Band Structure for Quantum Well with and without an Applied Field	7
2.3 Absorption Spectra of an EOAM	9
2.4 Reflectivity and Responsivity of an F-SEED	10
2.5 R-SEED Configuration and Transfer Function	11
2.6 Self Linearized Modulator	13
2.7 F-SEED Receiver and Transmitter	15
2.8 DMT for F-SEED	17
2.9 Plots of Reflectivity and I-V Characteristics for F-SEED	18
2.10 CELL and VCSEL Layout	21
2.11 HPT and VCSEL Current/Voltage Characteristics	22
2.12 VCSEL Output/HPT Input Transfer Function	22
2.13 Circuit Model of CELL	23
2.14 Logic from a CELL	24
2.15 DOES Device	26
2.16 Optical Cross Bar	28
2.17 SEED Logic Gates	28
2.18 Neuron	29
2.19 SEED Responsivity vs. Reverse Bias Voltage	29
2.20 The SEED Neuron	29

Chapter 3: Brief History of Optically Quenched Laser Devices

3.1 Basic Geometry for Laser Quenching	37
3.2 The First Gain-Quenched Laser	38
3.3 The Kosonocky Clock	38
3.4 The Grande-Tang Gate	39
3.5 The First V-LOGiC NOR Gate	39

Chapter 4: A Model for Optically Quenched Lasers

4.1 Carrier Deviation vs. Control-Photon Density	41
4.2 VCSEL Threshold Current vs. Control-Photon Density	47
4.3 RF Modulation Bandwidth	48

Chapter 5: V-LOGiC Devices

5.1 V-LOGiC Inverter and Modulator	52
5.2 VCSEL Threshold Current vs. Control-Photon Density	54
5.3 A V-LOGiC Memory Element	55
5.4 Length Scales for Vertical Cavity and In-Plane Lasers	55
5.5 V-LOGiC Signal Router	57

Chapter 6: Diode Laser Logic

6.1 Configurable Optical Gate	58
6.2 Inverter from Diode Laser Logic (DLL) Family	59
6.3 OR DLL Gate	60
6.4 AND DLL Gate	61
6.5 NAND DLL Gate	61
6.6 NOR DLL Gate	62
6.7 ADDER DLL Gate	64
6.8 Basic COG Circuit	64
6.9 Threshold Current vs. Modulator Voltage	65
6.10 A Solution Plot	66
6.11 Adding Hysteresis to a DLL gate	67
6.12 Heterostructure	69
6.13 Cross Section	69
6.14 Spectrum	70
6.15 I-V Characteristics	72

Chapter 7: Coupled Waveguide Detectors

7.1 Integrated Butt-Couple Laser and Detector	75
7.2 Coupled-Waveguide Detector	77
7.3 Top View of Coupled-Waveguide Detector	79
7.4 Test Setup for Prototype Coupled-Waveguide Detector	81
7.5 Distinction between Laser Length and Coupling Length	82
7.6 Linear Version of Coupled Waveguide Detector	83
7.7 Ring Laser with Coupled Waveguide Detector	83
7.8 Single Unit Coupled Waveguide Detector	84

Chapter 8: Introduction to Opto-Electronic Technology

8.1 Neural Network Node	86
8.2 Integrated FETs with Edge-Emitting Lasers	88
8.3 DLL OR Gate	88

Chapter 9: The Design of Integrated FETs and Lasers

9.1 N-Type Doped-Channel MISFET	93
9.2 Band Diagram and Carrier Concentration at Zero Bias	94
9.3 Band Diagram and Carrier Concentration for Reverse Bias	96
9.4 Band Diagram and Carrier Concentration at Zero Bias with AlGaAs Barrier	97
9.5 Band Diagram and Carrier Concentration for Reverse Bias with AlGaAs	98
9.6 MQW Graded Index Heterostructure	99
9.7 Wavefunctions for Conduction and Valence Bands	100
9.8 Transverse Laser Mode	102
9.9 Initial MISFET Design	104
9.10 Revised Design	105

Chapter 10: Preliminary Tests of Integrated FETs and Lasers

10.1 FETs	108
10.2 Completed FETs	109
10.3 Magnified Images of FETs	110

Chapter 11: Amorphous Silicon Elements for Memory (ASEMs)

11.1 Dangling Bonds vs. Illumination Time	113
11.2 Dangling Bonds vs. Anneal Time	114
11.3 Mobility-Lifetime Product	115
11.4 P-I for VCSEL	116

Chapter 12: Developing a Reliable Etch

12.1 Etch Rates and Selectivity for Citric Acid	126
12.2 Undesirable Surface Roughness	131
12.3 Laser Reflectometer	133
12.4 Sample Reflectometer Data	134
12.5 Sample Reflectometer Data for VCSEL	136
12.6 Effect of Surface Roughness for FET-Laser Heterostructure	137

Chapter 13: High Quality Gas Etching Using an ECR

13.1 Serpentine Laser	139
13.2 Threshold Current as a Function of Number of Bends	143

Chapter 14: Using a Laser Reflectometer as an In-Situ Monitor

14.1 In-Situ Reflectometer	144
14.2 Reflectometer Data for In-Plane Laser Heterostructure	147

Chapter 15: Etched-Surface Roughness Measurements from a Laser Reflectometer

15.1 SMR vs. Standard Deviation for Surface Roughness	152
15.2 Difference in Path Length	153
15.3 Geometry for Overlapping Images	157
15.4 Random and Systematic Variations of Surface Height	159

Chapter 16: Fabrication Methodology

16.1 Photolithographic Liftoff Procedure	163
16.2 Mask Sequence	166
16.3 Etched FET Mesas	167
16.4 Polyimide Vias	172
16.5 FET Vias	173
16.6 Cross-Sectional View of Gate Electrode	174
16.7 Completed FET	175

PART 1
DEVICES

Chapter 1: Introduction to the Smart Pixel

Signal processors are presently limited by the performance of the electronic logic gates and the electrical interconnections between those gates. Compared with projections for the performance of optical devices, present logic elements are slow in addition to their large power requirements.

There are two significant problems with present semiconductor device architectures that concern the interconnect. The first concerns the two dimensional aspect of integrated circuits where data signals are confined to a plane. Here, the complexity and density of the interconnections increases faster than that for the devices. Integrated circuit manufacturers now use multiple levels of metal interconnections between planar logic devices to overcome this problem, but this approach still has limitations, too. The second problem concerns the electrical nature of the interconnects. The bandwidth is limited by resistive and capacitive effects. In addition, the cross talk between channels and the power required to drive the interconnect increases with the driving frequency.

These problems can be solved by the use of interconnects that are optical rather than electrical ones. The preferred architecture for signal processors and communication systems makes use of a set of stacked wafers that communicate with each other by light. The use of out-of-plane optical interconnects increases the parallelism of the data link and, hence, also the speed of the system through efficient use of these dimensions.

The devices that produce or modulate the light for these interconnects can also be given logic functions. Thus, in effect, one device (the smart pixel) can serve as a logic element and as an interconnect. Smart pixels are generally viewed as single devices or small clusters of devices. Smart pixels can also be divided into at least two different types. The first type is the all-optical smart pixel. In this case, one or several beams of light interact within a small volume of matter to produce a resultant beam. The light must interact with the electric charge in the material to produce the desired effect. The other type is the opto-electronic hybrid that has both optical and

electronic components. In this case, photodetectors intercept the input light signals, electronic components implement a logic function and an optical transmitter generates the resultant beam. With clever enough designs, there would be little distinction between the all-optical and optoelectronic hybrid devices since both involve the interaction between light and electronic charge.

There are many different types of smart pixels. Monolithically integrated field effect transistors (FETs) and lasers have been available since the 1980's but they are only recently appearing in smart pixel designs. The AT&T self electro-optic effect devices (SEEDs) are probably the most developed of the smart pixels. However, most other types of smart pixels are still research grade devices.

Chapter 2: Review of SEEDs, CELLS and DOES Smart Pixels

The typical smart pixel can best be represented by the Self Electro-optic Effect Device. This chapter begins with a thorough discussion of the various varieties of SEEDs. For the purpose of power efficient, high speed computing circuits, the optimum design at present consists of the monolithic integration of photodetectors, lasers and electronic circuits. Although these circuits are still in the research phase, some commercial examples are included.

Section 2.A: Introduction to SEEDs

As the prototypical smart pixel, the Self Electro-optic Effect Devices (SEEDs) were developed as opto-electronic hybrids to bring optics into the realm of processing.² Large two dimensional arrays of SEEDs can be used as transmissive or reflective electro-optic modulators. The difference concerns only the manner in which the SEED handles the input and output light signals. In the transmissive mode, light enters one end of the SEED from a direction perpendicular to the 2D array and exits at the opposite end as a modulated light signal. In the reflective mode, light also enters the SEED perpendicular to the array. However, it is then modulated and reflected back out parallel to the incident beam but in the opposite direction. The reflective SEED is most commonly used since it is less sensitive to heat, has lower insertion loss and has greater modulation depth. Generally, these arrays are optically interconnected through free space using bulk optics.³

The SEED in its most basic form is derived from an electro-optic absorption modulator (EOAM). An EOAM consists of a semiconductor PIN diode structure with multiple quantum wells in the intrinsic I region as shown in Figure 2.1.⁴ Light enters the EOAM through the N-doped semiconductor and passes through the GaAs quantum wells and the $\text{Al}_{0.35}\text{Ga}_{0.65}\text{As}$ barriers. The light reflects off the Bragg reflector mirror stack which consists of alternating quarter-wave layers of GaAs and $\text{Al}_{0.19}\text{Ga}_{0.81}\text{As}$. The light then passes through the quantum wells for a second time where it is further modulated. The N and P semiconductors are used to apply bias voltage to

the quantum wells so as to modify their absorption characteristics using the quantum confined stark effect (QCSE).

The structure of Figure 2.1 is taken to form the basic SEED element and can operate as either a type of reverse-bias voltage-controlled photodetector or modulator. A PIN diode

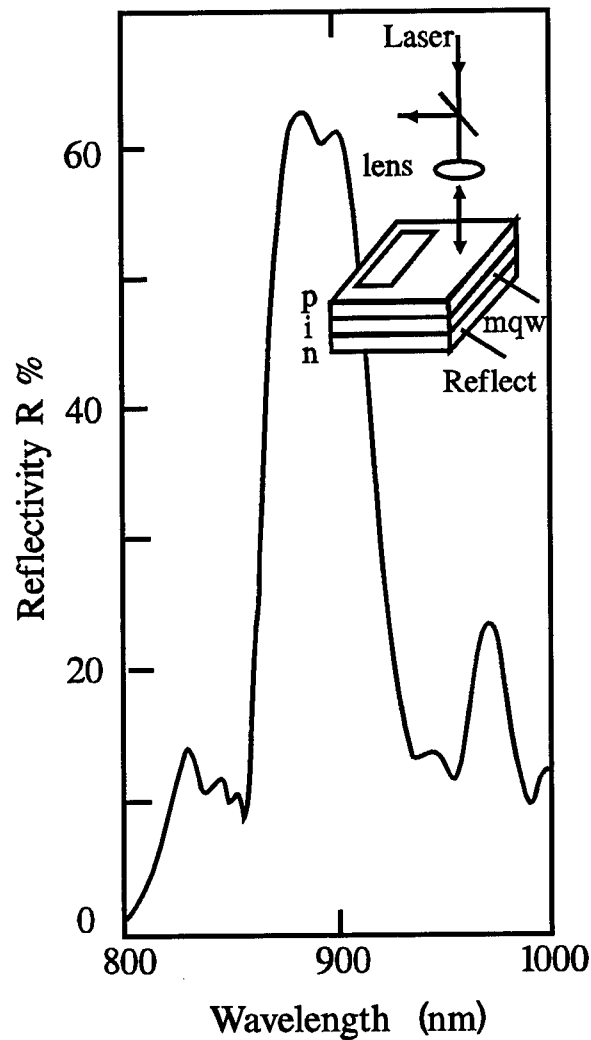


Figure 2.1: Structure of the MQW reflection modulator and a typical reflectivity spectrum of the wafer (with antireflection coating). x is the fraction of AL in the $\text{Al}_x\text{Ga}_{1-x}\text{As}$. Reprinted from Ref.4 with permission.

photodetector produces a photocurrent J that is related to the incident optical power P_{opt} according to

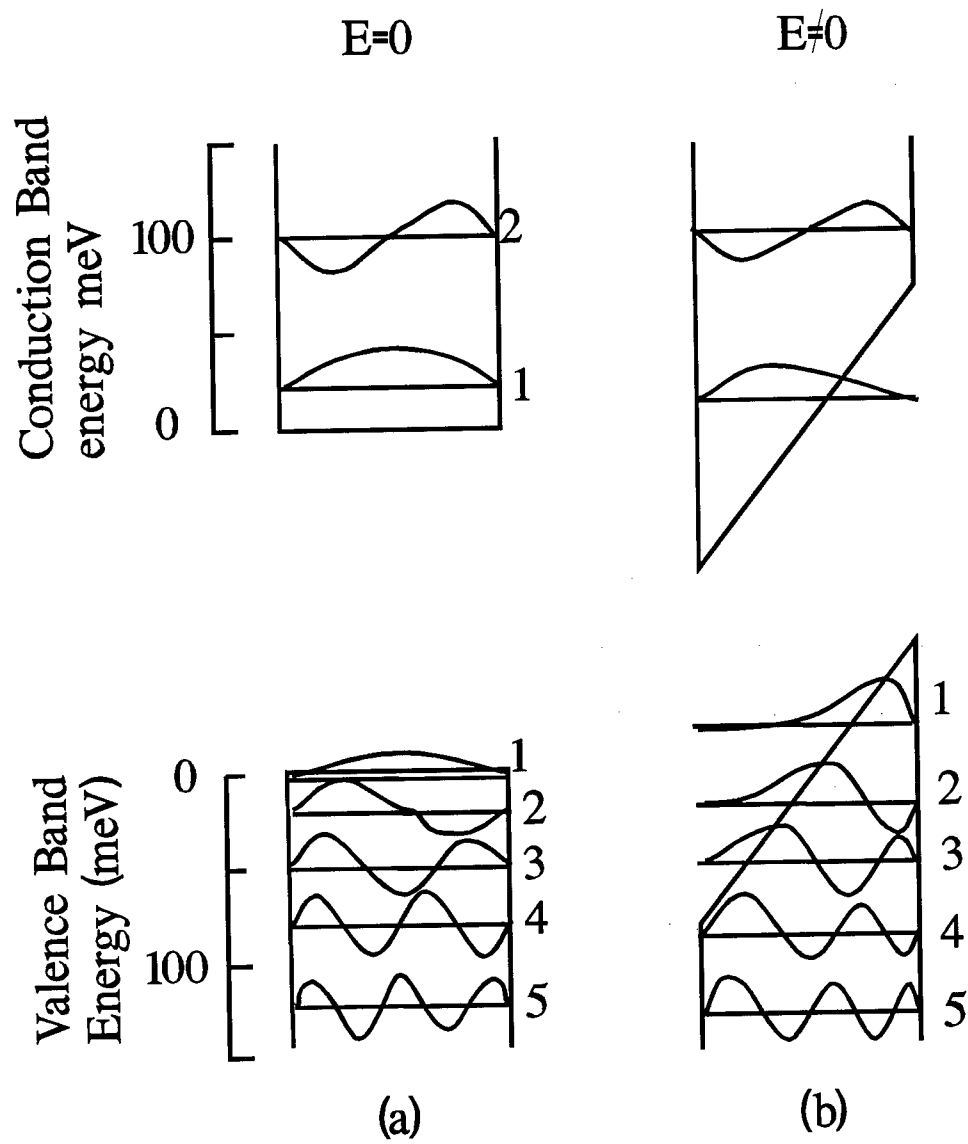
$$J = RP_{\text{opt}} \quad (2.1)$$

where R is the responsivity. Normally, photodetectors that operate at wavelengths shorter than (*i.e.*, energies above) the energy bandgap of the semiconductor material have a responsivity that is essentially independent of the magnitude of the applied reverse bias. However, the situation is different for a QCSE photodetector operated near the wavelength corresponding to the energy bandgap. In this case, the optical absorption of the quantum wells greatly depends on the applied reverse-bias voltage. Thus the photocurrent and hence, the responsivity, are also bias voltage dependent. As a note, the SEED can perform as a normal PIN diode photodetector for wavelengths sufficiently far from the exciton absorption energies.

The SEED, as an EOAM, relies on the ability of the applied bias voltage to alter the effective reflectivity R_{eff} of the SEED. Here, R_{eff} is defined as the ratio of the output optical intensity to the input optical intensity. Changes of the reverse bias voltage alter the optical absorption of the quantum wells and, thus, also the intensity of the light passing through the SEED.

The QSCE⁵ is responsible for the effect that an electric field has upon the optical absorption in the PIN diode structure of Figure 2.1. Figure 2.2a shows the band gap diagram for the quantum wells without an electric field present. The GaAs forms a quantum well for both the conduction and valence bands because its bandgap is smaller than that of the surrounding AlGaAs. For simplicity, the distinction between light and heavy holes is neglected. The figure

Figure 2.2: Energy band structure of a quantum well a) without an applied electric field and b) with an applied electric field. Reprinted from ATT with permission.



shows the energy levels for both electrons and holes. The narrow wells force the hole and electron wavefunctions to overlap and the Coulomb interaction causes the formation of an exciton or spatially confined electron-hole pair. In some respects, the exciton can be described by a hydrogen-like model. In bulk semiconductors without the wells, the carrier pairs still form excitons but they have short lifetimes since they are easily ionized. The confinement of the wavefunctions in the quantum wells results in an increased lifetime and an increased binding energy for the exciton. Figure 2.2b shows an energy band diagram for finitely deep quantum wells in the presence of an electric field. The triangular shape of the potential well decreases the energy difference between the electron and hole states and pushes the two particles to opposite sides of the well.⁶ Thus the energy required to produce an exciton is reduced and, as a result, the absorption curve shifts to longer wavelengths. The decreased overlap between the two wavefunctions results in a decrease in the peak of the absorption. Figure 2.3 shows three typical absorption curves for the SEEDs for three different bias voltages.⁷ Each curve is shown with two maxima. The largest maxima corresponds to the formation of excitons with electrons and holes in their corresponding lowest energy levels ($n=1$), the heavy hole exciton transition. The smaller maxima corresponds similarly to the $n=2$ light hole exciton transition.

The operation and application of the SEEDs are derived from the absorption curves in Figure 2.3. Normally, an application is designed for either λ_0 or λ_1 operation. For the case of λ_0 operation, the wavelength of the light is set at the peak of the $n=1$ exciton in the absence of any external bias applied to the SEED. An applied reverse bias voltage causes the peak to shift to longer wavelengths and the absorption at the operating wavelength tends to decrease. Note that the curve biased at 10 V has the $n=2$ exciton peak at the operating wavelength and, as a result, the absorption has actually increased slightly compared with the 5V bias curve. For the preferred λ_1 mode, the operating wavelength is set to a wavelength larger than the $n=1$ exciton peak. In this

case, increases in reverse bias voltage tend to increase the optical absorption. The reflectivity and responsivity of the SEED are shown in Figure 2.4 for λ_1 operation. For the proper range of reverse bias voltage, the photocurrent from the PIN structure increases since the responsivity increases and the intensity of the reflected light decreases.

SEEDs are fabricated into a variety of circuits. The R-SEED and D-SEED consist of the series combination of a SEED with a resistor and a diode, respectively. These are the simplest combinations to exhibit bistability. The Symmetric SEED or S-SEED consists of two SEEDs in series. They are intended for dual rail or differential optical input applications. The F-SEED is a SEED monolithically integrated with a field effect transistor.

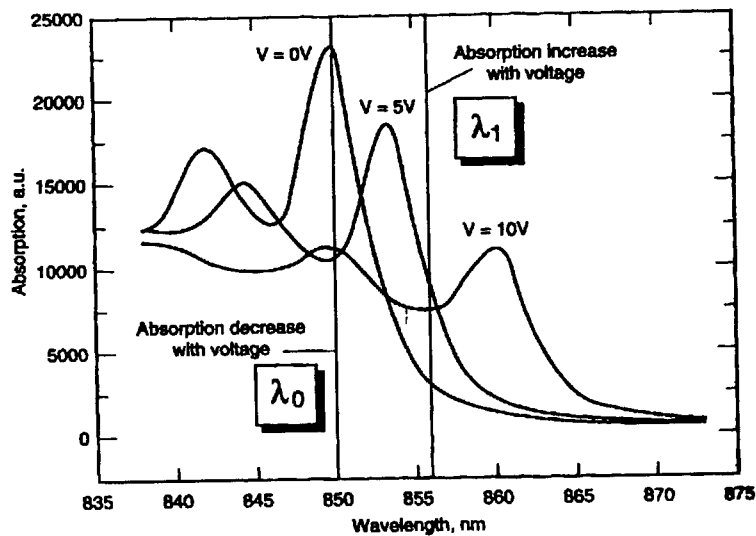


Figure 2.3: Absorption spectra of an EOAM for bias voltages of 0, 5 and 10 V. Reprinted from ATT with permission.

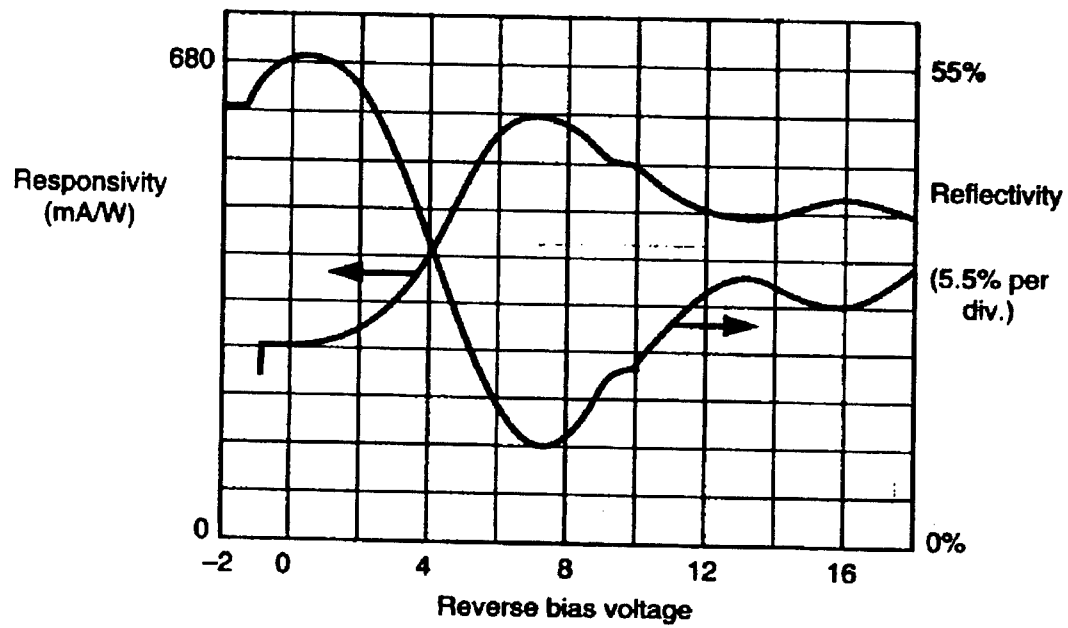


Figure 2.4: Reflectivity and responsivity for 500 μW incident power at 850 nm wavelength in a 3 μm diameter spot current FET-SEED modulator design operated at λ_1 (wavelength longer than zero-field exciton peak). Reprinted from ATT with permission.

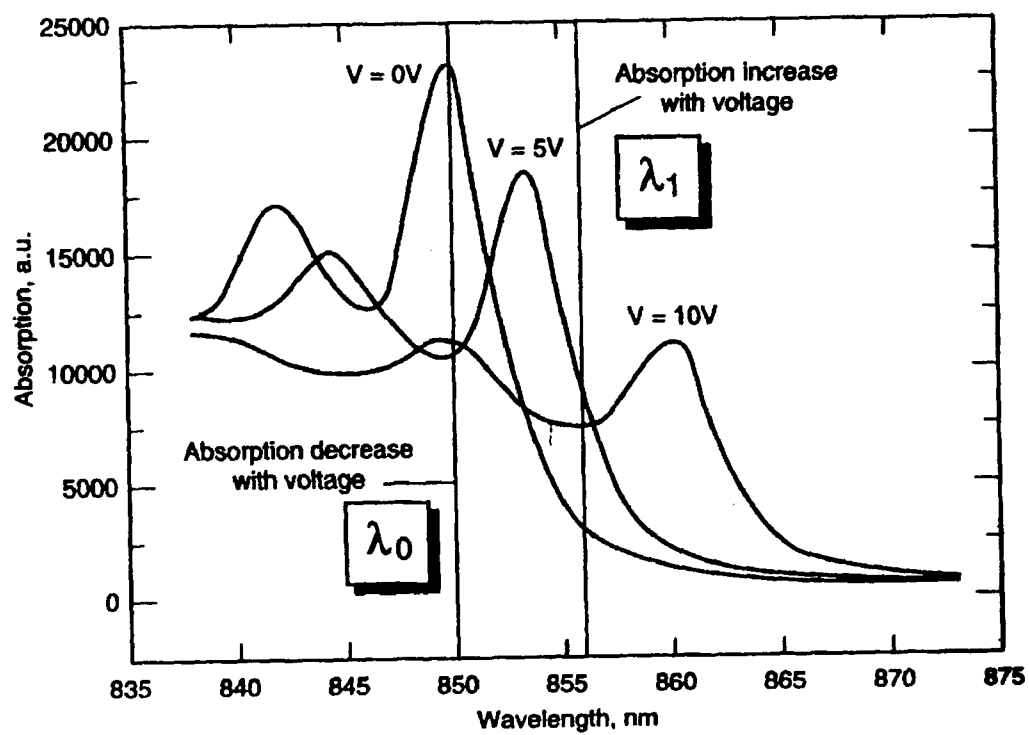


Figure 2.5: a) R-SEED configuration. b) R-SEED transfer function.

Section 2.B: R-SEED

The R-SEED consists of a SEED integrated in series with a resistor as shown in Figure 2.5. The device is operated at λ_0 so that the absorption of the SEED increases with decreasing voltage; this configuration sets up a positive feedback situation.⁷ Light of wavelength λ_0 incident on the SEED is absorbed and produces photocurrent J in the direction shown. Consider the upper branch first. Initially, as the incident power P_i increases, the reflected power P_r also increases as is appropriate for relatively constant reflectivity and absorption. However, the generated photocurrent J from absorbed photons increases the voltage drop across the resistor and thus reduces the voltage across the SEED. As the incident power further increases, the voltage across the seed reduces further and the peak in the absorption curve moves closer to λ_0 . All along the upper branch, the absorption is relatively low. Only at incident power P_2 does the absorption curve center at λ_0 . At this point, the absorption increases greatly and the effective reflectivity drops. Further increases in incident power appear as a reflected signal described by branch 2. The difference between branch 1 and 2 is that the SEED is in a highly absorbing state along branch 2 and thus, the SEED is producing significantly more photocurrent even at power P_2 than it did along branch 1. Thus, along branch 2, the incident power can be lowered to P_1 before the voltage across the SEED shifts the absorption curve away from λ_0 . At this point, the system shifts back up to the top branch. The width of the hysteresis loop is controlled by several factors including the voltage required to move the absorption peak to λ_0 , the value of the series resistance, and the difference between the absorption maximum and minimum.

The D-SEED is similar to the R-SEED except that a conventional photodiode replaces the resistor. The conventional photodiode is basically an optically controlled current source where the photocurrent is essentially independent of the reverse bias voltage. In this case, the load for the

SEED can be set by an external optical signal incident on the photodiode. Such a combination yields better switching characteristics.⁷

The Self-Linearized Modulator (S-LM)⁸, shown in Figure 2.6, is also related to the R-SEED. The current source replaces the series combination of the voltage source and resistor. Unlike the R-SEED, however, the S-LM is operated at λ_1 where the absorption increases with reverse bias voltage. Assume that the S-LM is operated in a range of bias voltage such that the quantum efficiency is unity (i.e. one electron-hole pair of carriers is created for every absorbed photon). The current J , set by the current source, must be identical to the photocurrent produced in the SEED since only negligibly small conduction currents flow through a reverse biased PIN structure. The voltage across the SEED adjusts the absorption in such a way that the number of absorbed photons produces the correct number of carriers for the photocurrent J . Thus,

$$P_i - P_o = \frac{hc}{e\lambda_1} J \quad (2.2)$$

where h is Plank's constant, c and λ_1 are the speed and wavelength of the light in vacuum, respectively, and e is the elementary charge.

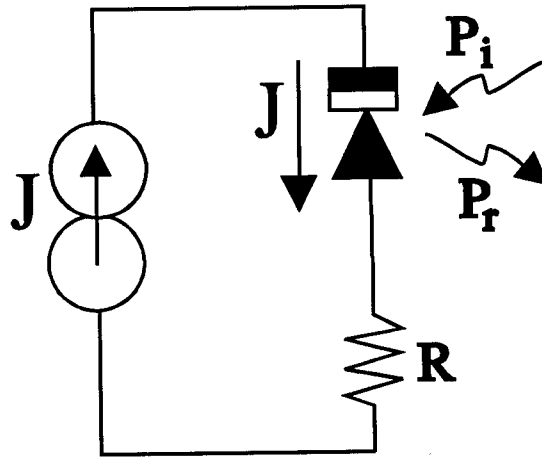


Figure 2.6: Self-Linearized Modulator.

Section 2.C: S-SEED

Some applications require a number of simple SEED circuits to be interconnected or cascaded. Such arrangements require optical gain (fan-out larger than 1) and good on-off contrast ratio. However, a single SEED absorbs power from the optical signal and the contrast ratio can be as low as 2:1. The symmetric or S-SEED alleviates these problems and offers significant advantages for the optical system.

The S-SEED consists of two SEEDs electrically connected in series and uses two parallel optical signals at λ_0 for input and output. One SEED serves as the load for the other as shown on the left side of Figure 2.7a. Two incident optical signals (P_1 and P_2) with equal intensity produce identical photocurrents in the two SEEDs so that the voltage V_1 at the node between them does not change. Only a change from unity in the ratio P_1/P_2 can toggle the S-SEED between stable states. An S-SEED can be used as the output modulator for a logic circuit as shown in Figure 2.7b. Two FETs force the voltage at the common node to change and thereby switch the S-SEED between states. This dual-rail input and output using two parallel optical signals has several advantages over the single ended input and output. First it allows for time-sequential gain where relatively weak optical signals set the state of the S-SEED and two strong optical signals of equal intensity read the state of the device. The read-out beams have equal intensity to ensure that the S-SEED remains in the original state. The fact that the read-out beams have larger intensity than the set beams means that more optical power is available for succeeding stages. The contrast ratio of the SEED no longer matters very much since a factor of two (or more) change in P_1/P_2 from unity is sufficient to switch states. Furthermore, the dual-rail architecture provides a convenient method for representing +1, 0, and -1 as, for example, by $P_1/P_2 > 1$, $P_1/P_2 = 1$ and $P_1/P_2 < 1$, respectively.

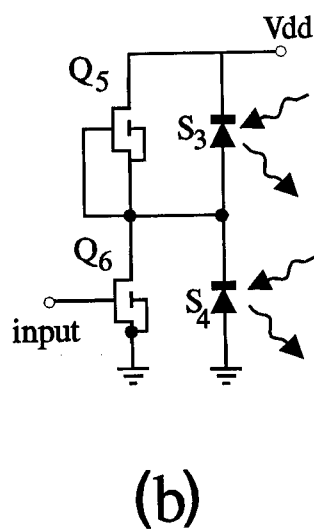
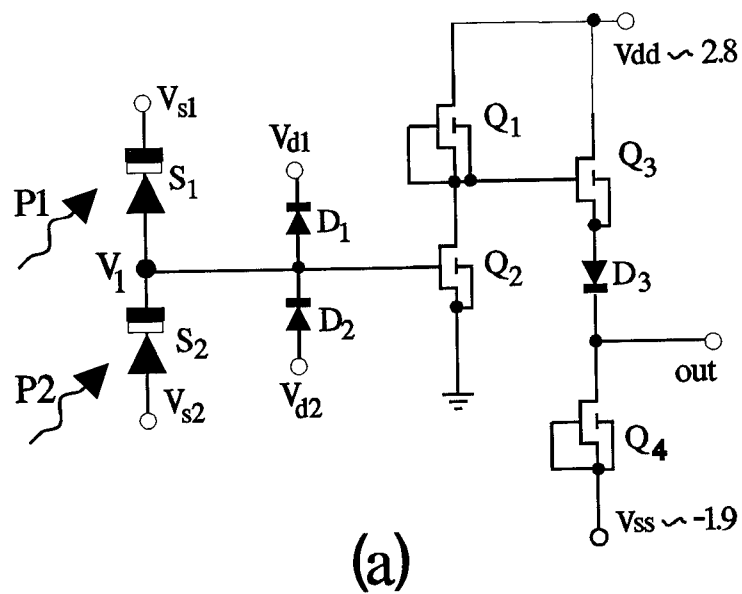


Figure 2.7: a) F-SEED receiver, where S-SEED forms the front end. b) F-SEED transmitter. Reprinted from ATT with permission.

Section 2.D: F-SEEDs

The F-SEED consists of an S-SEED monolithically integrated with a field effect transistor (FET). The F-SEED has optical input and output, and electronics to process logic functions. Figures 2.8a and 2.8b shows the structure of the F-SEED. The F-SEEDs do not need optical bistability⁹ and can be operated at longer wavelengths than the exciton peak. The doped-channel MISFET-like Transistor (DMT)^{9,10} is epitaxially grown on top of the SEED structure that has the P-side on the bottom. The 900 angstrom thick spacer layer functions as the insulator for the gate and the 200 angstrom buffer serves as an insulator between the FET and SEED structures. Source and drain electrical contacts are evaporated on top of the 1000 angstrom n-layer with further processing to make Ohmic contact with the n-channel. The SEED is epitaxially grown on top of a semi-insulating substrate. This type of substrate allows adjacent devices to be electrically isolated from each other. The P-type electrical contacts are made from the top side. As shown by the circuit symbols for the FETs in Figure 2.7, the source is electrically connected to a "backplane." This backplane is the p+ conducting layer below the SEED MQW region. The p+ layer prevents stray electrical fields from affecting the carrier concentration in the channel of neighboring FETs. Thus the p+ layer shields each FET. Light can easily propagate through the n-channel DMTs as is required for the operation of the SEEDs^{9,11}. Figures 2.8a and 2.8b show typical F-SEED circuits.¹² SEEDs S1 and S2 couple optical signals to the FETs. Voltage V_1 varies between V_{S1} and V_{S2} under the control of the optical signals. The voltage on the gate of FET Q2 relative to the voltage on the source should swing from -1 to +1 V. Gate voltages lower than -1 V have negligible effect on the drain current and might cause the transistor to break down. Gate voltages larger than approximately +1 V cause charge to be transferred between the gate and the channel.

Thus, large voltage swings in V_1 must be limited. Diodes D1 and D2 clamp the gate voltage to the range $V_{d2}-0.9 < V_1 < V_{d1}+0.9$. The F-SEED circuits consist of buffered FET logic

(BFL) Devices. Figure 2.7a is a BFL inverter that consists of transistors Q1 through Q4 and diode D3. Transistor Q1, which has a gate to source voltage of zero, serves as the load for Q1. The voltage on the source of transistor Q3 follows the voltage on the gate and they are essentially equal. Transistor Q4 is the load and diode D3 level shifts the voltage for the next gate. The level shifting diodes are necessary since the input stage of a logic gate (Q1 and Q2) always has a source tied to ground. The output voltage V_2 swings from -0.4 to 0.9 V. A second diode in series with D3 is sometimes used to further shift the voltage for different operating voltages. In addition, Q3 can be omitted

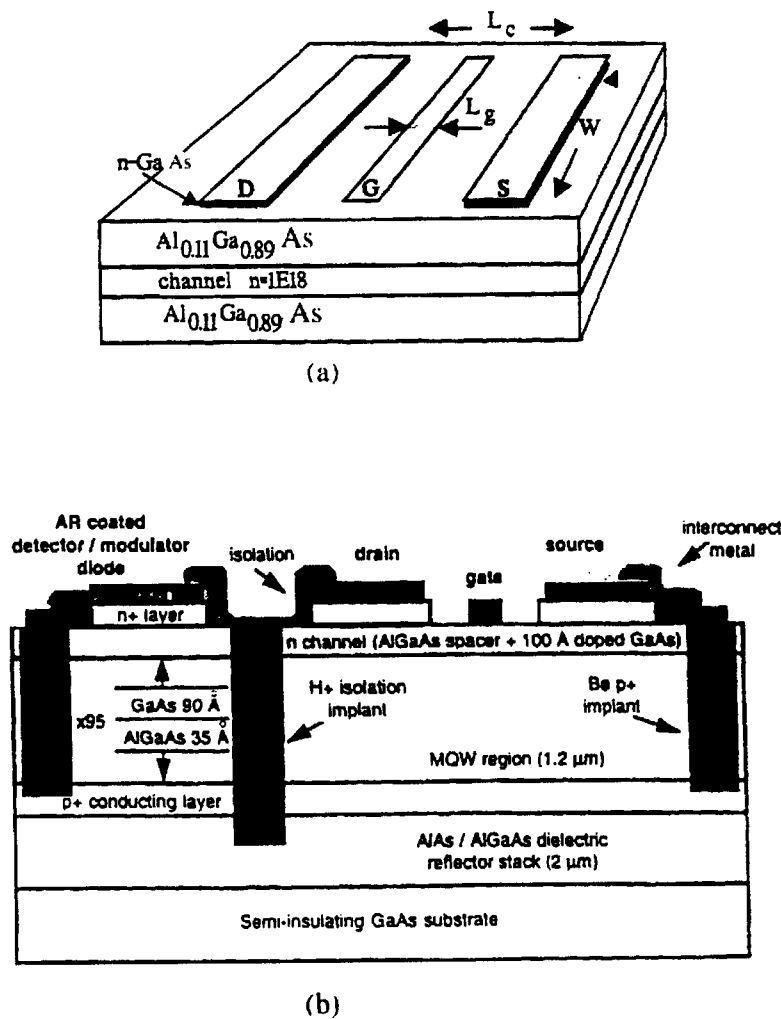


Figure 2.8: a) DMT for the F-SEED. b) F-SEED cross-section. Reprinted from ATT with permission.

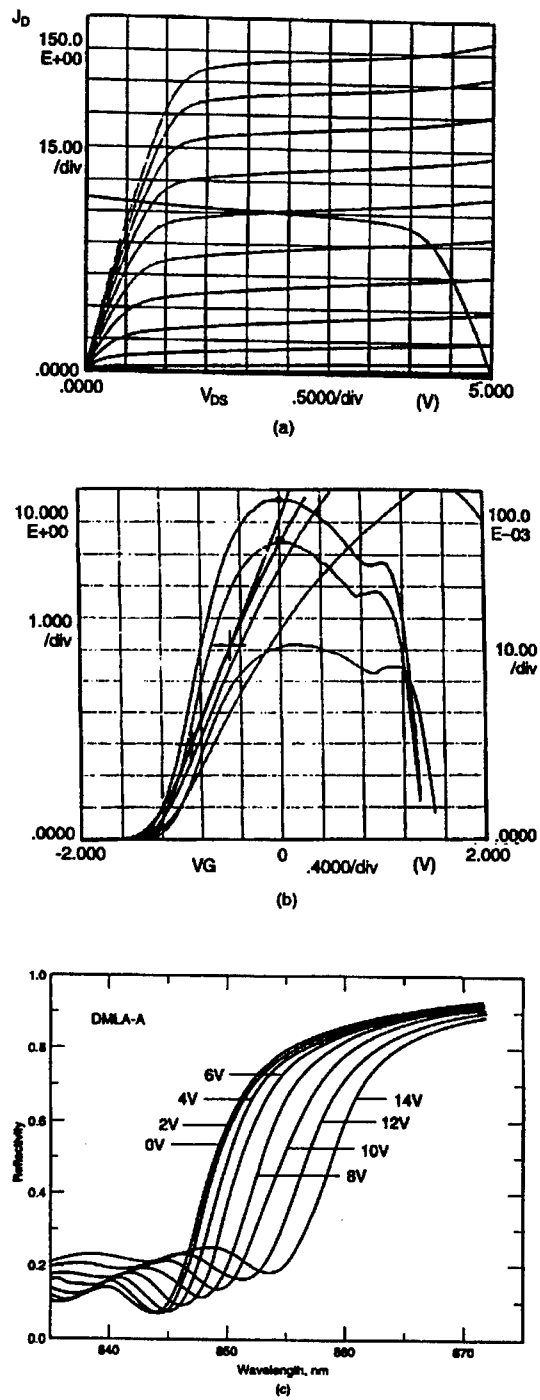


Figure 2.9: a) Plots of J_D vs V_{DS} at values of V_{GS} from -1.2V to +0.8V at 0.2V intervals for a 20 μm wide FET. Superimposed is a load FET curve where $V_{GS}=0V$, (also 20 μm wide). b) FET transfer function. c) SEED reflectivity spectra vs applied bias. Reprinted from ATT with permission

under certain conditions and the logic gate becomes unbuffered. A modulator circuit appears in Figure 2.7b. The voltage at the junction of transistors Q5 and Q6 modulates the voltage across the two SEED devices and, thus, also the reflectivity of the SEEDs.

Typical FET dimensions also appear in Figure 2.8a. The gate width L_g is $1\text{ }\mu\text{m}$ and the channel length L_c is $5\text{ }\mu\text{m}$. The characteristic curves for this device appear in Figure 2.9a. The vertical axis represents the ratio of drain current I_d to the gate width W . The figure shows that FETs with $W = 10\text{ }\mu\text{m}$ typically have drain currents of 1 mA . The FETs can have channel widths W as large as $70\text{ }\mu\text{m}$. Figure 2.9b shows the typical transfer function. Typical reflectivity as a function of bias voltage and wavelength for the SEEDs appear in Figure 2.9c.

The SEEDs and FETs can be combined into many novel and useful configurations. Some of the optical processing applications include edge detection, spatial differentiation, Laplacian operators and neural nets. These systems are made of more elemental circuits such as other logic gates, transimpedance amplifiers, and differential amplifiers.

Section 2.E: Surface Emitting Laser Logic Devices

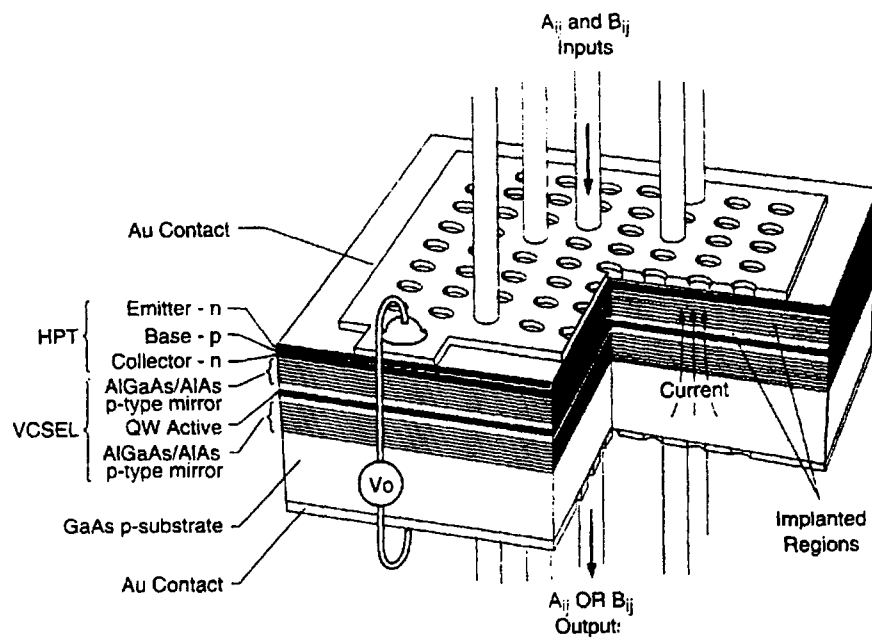
As is evident, SEEDs support a 3-dimensional architecture where the optical signals enter and leave perpendicular to the plane containing the SEED circuits. Such an architecture is important for signal processing applications where a large number of optical interconnections are required to handle large amounts of parallel data flow. Other smart pixel designs use integrated lasers to produce the optical signals. The vertical cavity surface emitting laser (VCSEL) is an ideal emitter for the 3-dimensional architecture.

Photonics Research Inc. (PRI -- now VIXEL Corp.)¹³ is developing surface-Emitting Laser Logic (CELLs) devices for multi-layer signal processing. Figure 2.10a shows the epi-material and device layout. The CELLs consist of a VCSEL and a heterostructure photo-transistor (HPT) that are electrically connected in series. As shown in Figure 2.10b, the VCSEL has distributed bragg

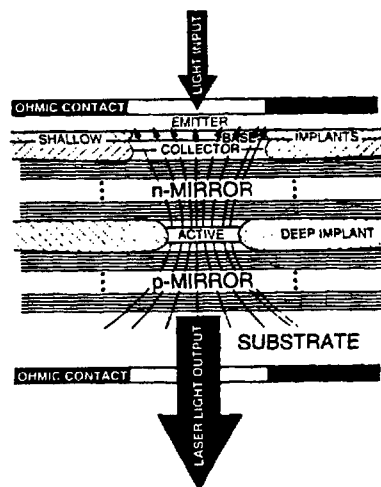
reflector (DBR) mirror stacks that consist of quarter-wave thick alternating layers of GaAlAs and AlAs. The multiple quantum well (MQW) active region is positioned between the mirror stacks. The HPT npn layers are grown on top of those for the VCSEL. Normally, the top mirror stack is almost 100% reflective and so little light enters the HPT from the VCSEL. Thus the epitaxial growth naturally defines a series electrical connection between the HPT and the VCSEL.

Typical performance data from early devices appear in Figures 2.11 and 2.12. The VCSEL has a threshold current on the order of 10 mA. Figure 2.11 shows typical characteristic curves for the HPTs. Figure 2.12 shows the output optical power from the VCSEL versus the input optical power to the HPT and Figure 2.12 shows the circuit schematic. Below 70 mW of input power, the HPT does not supply enough current to the VCSEL for it to lase. For sufficiently intensity input optical power, the VCSEL lases and the CELL has optical gain exceeding a factor of 20. The graph also indicates an on/off contrast ratio larger than 40 to 1. The inset to Figure 2.12 shows the single mode lasing spectrum from the VCSEL.

The CELL device can be connected in a variety of configurations to perform various logic functions. Figure 2.14 shows the AND, OR and XOR configurations and the oscilloscope graphs. The AND configuration requires the combined intensity of two beams for the HPT to provide sufficient current to the VCSEL for it to lase. For the OR configuration, either of two input beams have enough power to produce the result. The XOR operates as follows. One or the other of the two VCSELS will lase when the voltage at the emitter-collector node is above +V or



(a)



(b)

Figure 2.10: a) CELL device layout and material cross-section. b) VCSEL cross-section. Reprinted from PRI with permission.

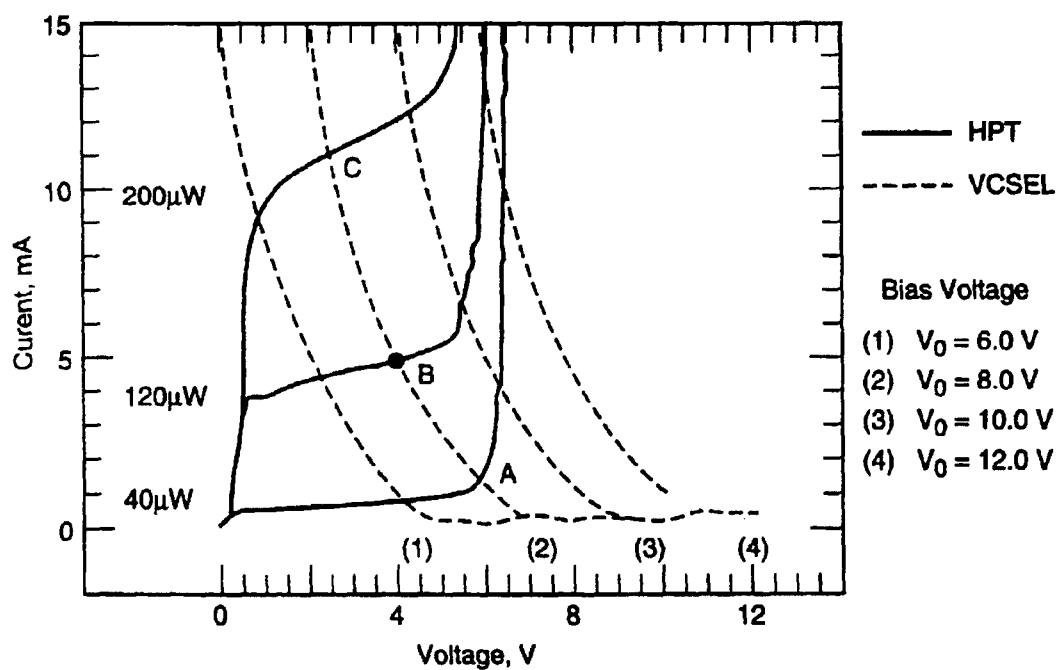


Figure 2.11: HPT and VCSEL current/voltage characteristics. ATT with permission.

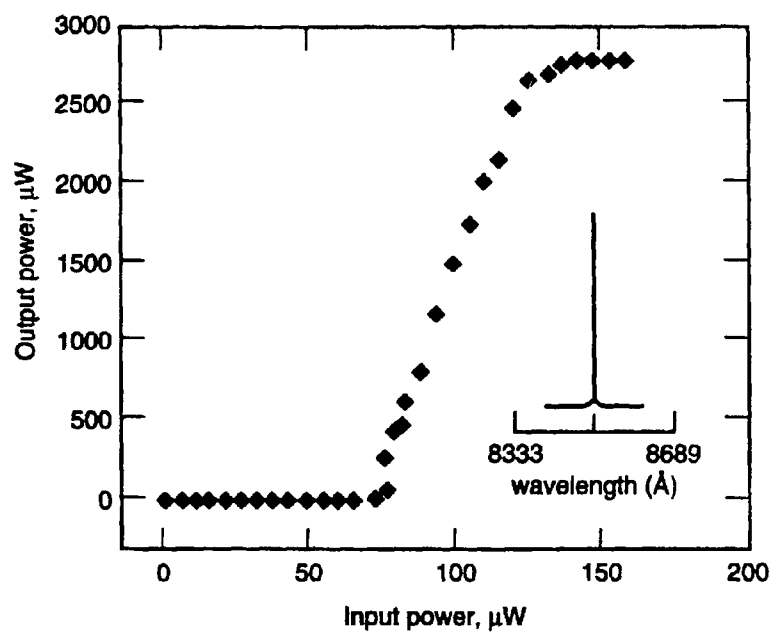


Figure 2.12: VCSEL output/HPT input transfer function. Reprinted from ATT with permission.

below $-V$. The voltage at the node V_{node} is controlled by the ratio of the two input beams A and B. If $A > B$ then $V_{\text{node}} = +V$ and if $B > A$ then $V_{\text{node}} < -V$. However, similarly to the SEED, if the ratio A/B remains constant then there is no change in the output state of the device.

The CELL device can also be used as an optical amplifier or an optical memory element. The CELL can be operated as an optical amplifier in the linear portion of the curve of Figure 2.12. An optical memory element would function as follows. As previously mentioned, the top mirror of the VCSEL is nearly 100% reflective. If this value is reduced slightly, an optical signal from the VCSEL will produce positive feedback from the HPT. With sufficient feedback, the VCSEL will latch in the "ON" state. Additional circuitry must then be included to reset the memory element.

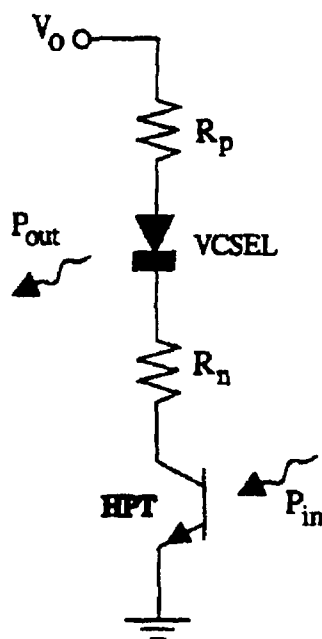


Figure 2.13: Circuit model of CELL.

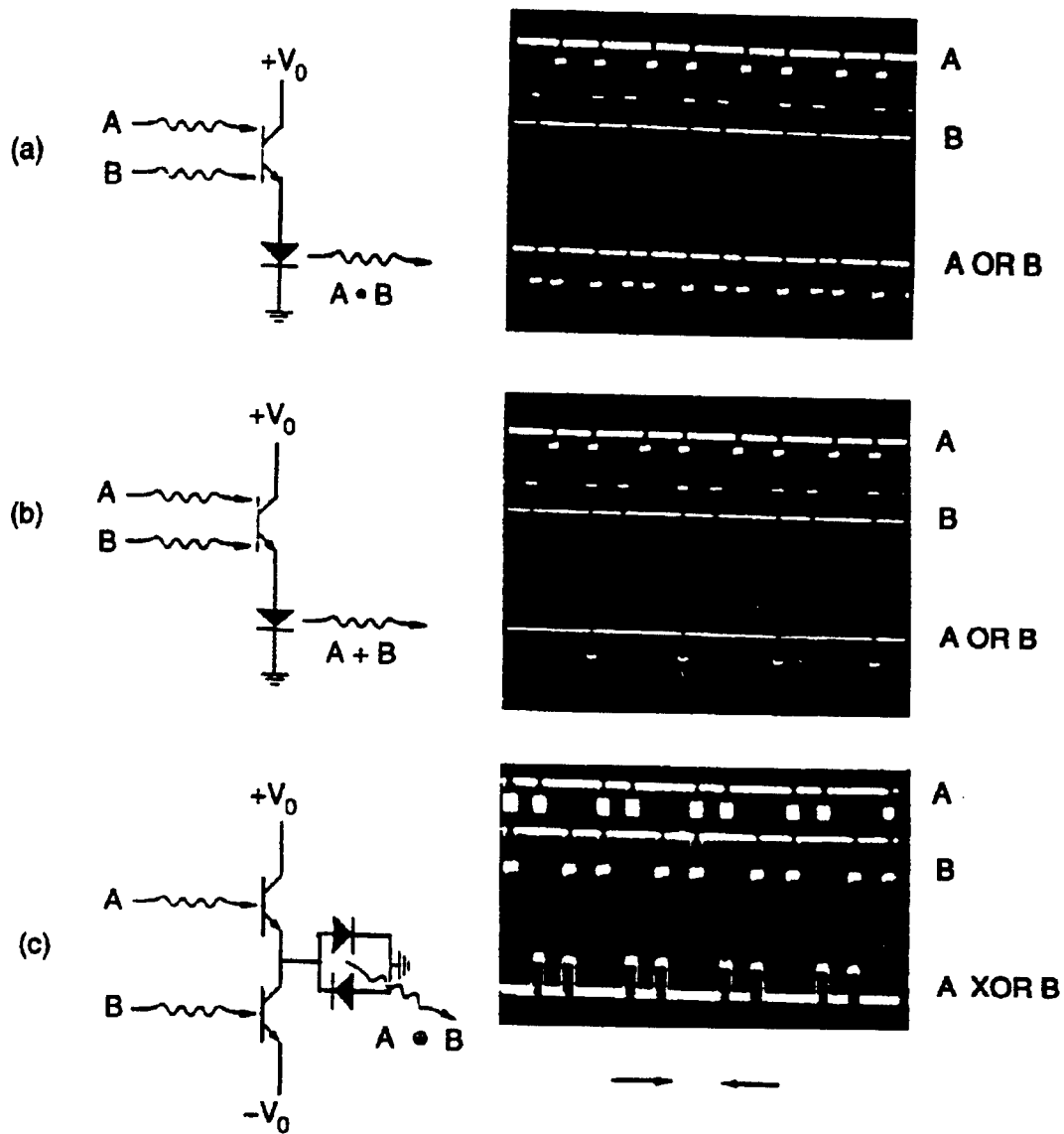


Figure 2.14: Optical input/output pulse sequences and equivalent circuit configuration for optical OR- and AND-gates using a CELL and an XOR-gate using a simple combination of VCSELs and HPTs.

Section 2.F: DOES Smart Pixels

As discussed previously, the F-SEED smart pixel incorporates SEEDs to manipulate optical signals and FETs for logic functions. Such hybrids have significant advantages.¹⁴ The double-heterostructure optoelectronic switch (DOES) is another hybrid smart pixel.

The DOES device¹⁵⁻¹⁷ is similar in operation to a thyristor except that it can emit and detect light. As an emitter, it can be fabricated as either an LED or laser. Figure 2.15a shows the three terminal schematic representation of the ppn (n-channel) device and the corresponding characteristic curves. In operation, the collector C has negative bias with respect to the emitter E. The off-state of the DOES corresponds to the lower branches of the curves that are designated as region 1. Applying negative bias to the inversion channel gate G switches the device from the low to high current state (region 3). These two states are connected by region 2 of the curves which have negative differential resistance. The fact that the current increases with decreasing voltage in region 2 explains why the device is driven towards the on-state once the switching signal is applied. Physically, the switching occurs as a result of adding electrons to the inversion region that forms the active region of the device. The device can be switched to the low current state by removing electrons from the active region. A significant portion of the on-state current pumps the GaAs active layer to produce either the spontaneous or stimulated emission for the LED or laser, respectively.

A cross-sectional physical view of the original npn DOES¹⁶ appears in Figure 2.15b. Note that the electrical biasing scheme is the opposite of that discussed for the ppn device

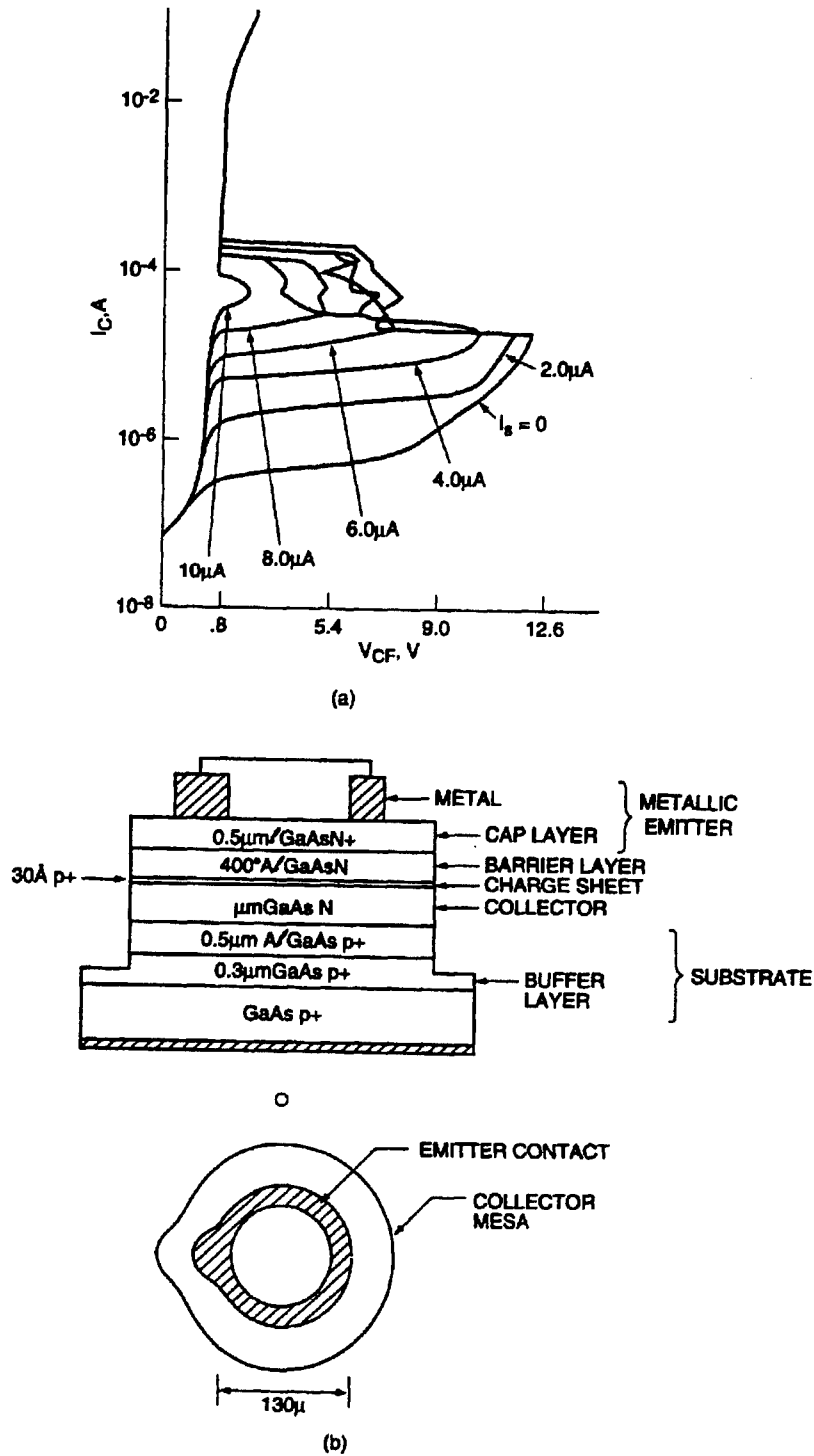


Figure 2.15: a) 3-terminal switching characteristics of an n-channel DOES. b) Physical structure of the DOES. Reprinted from Intelligent Automation with permission.

above. The structure is grown on p^+ GaAs substrate. The subcollector and collector consist of p^+ AlGaAs and n GaAs, respectively. A thin, highly p^+ doped charge sheet is grown into the collector to produce the desired band bending affect at the interface between the collector and an n-type AlGaAs barrier layer.

The DOES can be used in a variety of circuits as a smart pixel. Figure 2.16 shows an electrically addressable inverter. There are two outputs in the circuit. One is an optical signal from the DOES. The other is at the node between the load FET 1 and the DOES; in this case, the signal is a voltage. The smart pixel is electrically addressed to switch it between the emitting (ON) and non-emitting (OFF) states, respectively. For the ppn device shown, electrons or holes must be injected into the gate to switch the DOES to the ON or OFF states, respectively. FET 2 switches the DOES to the ON state and BICFET 1 switches it OFF.

In addition to the binary switch, the DOES can function as an optical memory element. As a result of operation similar to a thyristor, the DOES holds its present state until a signal sets or resets it.

2.G: A Smart-Pixel Cross-Bar

Figure 2.16 shows the block diagram of the cross-bar designed in the Photonics Center. The standard AND, NOR and OR gates are used to represent the functional blocks of the cross bar. The RCVR circuits receive an optical signal and amplify the produced electrical signals; the receivers

2 X 2 OPTICAL CROSS BAR

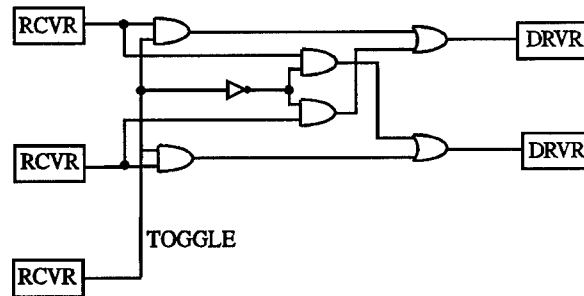


Figure 2.16: The 2x2 optical cross bar logic diagram.

entirely of FET logic. The driver Circuits drive SEEDs configured in the reflective mode.

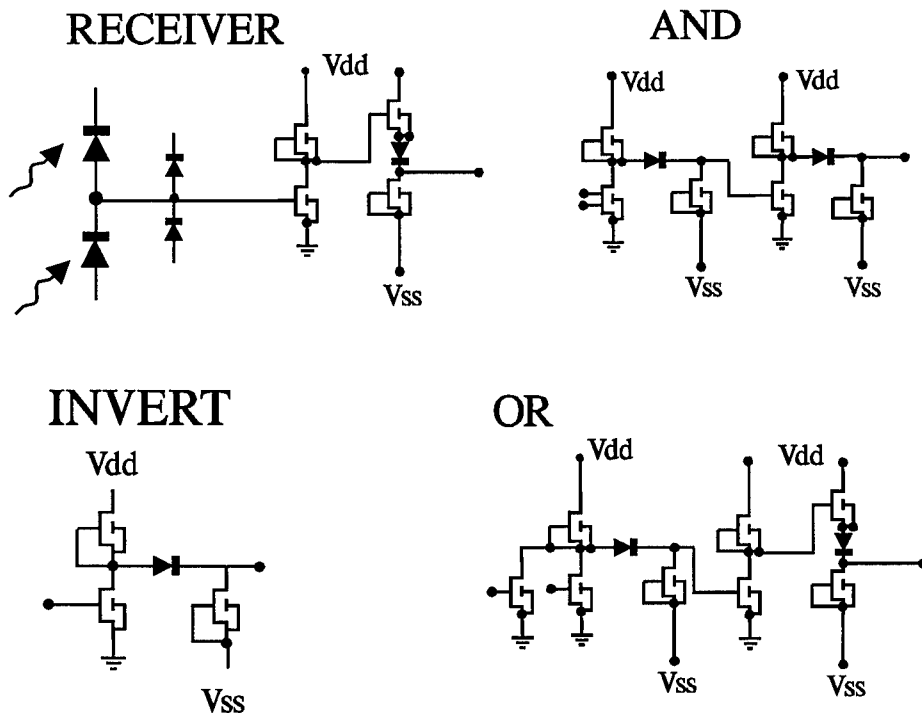


Figure 2.17: The circuits used in the cross-bar. The receiver circuit is shown elsewhere in Chapter 2.

These circuits appear in Figure 2.17 and operate in a manner similar to those described previously in the chapter.

2.H: A SEED Smart-Pixel Neuron

Field Effect Transistors (FETs) monolithically integrated with Self Electrooptic Effects Devices (SEEDs) offer great flexibility for optical processing

circuits.²⁸ This section describes an SEED-

based neuron invented by M. A. Parker (unpublished). Automated intelligence data classification schemes require digital computing and data storage resources beyond the state of the art. The computing and programming requirements can be reduced via the use of neural net architectures. Due to the high density and interconnectivity of large neural nets, optics can play a key role in communicating between planes of neurons. Integrated electronics and SEED-detectors or modulators allow the best features of electronics and optics to be used.

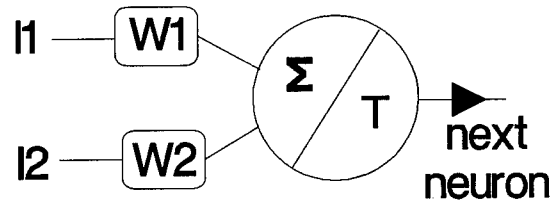


Figure 2.18: Functional diagram of a two input optical neuron.

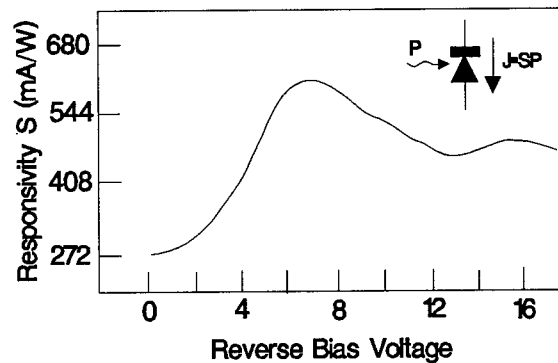


Figure 2.19: Responsivity of the SEEDs after references 2 and 3.

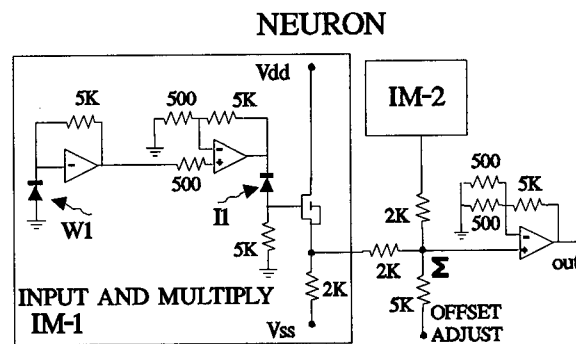


Figure 2.20: The SEED neuron.

Figure 2.18. The optical inputs I_i are weighted by W_i (also optical inputs) and summed. If the sum exceeds a threshold value T then the neuron fires and passes a logic 0 or 1 to other neurons. Thus, the neuron implements the function $\Psi = H[\sum I_i W_i - T]$, where H is the Heavyside step function and Ψ is the output. The multiplication in Ψ is normally difficult to implement with conventional

electronics. However, the multiplication can be easily performed in the SEED device by making use of the Quantum Confined Stark Effect. The photocurrent J produced by the SEED due to incident optical power P is $J = SP$ where S is the responsivity. Figure 2.19 shows^{12,29} the responsivity of the SEED (operated as a photodetector) as a function of reverse bias voltage. The responsivity increases by almost a factor of 3 for a six volt change in bias. Thus P and S can represent the input I_i and weight W_i , respectively, over that range.

The complete prototype neuron appears in Figure 2.20. Optical power incident on SEED W_1 representing the weight is amplified to 4 or 5 Volts by the two integrated amplifiers and applied across the series combination of the SEED I_1 and the resistor. The voltage drop across that resistor is negligible. However, optical power incident on SEED I_1 produces small photocurrents that raise the potential on the gate of the FET to no more than 0.1 Volts. Thus the multiplication of $I_1 W_1$ is relatively independent of the input power I_1 . The box IM-2 represents another circuit similar to the Input and Multiply circuit IM-1 just discussed. The resistor combination at point Σ provides the summing function. For this prototype, an amplifier takes the place of the thresholding function after the summing junction for testing purposes. After electrical summing of many in-plane neurons, SEEDs can also be used as modulators (not shown) to connect to other neural planes.

Section 2.I: Summary Discussion

The smart pixel is an opto-electronic device that functions both as an optical interconnect and as a logic element (analog or digital). It consists of a single device or a small cluster of monolithically integrated devices. As an optical interconnect, it transmits and receives information using light rather than electrical current. The logic function can be as simple as the amplification of an input signal to as complicated as a complete packet switching unit. Some smart pixels receive electrical information and simply convert it to the optical domain or vice versa.

Smart pixels are photonic devices that form a compact link between the electronic and optical domains. They represent the basic building blocks of future technology since they are built from both electronic and optical components. The definition above embraces a large number of devices. However, when electronic components are part of the pixel, they will generally be Field Effects Transistors (FETs), Heterostructure Bipolar Transistors (HBTs) or Heterostructure PhotoTransistors (HPTs). The optics can include integrated lenses, photodetectors, lasers, laser amplifiers and Self-Electrooptic Effect Devices (SEEDs).

There is presently a debate as to whether the most suitable devices to meet the future needs of the DOD and commercial sectors are all electronic or all optical. Electronic devices represent a trillion dollar industry especially for computer chips. But recently, industry has recognized the inherent advantages of some optical devices especially for Compact Disks, communications and special types of computing using optical images. The analyst naturally questions which technology is better and which one will survive into the 21st century.

This tends to be a complicated question of economics and technology. However, a simple argument proves that, during the next 10 to 20 years, the best suited devices will be opto-electronic (i.e., photonic). The argument proceeds as follows. Electronics is a well-established industry with products that permeate all aspects of our lives. The electronic devices are low cost and highly reliable. In addition, electronic devices can be made significantly smaller than optical ones

since, for light to interact with matter, at least several wavelengths (about 1/2 micrometer in GaAs) are required. On the other hand, optics has significantly larger bandwidths (more communications channels) since the electronic devices are limited by the long-range Coulomb interaction between charged particles. This long range interaction is also responsible for the unacceptable cross-talk in electronic circuits at high modulation frequencies. *Thus optics and electronics compliment one another.* But, *optics and electronics can never be separated* because light must interact with charge for it to be useful. As is evident, photonic devices should continue to become more important. The fact that there can be so many different types of smart pixels suggests that there are also many different applications. The following list contains example applications.

- * Distributed signal processing systems such as neural networks and packet switching networks consist of communication channels (optical fibers for example) that interact at nodes. These nodes intercept information, perform calculations or logic functions and then transmit the results to the next node. The most natural choice of device for the node is the smart pixel.

- * A telephone switching network is a prime example. Here, large numbers of telephone lines (fibers) must be interconnected. A smart pixel can be used as the router. As another example for switching networks, suppose that 1000 lines must be interconnected with another 1000 lines at a local node. Then 1,000,000 interconnections are required. It is possible to replace these interconnections with one dynamically reconfigurable interconnection so long as the reconfiguration speed is fast compared with the data.

- * Computers will one day use optical backplanes to transmit signals from circuit board to circuit board rather than using the slower electrical transmission lines used today. Speeds can be increased over 1000 fold by using smart pixels to tap into the optical data flow and converting it to the electronics domain.

- * The smart pixel can be used for image processing where, for example, an input image is corrected or enhanced in real time for the viewer or robotics system. These pixels can be integrated as a pre-processor to perform similarly to the retinas in many animals. Incidentally, such a smart pixel based pre-processor would significantly enhance the performance of present computer software for target and image recognition systems.

- * Fly-by-light for advanced jet fighters and commercial airlines will use variations of smart pixels for the interfaces between the computers and the actuators at the airfoils. Similarly, photonic fabrics in the airfoils (smart skins) can use local processing to reduce the data flow before passing it on to the main computer set.

Smart pixels as opto-electronic devices require further development. There are two considerations for ascertaining the present status. The first consideration is more of an architectural issue in the sense that various materials and techniques for fabrication are available. The second consideration focuses on the devices that are actually available at present.

The monolithic integration of FETs and lasers potentially has the highest near term payoff of all the smart pixels. The lasers can be used as emitters or detectors for optical signals while the FETs provide for the logic. These devices are presently under development at various laboratories including Cornell University and the Photonics Center at Rome Laboratory. These FETs and Lasers are expected to have considerable impact on neural network and packet switching technologies. Companies such as Photonics Research Incorporated (Boulder CO) and Intelligent Automation (MA) are developing the Surface Emitting Laser Logic (CELL) and the Inversion Channel Technologies, respectively. These smart pixels consist of VCSELs, HPTs, and thyristors that are epitaxially grown on GaAs. The devices are ideal as optical logic gates or amplifiers in 3-D computer architectures.

Vertical Lasers with Optical Gain Control (V-LOGiC) consist of VCSELs and In-Plane Lasers (IPL) with cross-coupled cavities. Laser emission from the IPL *optically* quenches the VCSEL. The patents on the devices describe applications such as optical ATM switches and spontaneous emission filters for laser amplifiers (Cornell University and Rome Laboratory, alphabetical order). Gain quenching has the highest modulation bandwidth out of any of the methods for modulating semiconductor lasers. Configurable Optical Gates (COGs) are another laser-based smart pixel (patent with Cornell University and Rome Laboratory, alphabetical order). Integrated detectors drive a modulator section within the cavity of the laser. The COGs form a complete Diode Laser Logic (DLL) family with all of the basic Boolean logical functions. In addition, the COGs greatly simplify the design of optical adders and optical crossbars. Variations of the COGs should find considerable application in switching networks and fly-by-light systems.

Smart pixels have applications in the area of optical memory and mass storage. Besides the use for reading or writing optical disks, the smart pixels can be configured as memory elements. Low Temperature GaAs and amorphous silicon are presently being investigated for weighting functions for neural networks. In addition, the advent of GaN lasers (Cornell University and Rome Laboratory, among others) promises to increase the storage capability of optical disks considerably.

There are applications for the department of defense. Surveillance requires high speed signal processors for radar, target detection, target identification, and jamming. Parallel 3-D architectures potentially offer the highest computational throughput for these purposes. Command and Control requires structures with multiple, dispersed nodes and distributed function (distributed processing systems). These distributed systems increase the speed, flexibility and survivability of the strategic systems. Communications need ATM and PACKET switches for tactical battlefield communications scenarios. Intelligence requires neural networks as an intelligent link between sensors and personnel for data classification purposes. The potentially large number of sensors place stringent requirements on the processing, such as correlation and fusion, and routing of data. As another example, it has been predicted that the time required to break codes can be greatly reduced by using opto-electronic computers consisting of quantum dots. Signal processing thrusts develops scalar, vector and special purpose signal processors. These thrusts explore the fusion of data from multiple surveillance radar units and IR cameras, advanced architectures, wafer scale vector processors, and integrated RISC processors. Avionics requires modules for fly-by-light and smart skins. All of these requirements can be addressed by distributed optical signal processing systems that use photonic smart pixels as the basic building blocks.

Present commercial developments are in optical interconnects, light emitters, GaAs electronics, personal communications services. The applications discussed in sections II and IV are just beyond the cutting edge of technology and require further research and development. The work

should continue to invent new components as alternatives to existing ones. Often there is the opinion that if existing components are available and serve the purpose then there is no need to invent new, untested technology. However, new ideas translate to new and improved systems, economic growth, and improved defensive capabilities in addition to the transfer of dual use technology, patents, publications and funding. The work should explicitly investigate new technology and employ the already developed technology when appropriate.

It is possible for government and academic laboratories to develop new technology and then transition it to the commercial sector for further development. Usually this requires well-developed concepts since the commercial sector tends to prefer near term payoffs. The laboratories are useful for this initial development since there is not the same degree or type of pressure for a product that can be sold. However, personnel in these laboratories need to be more aware of the needs and trends in other areas. Continued emphasis and practice of the basic premises of technology transfer and programs that support dual use technology should improve the situation.

Many of the devices are not available at this time. Once fully developed, commercialization will obviously reduce the unit cost, increase reliability and increase performance.

Present trends in communications should continue. Historically, communication has progressed through printing, AM and FM radio, television, cable TV, the internet and satellites. This growth will continue and the next 20 years will be critical. Development of distributed processing systems such as the packet switching network will be necessary for handling the massive routing problems associated with that growth.

Improvements in communications naturally implies increasing demands for mass storage systems and ultra high speed computers. These increasing demands are a result of many factors including economic growth, computerization of banking and business, growth in the film and music industry, increases in knowledge such as that found in professional journal publications and expansions in aviation routing. As a result, optical memory in the form of integrated memory

devices and mass storage systems will become more important. In addition, signal processors must become faster to sort through the data and also to meet the demands of future signal processing.

Research will begin on new types of computers. The opto-electronic signal processor will certainly be an area of intense interest in all sectors. Special attention must be given to the growth and fabrication of direct bandgap materials. As previously mentioned, a processor based on quantum dots might prove to make present security coding obsolete. Molecular computers that use molecules as the computing element might become more intensely researched especially if a DNA type of growth mechanism can be used to fabricate these devices. Neural networks will be essential for many diverse applications including pattern and target recognition, oversight of manufacturing processes and the automation of many medical procedures or artificial limbs.

Chapter 3: A Brief History of Quenched Laser Devices

The quenched laser devices were invented by W. F. Kosonocky in 1964. Although Figure 3.1 is a representation taken from J. Fitz's subsequent 1989 patent, it provides a convenient geometry for discussion. As shown in Figure 3.1, K_m and K_s are the propagation vectors for the optical modes in the main and side lasers respectively. The main laser is normally "on" with emission parallel to K_m . Turning

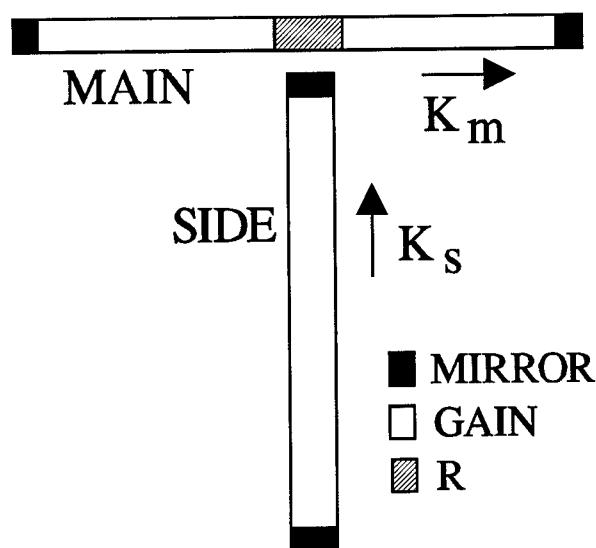


Figure 3.1: Basic Geometry for laser quenching.

"on" the side laser causes photons with wave vectors K_s to interact with the gain medium R of the main laser cavity. These K_s photons compete with the K_m photons for the gain of region R . As a result, the average gain along the main laser is lowered (for fixed bias current) and the output intensity of the main laser decreases. The competition for the gain causes an increase of the threshold current and a decrease in the external differential efficiency of the main laser. The exact quantum mechanical treatment will be discussed in the Technical Report for 4600P130 which should be available in 1997.

There are several relevant patents, publications and patent applications. The original patent covering certain types of gain-quenched devices is #3,431,437 by W. F. Kosonocky, "Optical System for Performing Digital Logic." Another patent is by J. L. Fitz, #4,825,442, which is titled "Planar Optical Logic." A relevant patent application by M. A. Parker, D. B. Shire, P. D. Swanson, C. L. Tang, R. J. Michalak, J. S. Kimmet covers "Vertical cavity surface emitting Lasers with Optical Gain Control (V-LOGiC)." More detail is available in the next few

chapters along with the publication by W. J. Grande and C. L. Tang on "Semiconductor Laser Logic Gates Suitable for Monolithic Integration," (Appl. Phys. Lett., 51, 1780 in 1995).

The invention by Kosonocky, shown in Figure 3.2, is the first gain-quenched laser gate. The semiconductor material directly between the two mirrors 22 and 24 forms the main laser cavity. Applying current to the entire section 20 results in laser oscillation along 26. The material in section 20 that is

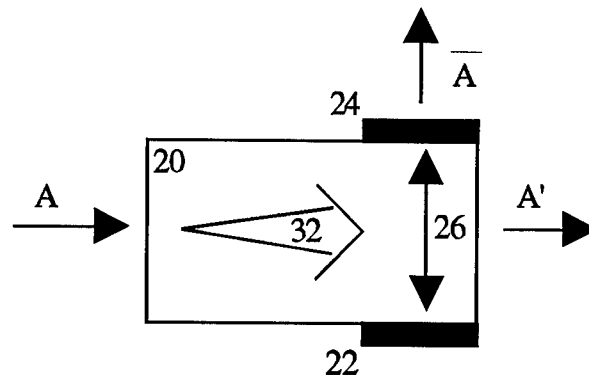


Figure 3.2: The first gain-quenched laser gate.

outside the main laser cavity (i.e., material to the left of mirrors 22 and 24) functions as a laser amplifier section. An input laser signal "A" is amplified (32) and competes with 26 for the gain between the two mirrors.

Kosonocky also describes an optical clock that is reproduced in Figure 3.3. The clock consists of the main laser (26) that is optically coupled to an optical fiber (90). The fiber provides the input to the laser amplifier (32). The fiber provides feedback and adds delay, and the amplifier quenches the laser. In operation, when the laser

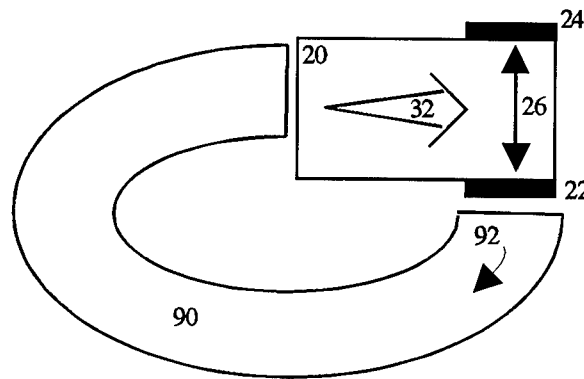


Figure 3.3: The Kosonocky clock.

begins to lase, the fiber directs the emission into the amplifier which in turn quenches the laser. In this way, the laser is modulated. The length of the fiber controls the repetition rate of the optical clock.

The patent by J. Fitz discusses optical logic gates that use the output from one in-plane laser to quench another in-plane laser. The geometry is similar to that shown in Figure 3.1. These devices do not use the laser amplifier described above.

W. Grande and C. L. Tang monolithically integrated the in-plane lasers and changed the geometry for higher efficiency as shown in Figure 3.4. The main laser is now included within the cavity of the side laser. The efficiency for quenching is increased because the intensity of the side-laser optical mode is larger inside the cavity than outside. Thus, the competition for the gain in region R tends to favor the side laser.

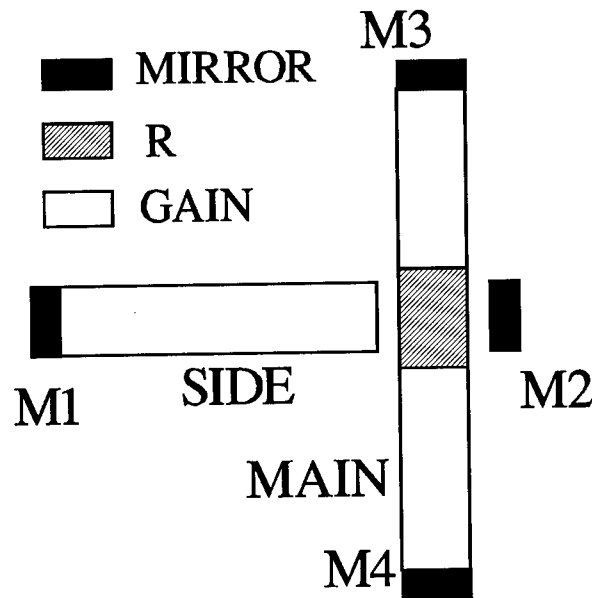


Figure 3.4: The Grande and Tang gate.

The patent application by Parker et al. describe Vertical cavity surface emitting Lasers with Optical Gain Control (V-LOGiC) as shown in Figure 3.5. The VCSEL is placed within the cavity of the In Plane Laser (IPL). Both the VCSEL and the IPL are formed from

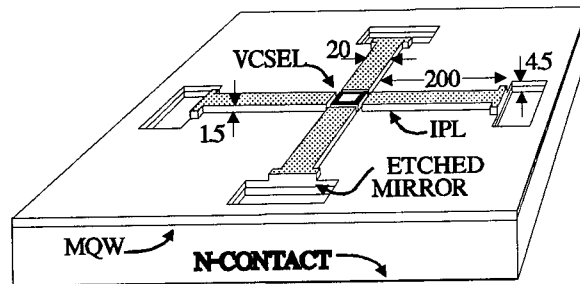


Figure 3.5: The first V-LOGiC NOR gate.

the same heterostructure which is normally used for VCSELs. The top and bottom mirrors for the VCSEL consist of epitaxially grown layers that form a DBR stacks. The four mirrors for the two IPLs are formed by etching the wafer (refer to Chapters 11-15) past the active region. As is evident, the geometry of the V-LOGiC device is suitable for a multiplanar architecture.

Chapter 4: A Phenomenological Model for Optically-Quenched Lasers

In this chapter, a model is presented for optically controlling the gain of a semiconductor laser by introducing photons from a second coherent source into the side of the laser. The threshold current of the laser increases in direct proportion to the overlap between the two modes and the photon density from the coherent source. An easy-to-use, closed-form expression relates the optical power emitted from the laser to the bias and threshold currents. The RF modulation bandwidth is obtained and is used to resolve a standing argument regarding the speed of the quenched lasers as switching elements. Using the Liouville Equation and the density matrix for multiple optical fields, a subsequent Technical Report (for 4600P130) will justify the assumed form of the optically-quenched laser rate equations and generalize these to include wavelength.

Section 4.A: Introduction

Recent work demonstrates the feasibility of optically controlling the gain of one laser with another.¹⁻⁵ These quenched laser devices can be monolithically integrated in a variety of laser heterostructure including that for strained and unstrained quantum well lasers, and Vertical Cavity Surface Emitting Lasers (VCSELs). Furthermore, the device operation is independent of wavelength, making it useful for future lasers such as GaN (blue-emitting), infra-red (1.5 μm) and visible lasers. These optically quenched lasers have myriad applications for all-optical high-speed switching. One of the most interesting applications consists of an all-optical 1:N signal router² employing a 3-D architecture. However, despite the growing popularity for the optically-quenched laser devices, a simple easy-to-use model is not available to describe the basic operating principles.

Models^{6,7} are available that use digital computers to numerically solve the three (or more) coupled, non-linear, differential laser rate equations. However, considerable insight into the operation of the quenched devices can be gained from an approximate closed-form expression for the main-laser output power (above threshold) versus the injected bias current. The quenched-laser

devices consist of a semiconductor laser, which is either an In-Plane Laser (IPL) or a Vertical Cavity Surface Emitting Laser (VCSEL), and a control source such as an optical amplifier or another laser (see the inset to Figure 4.1). The beam from the control source competes with the main-laser optical mode for the gain in the overlap length L_b . As the intensity of the control source increases, the intensity of the main laser is optically quenched and decreases.

We show that, with the main laser operating at currents above threshold, the photon-number density γ (cm^{-3}) in the laser is directly proportional to the current-number density \mathcal{J} ($\text{cm}^{-3}\text{s}^{-1}$) and the control-photon density γ_c as given by

$$\gamma = \tau_\gamma (\mathcal{J} - \mathcal{J}_{\text{thr}} - \epsilon \gamma_c / \tau_\gamma) \quad (4.1)$$

where ϵ is the fractional overlap of the two modes (i.e., $\epsilon = L_b/L$ in the inset to Figure 4.1), $\epsilon \gamma_c / \tau_\gamma$ is the increase in the threshold current-number density \mathcal{J}_{thr} due to quenching (for simplicity, \mathcal{J} and \mathcal{J}_{thr} will be referred to as current density). The cavity lifetime τ_γ for the main laser accounts for the distributed optical losses α and the power-reflection coefficient $R \cong 0.34$ for the mirrors through the relation⁸ $1/\tau_\gamma = v_g \alpha - (v_g/L) \ln(1/R)$. The constants v_g and L are the velocity of the optical modes and the length of the main laser, respectively. This expression shows that the threshold current (and, hence the output power density) of the main laser is linearly controlled by the power density of the control source as well as the size of the overlap

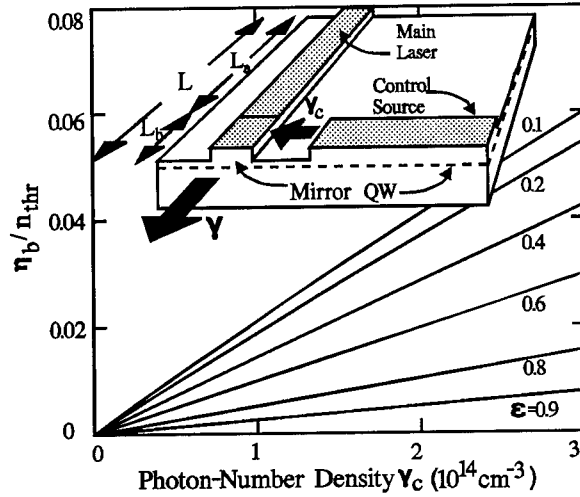


Figure 4.1: The inset shows a schematic view of a quenched laser device using an in-plane main laser and another in-plane coherent source. The output from the control source overlaps the main optical mode in the length L_b of the main laser. γ and γ_c are the photon densities in the overlap region due the main laser and the control source, respectively. The graph indicates the fractional deviation between the carrier density in length L_b and the threshold carrier density. Larger overlap $\epsilon = L_b/L$ between the beam from the control source and the main-cavity mode results in smaller deviations from threshold. For typical values of the parameters, the gain in the quenched section differs by less than about 5% from the threshold value.

coefficient $R \cong 0.34$ for the mirrors through the relation⁸ $1/\tau_\gamma = v_g \alpha - (v_g/L) \ln(1/R)$. The constants v_g and L are the velocity of the optical modes and the length of the main laser, respectively. This expression shows that the threshold current (and, hence the output power density) of the main laser is linearly controlled by the power density of the control source as well as the size of the overlap

region. For reference, Equation 4.1 can equally well be written in terms of optical output power $P_o = (hc/\lambda)(\gamma v_g/2)(1-R)A_m$, optical input power $P_i = (hc/\lambda)(\gamma_c v_g)A_c$ and the bias current $I = qVe$ as

$$P_o = m \left[I - I_{thr} - \epsilon P_i \frac{(1-R) A_m}{2m A_c} \right] \quad (4.2)$$

where $m^{-1} = [eV/\Gamma\tau_r](\lambda/hc)(2/v_g)[1/(1-R)]$. The undefined symbols are the optical confinement factor Γ , Plank's constant h , the speed c and wavelength λ of both optical modes in vacuum, the cross sectional area A_m of the main-laser mode, the cross sectional area A_c of the control beam, the volume $V = A_m L$ of the main laser and the elementary electronic charge e . Although macroscopic parameters such as optical power and bias current are the measured quantities, they lead to ambiguities in the final form of the equation. The absence of the factors of 2 and $(1-R)$ in P_i presume the control source is not a laser. Also, the exact sizes of the modal cross-sectional areas are not well defined. The factor of 2 in P_o occurs since only half of the photons travel toward the output facet of the main laser. If the control source is also a laser, then the form of Equation 4.2 must be changed. We will continue to use the basic quantities in Equation 4.1 since the equations appear simpler and slightly more general.

Section 4.B: Approximate Closed Form Solution of the Laser Rate Equations

The modified laser rate equations⁶ for the device shown in Figure 4.1 are given by

$$\frac{dn_a}{dt} = -g_a \gamma + \mathcal{J}_a - \frac{n_a}{\tau_n} - R_a \quad (4.3)$$

$$\frac{dn_b}{dt} = -g_b (\gamma + \gamma_c) + \mathcal{J}_b - \frac{n_b}{\tau_n} - R_b \quad (4.4)$$

$$\frac{d\gamma}{dt} = \langle g \rangle_\epsilon \gamma - \frac{\gamma}{\tau_\gamma} + \beta \langle R \rangle_\epsilon \quad (4.5)$$

where g_a and g_b are the saturated gain coefficients for the two sections that can be linearly approximated by $g_a = g_o(n_a - n_o)$ and $g_b = g_o(n_b - n_o)$, n_a and n_b are the carrier densities in the two regions, n_o is the transparency density, τ_n is the non-radiative carrier recombination rate, $R_a = sn_a^2$

and $R_b = s n_b^2$ are the recombination rates for spontaneous emission in the two sections, s is a coupling constant, the average gain is $\langle g \rangle_\epsilon = (1-\epsilon)g_a + \epsilon g_b$, the average rate of spontaneous emission is $\langle R \rangle_\epsilon = (1-\epsilon)R_a + \epsilon R_b$, and β gives the amount of spontaneous emission coupled into the main waveguide mode. As is well known, the noise $\beta \langle R \rangle_\epsilon$ initiates the laser oscillation but, above lasing threshold, $\beta \langle R \rangle_\epsilon$ is typically several orders of magnitude smaller than the other terms in Equation 4.5. The average carrier density $\langle n \rangle_\epsilon = (1-\epsilon)n_a + \epsilon n_b$ and the average current density $\langle j \rangle_\epsilon = (1-\epsilon)j_a + \epsilon j_b$ are obtained by considering the total number of carriers $\langle n \rangle_\epsilon V = n_a V_a + n_b V_b$ and the total bias current $\langle j \rangle_\epsilon V = j_a V_a + j_b V_b$ (V_a and V_b are the active volumes of the two laser sections). The two sections are assumed to have the same current density for the purpose of this discussion ($j_a = j_b = j$).⁹ There are several remarks regarding the rate equations: (i) carrier diffusion⁸ and Auger recombination⁸ are not included; (ii) passive q-switching is not included since it occurs when $\gamma_c = 0$ and separate carrier lifetimes (i.e. separate, unequal biases) are used for the two regions;¹⁰ (iii) any bistability in γ vs. γ_c is ignored since it generally requires a saturable absorber;⁷ and (iv) gain saturation and compression¹¹ can be included without affecting the analysis but they are both negligible for laser intensities that are small compared with the saturation intensity and gain compression is negligible for GaAs-AlGaAs semiconductor lasers.

A key observation in writing Equations 4.3-4.5, namely, the gain of the two sections can be written as an average along the length of the main laser $\langle g \rangle_\epsilon = (1-\epsilon)g_a + \epsilon g_b$. This observation is important since, for steady-state operation above threshold, the photon density γ is adjusted by the dynamics of the laser until the *average* gain locks to the optical losses as given by $\langle g \rangle_\epsilon \cong 1/\tau_\gamma$. However, using the linear approximation for g_a and g_b , the average gain of the laser can be written in terms of the average carrier density as $\langle g \rangle_\epsilon = g_0(\langle n \rangle_\epsilon - n_0)$. Therefore, the average carrier density locks to the threshold value according to $\langle n \rangle_\epsilon = n_{thr} = n_0 + 1/(g_0 \tau_\gamma)$ even though the carrier densities of each section might be different.

The fact that the averaged quantities are determined by the optical losses of the laser suggests that the average carrier density is a better variable to use in Equations 4.3-4.5. Multiplying Equation 4.3 by $(1-\epsilon)$ and Equation 4.4 by ϵ , adding the two together, and substituting for $\langle g \rangle_\epsilon$ yields

$$\frac{\gamma}{\tau_\gamma} + \epsilon g_b \gamma_c = \mathcal{J} - \mathcal{J}_{thr} \quad (4.6)$$

where the threshold current-number density for the main laser is given by $\mathcal{J}_{thr} = \mathcal{J}_n + \mathcal{J}_s = (n_{thr}/\tau_n) + (sn_{thr}^2)$, where \mathcal{J}_s and \mathcal{J}_n are the portion of the threshold current due to radiative and non-radiative spontaneous recombination, respectively. For simplicity, we assume steady-state conditions both here and for the remainder of the discussion. Equation 4.1 follows once we establish that $g_b \approx \langle g \rangle_\epsilon$.

Although the algebra is tedious, several interesting features emerge while showing that the control intensity has only a small effect on the carrier density and the optical gain. In principle, the constraint on the average $\langle n \rangle_\epsilon$ does not fix the carrier density for each section. The deviates $\eta_b = n_{thr} - n_b$ and $\eta_a = n_a - n_{thr}$ measure the departure of each from the average. Further, the deviate η_b is considered to be a second new variable for Equations 4.3-4.5. Similarly, define the quantity $\delta_\gamma = \gamma_u - \gamma$ to measure the amount of optical quenching in the main laser where γ_u is the un-quenched photon density that satisfies Equations 4.3-4.5 when $\gamma_c = 0$. The deviates η_a and η_b are both positive (i.e., $n_a > n_{thr} > n_b$) for non-zero control intensity ($\gamma_c \neq 0$) because (i) $n_{thr} = \langle n \rangle_\epsilon$ is an average and therefore, n_{thr} must have a value between n_a and n_b , and (ii) \mathcal{J} in Equation 4.3 is larger than $\mathcal{J}_{eff} = \mathcal{J} - g_b \gamma_c$ in Equation 4.4 and thus $n_a > n_b$. Finally, the important relation $g_b = (1/\tau_\gamma) - g_o \eta_b$ for Equation 4.6 along with other useful expressions, such as $\eta_a = \eta_b \epsilon / (1 - \epsilon)$, follow from the definition of $\langle n \rangle_\epsilon$, $\langle g \rangle_\epsilon$ and the linear approximation to g_b .

Two equations relating η_b to γ_c and η_b to δ_γ are necessary to show that η_b is small compared with n_{thr} and $n_{thr}-n_o$. Once the functional form of η_b is known, the gain $g_b=(1/\tau_\gamma)-g_o\eta_b$ can be found. As will be shown, there is less than 5% error (for typical values of the parameters) if η_b is neglected so as to obtain Equation 4.1 from Equation 4.4. If desired, higher accuracy can be achieved by retaining the lowest order terms for η_b . The equation relating η_b to γ_c obtains by subtracting Equation 4.4 (with the derivative set to zero) from Equation 4.6, and rewriting the result in terms of η_b and $\langle g \rangle_\epsilon$ to get

$$\frac{1-2\epsilon}{1-\epsilon} s \eta_b^2 - \left[g_o \gamma + (1-\epsilon) g_o \gamma_c + \frac{1}{\tau_n} + 2n_{thr} s \right] \eta_b + \frac{1-\epsilon}{\tau_\gamma} \gamma_c = 0 \quad (4.7)$$

where $\gamma=\gamma_u-\delta_\gamma$ and $\delta_\gamma>0$. The second equation relating δ_γ to η_b obtains by subtracting Equation 4.3 (with $\gamma=\gamma_u$ and $n_a=\langle n \rangle_\epsilon=n_{thr}$) from Equation 4.6 and inserting the deviates where appropriate.

$$\frac{\delta_\gamma}{\tau_\gamma} - \frac{\epsilon \gamma_c}{\tau_\gamma} + \epsilon g_o \gamma_c \eta_b - s \frac{\epsilon}{1-\epsilon} \eta_b^2 = 0 \quad (4.8)$$

To use $n_a=\langle n \rangle_\epsilon=n_{thr}$ in Equation 4.3 and the same n_{thr} in Equation 4.6, the carrier density $\langle n \rangle_\epsilon=n_{thr}$ must be independent of the magnitude of γ_c . But this is clearly the case since, as previously discussed, $\langle g \rangle_\epsilon=1/\tau_\gamma$ regardless of the size of either γ or γ_c so long as the main laser operates above threshold. Combining Equation 4.7 and 4.8 by eliminating δ_γ yields

$$\frac{\delta}{n_{thr}^3} \eta_b^3 + \frac{A}{n_{thr}^2} \eta_b^2 + \frac{B}{n_{thr}} \eta_b + C = 0 \quad (4.9)$$

where $\delta=\mathcal{J}_s[n_{thr}/(n_{thr}-n_o)]\epsilon/(1-\epsilon)$, $A=\mathcal{J}_s(1-2\epsilon)/(1-\epsilon) - \epsilon(\gamma_c/\tau_\gamma)[n_{thr}/(n_{thr}-n_o)]^2$, $C=(1-\epsilon)\gamma_c/\tau_g$, $-B=(\gamma_u/\tau_\gamma)[n_{thr}/(n_{thr}-n_o)]+(1-2\epsilon)(\gamma_c/\tau_\gamma)[n_{thr}/(n_{thr}-n_o)]+\mathcal{J}_n+2\mathcal{J}_s$, and $\mathcal{J}_s, \mathcal{J}_n$ are the portions of the threshold current density due to radiative and non-radiative spontaneous recombination, respectively. The form of Equation 4.9 and the coefficients show that η_b is expected to be small compared with n_{thr} and that γ_c/τ_γ is similar to a threshold current. The coefficient B can also be written in terms of the bias-current density \mathcal{J} rather than γ_u by using Eq. (6) with $\gamma_c=0$.

An interesting fact from algebra is useful for finding the solutions to Equation 4.9. If δ is small and treated as a perturbation, two approximate solutions to the cubic equation $\delta \cdot \eta^3 + A\eta^2 + B\eta + C = 0$ are obtained by continuous, single-valued transformations of the two solutions to the quadratic equation $A\eta^2 + B\eta + C = 0$ (where $\eta = \eta_b/n_{thr}$). In particular, if η_o is a solution of the quadratic equation then $\eta_o + \delta_\eta$ is an approximate solution of the cubic equation when $\delta_\eta = -\delta \cdot \eta_o^2 / (3\delta \cdot \eta_o^2 + 2A\eta_o + B)$. Here, δ_η must be small. Obviously, to span the full 4-D vector space of cubic equations, the third root is necessary but it cannot be reached by a continuous single-valued transformation of either quadratic root. We find self-consistently, that δ_η is, in fact, negligible. The desired root to the quadratic (and cubic) equation is $\eta_b/n_{thr} = (-B/2A) - [(B/2A)^2 - (C/A)]^{0.5}$. The negative square root is seen to be the correct one by examining A, B, and C and noting that the deviate η_b must become smaller when the intensity of the control mode drops off.

Using the typical values¹² for the parameters, the ratio η_b/n_{thr} can be plotted versus the control-photon density γ_c as shown in Figure 1. The curves are labeled by the overlap ϵ . For this plot, the un-quenched photon density for the main laser is $\gamma_u = 2 \cdot 10^{14}$ (an output power of approximately 6 mW). Most importantly, for typical values of the parameters, the graph in Figure 4.1 shows that the deviate η_b is small compared with the threshold carrier density and therefore, the gain in both sections of the main laser can be approximated by $g_a \cong g_b \cong \langle g \rangle_\epsilon \cong 1/\tau_\gamma$ (as required for Equation 4.1). The curves in Figure 4.1 have other important features. The deviate η_b decreases as the control-photon density γ_c decreases. This behavior occurs because the form of Equation 4.3 approaches that of Equation 4.4 (and, therefore, $n_a \rightarrow n_b$) as the effective bias current $\mathcal{J}_{eff} = \mathcal{J} - g_b \gamma_c$ approaches \mathcal{J} . In other words, with $\gamma_c = 0$, there is no distinction between the two sections of the main laser and the carrier densities n_a and n_b relax to the threshold value. Furthermore, the deviate η_b is seen to decrease as the overlap length ϵ increases. For example, near $\epsilon = 1$, the average $\langle n \rangle_\epsilon = (1 - \epsilon)n_a + \epsilon n_b = n_{thr}$ reduces to $n_b \cong n_{thr}$ and thus, the deviate η_b must be zero. For improved

accuracy, η_b can be calculated by retaining the linear term in Equation 4.9, and writing $\eta_b/n_{thr} \approx C/B$. Although not obvious from Figure 4.1, the curves become noticeably quadratic for small overlap ε or large γ_c .

The transfer characteristics between γ and γ_c are given by Equation 4.1. The equation shows that if the input photon density changes by $\Delta\gamma_c > 0$, then a plot of the photon density γ vs current density J (the L-I curve) linearly shifts to larger values of threshold current by $\varepsilon\Delta\gamma_c/\tau_\gamma$. Figure 4.2 shows this shift for (i) a VCSEL used as the

main laser and a cross coupled In-Plane Laser (IPL) as the control source¹ and (ii) a ridge-guided 5 quantum-well IPL (855 nm) as the main laser (approx. 200 x 10 μm)

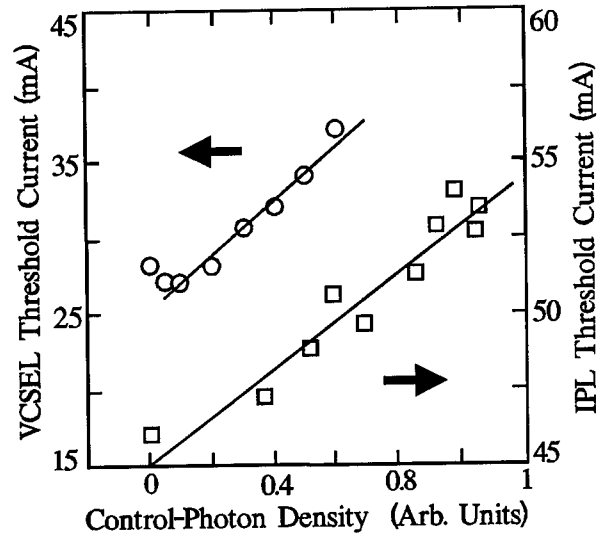


Figure 4.2: Experimental data showing the approximate linear relation between the threshold current and control-photon density γ_c . The top plot is from a VCSEL used as the main laser and a cross-coupled in-plane laser as the control source. The lower plot is from a ridge-guided 5 quantum well laser with an external laser focused into its side.

and an external 850 nm laser focused into its side as the control source. For case (ii), the IPL is butt-coupled to a fiber and the threshold current is approximately determined from a scanning spectrum analyzer. Both plots show that the control-photon density γ_c interacts with the inverted carrier population to linearly shift the threshold current. The steady-state transfer function is given by $\Delta\gamma/\Delta\gamma_c = -\varepsilon$ which reveals that the best possible quenching is achieved with full overlap ($\varepsilon=1$). As previously mentioned, the analysis depends on the average gain and carrier density remaining approximately equal to their threshold values; Equation 4.1 shows this to be valid when $\gamma_c < \gamma_u/\varepsilon$ (i.e., $\gamma_u/\tau_\gamma - \rho_{thr} > \varepsilon\gamma_c/\tau_\gamma$). Also, Equation 4.1 can be made more accurate by including the lowest order approximation $\eta_b \approx n_{thr}C/B$. The total shift in threshold current due to γ_c would then be

$\epsilon\gamma/\tau_\gamma - \epsilon\gamma_c g_o \eta_b$ where η_b depends on β , ϵ and γ_c . As a final note, Equation 4.1 can accommodate the optical confinement factor Γ by changing τ_γ to $\Gamma\tau_\gamma$ everywhere.

Section 4.C: The RF Modulation Bandwidth

The inset to Figure 4.3 shows the basic elements of a gain-quenched device. We consider only the full overlap case ($\epsilon=1$) for simplicity. It is essential to know the transient response of these switching elements but the information has hitherto been unavailable. In principle, knowing the Optical Amplitude

Modulation (OAM) bandwidth, which describes the response of the output intensity to a small sinusoidal variation of the *amplitude of the control beam*, is sufficient to predict the response to an arbitrary (small-signal) waveform. We will show that the OAM bandwidth of the quenched laser is identical to the Electrical Amplitude Modulation (EAM) bandwidth, which describes the response of the laser output intensity to a small sinusoidal variation of the *amplitude of the injected current*.

We assume that two beams with photon-density γ and γ_c (units of cm^{-3}) interact with the gain medium of the laser cavity according to the rate equations given by

$$\frac{dn}{dt} = -g_o(n - n_o)\gamma - g_o(n - n_o)\gamma_c + \beta - \frac{n}{\tau_n} - sn^2 \quad (4.10)$$

$$\frac{d\gamma}{dt} = g_o(n - n_o)\gamma - \frac{\gamma}{\tau_\gamma} + \beta sn^2 \quad (4.11)$$

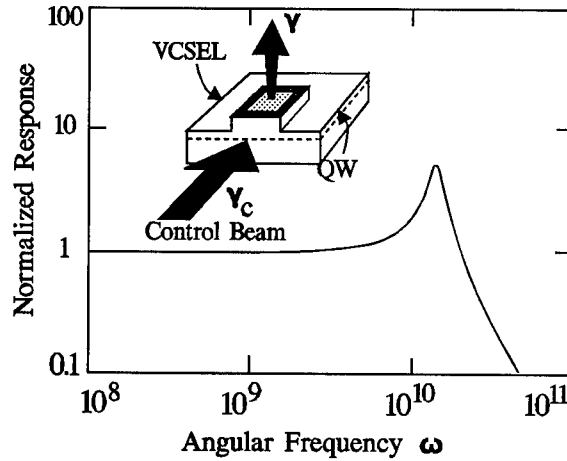


Figure 4.3: The inset shows the typical arrangement for quenching the gain of a VCSEL, for example, using a control beam. The graph shows a plot of the normalized response of the VCSEL to a small sinusoidal variation (with angular frequency ω) of the control beam.

where a linear approximation is used for the gain $g=g_o(n-n_o)$ and the two beams both fully overlap the gain region of the main laser, n is the carrier density (cm^{-3}), n_o is the transparency density, ρ is the current-number density ($\text{cm}^{-3}\text{s}^{-1}$), τ_n is the non-radiative carrier recombination rate, βsn^2 is the recombination rate for spontaneous emission, s is a coupling constant, and β gives the amount of spontaneous emission coupled into the main waveguide mode. The “cavity lifetime” τ_γ for the main laser accounts for the distributed optical losses α and the power-reflection coefficient R for the mirrors through the relation $1/\tau_\gamma = v_g \alpha - (v_g/2L) \ln(1/R_1 R_2)$. The constants v_g and L are the velocity of the optical modes and the length of the main laser, respectively.¹² As is well known, the spontaneous emission noise βsn^2 initiates the laser oscillation but, above lasing threshold, βsn^2 is typically several orders of magnitude smaller than the other terms in Equation 4.11. As a steady-state result, Equation 4.11 shows that $g_o(n_{th}-n_o) \cong \tau_\gamma^{-1}$ (here, the “th” subscripts refer to the value at threshold). There are several remarks regarding the rate equations: (i) carrier diffusion and Auger recombination⁸ are not included; (ii) passive q-switching is not included since both modes are assumed to fully occupy the gain region;¹⁰ (iii) any bistability in γ vs. γ_c is ignored since it generally requires a saturable absorber;⁷ and (iv) gain saturation and compression¹¹ can be included without affecting the analysis but they are both negligible for laser intensities that are small compared with the saturation intensity and gain compression is negligible for GaAs-AlGaAs semiconductor lasers.

The second rate equation shows that the duration of the switching transients dependent primarily on the *effective* cavity lifetime given by $(1/\tau_\gamma)-g$ regardless of the exact nature of the switching mechanism used in Equation 4.10. At steady state, the difference $(1/\tau_\gamma)-g$ is small and positive due to the positive βsn^2 term. If the fraction F is defined by $F/\tau_\gamma = (1/\tau_\gamma)-g$, then under approximately steady state conditions, Equation 4.11 yields $F = \beta sn_{th}^2 \tau_\gamma / \gamma$ or, for typical values, $F \cong$

1/100 (γ is the steady-state cavity photon density). If F could be kept approximately constant, then Equation 4.11 would have an exponential solution with a time constant of the form $\tau_\gamma/F=100\tau_\gamma = 200$ ps; therefore, the actual time required for the output beam to change due to a change in the control beam would be on the order of the effective cavity lifetime τ_γ/F . Equation 4.11 therefore suggests that the response to the control beam with an arbitrary modulation waveform is determined by the effective-loss of the cavity $(1/\tau_\gamma)-g$ which, in turn, is related to the carrier density (through g). Thus, the small signal analysis is expected to show that the OAM bandwidth (1) depends on the carrier dynamics even though the bias current density is held constant and (2) it is related to the effective cavity lifetime rather than just τ_γ .

To explicitly show the equivalence between the OAM and EAM bandwidths, we use a small-signal analysis to obtain an expression for the (angular) resonant frequency^{13,8} ω_r for the gain-quenched laser device. The small signal analysis proceeds by replacing n , γ , and γ_c by $\underline{n} + n e^{i\omega t}$, $\underline{\gamma} + \gamma e^{-i\omega t}$ and $\underline{\gamma}_c + \gamma_c e^{-i\omega t}$ where γ_c is now the amplitude of the driving term, the underlined quantities refer to the average steady-state values and ω is the driving angular-frequency. β is assumed to be time-independent as is appropriate for a current source. Substituting these expressions into Equations 4.10 and 4.11, and retaining lowest order terms yields

$$-i\omega n = -g_0 n(\underline{\gamma} + \gamma_c) - g(\underline{\gamma} - \gamma_c) - n/\tau_n - 2s\underline{n}n \quad (4.12)$$

$$-i\omega \gamma = g_0 n \underline{\gamma} + g \gamma - \gamma/\tau_g + 2\beta s \underline{n}n \quad (4.13)$$

Eliminating n between the two equations and rearranging terms gives

$$\frac{\gamma}{\gamma_c} = \frac{k}{A\omega^2 + B i\omega + C} \quad (4.14)$$

where $A=1$, $B=-(\underline{n}''-F/\tau_\gamma)$, $C=(F\underline{n}''/\tau_\gamma)-(d/\tau_\gamma)$, $\underline{n}''= g_0 \underline{\gamma} + (1/\tau_n) + 2s\underline{n}$, $d=g_0 \underline{\gamma} + \beta s \underline{n}$, $k=d/\tau_\gamma$. The square of the amplitude of Equation 4.14 is written as

$$\left| \frac{\gamma}{\gamma_c} \right|^2 = \frac{k^2}{(A\omega^2 + C)^2 + B^2\omega^2} \quad (4.15)$$

with phasor notation $\gamma = |\gamma|e^{i\phi}$ etc. The resonant frequency is found by setting the derivative of Equation 4.15 equal to zero

$$\omega_r = \sqrt{\frac{-B^2}{2} - C} \cong \sqrt{\frac{d}{\tau_\gamma}} \cong \sqrt{\frac{g_o \gamma}{\tau_\gamma}} \quad (4.16)$$

where the sequence of approximations follow from the typical values given in the references. This dependence of ω_r upon the steady-state value of γ and τ_γ is precisely the same¹³ as would have been obtained had the current \mathcal{I} to the semiconductor laser been modulated instead of γ_c . For reference, Equation 4.16 can be rewritten as $\omega_r = \sqrt{g_o \beta R_{sp} / F}$ where $R_{sp} = sn_{th}^2$ is the total rate of spontaneous emission above threshold for the model described by Equations 4.10 and 4.11. The graph in Figure 4.3 shows a plot of Equation 4.15 with the resonant frequency ω_r marked on the graph.

Section 4.D: Summary

In summary, we have found a simple expression relating the optical output power from a quenched laser to the optical input power, the bias current, and the overlap between the two modes. To a good approximation, the deviation between the actual carrier density and the threshold density can be ignored, and the primary effect of the control source output is to change the threshold current of the main laser. The model is applicable to a wide variety of lasers (including fiber lasers) that use similar rate equations to describe the photon and carrier dynamics.

Chapter 5: V-LOGiC Devices

The stimulated emission of a Vertical Cavity Surface Emitting Laser (VCSEL) can be controlled by the application of stimulated emission from an in-plane laser (IPL). The threshold of the VCSEL changes by over 70% which thereby modulates the output. This chapter contains information from the patent disclosure by Parker et.al. (refer to Chapter 3) and text from the publication by Shire et.al.¹ In addition, this chapter discusses new V-LOGIC devices and applications not appearing in either of the original documents.

5.A: The Basic V-LOGiC Switch

Previous work on gain control of one laser by another intra-cavity coupled laser has involved in-plane lasers only.²⁻⁵ While

Uenohara et.al.^{2,3} have demonstrated bistable operation in intersecting in-plane lasers sharing a common saturable absorber region, a fundamental limitation of this approach is the

small fraction of the total gain section area which is common to both lasers. Johnson⁵ used a folded-cavity geometry to maximize this overlap in constructing an optical flip-flop. From the point of view of constructing arrays of integrated, all-optical switching elements and interconnections between signal planes, it is desirable to use Vertical Cavity Surface Emitting Lasers (VCSELs) as the output devices. External optical control of VCSEL polarization and wavelength by injection locking has been achieved,⁶ and VCSEL threshold current has been reduced through external optical feedback,⁷ but both these scenarios are not obviously compatible with monolithic integration.

This report discusses the first observation of the optical control of the stimulated emission of a VCSEL by an intracavity coupled in-plane laser. AlGaAs/GaAs IPL and VCSELs have been

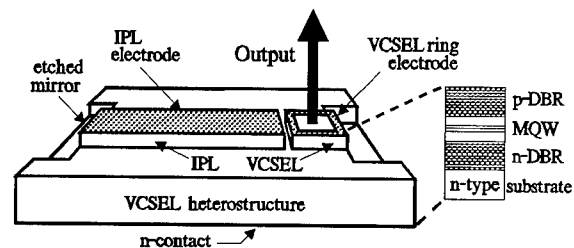


Figure 5.1: Sketch of an IPL with an intracavity coupled VCSEL. The end mirrors of the IPL are deep etched to a depth of 4.5 μm . The shallow etch elsewhere forms ridge waveguiding and it is proton implanted for electrical isolation especially in the 1 μm gap between the IPL and the VCSEL.

fabricated from the same epitaxial material (VIXEL Corp., LaseArray VW-850-S-2). A conceptual sketch of the combined device layout is shown in Figure 5.1, with a view of the two VCSEL DBR mirrors and active region. The IPL is ridge-guided and has one end mirror defined by electron cyclotron resonance (ECR) etching. A shallow 1 μm gap in the top p-contact metallization of the lasers separates the in-plane and VCSEL sections. The VCSEL section has a standard ring contact typical of top surface-emitting devices, and its gain region is defined partly by a proton implant and partly (on one side only) by a deep mirror etch. This 90° mirror serves as the other end mirror of the in-plane laser. In other devices, total internal reflection corner mirrors were also found to give adequate performance. The two etch depths are created in a one-step, two-level etching process similar to that used previously.⁵ A 150 nm thick Ni layer on top of the p-contact metallization serves as the etch mask for the deep BCl_3/Cl_2 ECR etching, and photoresist is used to define the shallow etched areas. After etching the exposed areas to a depth equal to the difference in height between the shallow and deep etched regions, the photoresist mask is removed in an O_2 plasma and etching is subsequently continued until the shallow etch depth (1.5 μm in this case) is reached, and the end mirrors reach their final depth of approximately 4.5 μm . Both the shallow and the deep etched areas were implanted with protons together with the coupling gap region. Last, the wafers were thinned and a NiGeAu Ohmic contact was made to the back of the wafer. The alloying step also served to anneal some of the optical damage from the implant. In this manner, two lasers are created which are capable of being biased independently. The structure is akin to that of an in-plane laser with a multi-quantum well saturable absorber section, with the important difference that the VCSEL section is capable of lasing output in the surface-normal direction. As the driving current to the VCSEL is increased, the power output from the IPL for fixed in-plane bias current also increases, due to the "saturable absorber" becoming more transparent. It should be noted that an external cavity arrangement in which the IPL output was

coupled through a polyimide-filled 3 μm gap to an air-post VCSEL device was also implemented. Only minimal effect on the VCSEL threshold current was observed in this case, owing to the drastically reduced photon density coupled into the thin VCSEL active region.

The VCSEL output (together with some scattered light from the IPL section) was measured using a 1 cm diameter Si photodetector mounted approximately 2 cm above the wafer. As the power is increased from a 20 x 200 μm in-plane laser, the threshold current of a 30 μm^2 VCSEL increases over 70%. A 20 μm^2 VCSEL does not lase at any current; rather, its spontaneous emission continues increasing until its power output becomes limited by heating. Figure 5.2 shows VCSEL threshold current

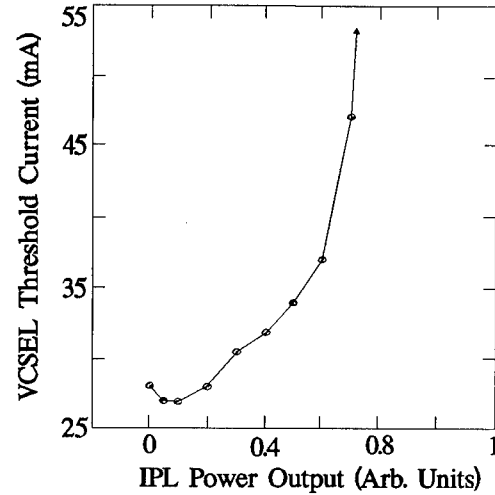


Figure 5.2: Threshold current of a 30 μm^2 VCSEL as a function of the IPL output power.

versus IPL output power for the 30 μm^2 . As shown, at sufficiently high VCSEL bias, the IPL cannot develop sufficient power to quench the VCSEL. It is believed that this is due to insufficient overlap between the gain regions of the in-plane laser and the wider VCSEL. Both devices may lase simultaneously. For low IPL output (below or near threshold), it can also be seen in Figure 5.2 that the VCSEL threshold current initially decreases. This is to be expected, as the situation is similar to a low level of optical pumping from an external laser lowering the lasing threshold by electrical pumping. The high threshold current density of approximately 6800 A/cm² for the VCSELs in this experiment is not believed to be due to inherent limitations imposed by the gain control mechanism shown here. Instead, we believe the cause to be either the highly resistive Bragg reflector stacks in the epitaxial material used, or processing problems; broad area, cleaved facet IPLs fabricated from the same wafer had threshold current densities of only 300-400 A/cm².

In fact, with improved devices, the gain quenching effects observed should be even more pronounced, particularly with higher power IPLs coupled to smaller VCSELs.

Applications for the intra-cavity coupled laser pair include integrated, all-optical logic devices (e.g., inverters and nor gates) and optical interconnection between signal planes with low-divergence output beams. The technology is compatible with existing, monolithic photonic integrated circuit (PIC) fabrication methods involving IPLs only, and it is very flexible. For example, one IPL may be used to control the output of multiple VCSELs, or multiple IPLs may be coupled to a single VCSEL to implement an all-optical NOR gate. While intra-cavity control of stand-alone VCSEL output is difficult due to the short cavity and obvious fabrication difficulties, the intra-cavity coupled IPL offers a wide variety of established options for controlling its output.

5.B: A V-LOGiC Memory Element

The V-LOGiC Devices can be used for a variety of functions. The active optical memory element is a new device but remains untested at present. The basic idea is to combine a VCSEL with an IPL in a single element as shown in the top view of Figure 5.3. The two laser cavities share almost the entire gain region. The square ring shaped electrode pumps the common gain region and supplies gain for both the VCSEL and the IPL cavities. Thought question: Does the in-plane cavity lase or does

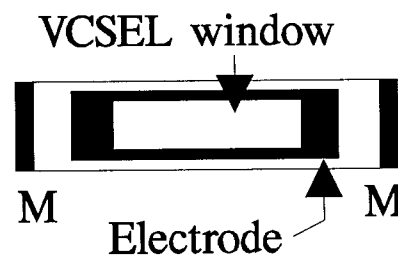


Figure 5.3: A VCSEL and IPL share almost the entire gain section. The electrode pumps both the IPL and VCSEL laser modes.

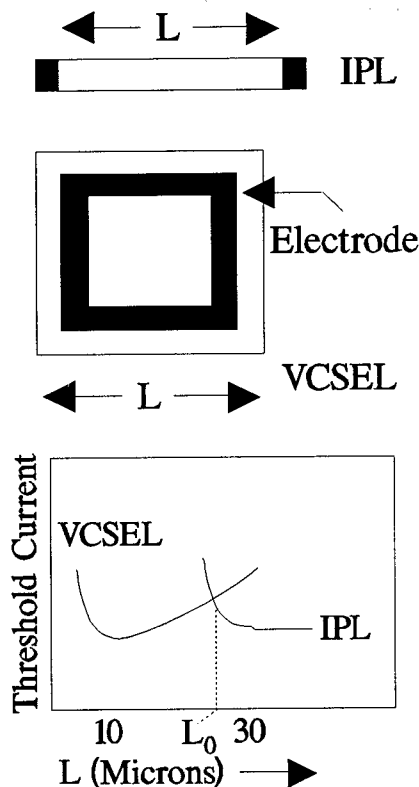


Figure 5.4: Top two diagrams show the lengths scales for an IPL and VCSEL. Graph shows the dependence of threshold current on the length.

the VCSEL lase? This question remains unanswered at present but the situation can be clarified and some insight provided on a possible memory element.

As is well known, the threshold current of a semiconductor laser depends on its length. The length of the IPL is shown in the top diagram of Figure 5.4 while a length scale is shown for the VCSEL in the middle diagram of Figure 5.4. The graph shows a cartoon representation of the threshold current as a function of the lengths for each device. For the IPL, the threshold current increases for small lengths since the gain in a multiple quantum well laser tends to saturate at high current density. As the length of the cavity decreases, the losses due to optical scattering and other distributed losses decreases, but the loss at the two end mirrors remains constant. However, as the length decreases, the *total* gain between the two mirrors also decreases (for a given current *density*) because the volume decreases. Therefore, more current must be supplied to the smaller gain medium to compensate for the mirror loss. Figure 5.4 also shows a similar curve for a VCSEL that occurs for different reasons. The large L region might occur due to reduced waveguiding while the small L regions might occur due to heating or surface losses.

One might reason that where the two curves coincide, the device is equally likely to lase in either mode. In fact, one might imagine the device spontaneously flipping between the two modes so long as other factors do not cause it to favor one over the other. The flipping between modes could be controlled by a modulator added into the IPL. The voltage of the modulator would then control the Q of the IPL and cause the device to switch between modes in a controlled manner.

5.C: The Spontaneous Emission Filter

The spontaneous emission filter is a device that uses a quenched laser for its sharp optical bandwidth. As will be shown in the technical report for 4600P130, the optical bandwidth of the quenching phenomenon is approximately the same as the width of the gain curve for the laser used as the main laser. The lower the dimensionality (a quantum well is 2d, a quantum wire is 1d and a dot is 0d) of the main laser, the sharper the gain curve as a function of optical frequency. For

example, a quantum dot laser is expected to have gain curve similar to a delta function. It is the width of this gain curve that determines the possible wavelengths that will quench the main laser. Thus, it is possible for a large number of wavelengths to be present in the control beam but only a very few of them near the laser frequency can actually quench the main laser.

An early version of the spontaneous emission filter appears in the technical report #RL-TR-94-103 by Parker et.al. (August 1994) and previously in a patent disclosure by Parker et.al. in 1992. The output of a laser amplifier is fed into the side of a monolithically integrated IPL. The amplifier produces both stimulated emission and an amplified version of an input signal. The V-LOGiC design can also be used by replacing the IPL laser with a VCSEL.

5.D: The Signal Router for ATM switching

Shire and Tang in collaboration with Rome Laboratory Photonics Center report an optical router based on the V-LOGiC. The V-LOGiC optical router consists of a series of VCSELs at the intersection of a long IPL with smaller perpendicularly oriented IPLs as shown in the top view of Figure 5.5. The long IPL consists of section I4a to I4d while the short laser run vertically across VCSELs V1-V3. The long laser is

modulated with a signal that passes through each VCSEL. The short lasers I1 to I3 can be enabled to quench the corresponding VCSEL. The signal will be transmitted up and out the plane of integration by the VCSELs that remain unquenched. For example, if I1 and I3 are enabled and quenching VCSELs V1 and V3, then a signal impressed upon the long IPL I4 will modulate VCSEL V2 by partially quenching it. Note that this is similar to the spontaneous emission filter using a VCSEL as the main laser.

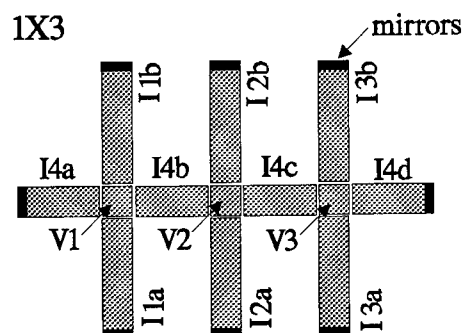


Figure 5.5: Top view of an optical signal router. Lasers represent by I are IPLs and the Vs represent VCSELs.

Chapter 6: Diode Laser Logic

Diode Laser Logic is a complete, new logic family comprised of Q-switched lasers and photodetectors. The lasers and detectors are monolithically integrated on multiple quantum well laser heterostructure with semi-insulating substrates. Preliminary results indicate an ON/OFF contrast ratio better than 500:1, gain in excess of 20 and variable I/O hysteresis characteristics. As a result, the devices can be cascaded to form more complex optical circuits. In addition to introducing the Diode Laser Logic family, a basic model is presented and the fabrication process is discussed.

6.A: The Logic Family

The Diode Laser Logic (DLL) gates form a complete logic family for use as smart pixels and in optical signal processing applications.¹ The individual gates, Configurable Optical Gates (COGs), of the family can be interconnected to form more complex circuits such as fully integrated optical adders and crossbars; however, in many cases, the unique features of the family simplify the circuits to one or two COGs.

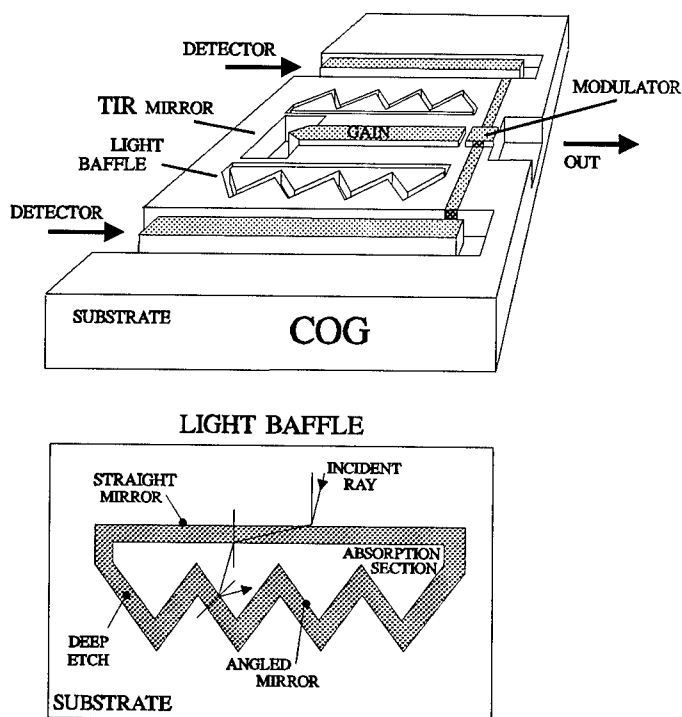


Figure 6.1: The top diagram shows a relief drawing of the NOR gate as an example. The anode of the modulator connects to the cathodes of the two photodetectors that are isolated from all other devices by a deep etch through the n-layer. The bottom diagram shows the light baffle that provides optical isolation between gain and photodetector sections.

Each COG consists of an integrated Multiple Quantum Well (MQW) Q-switched laser,^{2,3} one or more integrated photodetectors^{4,5} and, in some devices, an integrated current source. The Q-switched laser consists

INVERTER

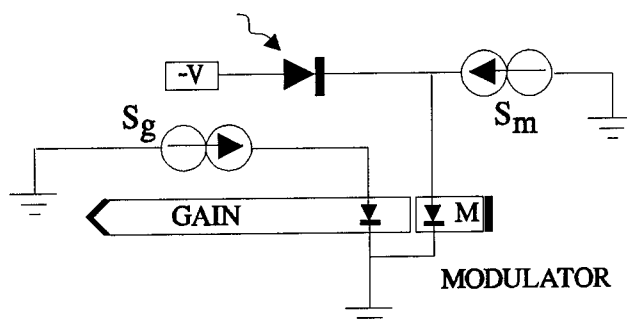


Figure 6.2: Schematic diagram of the inverter COG. For an optically unbiased detector, the current source S_m forward biases the modulator. The photodetector, with optical bias, sinks the current and reverse biases the modulator. The laser is ON and OFF respectively.

etched mirrors. In general, the current source, which connects to the modulator, sets the state of the laser (ON or OFF). Photocurrent from the photodetector modifies the current and voltage at the modulator and, thereby, changes the state of the laser. Figure 6.1 shows a relief drawing for a typical COG with two optical inputs (photodetectors) but without the current source.

The laser consists of gain and modulator sections that are located between an etched Total Internal Reflection (TIR) mirror⁶ on one end and an etched flat mirror on the other. The TIR mirror improves the efficiency of the laser by providing up to 100% reflectivity. In some devices, the TIR mirror is replaced by another flat mirror for a second output. The modulator and gain sections are separated by a shallowly etched region with an oxygen implant;⁷ this region provides electrical isolation between the two sections without significantly altering the index of refraction. A large index difference would prevent the device from operating properly by introducing a partially reflecting surface there and possibly setting up sub-cavities.

Reverse bias on the modulator inhibits laser action by increasing the optical absorption within the quantum wells. Increasing the reverse bias on the modulator results in an increasing threshold current for the laser. The laser bias current, however, is fixed between the threshold

An optical inverter is shown in Figure 6.2. The cathode of the photodetector is electrically connected to the modulator. Under normal operating conditions, the anode of the photodetector and the n-layer are all grounded while the p-contact on the laser is positively biased. Without illumination on the photodetector, the modulator current source S_m forward biases the modulator and lowers the

The diagram shows a quantum Hall effect setup. A central Hall bar contains a quantum Hall region (shaded gray) with contacts A and B. A voltage source $+V$ is connected to the contacts. A current source S_g is connected to the Hall bar. A TIR mirror is connected to the Hall bar. A modulator M is connected to the Hall bar. Detectors are connected to the Hall bar. The Hall bar is labeled GAIN.

Figure 6.3: Without optical bias to the detectors, the current source S_m reverse biases the modulator. Optical bias applied to either detector produces sufficient photocurrent to satisfy the source and forward bias the modulator. The laser is OFF and ON respectively.

threshold current of the cavity; this causes the cavity to lase. The modulator current source is not actually needed in this circuit since emission from the gain section produces charge in the modulator that can forward bias it. When the photodetector is illuminated, it sinks both the current from the current source and the photocurrent from the modulator. The modulator becomes reverse biased and the cavity quenches.

60

Two distinct versions of the AND gate are possible. The *series detector* configuration appears in Figure 6.4. The current source S_m reverse biases the modulator as before. A single

illuminated photodetector forward

biases itself and produces negligible

photocurrent. Both detectors must be

illuminated to satisfy the modulator

current source and forward bias the

modulator. The other AND gate

configuration uses a dual modulator

design that operates similarly to the

OR gate previously discussed. One

modulator is located at each end of the

cavity. This second version has the

disadvantage that the two modulators

introduce higher cavity loss than the

single modulator; thus, the lasing

threshold currents are necessarily

higher. However, when both ends of

the cavity are to serve as outputs, the

double modulator design has an advantage. The modulators absorb significant amounts of

spontaneous emission when reverse biased. Thus, photodetectors coupled to each end of the

cavity have higher on/off contrast ratios.

AND GATE

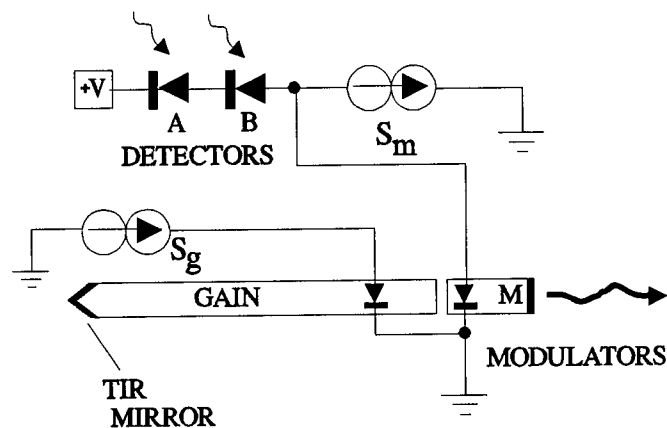


Figure 6.4: For the series-detector AND gate, both detectors must be illuminated for the laser to oscillate.

NAND GATE

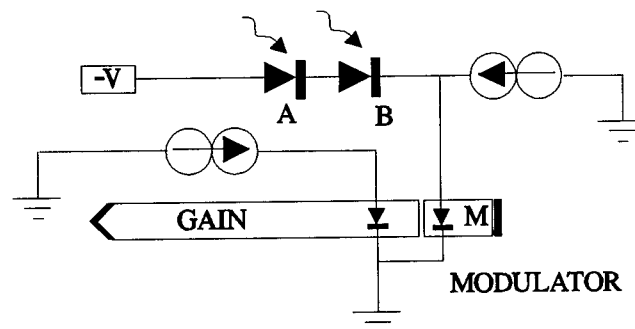


Figure 6.5: Both detectors must be illuminated for the gate to switch.

Only one version of the NAND gate (Figure 6.5) is possible with the fabrication techniques presently used. Any other design requires the cathode of the modulator to be electrically isolated from the cathode of the gain section. At present, deep etches through the active region are used to electrically isolate sections of the N-layer. Such an etch around the modulator introduces a mirror between the gain and modulator sections and, thereby, degrades the performance of the device.

An optical NOR gate is shown in Figure 6.6. It operates similarly to the inverter except for the two photodetectors in parallel.

A note is in order concerning the possible optical coupling between the laser and photodetectors. If

necessary, a light baffle can be included with the device. The light

baffle helps to optically isolate the detectors from the laser (refer to the close-up shown in Figure 6.1). The light baffle consists of two deep etch regions, two mirror surfaces and an absorption region with a metal electrode. The flat mirror totally reflects light with wave- vectors making more than a 17° angle with respect to the normal; thus most of the stray light is reflected back. The light falling within the 17° angle is refracted and enters the absorption region; the wave vector within this absorption region again falls within the 17° of the normal to the flat surface. The absorption region reduces the intensity of light passing through it. The absorption is enhanced by applying reverse bias to the metal electrode on the top of the absorption section. The angled

NOR GATE

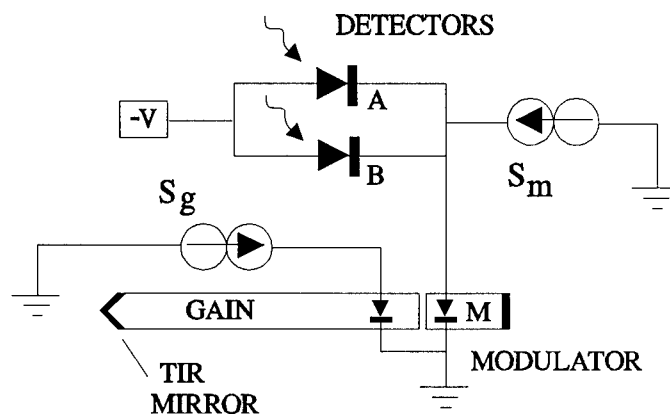


Figure 6.6: The optical NOR gate operates similarly to the INVERTER except for the two detectors in parallel.

reflecting surfaces totally reflect the remaining light because the angle between the wave vector of this light and the normal to any of the reflectors is always larger than 170° .

Elements of the DLL family can be combined to build larger circuits. With standard Boolean logic, on the order of 10 gates are required for a 2 X 2 CROSS BAR or an ADDER. Unique features of the COGs can be used to greatly simplify the designs. Any function that can be realized through Boolean logic can be implemented with the DLL family.

The integrated optical ADDER appears in Figure 6.7. The ADDER has two optical inputs and each has two photodetectors electrically isolated from one another on the P side. There are two output lasers. The one on the left (right) represents the *carry (sum)* bit. To illustrate how it operates, consider the following cases. CASE 1: Optical bias is not present on either set of detectors. In this case, the two modulators on the *carry* laser are reverse-biased. As a result, detector D5 is not illuminated and source S3 forward biases the top modulator on the *sum* laser. However the lower modulator is reverse-biased so the *sum* laser is off. CASE 2: Optical bias is applied to exactly one detector. The *carry* laser is quenched since only one modulator is forward-biased. Thus S3 forward biases the top modulator in the *sum* cavity. Light strikes either D2 or D3 so the lower modulator in the *sum* cavity is forward-biased. The *carry* laser is *off* and the *sum* laser is *on*. CASE 3: Optical bias is applied to both sets of detectors. Light incident on both sets of detectors causes both modulators on the *carry* laser to be forward-biased and the cavity lases. As a result, D5 reverse biases the top modulator on the *sum* cavity and the cavity does not lase.

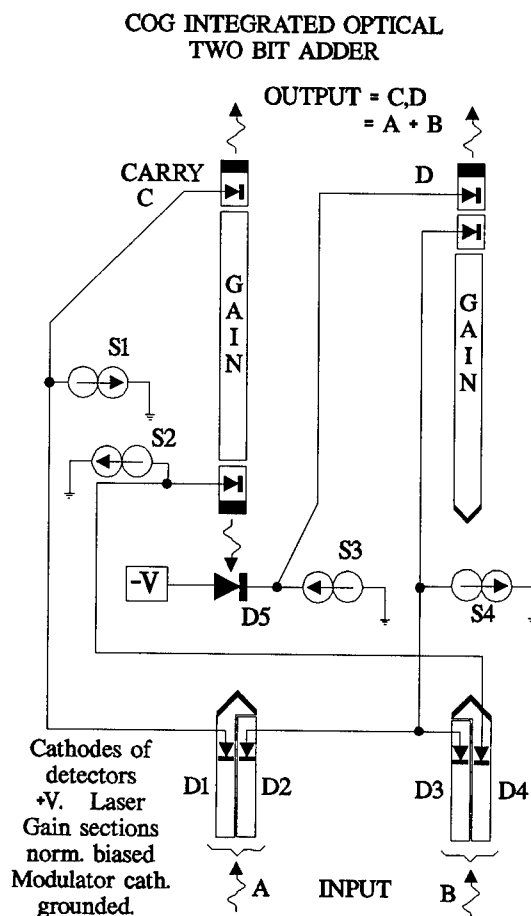


Figure 6.7: An integrated optical adder.

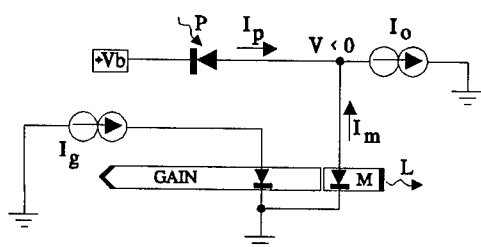


Figure 6.8: The basic circuit for the model of the COGs.

Section 6.B: Simple Model

It is possible to provide a simple model for the operation of the COGs. The Q-switched laser consists of the gain and modulator sections. Due to a two-dimensional Franz-Keldysh effect, the optical absorption in the modulator increases with larger reverse-bias. The resulting photocarriers either recombine in the wells or tunnel through the barriers to be swept out.⁸ The radiative recombination rate decreases with field in the well since the overlap of the electron and hole wavefunctions decreases. The tunneling rate increases exponentially with electric field because, at high fields, the barrier is triangular.

Thus, the electric field in the modulator determines the ratio of recombination to sweep-out currents. For the modulators with a PIN structure, the application of bias voltage alters the existing built-in field and, thus, also, the ratio of currents. For a cavity to lase, its gain must

balance out its losses. The loss in the cavity of the COG can be controlled with the voltage applied to the modulator because of the sweep-out process.

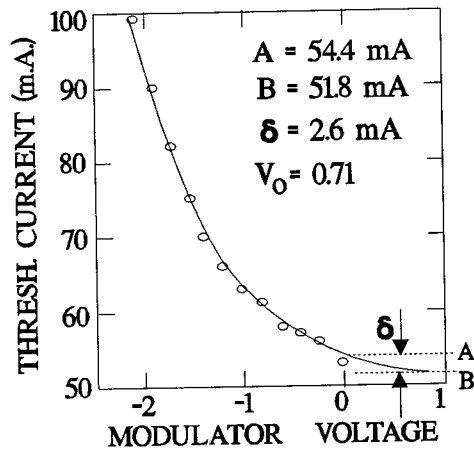


Figure 6.9: Typical threshold current data for a 20 μm X 20 μm modulator.

A simple model explains the operation of the COG shown in Figure 6.8. For a Q-switched laser near threshold, assume that the optical power through the modulator L is approximately related to the gain-section bias current I_g and the threshold current I_{th} by

$$L = L_o \left[\exp(I_g / I_{th}) - 1 \right] \quad (6.1)$$

where L_o is a constant. Here, I_g is fixed and I_{th} is considered to be the variable since the switching is controlled by the modulator bias.

Referring to Figure 6.8, the photodetector and modulator are considered to be optically controlled current sources with some bias voltage dependence characterized by resistance R_p and R_m respectively. (Measured resistance might have some voltage dependence.) The currents I_m and I_p are both combinations of photocurrents and the reverse bias leakage current. It follows that

$$\begin{aligned} I_m &= k_m L - \frac{V}{R_m} \\ I_p &= k_p P - \frac{[V - V_b]}{R_p} \end{aligned} \quad (6.2a,b)$$

where P is the optical power absorbed by the photodetector, k_m and k_p are constants. For large values of current from the I_o source, the reverse bias voltage must be limited by additional circuitry to prevent break-down of the modulator and detector diodes.

Typical data for the threshold current vs. modulator bias voltage appears in Figure 6.9. The gain section is 20 μm X 200 μm and the modulator is 20 μm X 20 μm for the plot. The curve is best approximated by an exponential function:

$$I_{th} = \delta e^{\frac{-V}{V_o}} + b \quad (6.3)$$

where δ , V_o and b have the approximate values of 2.65 mA, 0.714 V and 51.85 mA respectively.

These values change for smaller modulators and waveguides. The smaller devices yield the high gain quoted previously. The previous equations can be combined with $I_o = I_m + I_p$ to yield:

$$\exp(I_g / I_{th}) - \frac{V_o}{R_{//} k_m L_o} \ln \frac{\delta}{I_{th} - b} = 1 + \frac{I_o - k_p P}{k_m L_o} \quad (6.4)$$

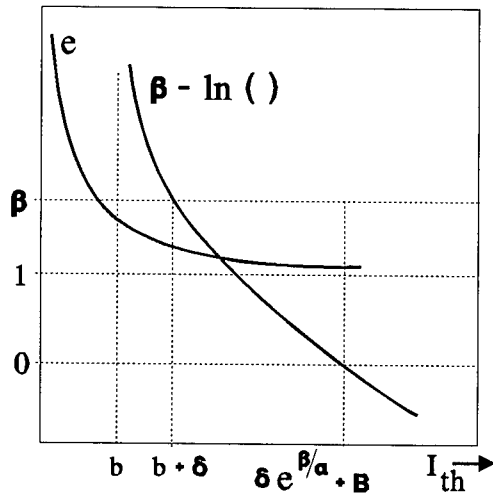


Figure 6.10: Both sides of equation 6.5 plotted on the same set of axes. The intersection is the threshold current.

Equation 6.5 can be interpreted as follows. β is the independent variable and I_{th} is the dependent one. The left-hand side represents the L-I characteristics. On the right-hand side, β represents the difference in the currents at the modulator. The logarithmic term is a result of the I_{th} -V characteristics for the Q-switched laser.

The left-hand and right-hand sides of Equation 6.5 can be plotted on the same set of axes as shown in Figure 6.10. The effect on I_{th} of changing I_o or P is evident from the graph. Suppose, for example, that the power P incident on the detector increases. In this case, β will decrease and

where $R_{//}$ is the parallel combination of R_m and R_p and where V_b/R_p is negligible in comparison to I_o . This can be rewritten as

$$\exp(I_g / I_{th}) = \beta - \alpha \ln \frac{I_{th} - b}{\delta} \quad (6.5)$$

where

$$\beta = 1 + \frac{I_o - k_p P}{k_m L_o} \quad (6.6)$$

and

$$\alpha = \frac{V_o}{R_{//} k_m L_o} \quad (6.7)$$

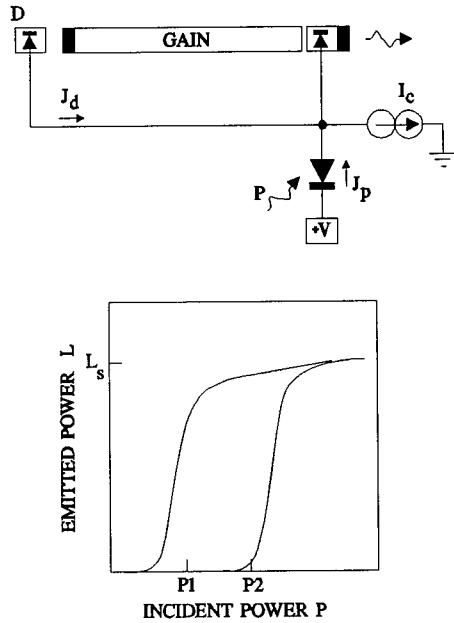


Figure 6.11: Positive feedback has been added in the top circuit to add control over the width of the hysteresis loop shown in the bottom part of the figure.

limit) and $k_m L_O \ll I_O$, β/α simplifies to $(I_O R_{//})/V_O$. Thus the threshold current for large β can be written as

$$I_{th} = \delta \exp(I_O R_{//} / V_O) + b \quad (6.9)$$

This equation is essentially the curve shown in Figure 6.9 where $I_O R_{//}$ is the voltage across the modulator. The laser is off in this case.

Hysteresis in the input-output characteristics can be adjusted by changing the geometry and bias of a photodetector D coupled to the output of a gate as shown in Figure 6.11. The photocurrent J_d is added to the input signal in a positive feedback arrangement. The length, bias and coupling of detector D can be adjusted. The branches of the resulting hysteresis curve for the circuit can be explained as follows.

As the input power increases along the lower branch up to point P2, the cavity produces spontaneous emission; the detector D produces photocurrent J_d that is small compared to the

the LN curve shifts down and to the left. The intersection point moves to the left to indicate that the threshold current decreases. The other cases are similar.

There are two simplifying cases. The first occurs when the cavity is lasing (β near 1), i.e., for the approximate range of $b < I_{th} < b + \delta$:

$$I_{th} \cong b \quad (6.8)$$

The second case occurs for large β . Under this condition, the intersection point in Figure 6.10 is far to the right where $\exp(I_g/I_{th}) \cong 1$. This condition yields $I_{th} = \delta \exp(\beta/\alpha) + b$. Assuming $k_p P \ll I_O$ (i.e. the large β

photocurrent $J_p = k_p P$ produced by input power P . The output power L remains small. At point P_2 , the photocurrent J_d is still small but J_p is sufficiently large to satisfy the current source. The cavity begins to lase.

$$J_p = I_c \text{ or } k_p P_2 = I_c \quad (6.10)$$

Thus,

$$P_2 = I_c / k_p \quad (6.11)$$

As the incident power P increases, the amount of gain available from the modulator will saturate. The output power L saturates at L_s for a given bias current to the gain section. Furthermore, L remains relatively constant along the top branch as the incident power is decreased to P_1 since photocurrent J_d is also helping to satisfy I_c . As a note, the saturation intensity increases with bias current to the gain section. At power level P_1 , the lasing intensity decreases since the photocurrents are no longer large enough to satisfy the modulator current source (the reverse bias voltage across the modulator is limited by additional circuitry).

$$J_p + J_d \cong I_c \quad (6.12)$$

$$k_p P_1 + k_d L_s \cong I_c \quad (6.13)$$

where k_d accounts for the responsivity, coupling and the length of modulator D . Thus,

$$P_1 = \frac{I_c}{k_p} - \frac{k_d}{k_p} L_s \quad (6.14)$$

As the incident power continues to decrease past P_1 , the emitted power L also decreases. The width of the hysteresis loop is approximately the difference between P_2 and P_1 .

$$Width \cong \frac{k_d}{k_p} L_s \quad (6.15)$$

The width of the hysteresis loop is controlled by changing the parameter k_d . This parameter increases with increased optical coupling between the laser and the detector and also with increased absorption within the detector due either to increased detector lengths or increased reverse bias. However, if this parameter becomes too large, then P1 becomes negative (i.e. Width > P2) which means that the laser can not be quenched by removing the illumination P from the photodetector.

Section 6.C: Fabrication

The DLL family uses semi-insulating substrates; however, the preliminary devices described in the EXPERIMENTAL RESULTS section use N-type substrates. Similar processing is used on both types of substrates and the differences will be noted as the discussion progresses. Figure 6.12 shows the laser heterostructure, with five quantum wells, epitaxially grown on N-type substrates. Lasers fabricated on the heterostructure emit at 860 nm.

The wafers with the N-type substrate are processed as follows (See chapter IV for a complete discussion). The laser and photodetector waveguides are defined by photolithography with an image reversal process and the liftoff of a metallization layer. The metals, in the order evaporated onto the p-side of the wafer, are Ti, Pt, Au and Cr. The mirrors and waveguides are formed by etching the wafer in a Chemically Assisted Ion Beam Etcher (CAIBE)⁹ twice. The chrome in the metallization provides the etch mask and the edge of the Cr defines the mirror surface. For the first etch, a thick (3 μ m) layer of photoresist covers the wafer except in the regions of the deep etches.

MULTIQUANTUM WELL STRUCTURE

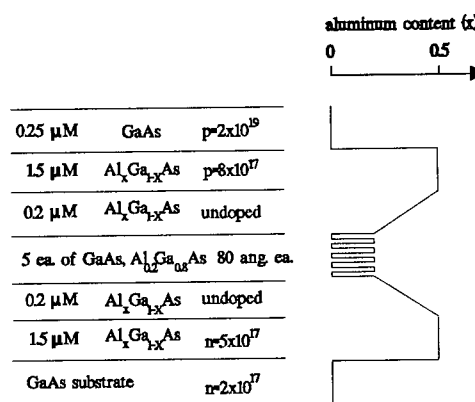


Figure 6.12: The heterostructure for the N-type substrates.

EXAMPLE CROSS-SECTIONAL VIEW

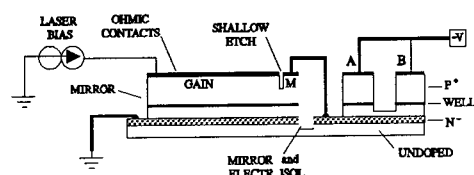


Figure 6.13: An example cross sectional view showing the various etches.

The photoresist is removed after the initial etch. The second etch, a shallow etch, forms the waveguides, the electrical isolation region between the modulator and gain sections and also continues the deep etch for the mirrors. The electrical isolation is accomplished with the ion implanting of oxygen⁷ in the shallowly etched regions. Polyimide is spun on the wafer and vias are etched through the polyimide for electrical contacting. The polyimide acts as both an insulator for the electronics and a transparent dielectric for the optics. After the polyimide is fully cured, a final metallization is used for electrical connections. The wafer is thinned and an n-type Ohmic contact, consisting of Ni, Ge, Au, Ag and Au, is evaporated on the back surface. The devices are alloyed, cleaved and mounted in preparation for testing. For semi-insulating substrates, the above procedure is followed by a wet selective etch to expose the n-type GaAs, and the same photoresist mask is used to define the n-type contact by

means of liftoff. Deep etches in the semi-insulating wafers extend into the substrate for electrical isolation between neighboring devices. An example cross-section of a semi-insulating device can be seen in Figure 6.13.

Section 6.D: Experimental Results

This section discusses the results from two prototype COGs with differing sizes for the gain and modulator sections.

The larger laser cavity measures $20 \times 200 \mu\text{m}$ with a $20 \times 20 \mu\text{m}$ modulator while the smaller cavity measures $5 \times 85 \mu\text{m}$ with a $5 \times 5 \mu\text{m}$ modulator. An external current source and external silicon photodetector connect to the modulator. The device geometry is similar to that shown in

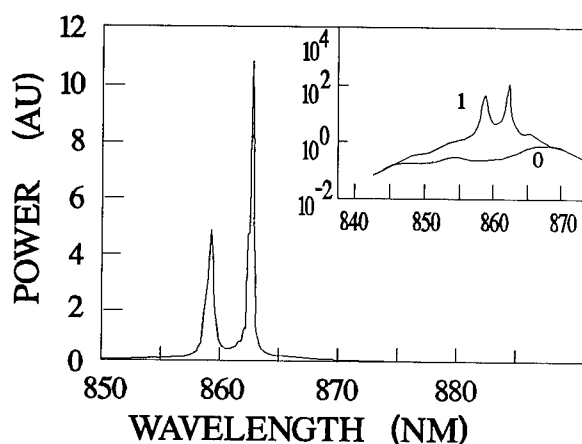


Figure 6.14: The emission spectrum for the larger COG in both the logic 0 and 1 states. The 0 state is coincident with the horizontal axis in the linear plot. The inset shows the semi-log plot of the two states. The 0 state corresponds to spontaneous emission which is 500 times smaller than the stimulated emission for the logic 1 state.

Figure 6.1 except that (1) the light baffles are not required for the externally mounted photodetectors and (2) both mirrors are flat.

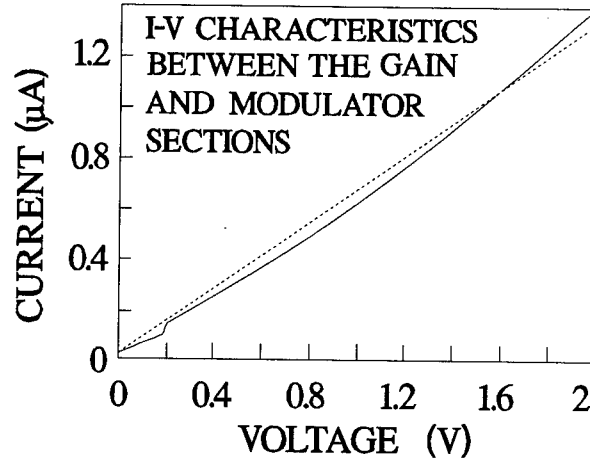
Several experiments were performed on the gates. (1) Optical logic was demonstrated. (2) Optical emission spectra were determined for the 0 and 1 logic states as proof of the switching. (3) The lasing threshold current of the laser as a function of modulator bias voltage was measured. (4) The responsivity of the integrated photodetectors was investigated. (5) The quality of the electrical isolation was ascertained. (6) The current vs. voltage (I-V) characteristics of the modulator in forward and reverse bias were determined. (7) The gain of a gate was determined.

The optical logic was demonstrated by directing a HeNe laser beam onto the two photodetectors; the laser was switched *on* when either photodetector was illuminated. The modulator current source was set to 0.7 mA for the larger COG and 2 μ A for the smaller one. The reverse bias on the modulator was limited to -4 V; this negative limit occurred when the current source could not supply the 0.7 mA due to the large reverse bias resistance of the diodes (modulator and photodetectors). The voltage to the gain section was pulsed to prevent thermal damage; the pulse width was 10 μ s. When either photodetector was illuminated, the voltage on the modulator rose from -4 V to -0.1 V for the larger COG.

The emission spectra were obtained by directing the laser emission from the larger COG into a fiber and coupling the fiber to an Anritsu Spectrum Analyzer. The experimental conditions were the same as for the switching experiments. Figure 6.14 shows the emission spectra for both logic states. The spectrum for the 0 state (modulator reverse-biased at -4 volts) is essentially a straight line coincident with the horizontal axis. The inset to the figure shows the same data plotted in semilog format. The 0 state corresponds to spontaneous emission that is a factor of 500 smaller than the stimulated emission representing the 1 state (neg 0.1 V bias on the modulator).

In addition, the modulator quite effectively absorbed most of the spontaneous emission that was incident on it (not shown).

The threshold current of the larger COG laser as a function of the modulator bias voltage was determined by applying a reverse bias voltage to the modulator, then



noting the minimum current at which the COG laser would lase. The voltage applied to the gain section consisted of 60 Hz, full-wave rectified sinusoidal signals. Figure 6.9 shows the threshold current vs. modulator bias voltage. Note that a change of 2 Volts yields a factor of 2 change in the threshold current. As an example of modulator control, if the quiescent current of the laser is set to 60 mA, then modulator voltages larger than -0.75 V turn the laser *on* and voltages less than that turn the laser *off*.

The capacitance and response of the integrated photodetectors were investigated. The capacitance was verified to depend on the area of the electrode structure as $0.004 \text{ pF}/\mu\text{m}^2$ at a reverse bias of -5 V. The photocurrent was found to be essentially independent of the wavelength of incident laser light for wavelengths between 800 and 870 nm; beyond 870 nm, the response decreased. The photodetectors were found to be relatively linear in photocurrent vs. incident light intensity for a wide range of intensity.

The quality of the electrical isolation between the gain and modulator section was checked. As discussed previously, the electrical isolation between the two sections was formed by the new process of etching away the P^+ layer to within a few thousand angstroms of the active region and then implanting O_2 as a deep trap. Without the implant, the resistance was found to be 300Ω to

1 K Ω . Figure 6.15 shows the I-V characteristics measured for this 2 μm wide region after the oxygen implant. The isolation resistance was thus determined to be about 1.7 M Ω .

The reverse bias I-V characteristics of the modulator with the gain section floating were determined. For voltages in the range of $-5 < V < 0$, the resistance is larger than 3.5 M Ω . Thus, there are three sources for current flow to the modulator: leakage current between the gain and modulator sections; reverse bias leakage of the modulator; and the photocurrent produced in the modulator due to emission from the gain section.

The gain of the COG is defined as the ratio $P_{\text{out}}/P_{\text{in}}$ where P_{out} is the intensity of the light emitted from the laser through the modulator, and P_{in} is the intensity of light absorbed in the photodetector that causes switching. For the COG, the gain is determined by the current from the current source. The photodetector must supply enough current to satisfy the current requirements of the source before the potential of the modulator can change. For unity quantum efficiency, the power of light absorbed must be

$$P_{\text{in}} = hcJ/e\lambda \quad (6.16)$$

where h , c , J , e , λ are Planck's constant, the speed of light in vacuum, the current through the current source, the electronic charge and the wavelength of light in vacuum, respectively.

The gain was determined for the smaller COG. The current source was set for 2 μA with a maximum reverse bias voltage of -4 V. The ON/OFF contrast ratio was better than 10:1. For these operating conditions, an input optical power of 4 μW switched the laser with an emitted optical power of 83 μW . These numbers correspond to a gain of 20.

E. SUMMARY

The DLL family is a new concept for optical computing and smart pixels. The features include: (1) an intra-cavity modulator that provides sensitive control of the laser output; (2) integrated detectors capable of being electrically contacted at both the anode and cathode; (3) integrated current sources; (4) substrates for complete isolation of individual components in the COG and for electrical connections between anodes and cathodes; (5) oxygen implanted shallow etches for electrical isolation between P^+ regions; (6) integrated light baffles employing Total Internal Reflection to prevent accidental optical coupling between the laser and detectors; (7) integrated photodetectors with wide optical bandwidth so that the transfer characteristics of the device are relatively independent of wavelength; (8) compatibility with silicon logic since only a lower voltage swing is required. For the first time, with the DLL family, integrated optical circuits can be fabricated. One key component is the intra-cavity modulator with the oxygen implanted shallow etches since it can control 10 to 20 fold more optical power at the COG output than is present at the input to the detectors as proved by the prototype device discussed above.

Since the modulator can be driven by a photodetector in reverse bias, a COG can be used as an optical amplifier. Linearity might be a problem for a small signal amplifier; however, for binary logic, the inverter COG can be used in a mode such that the laser is either *on* or *off*. The *on* state consists of maximum laser emission while the *off* state consists of spontaneous emission from the laser. However, the modulator absorbs most of the spontaneous emission and thus almost no light is emitted from the laser in the *off* state.

Chapter 7: Coupled Waveguide Detectors

The integrated Coupled-Waveguide Detector (CWD) is an alternative to the integrated butt-coupled detector¹⁻³ and an improvement on present coupled-waveguide technology.⁴⁻⁶ The device is primarily designed to couple the stimulated emission from an integrated semiconductor laser into a co-integrated detector. With this design, the end facets (mirrors) of the laser are accessible for other uses such as coupling into fiber; consequently, the CWDs are especially useful as detectors for the new ring lasers⁷ for which there is only one output facet. In all applications, the CWDs provide larger, more uniform, and more reproducible coupling coefficients than the typical butt-coupled detectors. The geometry of the CWD is designed to reduce the amount of spontaneous emission coupled into the photodetector while using the same spontaneous emission to decrease the optical losses in the device. The CWDs can be integrated into any of the common semiconductor laser material systems.

7.A Introduction

Integrated detectors are necessary in many applications of semiconductor lasers. For example, the integrated detector might monitor the laser emission so that feedback circuits can regulate the intensity. As another example, some devices use lasers and detectors for integrated optical logic circuits.⁸ There are many designs for integrated detectors but the most common consists of a laser that is butt-coupled to a detector as shown in Figure 7.1. With this geometry, the semiconductor laser emits directly into the detector. The laser has two mirrors (facets) formed by chemically etching into the wafer deep enough so that the active region of the wafer forms an interface with air. This semiconductor-air interface forms the mirror. As shown, the geometry of the butt-coupling scheme requires a deep etch (on the order of several microns) between the laser and detector.

There are several consequences to the butt-coupled geometry:

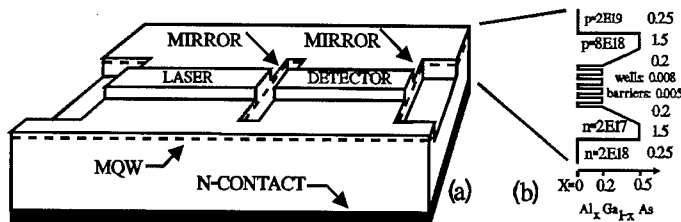


Figure 7.1: (a) Typical butt-coupled detector and laser. (b) The laser heterostructure.

(1) The detector architecture blocks one facet of the laser thereby leaving only a single laser facet available for output purposes.

(2) The deep etch drastically reduces the optical coupling between the laser and detector due to divergence and scattering. For typical Multiple Quantum Well (MQW) lasers, the light diverges due to diffraction at an angle of 60 degrees perpendicular to the plane (axial direction) and 30 degrees parallel to the plane (lateral direction) according to diffraction theory. Thus, most of the light from the laser emission diverges away from the wafer in the axial direction and does not couple into the detector. Attempts to increase the coupling between the laser and detector by decreasing their separation result in several problems with the laser mirrors. (a) Observations have shown that the gas-plasma etching becomes more difficult and leaves bridges of material between the laser and detector. These bridges of material seriously degrade the mirror quality and increase electrical crosstalk between the detector and the laser. (b) The parallel interfaces on opposite ends of the deep etch form a Fabry-Perot cavity. The separation between the laser and detector determines the effective reflectivity of both interfaces as a result of the interference between the multiple reflections within the deep-etch cavity. To some extent, the exact reflectivity cannot be predicted because of fabrication tolerances in the laser-detector separation. Thus the bridging and Fabry-Perot effects seriously affect the coupling coefficient and limit the performance of the butt-coupled detector.

(3) When the laser operates near threshold, the stimulated emission can have approximately the same intensity as the spontaneous emission, and the butt-coupled detector can produce a larger

response to the spontaneous emission than to the stimulated emission. Thus, the signal-to-noise ratio is poor at low intensity. For these reasons, it is desirable to investigate alternative coupling methods.

7.B Description of the Coupled-Waveguide Detectors

The Coupled-Waveguide Detector (CWD) has several typical aspects of coupled waveguides. However, its use and geometry are significantly different. Figure 7.2 shows the 3-D view of the preferred embodiment. All of the devices on the wafer

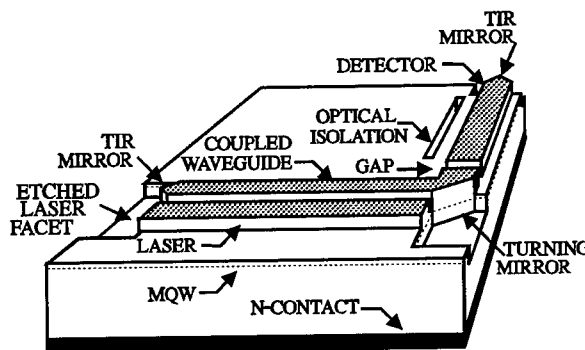


Figure 7.2: The Coupled-Waveguide Detector.

are ridge waveguides that are formed by shallow gas-based etches through the semiconductor contact and cladding layers; for our 5 quantum-well heterostructure, the height of the ridge is about $1.6\text{ }\mu\text{m}$. Metal electrodes (Ti-Pt-Au) are placed on top of the ridges for electrical bias. A shallow, oxygen ion implanted, $1\text{-}\mu\text{m}$ -wide etch separates the metal contacts and the respective underlying p-doped layer for electrical isolation. The laser ($5 \times L\text{ }\mu\text{m}$) has two facets that are accessible for output signals. The CWD itself has two sections. The coupled-waveguide section ($5 \times L\text{ }\mu\text{m}$) is placed within a distance S of the laser. The overlap length L is the same as the laser length. Both S and L affect the coupling coefficient. Typically S is less than $2\text{ }\mu\text{m}$ and L is on the order of $150\text{ }\mu\text{m}$. The coupled waveguide has a Total-Internal Reflection (TIR) mirror at one end to reduce optical losses. An etched 90° turning mirror directs the optical mode propagating in the coupled waveguide into the detector. The detector also has a TIR mirror at one end to decrease the optical losses. A deep etch serving as a mirror is placed about 10 microns away from the detector in order to reflect away any spontaneous emission from the laser.

As is typical for ridge waveguides, the small difference in refractive index across the edge of the laser ridge allows the laser optical mode to extend laterally well beyond the ridge.⁴ The portion of the mode outside the waveguide is the evanescent tail that decreases exponentially with distance from the waveguide due to its imaginary propagation constant. Typically, such tails do not carry away optical energy. Placing a second waveguide within the evanescent tail of the first, however, results in coupling between the tail and that waveguide. Hence, there is coupling between the two waveguides. The evanescent tail takes on a real propagation constant within the second waveguide which results in the flow of optical energy along the second waveguide. Thus, the second waveguide serves as a type of optical-energy tap. Only the energy that flows as a mode in the laser can properly couple into the second guide. As a result, spontaneous emission produced in the laser that is emitted in all directions will not couple into the second waveguide and it will not, therefore, produce a signal in the photodetector.

There are three points to be made regarding optical losses in the coupled waveguide.

- (1) A Total Internal Reflection (TIR) mirror is included on the left end of the coupled waveguide to reflect any of the mode traveling to the left. This mirror increases the light collection efficiency.
- (2) Any spontaneous emission from the laser that is absorbed in the coupled waveguide section tends to reduce the absorption losses there even though this spontaneous emission is not coupled into the mode of the second guide. This occurs because the absorption of spontaneous emission increases the carrier density in the active region and those carriers are available for stimulated recombination by the coupled mode. On the other hand, a deep etch is placed near the *detector* section to reflect any spontaneous emission from the laser. Without such an etch, the detector would produce a signal in response to the spontaneous emission passing through it.
- (3) In a similar fashion, the metal on the coupled waveguide can be used to electrically forward bias the waveguide and, thereby, reduce the optical losses by carrier injection. However, even though the forward bias increases the detected signal, it also produces spontaneous emission in the

coupled waveguide that can propagate to the detector section. The use of forward bias in this manner depends on the intended use and the required sensitivity of the CWD.

Figure 7.3 shows a top view of the CWD discussed above except for a change in design of the detector section. The detector is widened to collect more of the laterally diverging light from the waveguide as it passes through the electrical-isolation gap. The light diffracts at the gap since the waveguiding is lost over this $1\text{ }\mu\text{m}$ length.

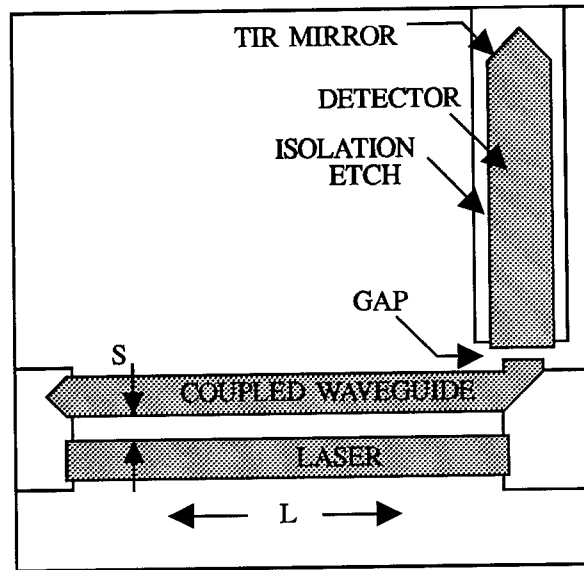


Figure 7.3: Top view of a CWD with an isolation etch around the detector.

In typical waveguides, light entering the waveguide at more than several degrees from parallel to the length of the guide will just pass out the sides due to the small index difference.⁴ The new detector design includes a deep etch around the detector which serves three purposes. First, light accepted into the input facet of the detector is totally internally reflected back into the detector which increases the collection efficiency. Second, the etch replaces the optical isolation etch as shown in Figure 2. Third, it improves the electrical isolation of the detector by etching through the p-doped cap layer of the laser heterostructure.

7.C Fabrication Notes

The CWDs can be fabricated with either semi-insulating or n-type substrates for the heterostructure. The fabrication procedure is as follows for the laser heterostructure grown on the n-type substrate (inset to Figure 7.1) with the p-type cap layer. First, a photolithography step defines the waveguide structures on the heterostructure. Using photoresist as a mask, the following metals are deposited: 400 Å of Ti, 200 Å of Pt, 3000 Å of Au, and 4000 Å of Ni. The nickel is used as an etch mask for a subsequent gas plasma etch in the Electron Cyclotron Etcher (ECR). A liftoff step leaves the metal where the electrical contacts and the waveguide will be placed. Next, photoresist is patterned so as to leave the deep etch regions exposed to BCl_3 and Cl_2 in the ECR. Two microns of material are etched in these openings. After removing the remaining photoresist, the sample is further etched using the metal areas as a mask, to remove an additional 1.6 μm of material across the surface of the entire wafer. Thus the deep etches that form the mirrors have a total depth of 3.6 μm and the shallow etches are 1.6 μm below the top of the waveguide ridges. As a side note, the uniformity and reproducibility of the ridges can be improved by epitaxially growing an AlAs etch-stop layer into the heterostructure. In this case, the gasses in the ECR would be selected to stop etching at the AlAs layer which would then define the ridge height. After the etching, the wafers are lapped to a thickness of about 150 μm . The back contact is deposited as 150 Å of Ni, 400 Å of Ge, 800 Å of Au, 500 Å of Ag, 1000 Å of Au. The electrical isolation is increased by implanting oxygen ions into the front surface at the following doses: 10^{13} ions/ cm^2 at 150 keV, 10^{12} at 60 keV.

7.D: Experimental Results

The effective responsivity of a Coupled-Waveguide Detector is defined as $\mathcal{R} = J/P$ (refer to Figure 7.4) where P is the power emitted from one of the laser facets and J is the photocurrent produced by the integrated detector. The optical power P emitted from the laser is measured by a 1

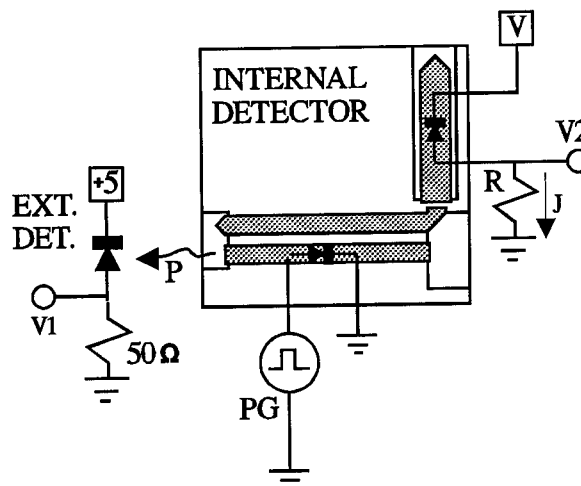


Figure 7.4: Test set-up for the prototype CWD

cm^2 photodetector moved to within several millimeters of the laser facet. The integrated detector is reverse-biased by setting $V = 5$ volts. At this bias, the responsivity is known to be independent of bias voltage. The photocurrent J is determined by measuring the voltage drop across a discrete resistor R placed in series with the integrated detector. The bias current to the laser is pulsed (10 μsec pulse width) by pulse generator PG. The output from each detector is routed to a digital oscilloscope as voltage signals V_1 and V_2 .

<u>L μm</u>	<u>\mathcal{R}, A/W</u>
185	0.28
167	0.31
149	0.27

Table 7.1: Preliminary results on the effective responsivity of the CWD as a function of overlap L . The separation is approximately $S = 2 \mu\text{m}$ (refer to Figure 7.3).

Preliminary tests on the effective response for several prototype coupled-waveguide detectors appear in Table 7.1. As noted in the table, the unit for the effective response is Amps per Watt.

The CWD measurements given in Table 7.1 can be compared to those obtained for an integrated laser that is butt-coupled to a detector. The butt-coupled detector architecture is similar to the one shown in Figure 7.3 except the deep etch extends around all sides of it. The deep etch around the detector increases the efficiency of light collection since most of the light incident on

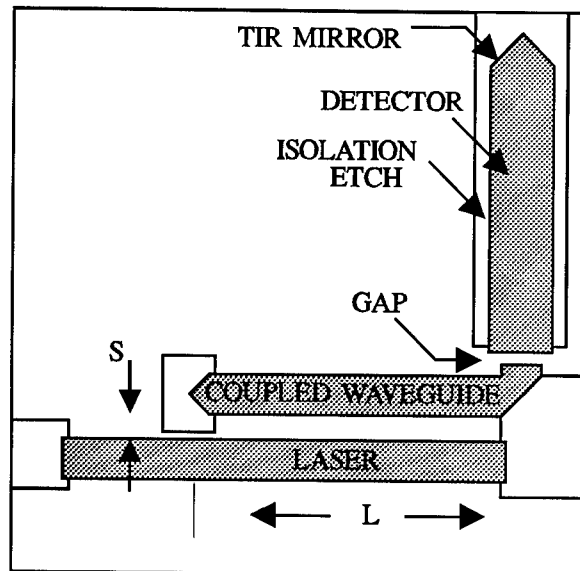


Figure 7.5: The length of the laser is different from that of the coupling length.

the sides of the detector from within will be totally internally reflected back into the detector interior. The laser is $10\text{ }\mu\text{m} \times 200\text{ }\mu\text{m}$ and the detector is $30\text{ }\mu\text{m} \times 200\text{ }\mu\text{m}$. For planarization during fabrication, polyimide is added to the wafer. The deep-etch between the laser and detector is filled with polyimide while the laser facet next to the external detector forms an air interface. The polyimide has three effects. (1) The output power from the laser is twice as large at the polyimide interface as it is at the air interface. This is easily shown by calculating the round trip gain in the laser cavity and using the correct relative index of refraction for each laser facet. (2) The coupling between the lasers and detectors varies by up to a factor of 5, presumably due to non-uniformity in the polyimide coating in the deep etch. (3) The polyimide also helps to reduce the optical loss due to the diffraction of light from the laser. The coupling gap is $3\text{ }\mu\text{m}$ for this particular laser-detector pair. The effective response is found to be 0.077 Amps/Watt.

The effective response of the integrated detector changes by about 15% with bias voltage for the range of 0 to 8 VDC. Preliminary tests show that the responsivity is essentially independent of reverse bias for $V > 3$ volts.

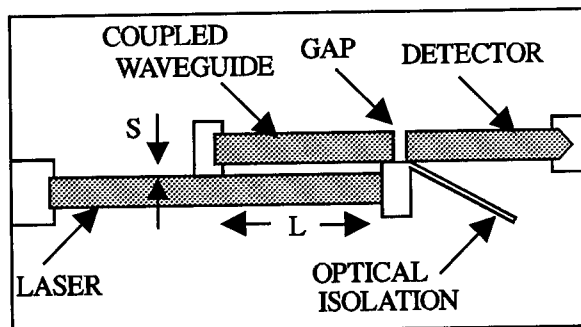


Figure 7.6: Linear version of the CWD.

Section 7.E: Discussion

The CWD has significant advantages over other methods of coupling detectors to lasers.

New features:

1. The combination of the detector with the coupled waveguides.
2. The use of a deep etch around the detector for the following purposes: (i) improved light collection efficiency, (ii) improved electrical isolation, (iii) reflection of spontaneous emission away from the detector.
3. The electrical isolation gap between the coupled waveguide and the detector allows the detector to be biased differently than the coupled waveguide.
4. The right angle geometry of the CWD.
5. The use of spontaneous emission to lower the optical losses. The coupled waveguide can be forward biased to further decrease loss.

Advantages:

1. It does not require a laser facet for coupling. Thus all of the laser facets are accessible for other applications. This is important for ring lasers.
2. More uniform coupling coefficients.
3. Higher effective response.
4. Better rejection of spontaneous emission than other methods of coupling.

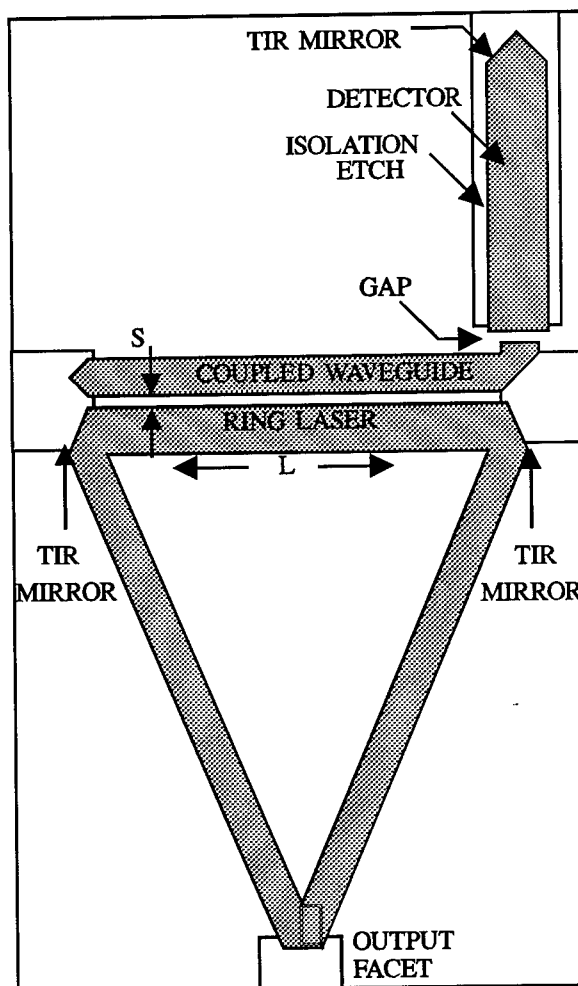


Figure 7.7: Ring laser with a CWD.

Figure 7.5 shows an example for which the overlap length L between the two waveguides is different than the length of the laser, allowing the coupling coefficient to be tailored to any desired value.

Figure 7.6 shows a linear version of the CWD. As before, the detector is electrically isolated from the coupled waveguide by a shallow etch. A deep etch serves as optical isolation. Light incident on the etch is totally internally reflected away from the detector.

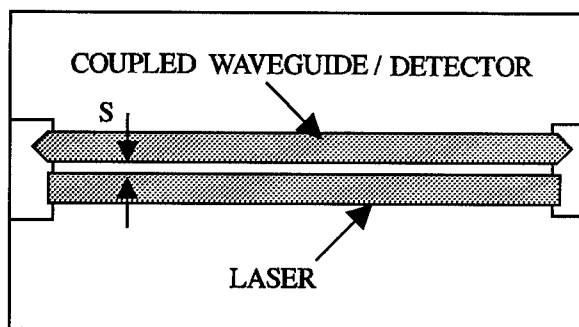


Figure 7.8: CWD with the detector and coupled-waveguide sections combined into one unit.

Figure 7.7 shows a ring laser with the coupled-waveguide detector. Note that the ring laser has only one output facet. The other facets are TIR turning mirrors.

It is possible to replace the coupled waveguide with a detector as shown in Figure 7.8. This arrangement would minimize the optical losses and maximize the coupling. However, for some lasers the spontaneous emission might saturate the detector.

Chapter 8: Introduction to Opto-Electronic Technology

The development of efficient semiconductor lasers has created a market with huge potential for the semiconductor industry.¹ Inexpensive and reliable, semiconductor lasers capable of emitting at the minimum dispersion (1.3 μm) or absorption (1.55 μm) wavelengths of silica fiber offer the perfect light source for optical fiber communications²⁻⁵. Long-distance communications systems are currently being retrofitted to take advantage of the inherently high bandwidth associated with optical signals, combined with the lower loss and increased noise suppression of optical fiber compared to electrical cable. In a similar way, *integrated* semiconductor lasers are being examined as a means of utilizing optical interconnects locally, *i.e.* chip-to-chip upon a computer expansion board, or even between devices on a single IC chip. The use of such optical interconnects eliminates the speed limitations imposed by electrode capacitance, and reduces signal interference and crosstalk. Perhaps the greatest advantage, however, is the ability to massively interconnect by means of planar (2D) optical arrays as opposed to the current linear (1D) electrical buses. Whereas the number of electrical contacts to an integrated circuit is limited by the density of pins spaced around the chip periphery, accessibility can be improved by orders of magnitude by optically addressing the circuit through a transparent window normal to the chip surface.

In the case of local optical fiber interconnects, fiber loss and dispersion are irrelevant because of the short distances involved. But an even simpler design can be implemented by completely eliminating the optical fiber in favor of *free-space* optical interconnects, which rely on precision alignment between emitters and detectors placed in close proximity. Lasers based on the well-known lattice-matched AlGaAs / GaAs material system (~ 850 nm emission) are a more reasonable choice for these applications, since the emission wavelength need not be at 1.3 or 1.55 μm .

One computer architecture especially suited for opto-electronic integrated circuitry is the neural network. This system consists of arrays of nodes on each of several adjacent planes. The outputs of nodes on one plane are connected to the inputs of nodes on the adjacent plane. The inputs of each node are individually weighted according to the particular algorithm to be implemented, then summed and applied to a nonlinear thresholding function, as shown in Figure 8.1. If the sum of the weighted inputs exceeds the threshold value, also programmed for a particular algorithm, then the output of the node is energized. Neural networks typically require massive interconnection between each set of planes, which is not feasible to perform electrically. Free-space optical signals, however, are perfectly suited to perform this connectivity, since laser output beams can be steered to the appropriate input nodes on the successive level using integrated micro-lenses⁶ or micro-mirrors, and there is no crosstalk between intersecting beams. Opto-electronic integration can further enhance the utility of the neural network by making both the input weights and the threshold values electronically programmable, and even dynamic.⁷

Image processing is another application which can benefit greatly from the development of integrated

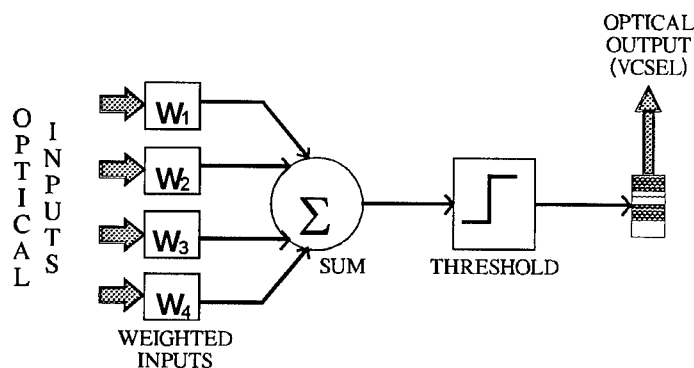


Figure 8.1: Optical-In, Optical-Out Neural Network Node

opto-electronics. Conventional electronic circuits process pixelated two-dimensional images by first digitizing each pixel's color and intensity, then applying some logic operation to this digital representation before rebroadcasting the image (by CRT, for example). Images are moved around within the computer by serially transmitting each pixel in order across the data bus, an inherently

slow process for which speed is inversely proportional to resolution. By transmitting the 2D image optically intact within the computer, image processing is expedited by replacing the serial data transmission with a parallel optical process. Furthermore, by integrating the necessary electronic functionality at each "smart pixel" location, the image processing can be performed at each pixel simultaneously, rather than sequentially, vastly reducing processing time and removing the dependence of speed on resolution.

There are many proposed schemes for developing modulated light-emitting semiconductor devices for the optical communication and signal processing applications discussed above. One feasible near-term solution is to combine the maturity of silicon electronics technology with III-V laser heterostructures. This can be accomplished either by post-fabrication hybrid bonding of the two substrates, or by epitaxial growth of GaAs thin film heterostructures on silicon substrates prior to circuit fabrication.⁸⁻¹² The time and expense required for these procedures, however, will make them less attractive as other, more efficient, opto-electronic integration technologies are developed. An alternative approach which has been investigated is the development of porous silicon light emitters,¹³⁻¹⁷ for direct integration with silicon-based electronics. Porous silicon, however, has poor durability and operational lifetime. Because of its porous structure, it is difficult to contact with conventional metalization techniques, and is most often biased through submersion in an electrolytic solution.¹⁶ Porous silicon has not demonstrated a power conversion efficiency comparable to that of III-V compound semiconductors,¹⁷ and cannot be considered a competitive optical source. Much further material characterization and development is required if this technology is to offer a viable opto-electronic alternative.

The most promising technology for opto-electronic circuitry is monolithic integration of lasers and electronics on the same III-V substrate.^[18-22] High-speed GaAs electronics and lasers have each been produced and marketed individually. Their integration into a single heterostructure,

however, presents new difficulties.²³⁻

³⁰ High-performance transistor designs, which typically require a thin channel layer, cannot be directly implemented into commonly-used laser heterostructures, such as the graded-index separate-confinement heterostructure (GRINSCH),

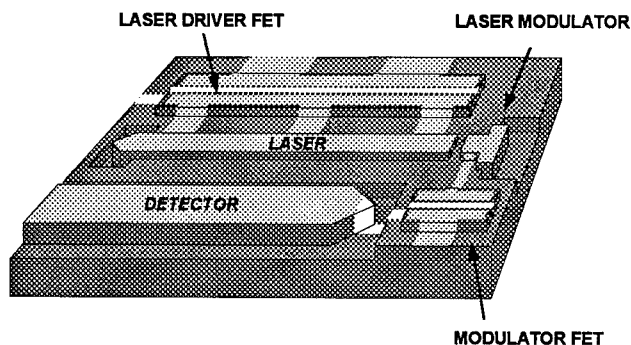


Figure 8.2. Integrated FETs with Edge-Emitting Lasers

because of the larger layer thicknesses. The transistor layer structure must then be included either underneath or atop the laser structure. One of the resulting problems with GaAs opto-electronic integration is reliable electrical interconnects between the electronics layers and the laser structures, because of the large vertical steps involved. A conceptual diagram of an opto-electronic integrated circuit (OEIC) is shown in Figure 8.2, consisting of a photodetector, laser, and intra-cavity modulator, integrated with FET control circuitry.

A unique family of integrated logic gates, called Diode Laser Logic,³¹ has been designed for opto-electronic implementation.

These particular devices utilize optical inputs and outputs, and can be configured to perform any Boolean logic function, or combination thereof. The output signal is generated by an etched-ridge index-guided laser with vertically etched end mirrors. Within the laser cavity, but electrically isolated from the

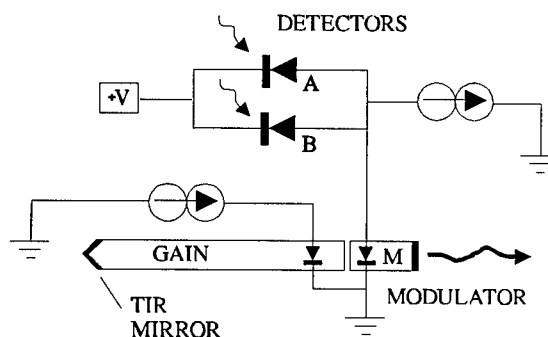


Figure 8.3. Diode Laser Logic (OR Gate) Schematic.

main laser contact, is a modulator region, as shown in Figure 8.3. This modulator is connected to a constant-current source which, according to the particular logic configuration, either provides or draws away current. By supplying current, the source forward-biases the modulator which provides gain to the laser cavity. When connected in reverse (as in Figure 8.3), the source sweeps carriers out of the modulator. This increases the cavity losses, since the modulator becomes absorptive, thereby increasing the output laser threshold. Also connected to the current source are the integrated photodetectors, which when reverse-biased convert incident optical energy into electrical current through carrier generation. The current-source is designed so that its capacity matches the detector photocurrents whenever optical input signals are present. Thus, in Figure 8.3, the presence of an optical input signal at either Detector A or B produces a photocurrent which satisfies the current-source, allowing the photon density to rise in the intra-cavity modulator, and the output laser to emit an optical signal. By appropriately biasing the output laser near threshold, its on/off state can be controlled by the absorption of the intra-cavity modulator, which is in turn determined by the presence or absence of optical inputs focused onto the detectors.

The Diode Laser Logic gate performance can be improved by integrating the constant-current source directly on the same substrate as the lasers, detectors, and modulators. The electrical interconnects between the devices would then have much lower parasitic inductance than bonded wires leading to external drivers. In addition to the current sources, however, the ability to integrate electronics with the optical devices has many other implications. Field-effect transistors (FETs) have a much smaller footprint than lasers and detectors, so the packing density of electronic logic gates would most likely be greater than that of comparable laser logic gates. Furthermore, the GaAs electronics can potentially outperform the lasers/detectors in modulation speed and power consumption. Finally, electronic implementations of certain auxiliary functions such as clocking could be added to the integrated circuits.

In summary, applications exist for OEICs as transmitters and receivers in long-distance optical communications systems and as local optical interconnects. Integrated lasers can generate free-space optical signals for high-density neural network connections. Image processing speeds can be significantly reduced by incorporating "smart pixel" processing on a two-dimensional optical data bus. The most feasible design for these applications, using currently available technology, is the monolithic integration of optics and electronics in a III-V compound semiconductor heterostructure. As an example of the capabilities of this integration approach, a family of integrated opto-electronic Boolean logic circuits has been designed. While optical signals carry information between devices and perform the primary logic operations, integrated electronics can provide the proper electrical biasing of the optical components as well as perform additional digital processing.

Chapter 9: The Design of Monolithically Integrated FETs and Lasers

The monolithic integration of Field Effect Transistors (FETs) and lasers is an intensive area of research at present. It is possible to first grow one device, for example the laser, process the wafer in the clean room, then use a regrowth process to grow the FET by placing the wafer back into the MBE or MOCVD equipment, and finally finishing the processing on the FET. Another method consist of epitaxially growing the FET and laser (IPL or VCSEL) sequentially during the same growth run. The layers must be carefully designed for the two types of devices to operate independently of each other. Although not used for the present study, the use of the new oxidation process of AlGaAs layers should prove to be the ultimate form of electrical isolation between the FET and laser and for the gate isolation for the FET.

9.A FET Design

The silicon metal-oxide-semiconductor field-effect-transistor (MOSFET) is the bulwark of today's electronics products. The affordability and availability of silicon, combined with the maturity of silicon processing technology, have allowed electronic circuits to influence our lives in innumerable ways. With the developing trends in high-speed *optical* communications,¹ however, the inability of silicon devices to emit light, as well as the limitations in their modulation speed, require investigation into other material systems, such as direct-bandgap III-V compound semiconductors. High-purity epitaxial growth methods (such as MBE and MOCVD) and device fabrication processes have not yet been perfected for the III-V materials, resulting in only moderate yield. However, the benefits to be derived from higher carrier mobility and optical emission capability outweigh the expensive growth and fabrication processes required for their implementation.²⁻³

A wide variety of GaAs transistor types have been designed, due to the fact that GaAs lacks the ability to grow a suitable native surface oxide required to directly implement MOSFET technology.² Epitaxial heterostructures and new fabrication processes have been developed to implement logic functions analogous to those performed by the more common silicon CMOS technology. The simplest transistor design implemented in GaAs is the metal-semiconductor field-effect transistor (MESFET), consisting of a rectifying contact placed directly onto the doped channel. This Schottky contact is the gate electrode used to modulate the channel current flow. MESFETs, however, have a small voltage threshold because of tunneling leakage current through the forward-biased Schottky gate contact into the highly-doped channel. A modulation-doped transistor (MODFET) consists of an undoped channel layer of a small-bandgap material, underneath a larger-bandgap, doped barrier layer. At thermal equilibrium, band-bending induces a two-dimensional electron gas at the barrier-channel interface. Since the ionized impurities (within the barrier) are separated from the moving carriers in the channel, the scattering rate is significantly reduced, and carrier velocity is increased. Doping limitations exist, however, since highly-doped AlGaAs is difficult to grow, and contains a high defect density and DX trap centers. Additionally, higher doping increases gate leakage current by narrowing the tunneling barrier. Further enhancements in MODFET performance can be attained by including an undoped spacer layer between the barrier and channel to further separate carriers from the ionized impurities, and by employing planar doping⁴ to further control gate capacitance,⁵ gate leakage current, and photoconductivity in the doped AlGaAs layers.

A more direct GaAs analogy to the silicon MOSFET, called the metal-insulator field-effect transistor (MISFET) or doped-channel MIS-like transistor (DMT),⁶⁻¹¹ is shown in Figure 9.19.1. This transistor employs a doped channel like the MESFET, but adds an epitaxially-grown undoped (insulating) barrier on top. The gate leakage problem of the MESFET is resolved, and the device

heterostructure does not have the tight growth tolerances of a planar-doped MODFET. It has been shown that despite the high concentration of ionized donors within the channel, devices with high transconductance can be obtained.^{6,11} The MISFET boasts a high current capability, due to the high carrier density in the

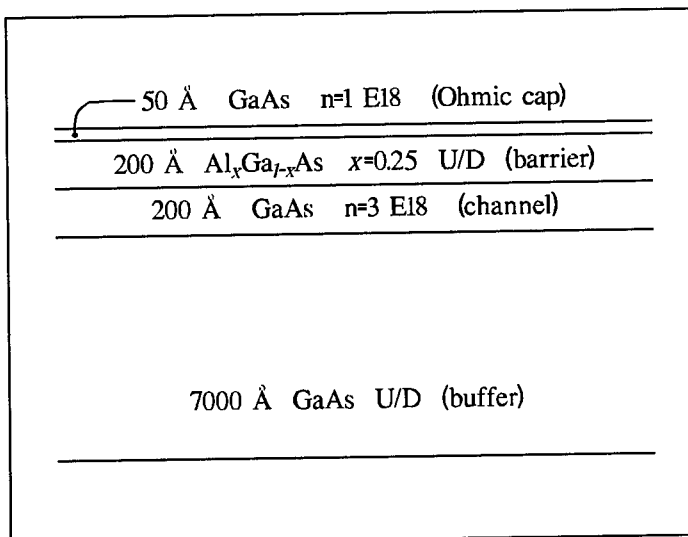


Figure 9.1: N-type Doped-Channel MISFET Heterostructure

channel. Additionally, photoconductivity effects caused by the DX centers in n-doped AlGaAs are avoided.

The band structure of a MISFET device can be calculated at thermal equilibrium (*i.e.* no source-drain current) for any applied gate voltage. The analysis consists of simultaneously solving Poisson's equation in the undoped barrier, the doped channel, and the underlying undoped buffer layer, with the appropriate boundary conditions. Within the undoped layers, Poisson's equation reduces to Laplace's equation, since the charge density is negligible. For the case of the degenerately-doped channel, however, one must consider the overall position-dependent net charge density $\rho(z)$, given by:

$$\rho(z) = q[p(z) - n(z) + N_D(z) - N_A(z)] \quad (9.1)$$

where q is the unit electronic charge, p is the hole density (negligible in highly n-doped material), N_D is the ionized donor density, and N_A is the ionized acceptor density (zero in this case, since no p-type doping is employed). The free-electron density, $n(z)$, in degenerate material is proportional to the Fermi integral of one-half order:

$$n(z) = N_c F_{1/2} \left[\frac{\xi_F - E_c(z)}{k_B T} \right] \quad (9.2)$$

where N_c is the conduction band-edge density of states, k_B is the Boltzmann constant, T is the lattice temperature, ξ_F is the Fermi energy, and $E_c(z)$ is the position-dependent conduction band-edge energy. A FORTRAN computer program, named C-BAND,¹² can be used to perform this numerical analysis at multiple gate bias points. The C-BAND program provides further accuracy by including quantum energy effects caused by the narrow channel layer thickness in the growth direction. C-BAND calculates the position-dependence of the conduction band-edge energy by considering the boundary values, the carrier distribution effected by the quantum wave equation, and the potential energy resulting from such a carrier distribution. The potential energy function is carried through multiple iterations, repeatedly solving for the wave equation, until the program converges.

$E_c(z)$ and $n(z)$ are plotted in Figure 9.2 for the MISFET structure shown in Figure 9.1. The Schottky barrier height for AlGaAs materials is typically pinned near mid-band by surface

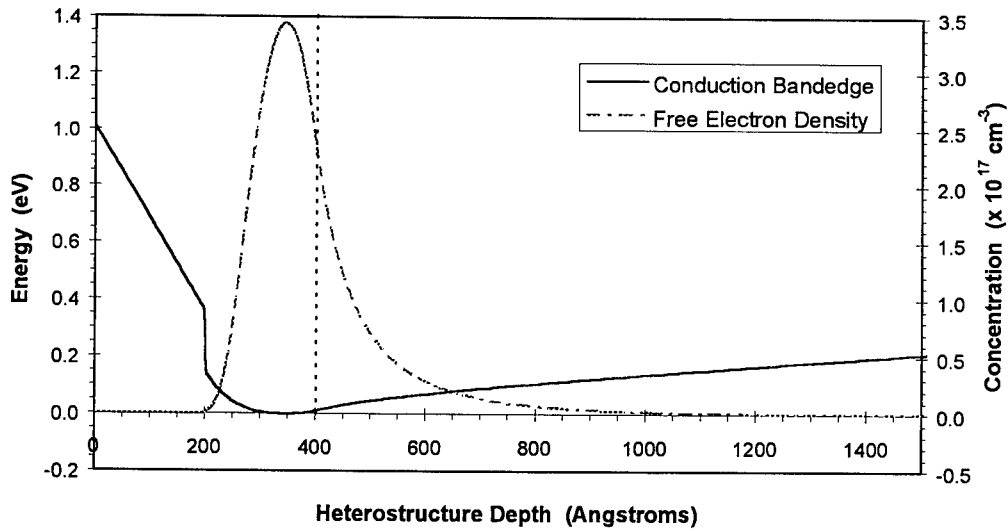


Figure 9.2: Conduction Band Diagram and Carrier Concentration at Zero Gate-to-Channel Bias

states, and is approximately 1.0 eV for $\text{Al}_{0.25}\text{Ga}_{0.75}\text{As}$.⁴ The conduction-band discontinuity, DE_c , at the $\text{Al}_{0.25}\text{Ga}_{0.75}\text{As}$ / GaAs heterojunction is taken as $0.6 \times \text{DE}_g^G = 0.187$ eV,¹³ where the overall bandgap increase,¹⁴ $\text{DE}_g^G = 1.247 x$, for $x \leq 0.45$. For aluminum mole-fractions larger than 0.45, the AlGaAs bandgap is no longer direct, and electron transport is further complicated by inter-valley scattering events.

Note that, since there is a very small charge density within the undoped AlGaAs barrier layer ($0 \leq z \leq 200$ Å), the electric field is (approximately) constant and the potential has no curvature in this region. The Schottky barrier potential induces a space-charge region in the doped channel ($200 \leq z \leq 400$ Å), the width of which is a function of both the channel doping density and the barrier width. The lower edge of the channel is marked in Figure 9.2 by a dotted vertical line at 400 Å. Notice that the channel electrons tend to “spill over” with a significant density into the undoped buffer layer beneath. This is due to the fact that the conduction band is continuous at this interface, and the doping in the buffer layer is so low (1×10^{15} p-type in this C-BAND simulation).

Integration of the position-dependent carrier density indicates a two-dimensional electron density of $3.69 \times 10^{12} \text{ cm}^{-2}$, of which 6% ($2.21 \times 10^{11} \text{ cm}^{-2}$) is carried in the undoped buffer. These values include not only free electrons in the conduction band, but also those bound to the shallow, hydrogenic level of the donors, since both of these states contribute to conduction through the channel.

Depending on its polarity, an applied voltage at the gate terminal can either increase or decrease the depletion in the doped channel, thus modulating the source-drain channel current. Figure 9.3 shows the C-BAND data generated for a gate-to-channel bias of -2.0 V, corresponding to the pinchoff voltage for this particular device. Note that the scale for carrier concentration is four orders of magnitude less than in Figure 9.2. The integrated sheet density at this bias is calculated to be only $7.46 \times 10^8 \text{ cm}^{-2}$, for a cutoff ratio of nearly 5000. Further negative gate bias results in

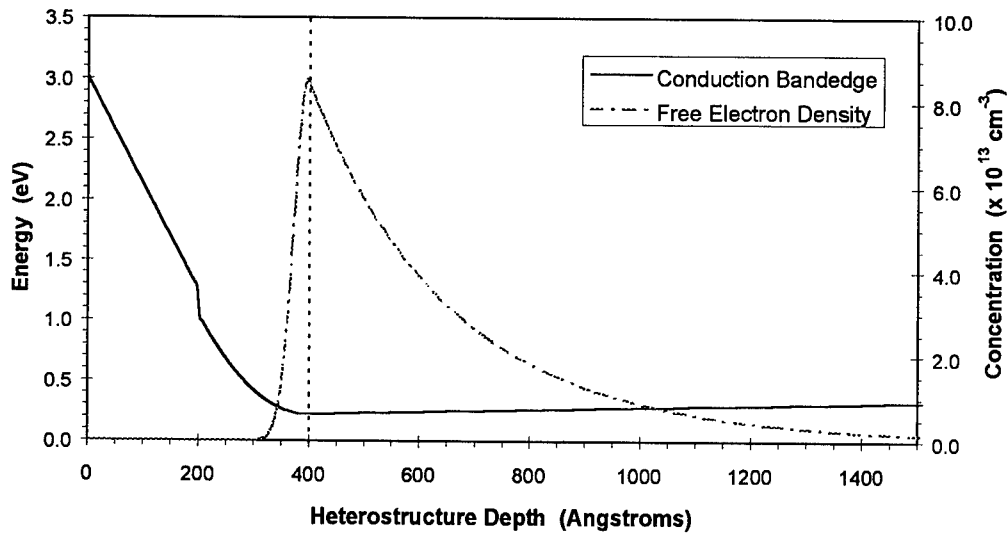


Figure 9.3: Conduction Band Diagram and Carrier Concentration at -2.0 V Gate-to-Channel Bias (Channel Cutoff)

even more complete channel depletion. One noticeable disadvantage of this particular heterostructure design, however, is the leakage of electrons into the buffer layer. Although the buffer layer only supports 6% of the sheet density at 0-V bias, 30% of the conducting electrons are carried by the buffer layer at -2 V. This carrier leakage is detrimental to the cutoff properties of the transistor, since larger electric fields simply repel the carriers further into the buffer layer without completely depleting them.

MISFETs can also operate in an enhancement-mode,⁷ in which *forward* gate bias is applied to create a carrier accumulation effect in the doped channel. By optimizing the layer thicknesses and channel doping, it is possible to integrate both enhancement-mode and depletion-mode transistors.

Better carrier confinement, as well as a higher channel free-electron density, can be obtained by adding a heterostructure barrier underneath the doped channel. Figure 9.4 shows the calculated C-BAND data for the same MISFET with a 400Å undoped $\text{Al}_{0.25}\text{Ga}_{0.75}\text{As}$ barrier added beneath the channel, for comparison with Figure 9.2. Note the better confinement of electrons

within the channel, increased peak carrier concentration, and lower “spill-over” of electrons into the undoped buffer layer. The two-dimensional sheet density for this structure at 0-V bias is calculated to be $3.63 \times 10^{12} \text{ cm}^{-2}$, with only 0.2% of the population outside of the doped channel.

The real significance of the added heterostructure barrier is revealed in the cutoff condition shown in Figure 4. The sheet density has been reduced to $1.93 \times 10^8 \text{ cm}^{-2}$, for a cutoff ratio of over 18000. Additionally, the population within the GaAs buffer is only $2.95 \times 10^6 \text{ cm}^{-2}$, or 1.5% of the total carrier density. Thus the conduction electrons are confined to the channel even under cutoff conditions, allowing for excellent transistor modulation characteristics.

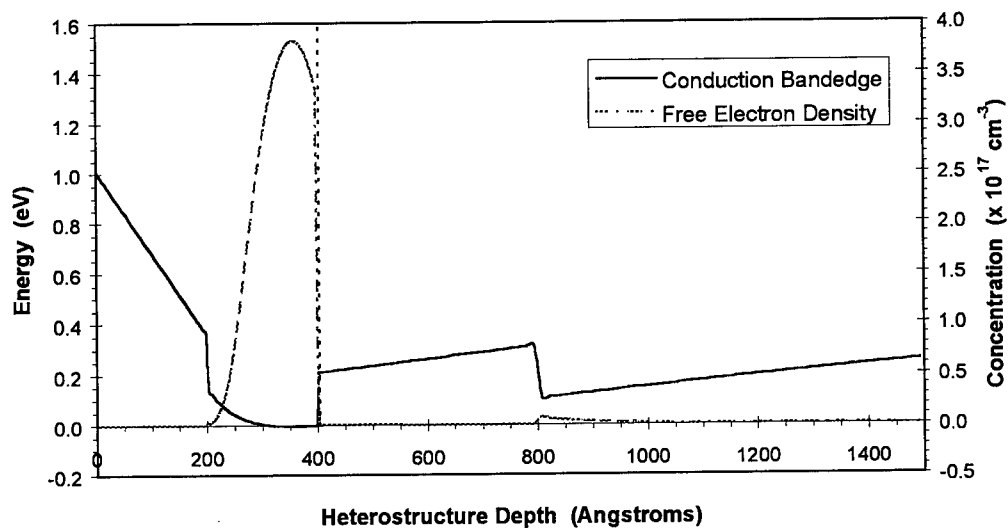


Figure 9.4: Conduction Band Diagram and Carrier Concentration at Zero Gate-to-Channel Bias, with an AlGaAs Barrier Added Under the Channel

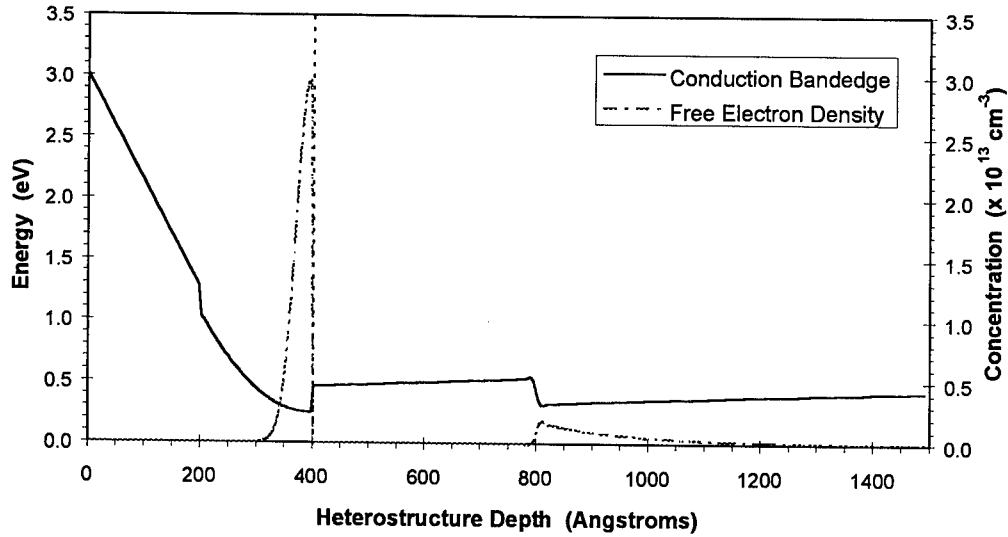


Figure 9.5: Conduction Band Diagram and Carrier Concentration at -2.0 V Gate-to-Channel Bias, with an AlGaAs Barrier Added Under the Channel

MISFETs have been fabricated and tested by Hida *et al.*⁶ They report 0.5- μm gate-length devices with transconductance $g_m = 310 \text{ mS/mm}$ and an average electron velocity $\langle v_e \rangle = 1.5 \times 10^7 \text{ cm/s}$ at room temperature ($g_m = 410 \text{ mS/mm}$ and $\langle v_e \rangle = 2.0 \times 10^7 \text{ cm/s}$ at 77 K). These values rival those of conventional doped-barrier MODFETs with similar (-2.0 V) pinchoff voltages. The MISFET especially stands out because of its higher saturation current (650 mA/mm at room temperature, 800 mA/mm at 77 K) and higher breakdown voltage $V_{GS} > +1.0 \text{ V}$. Because MESFETs and conventional MODFETs use a doped layer directly beneath the gate contact, a thinner tunneling barrier results, leading to a higher gate leakage current than with the MISFET.

In summary, transistors implemented in GaAs can take advantage of higher carrier mobility and saturation velocity than in silicon. Of the many heterostructure transistor designs, the doped-channel MISFET has the attractive features of a high two-dimensional electron density, good transconductance characteristics, and a layer structure which is simple to epitaxially grow.

Additionally, because of the undoped barrier layer beneath the gate electrode, gate leakage current is minimized and the transistors can operate in the enhancement mode. Computer simulation of the conduction band diagrams and carrier concentrations for this particular MISFET design indicate a pinchoff voltage of -2.0 V, with cutoff characteristics improved by the addition of another heterostructure barrier beneath the channel layer. The simplicity of the MISFET epitaxial structure facilitates its integration with the optical waveguiding structure described in the following chapter.

9.B: Laser Design

The edge-emitting laser material implemented in this project consists of five GaAs quantum wells separated by $\text{Al}_{0.2}\text{Ga}_{0.8}\text{As}$ barriers, surrounded by a graded-index separate-confinement heterostructure (GRINSCH) and an $\text{Al}_{0.5}\text{Ga}_{0.5}\text{As}$ doped cladding, as shown in Figure 9.6.6. The quantum wells provide a high degree of spatial carrier confinement, thus requiring a lower threshold current to achieve population inversion. The graded-index layers create an internal electric field which compels both electrons and holes toward the quantum wells. The injected carriers relax into the wells through phonon scattering within the graded-index structure.¹⁵

A single transverse optical mode (normal to the epitaxial planes) is defined by the

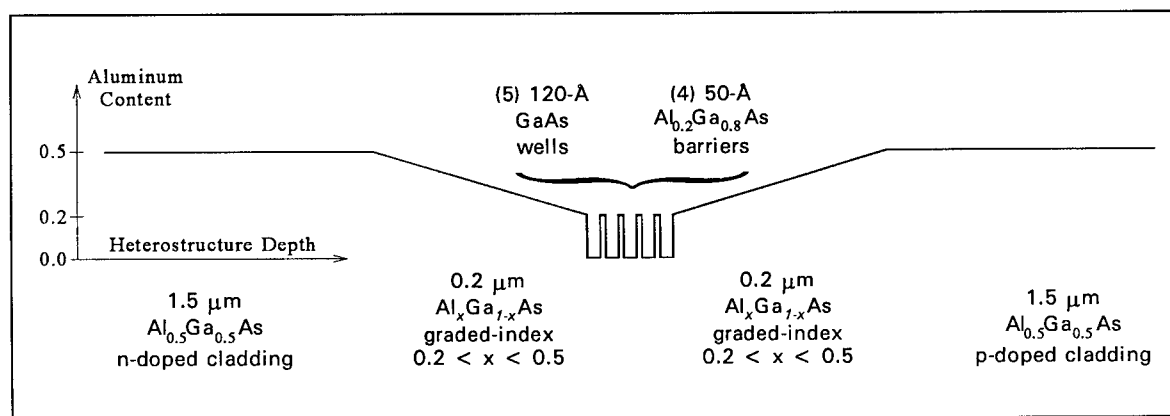


Figure 9.6: Multiple-Quantum-Well Graded-Index Heterostructure

GRINSCH, which is designed to provide a high optical confinement factor, optimizing the stimulated emission rate. Lateral confinement (parallel to the epitaxial planes) is provided by etched-ridge index-guiding, as described in Section 9.C below. Fabry-Perot cavities are created by vertically etching mirror-like facets at both ends of the laser stripe, down through the entire heterostructure and into the substrate. Typical fabricated laser dimensions are 5-20 μm wide \times 100-500 μm long.

As calculated in J. Kimmet's Thesis (refer to Acknowledgements), 120 \AA GaAs quantum wells emit laser radiation at $\lambda_o = 856 \text{ nm}$. Carrier confinement is provided by the bandgap discontinuities in both the conduction and valence bands at the well / barrier interfaces. For $\text{Al}_{0.2}\text{Ga}_{0.8}\text{As}$ barriers, these steps are calculated¹³⁻¹⁴ to be $\Delta E_c = 0.149 \text{ eV}$, and $\Delta E_v = 0.100 \text{ eV}$. The 50 \AA barrier width is designed for a compact multiple-quantum-well (MQW) structure, while minimizing the coupling of carrier wavefunctions between adjacent wells (tunneling).¹⁶ Figure 9.7 shows the ground-state conduction-band wavefunction, with less than 5% coupling between quantum wells. Note how rapidly the wavefunction decays beyond the outer wells ($\pm 400 \text{ \AA}$).

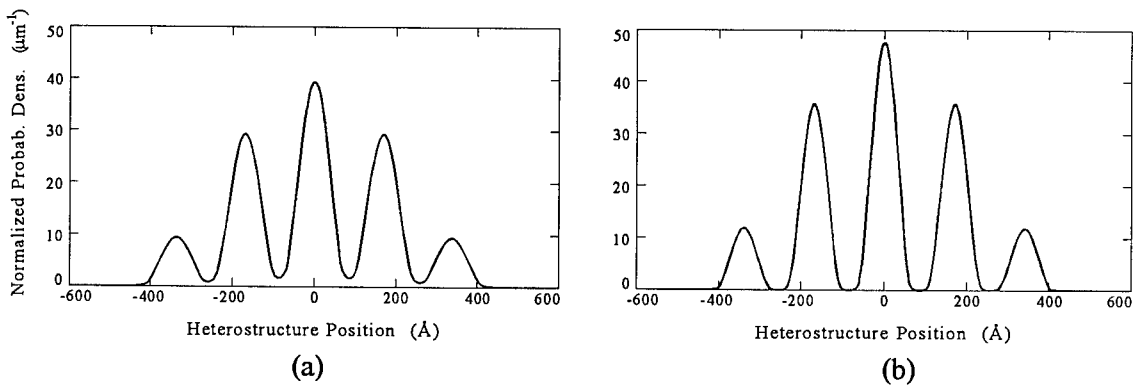


Figure 9.7: Ground-State Quantum-Well Wavefunctions for the (a) Conduction Band and (b) Valence Band

The ground-state valence-band wavefunction shows similar characteristics, with even better isolation between wells (Figure 9.7b). These envelope wavefunctions are obtained by simultaneously solving Schrödinger's Equation within each epitaxial layer of the active region, using continuous boundary conditions.

This analysis ignores carrier scattering, and assumes that the particles are non-interacting. Band-bending is also assumed to be negligible at the operating bias. The solution method is greatly simplified by considering the valence band to be parabolic. This approximation is valid near the bandedge, where the light-hole and heavy-hole effective-mass equations decouple.¹⁷ The heavy-hole effective mass is used to determine the quantized valence-band energy levels, since at low injection levels, radiative recombination occurs primarily between conduction-band electrons and heavy holes.

The solution obtained in Appendix A reveals energy-level splitting in the conduction band, due to the wavefunction overlap between adjacent wells. The close proximity of the five quantum wells causes the ground-state to split into a "band" of five closely-spaced energy levels,¹⁸ listed in the table below. Since these energies are separated by only 2.4 meV, they are expected to each be populated by electrons at room temperature. Simultaneous recombination from each of these occupied states may result in a broadening of the emission spectrum by about 1.4 nm (toward the blue). Although the calculations show that the *valence* band has many allowed energy levels, it is assumed that holes occupy only the ground state at reasonable injection levels due to the large density of states.

Transverse optical mode confinement is provided by index guiding in the graded-index layers

Quantum Number	Conduction Band Energy
0	19.7 meV
1	20.2 meV
2	20.9 meV
3	21.6 meV
4	22.1 meV

shown in Figure 9.6. The transverse electric field distribution within the waveguide is calculated

by modeling the graded-index layer as a piecewise-linear step function consisting of six steps on each side of the active layer. The refractive index for each epitaxial layer is calculated as the square-root of the corresponding dielectric constant ϵ , which varies with the aluminum mole-fraction in $\text{Al}_x\text{Ga}_{1-x}\text{As}$ materials.¹⁹

$$\epsilon = 13.18 - 3.12x \quad (9.3)$$

The calculation includes the simultaneous solution of the Wave Equation within each epitaxial layer of the waveguiding structure, using continuous boundary conditions. The analysis reveals only a single supported transverse mode which is plotted in Figure 9.8. The shaded region identifies the MQW active region, while the dashed lines delineate the outer edges of the GRINSCH. The calculated optical confinement factor for this particular mode is about $\Gamma = 18\%$.

Figure 9.8 shows the excellent waveguiding provided by the GRINSCH. Calculations indicate that

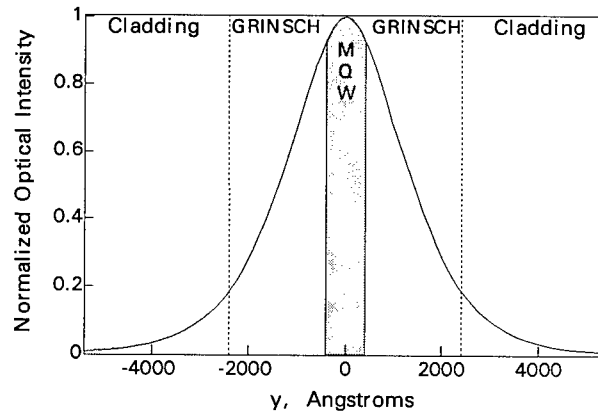


Figure 9.8: Optical Intensity of the Transverse Laser Mode

the optical intensity decays to 0.1% of its peak value within the first 450 nm of the cladding layers, and to 0.01% within 530 nm. In practice, however, thicker cladding layers are typically grown, to allow for a graded doping profile. Heavily-doped AlGaAs contains a high density of induced deep-level traps, called DX centers, which are optically absorptive. It is therefore desirable to use a low doping concentration for the inner 0.5- μm of the cladding, where the optical mode has sufficient intensity to introduce optical loss. For the integrated opto-

electronic heterostructure, cladding layers were grown with a total thickness of 1.5- μm , to allow for a dopant gradient.

In summary, a multiple-quantum-well edge-emitting laser structure has been designed for integration with the MISFET structure in a combined opto-electronic heterostructure. A graded-index layer is grown on each side of the active region, to improve the optical mode confinement and to facilitate the relaxation of injected carriers into the quantum wells. The quantum well and barrier widths are designed for efficient gain characteristics without tunneling interaction between wells. The waveguide is shown to support a single transverse optical mode at an emission wavelength of 856 nm, with a confinement factor of 18%. AlGaAs / GaAs MQW lasers, with a reputation for high quantum efficiency and reliable performance, are an ideal choice for opto-electronic integration, due to the relatively simple fabrication process required to produce etched-ridge waveguides.

9.C: Heterostructure for the Monolithically Integrated FETs and lasers

In order to combine lasers and photodetectors with monolithically integrated electronics, GaAs / AlGaAs heterostructures have been designed which combine a MISFET layer structure with a GRINSCH for in-plane lasers. The semiconductor layer structure designed for transistor implementation is grown on top of the GRINSCH laser structure presented in 9.B. An undoped GaAs buffer layer is sandwiched in between, with sufficient thickness to isolate the electric fields between the disparate devices. The combined FET / Laser heterostructure is grown on GaAs semi-insulating (S.I.) substrates by metal-organic chemical-vapor deposition (MOCVD) in a single growth session. Some researchers grow either the laser or transistor structure first, and complete the initial fabrication of such devices, followed by an epitaxial regrowth of the remaining device structure and further processing. Such regrowth methods, however, are not feasible for mass production because of the low yield resulting from poor surface conditions upon which regrowth

must take place. Epitaxial growth techniques require atomically clean and smooth surfaces, in order to properly seed single-crystal growth. Contaminants, surface roughness, and other surface damage induced during the processing of the primary devices hinders the success of subsequent regrowth for the secondary devices.

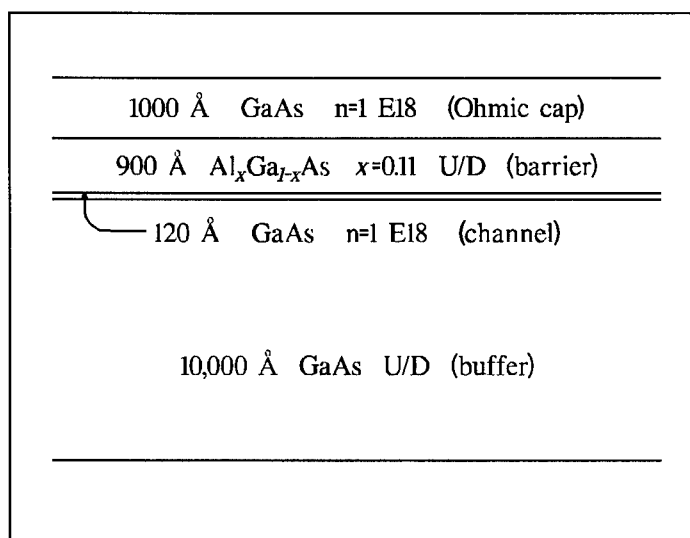


Figure 9.9: Initial MISFET Design

The first single-growth opto-electronic heterostructure designed for this research was based on the MISFETs reported by D'Asaro *et al.*²⁰⁻²¹ shown in Figure 9.9. AT&T designed this layer structure for monolithic integration of transistors with their self-electrooptic-effect devices (SEEDs).²⁰⁻²⁴ In particular, the doped-GaAs channel is kept thin, and an undoped AlGaAs gate barrier is used, so as to minimize the absorption of optical signals which must propagate through the transistor layers to reach the underlying SEED MQW absorption / reflection region. To properly fabricate MISFETs in this structure, the heavily-doped cap layer must be removed under the gate metal electrode, so as to form a Schottky contact and eliminate gate leakage current. AT&T used a highly-selective Freon-12[®] plasma etch to perform this step. Without the use of Freon[®], such etch selectivity is difficult to reproduce, primarily due to the small aluminum mole-fraction ($x = 0.11$) in the gate barrier layer.

The elusiveness of a substitute selective etching technique meant changes in the design of the transistor heterostructure, to that shown in Figure 9.1. This structure is patterned after the successes reported by Hida *et al.*^{6,8} Besides the increased aluminum mole-fraction in the gate

barrier layer, several layer thicknesses in this design are better suited for transistor performance and the integrated fabrication process. Since this opto-electronic heterostructure is not intended to support vertically propagating optical signals, optical absorption is not a consideration. The thickness of the doped-GaAs channel is therefore increased, for a higher carrier sheet density and a corresponding increase in saturation current. A thinner AlGaAs gate barrier is used, to reduce the voltage drop across this layer, and the corresponding voltage range required at the gate terminal to induce channel cutoff. The cap and buffer layer thicknesses are also decreased, reducing the overall vertical dimension of the integrated structure. Finally, the thickness of the laser n-contact layer is significantly increased to ease the tolerance on the mesa etch depth, due to etching difficulties described in the following chapter.

A separate heterostructure was grown with the heavily-doped top cap layer replaced by 100-Å of *undoped* GaAs. Device fabrication is considerably simplified with this structure, since there is no need to perform a gate recess etch. A non-annealed gate electrode can be placed directly

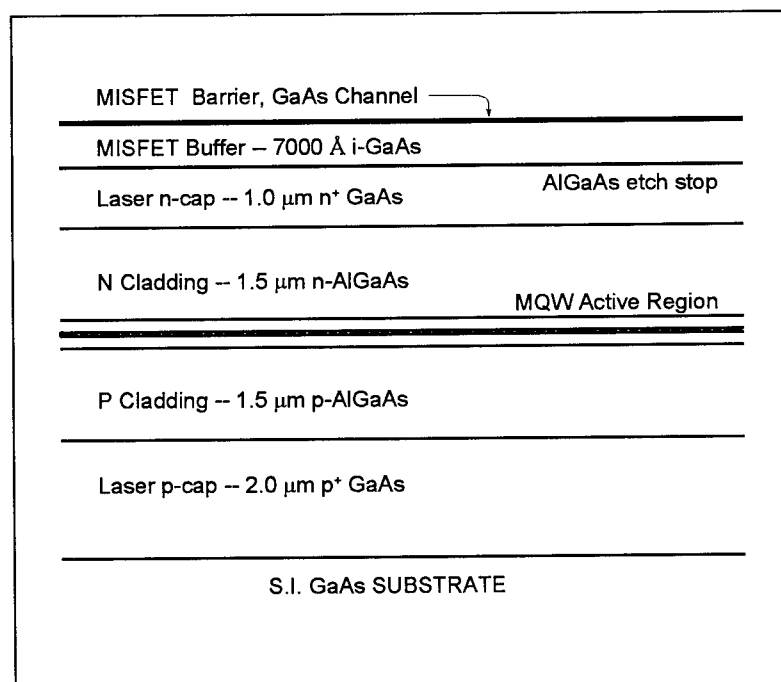


Figure 9.10: Revised FET/Laser Integrated Heterostructure

on the wafer surface, and gate leakage current will still be negligible because of the high resistivity of the undoped cap material.⁵

The complete opto-electronic heterostructure is shown in Figure 9.10. The transistor layers are much thinner than the layers comprising the optical waveguide. On the scale of Figure 9.10, the MISFET layers appear compressed into the topmost line. This integrated structure allows independent operation of individual electrical and optical devices, yet provides the capability to interconnect these devices into complex opto-electronic circuitry. The MISFET layers, including the buffer, are removed to form optical devices by selectively etching these areas of the wafer. This leaves the fabricated transistors on raised mesas above the lasers and photodetectors. High-quality laser mirrors are created by anisotropic plasma etching down through the entire waveguide structure. The ability to fabricate vertical laser mirrors away from the edges of a wafer die, without requiring cleaved facets on both ends of each laser cavity, is essential for the complete integration of opto-electronic circuits. The growth of the epitaxial structure upon a semi-insulating substrate allows electrical isolation of the buried p-contact layer between optical devices, facilitating the independent biasing of lasers, modulators, and detectors.

Chapter 10: Preliminary Tests of Monolithically Integrated FETs and Lasers

The initial batch of devices to be fabricated was an array of MISFETs with varying channel width and gate length. This array was designed to provide an adequate number of devices to statistically determine the operating characteristics of the transistors. Channel widths ranged from 5 μm to 100 μm , controlling the saturation current level of each transistor. The gate lengths varied from 0.5 μm (the lower limit of optical lithography) to 10 μm , affecting the transconductance and switching speed of each device. The transistor fabrication was simplified by omitting the waveguide processing steps. Fabrication was performed with heterostructure wafer pieces from the initial transistor design. Mesa isolation was achieved with a timed reactive-ion etch (RIE) using BCl_3 / Ar / SF_6 , which penetrated midway into the $\text{Al}_{0.6}\text{Ga}_{0.4}\text{As}$ etch-stop layer beneath the GaAs buffer. The gate recess was performed with a timed citric acid / hydrogen peroxide wet etch. The conducting channel, however, was destroyed by the affinity of the wet etch for the metalized source and drain contacts. Although the devices could not be tested in operation, this initial fabrication batch was useful for determining the tolerances of many of the processing steps, as well as the overlay alignment accuracy of the many photolithographic layers. An SEM micrograph of one of the completed MISFET devices is shown in Figure 10.1a. The smaller recessed rectangle to the right of the FET mesa shows the induced roughness on the RIE-etched surface. The magnified image in Figure 10.1b shows damage to the metal contacts, but the over-etched depth of the gate is not clearly evident from these photos. Subsequent measurements of the gate recess using atomic force microscopy (AFM) indicate an etched depth of 2500 \AA , well past the channel depth.

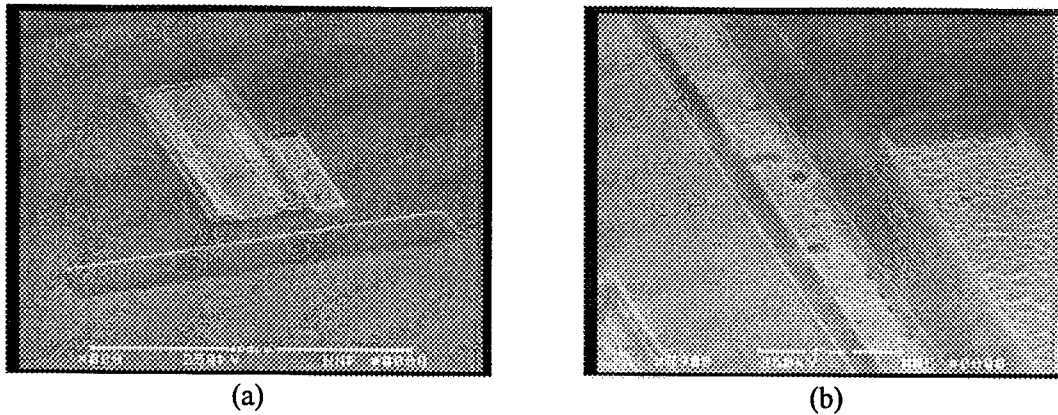


Figure 10.1: Completed FET Device from the First Fabrication Batch. (a) view of the entire device; and (b) magnified image, showing the damage to the metal contacts caused by the wet gate recess etch.

A second fabrication batch was begun, with the same objective to produce testable MISFET devices. The same mask set was used, so as to produce the FET array described above. This second batch used heterostructure pieces grown with the revised transistor design and substituting a 100 \AA *undoped* cap layer, to preclude the necessity of recessing the gate electrode through the highly-doped cap. Once again, a timed RIE etch was used to define the transistor mesas, this time with a resulting depth variation from 6500 \AA - 11000 \AA . The etched wafers exhibited a “ringed” surface feature centered within the wafer, corresponding to the etch depth variation, the deeper etch being around the wafer perimeter.

Since only transistors were being fabricated during this batch, the nonuniformity of the mesa etch was ignored. Rapid thermal annealing and polyimide application, curing, and etching procedures were all developed and tested during this batch. Since no gate recess etch was necessary, the top metal pads were deposited immediately after definition of the gate electrodes in the mesa via etch. Figure 10. shows several FET devices after completion of the entire transistor fabrication sequence.

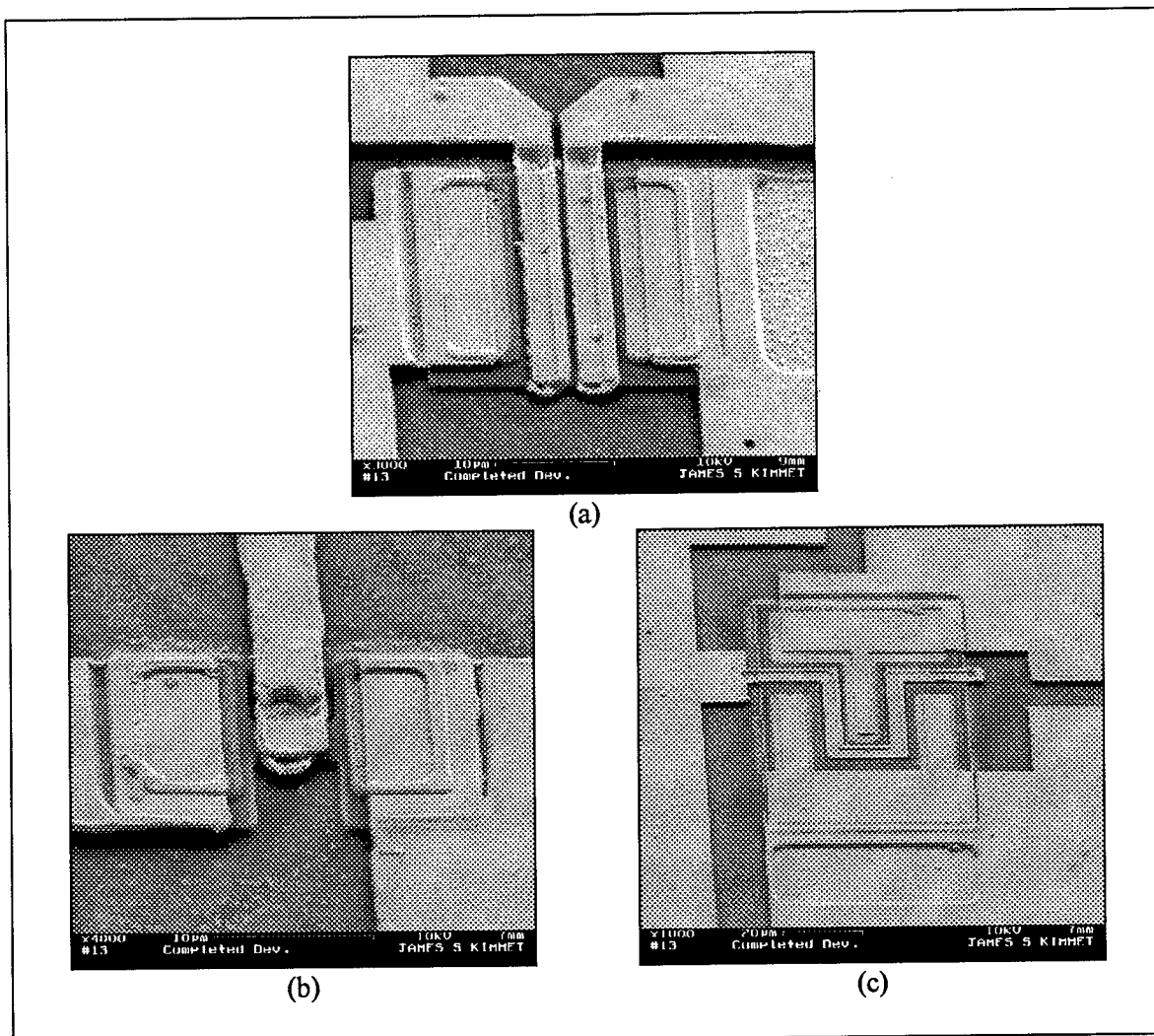


Figure 10.2: Completed FET Devices from the Second Fabrication Batch. (a) dual-gated FET; (b) very narrow channel for ultra-small saturated currents; and (c) interdigitated configuration, designed to fit a large-channel-width transistor within a smaller area.

One noticeable trait in the SEM micrographs shown in Figure 10. is the “dip” in the gate electrodes at the edges of the mesas. Alignment errors during exposure of the polyimide via pattern (Layer 6) resulted in a trench between the mesa and polyimide, along two adjacent edges of each mesa. The gate electrodes of most of the transistors were forced to bridge that gap. Magnified images of these gate “bridges” are shown in Figure 10.. This undesirable predicament weakened the gate electrodes, and consequently degraded transistor reliability.

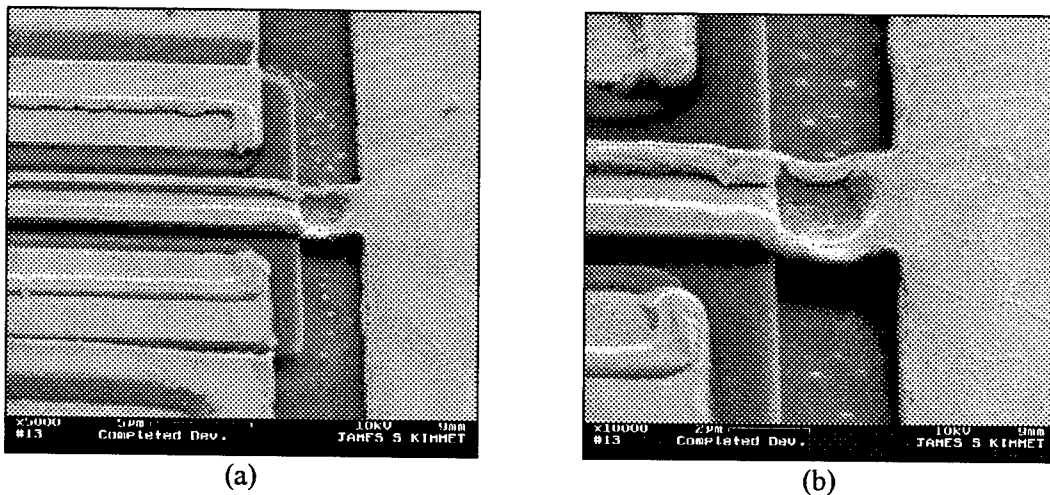


Figure 10.3: Magnified Images of the Gate Electrode at the Mesa Edge

The completed transistors were mounted in a probe station with microscopic probe placement for electrical characterization. The gate characteristics were tested, to evaluate the quality of the Schottky contact metalization. The gates showed excellent diode-like forward-bias characteristics, with an average 0.4-V knee. The contacts had about 4.0-V reverse breakdown.

The source-drain characteristics were not as pleasing. The channel current had a linear characteristic which showed no saturation. The channel conductivity could not be modulated by the gate voltage. With the application of several negative volts to the gate terminal, the aforementioned “bridges” in the gate electrodes (at the mesa edges) would fail catastrophically, destroying the device under test.

Consideration of the possible causes for the nonsaturating linear characteristic lead to the conclusion that the GaAs buffer layer, as grown, is unintentionally doped slightly n-type. The layer specifications submitted to the epitaxial growth vendor requested that this layer be *undoped*. Practical growth methods, however, inevitably result in some residual doping due to chamber contaminants, adsorption from chamber walls, etc. The simulated band structures and carrier concentrations shown in Section 9.A were obtained by assuming a light p-type doping in the buffer layer. It is suggested that material be grown with a specification for light p-type doping ($\sim 10^{15} / \text{cm}^3$) within this layer, as well as the addition of an $\text{Al}_{0.25}\text{Ga}_{0.75}\text{As}$ barrier immediately beneath the channel to deter leakage current through the buffer layer.

Chapter 11: Amorphous Silicon Elements for Memory

The main working component of the Amorphous Silicon Elements for Memory (ASEMs) is a thin film of hydrogenated amorphous silicon (a-Si:H). The ASEM converts an optical power signal P and an applied voltage V into an electrical current signal J according to $J = C_{vp} V P + C_v V$. The memory function is implemented through the proportionality coefficient C_{vp} which can be dynamically adjusted by more than ten-fold over a continuous range of values. The dark conductance C_v is also adjusted simultaneously with C_{vp} . The changes in the conductance are accompanied by modifications of the optical absorption spectrum of the a-Si:H. The value of the memory is retained indefinitely without applying power. The ASEM is monolithically integrable with other opto-electronic devices using a variety of materials including silicon and GaAs based electronics. The devices are suitable for optical memory, multipliers and neural net weight functions.

11.A: Introduction

Hydrogenated amorphous silicon (a-Si:H) is the non-crystalline form of silicon. The crystalline state is the most commonly studied and finds the most application in modern solid state technology. The atoms form a periodic array with each one bonded to four others; the bond lengths and angles are identical for each atom and long range order exists.

In the amorphous state, the long range order does not exist¹. The bonds all have essentially the same length but the dyhedral angle can vary (a change in the dyhedral angle occurs when two bonded atoms are rotated with respect to each other around the bond axis). In some sense, a cluster of fully coordinated silicon atoms produces local order but the distribution of dyhedral angles yields variation in the spatial orientation of the clusters. Furthermore, some of the atoms are less than four-fold coordinated and have unsatisfied bonds.² These dangling-bonds have three charge states: the D^+ has no electrons, the D^0 has one electron and the D^- has two electrons (D^- =

$D^0 + e^- = D^+ + 2e^-$). Under the proper conditions for the preparation of the amorphous silicon, many of the dangling bonds terminate in hydrogen atoms to produce hydrogenated amorphous silicon (a-Si:H).

Hydrogenated amorphous silicon grows as a thin film (several microns thick) on top of other materials most commonly through the process of Plasma Enhanced Chemical Vapor Deposition (PECVD). The deposition

conditions determine the minimum number of

dangling bonds in the material. Hydrogen reduces the minimum number by satisfying the bonds; this process reduces the number of

mobility-gap defects and improves the quality of the material for electrical conduction. However, the application of intense illumination, which is sometimes referred to as light-soaking, increases the number of dangling-bonds through a mechanism for the breaking of weak Si-Si bonds³ (the Staebler-Wronski Effect-SWE). The rate at which the bonds are reconfigured depends on the intensity which is typically on the order of 200 mW/cm². Figure 11.1 shows the dependence of the density of dangling bonds on the illumination time and the intensity. The illumination can be switched off and the number of dangling bonds stays at this larger value. The number of dangling bonds can be returned to the original pre-light-soaked value by annealing the a-Si:H film at elevated temperatures for a period of time. Figure 11.2 shows the reduction of the density of light induced defects N_{ind} as a function of temperature and annealing time.³

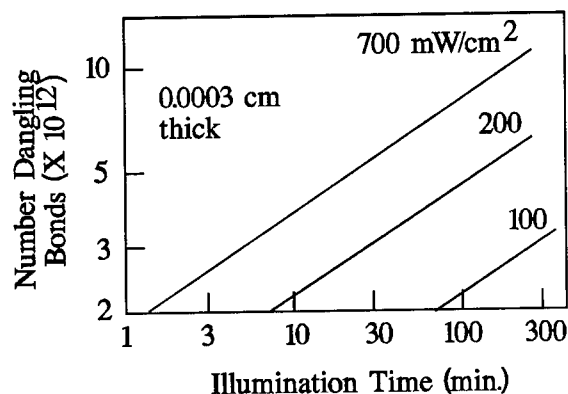


Figure 11.1: Number dangling bonds for an undoped amorphous silicon sample with volume 3 $\mu\text{m} \times 0.5 \text{ cm}^2$. Data taken from Stutzmann et. al., Ref 2.

There are two optical processes for the ASEM. The light-soak is the first process and photoconduction is the second. For photoconduction, a less intense optical signal is applied to the a-Si:H to produce an electrical current. The intensity is generally ten to a hundred fold less than

the intensity used for the light-soaks. The predominate photocarrier in undoped a-Si:H is the electron. Neglecting transient deep trapping effects,^{4,5} the steady-state photoconductivity can be expressed as

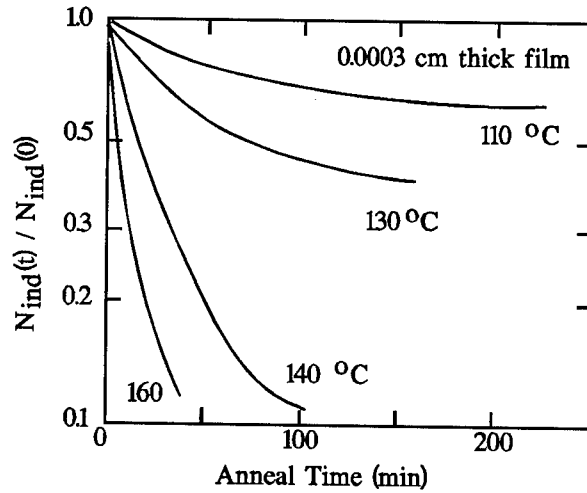


Figure 11.2: Number of dangling bonds as a function of anneal time. The mobility lifetime product is inversely related to the number of dangling bonds. Data taken from Stutzmann et. al. in Ref. 2.

$$\sigma_p = e G \tau \mu \quad (11.1)$$

where the symbols represent the elementary charge, the average rate of photocarrier generation per unit volume, the electron lifetime and the electron drift mobility, respectively. The generation rate G can be written as

$$G = \eta (1-r) \lambda P (1-e^{-\alpha T}) / hcT \quad (11.2)$$

where the equation relates the generation rate G to the reflectivity r at the air-silicon interface, the wavelength λ and speed of light c in a vacuum, the quantum efficiency $\eta(\lambda)$, the incident optical power per unit area P , the thickness T of the a-Si:H film, the absorption $\alpha(\lambda)$, the fractional decrease of intensity through the film $e^{-\alpha(\lambda)T}$ and Plank's constant h .⁶ In many practical situations $\eta \cong 1$ and $e^{-\alpha(\lambda)T} \cong 0$. Further neglecting surface effects, the photocurrent J_p produced by an applied voltage V is given by

$$J_p = (\sigma_p A_c / L) V \quad (11.3)$$

where L is the distance between the two electrodes and A_c is the cross-sectional area of the film taken normal to the length L . Figure 11.3 shows typical values for the mobility-lifetime product for undoped samples that are not light-soaked.⁷ The figure illustrates the results for both steady

state (SS) and transient (charge collection CC) measurement techniques. Photocurrents are on the order of $2 \mu\text{A}$ for a square a-Si:H film with 2 mW/mm^2 striking the surface and $\mu\tau \cong 10^{-5} \text{ cm}^2/\text{V}$.

The photoconductivity depends on the history of the light-soaking and the annealing. This is true since the light-soaking increases the number of dangling bonds which, in turn, decreases the photocarrier lifetime τ , the mobility-lifetime product $\mu\tau$, and the drift length $\mu\tau F$ (where F is the applied electric field). As already mentioned, the annealing reverses the process. Figure 11.2 shows that the photoconductivity increases with annealing time and temperature.

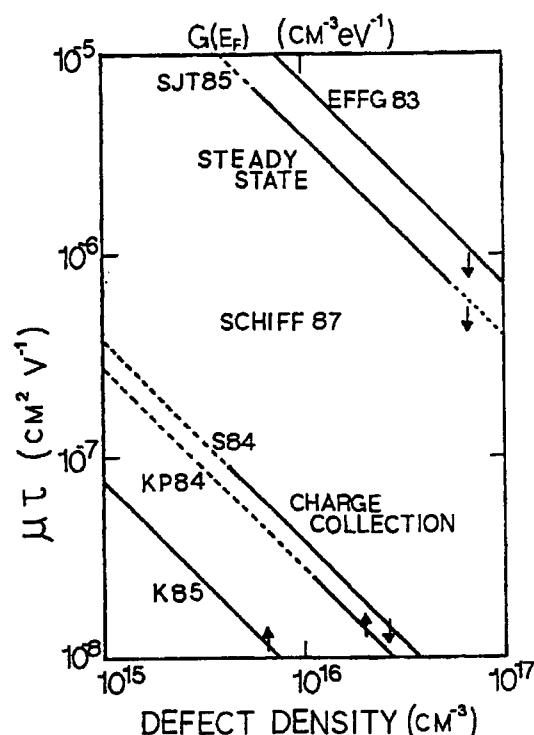


Figure 11.3: Mobility-Lifetime product taken from Parker Ref 1.

The dark conductivity also depends⁹ on the induced number of dangling bonds. At room temperature there is better than a factor of 1000 between the conductivity for the annealed and the light-soaked states. Thus the entire current flowing through the a-Si:H can be written as

$$J = C_{vp} V P + C_v V \quad (11.4)$$

In addition, the absorption of the a-Si:H film depends on the density of gap states. There are two primary regions of the spectrum affected by the Staebler-Wronski Effect (SWE). The first is between 2500 and 5000 nm as shown in figures 11.8 and 11.9.¹⁰

11.B: Description and Use of the Memory Elements

The memory element consists of two parts. The first part uses the optically induced defect in amorphous silicon for optical memory. The second part consists of an integrated device to modify

the density of defects. The methods for growing a-Si:H films are well known. The films for this device are grown from the plasma decomposition of pure silane gas by Plasma Enhanced Chemical Vapor. The substrate temperature during growth is 200 °C and the growth rate is approximately 1 angstrom per second.

There are several embodiments of the Amorphous Silicon Elements for Memory (ASEM). The first embodiment uses the ASEM as a programmable photoconductor. For example, the amorphous silicon film is integrated with a Vertical Cavity Surface Emitting Laser (VCSEL). Light from the laser forms dangling bonds in the film and heat from the same laser anneals the film. The VCSEL must emit in the 600 to 700 nm range. The typical VCSEL consists of a two Distributed Bragg Reflector (DBR) mirrors on either side of a quantum well active region. The DBR mirror with the p-doped layers is usually grown on the top the laser. This mirror is partially transmissive and allows the laser to emit perpendicular to the plane of the heterostructure. The laser is typically biased through the top mirror by applying current to a ring shaped electrode around the periphery of the DBR mirror. A transparent polyimide film electrically isolates the amorphous silicon film from the VCSEL. Electrical contacts on the amorphous silicon are used to supply the bias voltage and also to extract the photocurrent signal.

Figure 11.4 shows a typical plot of the emitted optical power as a function of the bias current I . Point T is the threshold current of the VCSEL. In the current range between T and M, the light output is approximately linear with bias current. For large bias current, the temperature of the VCSEL causes the gain curve (gain

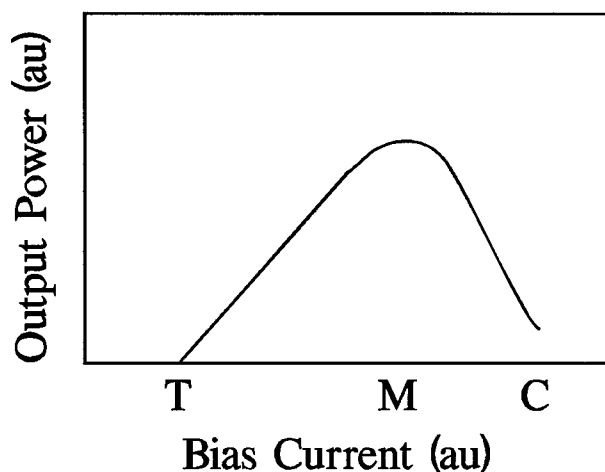


Figure 11.4: Typical output power vs. bias current for a VCSEL.

versus wavelength) to shift with respect to the reflection curve for the Fabry-Perot resonator that is formed by the two DBR mirrors. Increases in the bias current in the region between the maximum output M and cut-off C result in a decrease in emitted-optical power but an increase in heat and temperature. The placement of the three points T, M, C can be controlled by the geometry and construction of the VCSEL. The region between threshold T and maximum optical power M can be used to create dangling bonds and the region between the maximum M and the cut-off C can be used to anneal the film. In fact, with proper design, it should be possible to use the range between maximum M and cut-off C for both inducing and annealing dangling bonds in a continuous fashion. In such a case, the exact number of dangling bonds could be set and maintained by the bias current I. That is, annealing and induction proceed simultaneously and the density of dangling bonds reaches a steady state value. As a final comment, an external optical source such as another laser, provides the optical signal to produce the photocurrent J in the amorphous silicon film.

An application of the ASEM in a memory element for an optical neural net (refer to Ch. 2, Figure 2.18). An optical neuron implements a function of the form

$$O = \Theta(\sum I_i W_i - T_o) \quad (11.5)$$

where O is an output value. Θ is the Heavyside step function such that if the sum is larger than the value T_o then the output O is equal to the constant a; otherwise the Heavyside function produces a zero value. I_i and W_i are the input and weights for the neuron. The weights are normally adjustable so that the neural net can tailor its output to achieve a desired response for a given set of input conditions. Thus the net learns by adjusting its weights. The multiplication is normally the more difficult portion of the function to implement in a simple manner. The monolithically integrable circuit in Figure 2.20 can implements the function of Equation 11.5 for the case of a single input I_1 and weight W_1 (the SEED diode I1 is replaced by the amorphous silicon film). Optical signal W_1 incident on photodetector D1 produces a photocurrent that is amplified and

converted to a voltage V_1 by transimpedance amplifier (the amplifier can be as simple as a single resistor). This output is applied across the series combination of the ASEM and a resistor. The resistor has a small enough value such that the induced photocurrent does not significantly alter the voltage across the ASEM. The photocurrent J and, hence, the voltage V_2 are given by

$$V_2 = JR = C_{vp} R V_1 W_1 = C_{vp} R g I_1 W_1 \quad (11.6)$$

where I_1 and W_1 are the optical signals that represent the input and weight functions respectively, and g is the transfer function of the transimpedance amplifier. Equation 11.6 follows from Equation 11.3 by assuming that the dark current is small enough to be neglected. The comparator $C1$ provides an output if $V_2 > T_0$. If W_1 is a fixed intensity then C_{vp} controls the weight of the neuron. For most applications, it is essential that if power to the neural net is temporarily interrupted that the weights resume their previous value after the power is restored. Thus a memory function is critical for the proper operation of the net. The ASEM provides this capability and, in addition, the value of the weight can be adjusted while the neural net is operating. The weight ($C_{vp} W_1$) is adjusted by applying a bias current to the "weight adjust" input. The ability to adjust the weight is essential for the neural net to learn.

For a second and third embodiment of the ASEM, the current flow through either an integrated resistor or a PN junction supplies the heat to anneal the film. One external light source increases the number of dangling bonds and another produces the photocurrent signal. The fabrication of such a device uses normal fabrication procedures for integrated circuitry. This device has the same applications as the previous one.

A forth embodiment uses three distinct external light sources to (1) produce the photocurrent in the a-Si:H film, (2) increase the density of dangling bonds and (3) anneal the film. A focused laser can be used to anneal the film by using a wavelength such that the a-Si:H is transparent and the substrate is opaque to the laser emission. A small area of the film or substrate is heated by the absorbed laser light. For the case of light absorbed on the substrate, the small area heats the

amorphous silicon film that is grown on top. For example, if an a-Si:H film is grown on a germanium substrate then light with a wavelength of 800 nm passes through the amorphous silicon and heats the substrate below. A second example (refer to Figure 11.3), if a first film of amorphous silicon is annealed at 848 °K (curve 1) and a second film (curve 4a) is grown on top of it, then light with a wavelength near 700 nm is preferentially absorbed in the lower film to provide heat.

Section 11.C: Summary Discussion

Except for the memory where the physical medium is altered (photographs, holograms, Cds), removing power from the system generally causes a loss of the stored contents. In addition, the circuits are generally quite complex. The devices using changes in the physical medium generally can not be erased and written again.

Amorphous silicon has a variety of applications¹⁰ including solar cells, thin film transistors, charge coupled devices, sensors and detectors. In addition, amorphous silicon is used for optical recording.¹¹ All of the techniques use a physical change in the material to store the information. As a result, the memory can not be erased and written again. The information is generally written and read with a laser. Several examples are in order

(1) For one type of amorphous silicon optical memory, the amorphous silicon film is heated in such a way that hydrogen produces bubbles in the film. The reflectivity of the bubbles are significantly lower than that for the flat surface. A scanning laser beam can then read the information stored as a series of bubbles since the reflected beam will be modulated by the variations in surface reflectivity.

(2) Various combinations of lasers and voltage sources can be used to ablate the top layers on a disc where one of those layers consists of amorphous silicon. The resulting holes change the surface reflectivity.

(3) Laser annealing of amorphous silicon produces changes in the film morphology. The annealing changes the surface reflectivity as a function of wavelength. The film color changes from black to red to yellow.

(4) The phase transition from crystalline to amorphous silicon can be used for memory purposes. Fast laser pulses can be used to amorphize the silicon. The reflectivity of these regions are different from the crystalline regions.

There are several possible alternative modes of operating the ASEM.

(1) The ASEM should prove useful as an optically programmable resistor (as opposed to a photoconductor). Changes in the photoconductivity are accompanied by changes in the dark current. The structures shown in part C can also be used for the programmable resistors.

(2) The Staebler-Wronski effect involves changes in the density of dangling bonds in the gap and near the electron and hole mobility edges. The dangling bonds increase the absorption of light. As a result, with sufficient dangling bond density, the film should function as a modulator for the light. In such a case, an erasable Compact Disk should be possible. The device should operate in either a reflective or transmissive mode.

(3) It should be possible to use small wavelength particles, such as electrons to change the structure of the film for nanometer sized memory elements. Such a scheme should prove suitable for other materials that exhibit structural changes when illuminated.

PART 2
FABRICATION

Chapter12: Developing a Reliable Etch

An issue of equal importance to the design of the opto-electronic heterostructure layers is the establishment of fabrication processes which can define the individual devices and allow the application and retrieval of electrical and optical signals. Three methods exist to perform these objectives. Devices can be easily isolated by cleaving the crystal along the edges of each device. Although this method is sometimes applied to produce strips of broad-area lasers, it is not feasible for most electronic and optical devices, which are created on a much smaller scale, and is certainly not an option for creating integrated circuits.

A second technique is ion implantation, which can be used for both isolation and electrical contacting, depending upon the ion species being implanted. Isolation implants typically create highly-resistive regions by causing irreparable lattice bombardment damage and trapping centers due to interstitial ion placement. Doping implants, on the other hand, usually replace lattice atoms substitutionally and require a thermal annealing step to repair the lattice damage caused by ion penetration. Implant boundaries can be laterally defined by masking surface areas prior to implantation, and the depth of ion penetration is controlled by the ion acceleration voltage. The implant profiles, however, are Gaussian both in depth and laterally beneath the mask. This effect tends to make uniformly doped or isolated regions difficult to obtain. It is not possible, for example, to form a highly-doped implant region down to a buried contact layer, without having some doping effect in the layers immediately below the contact layer. The lattice damage induced by implants also effects the optical properties of waveguides, so this technique is not optimal for integrated optical devices. Finally, the high temperatures required to activate doping implants leads to material diffusion at the heterojunctions, thereby destroying certain heterostructure properties.

The third method utilized to define device dimensions and contact buried layers is etching, which is the controlled recessing of a heterostructure surface to a desired depth, by physically removing the overlying material. Similar to ion implantation, the wafer surface can be masked prior to an etch, to define the boundaries of the etching process. Depth is controlled by ceasing the etch after the appropriate duration as determined by a previous calibration of the reaction rate for the particular material. One problem with etching heterostructures, however, is that most etchants react differently with the specific materials present in each layer of the structure. This makes prediction of the etch results difficult if an etch is to penetrate several dissimilar layers. Furthermore, due to the physical nature of the etching process, etched surfaces sometimes tend to become roughened. Despite these complications, etching is the most common means employed both to define device dimensions and to access buried layers for electrical contact.

In order to fabricate *optical* devices in the integrated opto-electronic heterostructure presented in the previous chapter, for example, it is necessary to remove the five topmost layers which are used only for *transistor* implementation. Well-behaved etch processes are also required to form the mirror facets for integrated laser cavities, as well as recesses for metalizing the buried p-type contacts. Considerable effort was thus expended in an attempt to identify etching processes which would reliably and consistently produce the desired results. Wet chemical etches and dry plasma etches in a variety of machines were explored, and a resulting etch monitoring system was developed which allows real-time measurement of the etched depth, based on the unique properties of compound semiconductor heterostructures.

Both wet and dry etches work by continuously supplying ions which react with the Group-III and Group-V atoms at the exposed crystal surface, then desorbing the etch products from the surface, effectively removing one atomic layer at a time. The best way to reach the proper depth within a heterostructure without removing too much material is to perform a *selective* etch,

utilizing certain etchants which are only reactive with the material to be removed. A semiconductor layer with much lower reactivity to the etchant can be designed into the heterostructure at the desired stopping depth. Selectivity is attained because the etchant reacts with this "etch-stop" layer to form *nonvolatile* etch products, greatly slowing the etch. The ratio of etch rates between the layers to be removed and the stopping layer is called the selectivity of the particular etchant. Both wet and dry etches have been developed¹ with high selectivities in particular semiconductor material systems.

In the GaAs / AlGaAs material system, a selective etch is commonly required which removes GaAs, but stops at an underlying AlGaAs layer.² An etchant which selectively etches GaAs must produce nonvolatile aluminum compounds upon reaching the AlGaAs etch-stop layer. A continuous plane of these compounds with strong surface adhesion creates a barrier to further etch penetration. Of course, the effectiveness of the selective etch depends on the concentration x of aluminum in the ternary alloy $\text{Al}_x\text{Ga}_{1-x}\text{As}$. For low values of x , the nonvolatile aluminum compounds form isolated islands as the surrounding GaAs continues to etch. These islands can then be undercut and removed by the etchant, thereby bypassing the "etch-stop" barrier.

12.A: Selective Wet Etching

Wet selective etches were examined for the recessed gates required for this project, because of the slower etch rates available and the lack of ion-bombardment damage which typically occurs with a dry plasma etch. A consequence of wet chemical etching, however, is the slope of the sidewalls created at mask boundaries. These sloped walls are the result of chemical affinities to the differing crystallographic planes exposed during etching. Although sloped walls are undesirable for laser facet fabrication, their presence actually facilitates multi-layer interconnectivity by allowing smooth continuous metalizations between layers, rather than over abrupt vertical steps. Most wet etches for III-V materials work through the so-called re-dox

reaction.³ An oxidizing chemical, usually hydrogen peroxide, forms a thin oxide film on the exposed surface of the crystal. Another reagent, typically an acid, dissolves this oxide to remove one layer of the crystal. Selectivity to AlGaAs in a wet etch is attained by forming the stable reaction product Al_xO_y at a faster rate than its removal,¹ which requires correct proportionality between the oxidizing and reducing agents in the etchant mixture.

For the GaAs / AlGaAs material system, selective etching has been performed by mixing hydrogen peroxide with either ammonium hydroxide⁴⁻⁵ or succinic acid.⁶⁻⁷ Both of these mixtures, however, are quite sensitive to pH-level and temperature. A pH meter is required during mixing to monitor the relative concentrations of reactants. Within the desired concentration range, the addition of just a couple drops per liter causes a wide swing in the pH level. Besides the difficulty in accurately mixing the etchants, the ammonium-hydroxide etch also attacks photoresist because of its alkalinity.

The wet etchant tested in this effort was a citric acid / hydrogen peroxide mixture,⁸⁻¹¹ due to its availability, ease of preparation, and reported successes. The citric acid solution does not erode photoresist masks, is not pH-sensitive, provides a slower etch rate for more controllability, and results in better etched-surface quality than ammonium-hydroxide.

Tong *et al*¹ showed that all $\text{Al}_x\text{Ga}_{1-x}\text{As}$ compounds exhibit an etch rate threshold (in terms of the volume ratio between citric acid and H_2O_2 in the mixture), at which the etch rate abruptly increases by a factor of about 100, as shown in Figure 12.1a. The threshold shifts to lower volume ratios as x decreases. This variation in thresholds creates a “window” of volume ratios, as shown in Figure 12.1b, for which GaAs can be selectively etched over a layer of $\text{Al}_x\text{Ga}_{1-x}\text{As}$ with any given value of x . As x decreases, however, the selectivity window narrows, increasing the mixing precision required for the preparation of a selective etchant.

The initial heterostructure design for this project required a selective gate recess etch down to an $\text{Al}_{0.11}\text{Ga}_{0.89}\text{As}$ barrier layer. During experimentation, however, the threshold volume ratios for $\text{Al}_{0.11}\text{Ga}_{0.89}\text{As}$ and GaAs were indistinguishable. The selectivity window for $x=0.11$ was thus determined to be too narrow to effectively implement a selective etch.

An alternative technique for gate recessing, without relying on etch selectivity, is to perform a timed etch at a slow reliable etch rate. Experimentation determined that a 1.5 : 1 volume ratio reproducibly etches between 1000-1400 Å of the heterostructure in 14.0 minutes. This

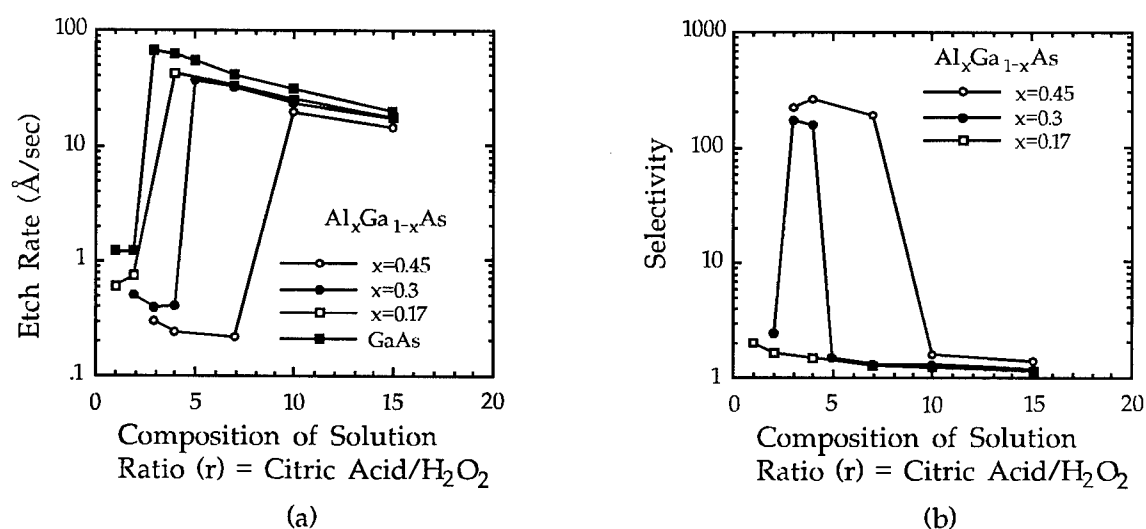


Figure 12.1. (a) Etch Rates and (b) Selectivities of $\text{Al}_x\text{Ga}_{1-x}\text{As}$ in Citric Acid/ H_2O_2 , from Reference [54].

specific etchant mixture yielded excellent surface smoothness during etch rate experiments. An attempt to use this etch on partially-processed FET devices, however, had catastrophic results. The etch was greatly accelerated in the vicinity of metalized areas on the wafer surface, despite the metal being entirely covered by an insulating silicon-nitride layer. Surrounding each metal pad was a trench created by enhanced acidic action. Kenefick⁵ reported a similar galvanic action when metal wafer tweezers were used in the $\text{NH}_4\text{OH} / \text{H}_2\text{O}_2$ system. Subsequent etch tests performed on wafers with metal stripe patterns (both covered and exposed) confirmed this phenomenon. The citric acid selective etch was thus determined to be incompatible with the fabrication process being developed, because of the unavoidable presence of metals throughout circuit fabrication.

Wet etches are, nevertheless, still useful for certain fabrication processes. Because of the natural affinity of acid mixtures for metalized regions, however, non-uniformity of the etch depth across the surface of the wafer is an inherent drawback when wet etching. The etch rates derived from simple homogeneous materials can provide only an estimate of the rates which will be attained when etching a partially-processed heterostructure wafer. Accurate etch control requires periodic removal of the wafer from the etching solution for either physical or electrical measurement of the etch depth. Repeated removal and submersion of wafers in a wet etch, though, can induce even further etching nonuniformity, since the liquid surface tension and trapped air tend to prevent the etchant from completely penetrating narrow holes and channels.

12.B: Selective Reactive Ion Etching

Plasma etches are desirable for many integrated circuit applications because of the higher etch rates attainable, uniformity across the wafer surface, and the vertical sidewalls which result from the directed acceleration of reactive ions within a high-vacuum etching environment. Dry etches are easier to implement, since the etching process can be instantaneously activated (or stopped) by switching the plasma power, and there is no need to accurately proportion and mix wet

chemicals. The etches are also more reproducible, because of their invulnerability to environmental conditions outside the etching chamber, such as ambient temperature. Plasma etching of the GaAs / AlGaAs material system requires a chlorine-containing compound,¹² such as chlorine gas (Cl_2), Freon[®]-12 (CCl_2F_2), or boron trichloride (BCl_3). Selectivity is attained by incorporating into the plasma a fluorine-containing gas, which produces the nonvolatile compound AlF_3 at the etched surface.¹³⁻¹⁵

Until recently, the most widely-used selective plasma etch for the GaAs / AlGaAs material system was a reactive-ion etch (RIE) utilizing¹³⁻²¹ Freon[®]-12. Etches with a selectivity of 4000 have been reported.¹⁹ According to Smith,²² Freon[®] is non-toxic, non-flammable, and non-corrosive, but is a Class-1 ozone-depleting chemical. The outstanding success of Freon[®] as a selective etch, therefore, has been overshadowed by environmental legislation which currently prohibits its manufacture and distribution, and precludes future use altogether.²²⁻²³

Silicon tetrachloride (SiCl_4) has been favored as a substitute GaAs etchant, made selective by the addition of SiF_4 (References 76-77) or SF_6 (References 78-83). Selectivities of 500 have been reported²⁴⁻²⁶ with this plasma system. Murad *et al* report a selectivity approaching 10000 at a very low pressure and flow rate²⁷, but the selectivity mechanism seems to be a factor of residual oxygen / nitrogen content in their non-loadlocked etching chamber and therefore is not well understood. Despite its touted praises, SiCl_4 has an undesirably high boiling point and low vapor pressure; *i.e.* it is in a liquid state at room temperature. The Cornell Nanofabrication Facility (where all fabrication work for this research has been performed) is unwilling to support the use of this etchant because of previous experiences with condensation within the gas lines and the subsequent corrosion of the mass flow controllers.

Another substitute selective plasma etchant described in the literature is BCl_3 in conjunction²⁸⁻³¹ with SF_6 . In contrast to Freon[®] etching, no polymer products are formed on the etched surface^{18,20,32,33} because of the absence of carbon in the etchants. BCl_3 has the further advantage of decreasing, or even eliminating,^{30,34} the "dead-time" (lag time) associated with etching through surface oxides, due to its oxygen and water vapor scavenging properties.³⁵ With the lack of availability of both CCl_2F_2 and SiCl_4 at the fabrication facility, etching experiments for this project were limited to the BCl_3 plasma system.

Initial experimentation was performed in the parameter space of gas flow ratios (between BCl_3 , SF_6 , and Ar), chamber pressure, and plasma power. Argon is added to the plasma as a buffer gas, to stabilize the plasma while reducing the reactive ion concentration.^{20,36} GaAs substrate pieces were used to obtain etch rates, while pieces of the original epitaxial heterostructure were etched to test the selectivity of each recipe. Analysis of the etched pieces reveals some unfavorable results. The etched surfaces of most pieces became severely roughened, and in some cases, were covered by a filmy residue. The etch rates were unstable and had poor repeatability. Furthermore, despite reports that the use of BCl_3 as an etchant eliminates dead-time,³⁰ etch rate experiments indicated lag times of 30-60 seconds between plasma activation and commencement of any etching activity.

Test results also indicate that the BCl_3 / SF_6 / Ar plasma system could not *selectively* etch the original MISFET heterostructure design. Although the etch rate decreased somewhat while etching through the $\text{Al}_{0.11}\text{Ga}_{0.89}\text{As}$ gate insulator layer, the low aluminum mole-fraction ($x=0.11$) was apparently insufficient to create an impervious barrier to the etching reaction. Attempts to compensate for the aluminum deficiency by increasing the fluorine concentration failed to produce repeatable results. As the etch depth approached the $\text{Al}_{0.6}\text{Ga}_{0.4}\text{As}$ laser etch-stop layer, after etching through 1.2 μm of overlying material, the increasing magnitude of surface roughness

seemed to cause similar problems in forming a continuous etch barrier. It is presumed that the pitted surface created by this particular plasma allows the etchant gases to penetrate the thin $\text{Al}_{0.6}\text{Ga}_{0.4}\text{As}$ etch-stop layer, defeating its intended purpose.

Although a *selective* etch recipe was not identified, a successful *timed* mesa etch was performed with the original heterostructure, after narrowing the etch rate margin of error to within reasonable limits. In this first batch of devices, the etched chip was further processed through the remainder of the fabrication sequence, but the MISFET devices were destroyed by the final wet gate recess etch. As described above, the acid etchant exhibited an accelerated etch reaction in the metalized regions of the wafer.

Based on the negative results of the etch selectivity tests, the opto-electronic heterostructure design was revised, incorporating a higher aluminum mole-fraction ($x=0.25$) in the gate insulator layer, and decreased thicknesses of several layers (especially the buffer layer). By obtaining additional wafers with a single, thick epitaxial layer of $\text{Al}_{0.3}\text{Ga}_{0.7}\text{As}$, etch rate and selectivity tests could be performed without wasting valuable heterostructure material, while yielding more definitive results by removing multi-layer considerations. Etches performed on homogeneous $\text{Al}_{0.3}\text{Ga}_{0.7}\text{As}$ material in 40 : 40 : 8 BCl_3 / Ar / SF_6 at 50 mT and only 10-V bias (30 W power) showed almost negligible etching and no surface roughness. This plasma recipe is modeled after Kazior and Patel⁸⁴ who reported selectivity > 1000 in the BCl_3 / Ar / SF_6 system, by using pressures > 50 mT and driving the DC bias nearly to zero. These latter parameters are designed to effect a more chemical than physical etching mechanism,²⁹ and to minimize the energetic ion bombardment which presumably causes surface roughness.³¹

The corresponding GaAs etch rate obtained in this same plasma was measured to be nearly 8000 Å/min, for a selectivity > 300. Inspection of the GaAs etched surfaces under optical and scanning electron microscopes, however, revealed an extremely roughened surface, as shown in

Figure 12.2. Additionally, a macroscopic ring-shaped feature was observed on the etched surfaces, centered on each wafer piece. This feature has been attributed to the bending of the plasma electric field around the semi-insulating wafer piece, enhancing the etching near the wafer perimeter.

An experiment was undertaken to improve the etch selectivity for the transistor mesa definition, by reducing the magnitude of surface roughness generated while etching down to the etch-stop layer. Franz²⁹ reported nearly *non-selective* etching of GaAs and AlGaAs using a BCl_3 plasma *without* the addition of SF_6 , resulting in extremely smooth surfaces. This smooth etching property of BCl_3 / Ar could be applied to initially etch through the GaAs and AlGaAs barrier layers. As the etch approaches the depth of the etch-stop layer, SF_6 could be introduced into the plasma for selectivity. The absence of SF_6 during the first portion of the etch minimizes the induced surface roughness, enabling a better selectivity reaction upon reaching the $\text{Al}_{0.6}\text{Ga}_{0.4}\text{As}$ layer. Etch tests with homogeneous materials showed good selectivity (> 140) between GaAs and $\text{Al}_{0.3}\text{Ga}_{0.7}\text{As}$; however, tests of etching through the heterostructure, in which SF_6 was added during the progress of the etch, failed to produce the desired results.

A second batch of devices was etched in the non-selective 40 : 24 BCl_3 / Ar plasma, to create the transistor mesas with smoother etched surfaces. As with the first device batch, the lack of a *selective* etch recipe required reliance on a *timed* etch. This second batch of MISFET devices incorporated

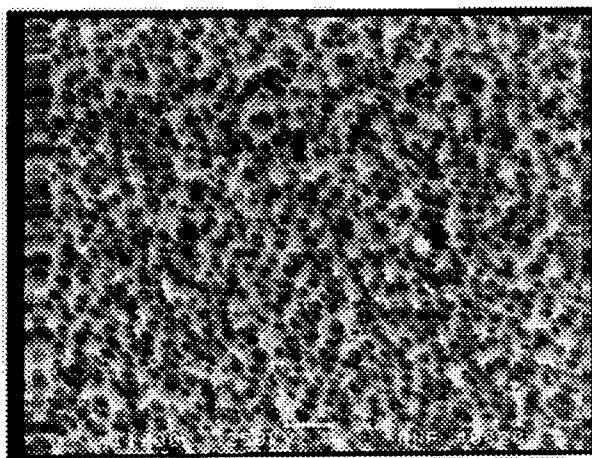


Figure 12.2: Undesirable Etched-Surface Roughness. GaAs Etched in 40 : 40 : 8 BCl_3 / Ar / SF_6 , 50 mT, 10 V, for 1 minute.

an undoped cap layer, and therefore did not require a gate recess etch.

As a final note on *selective* RIE, tests were also performed in which Cl_2 and CF_4 were combined in a plasma, in an effort to simulate the radiative dissociation of CCl_2F_2 . Different flow ratios of $\text{Cl}_2 / \text{CF}_4 / \text{Ar}$ were tested, but in each case a 10-minute etch resulted in negligible etch depth in GaAs.

An important issue to be addressed when plasma etching heterostructure transistors is the resultant ion bombardment damage to the remaining layers.³⁷⁻⁴⁵ RIE plasmas generally develop hundreds of volts across the plasma sheath, causing accelerated plasma ions to bombard the crystal surface with considerable force. Indeed, in certain cases, this ion “sputtering” mechanism is essential to the etch performance,⁴⁵ and is actually responsible for the vertically-etched sidewalls (anisotropy) characteristic of physical (vs. chemical) etching. For gate recess etches, however, ion bombardment creates electron traps in the surface layer, which decrease the free-electron concentration and low-temperature mobility in the transistor channel,⁴⁰⁻⁴³ due to ionized-defect Coulomb scattering. Surface traps can also increase the surface recombination rate. Room-temperature mobility is not affected, as phonon scattering dominates. RIE-induced damage has been detected as deep as 1000 Å below the etched surface,^{38,43} for a plasma DC bias > 50 V. Crystal damage must therefore be minimized by decreasing the DC bias across the plasma sheath. In typical RF-coupled RIE chambers, however, DC bias is a function of RF power; hence, a reduction in the plasma sheath voltage is accompanied by a reduction in the plasma ion density, and a corresponding reduction in the reaction rate.⁴⁵

12.C: Electron Cyclotron Resonance Etching

A different means of implementing dry plasma etching is with an electron cyclotron resonance (ECR) source,⁴⁴⁻⁴⁸ which decouples the DC bias and RF power by using a remote microwave source to excite the plasma outside of the etching chamber. This mechanism enables high etch rates due to high ion densities, while minimizing the energetic ion bombardment and

lattice damage by independently controlling the plasma sheath voltage.^{46,48} The fact that separate controls are used for etchant gas dissociation and ion acceleration, introduces an element of flexibility into the etching process.

The ECR has previously been used as an integral part of the fabrication process for *laser* devices, because of its very-high etch rate and its ability to create high-quality vertical sidewalls for integrated in-plane laser mirrors.⁴⁹ In particular, a Cl_2 / BCl_3 gas mixture is used at 0°C platen temperature. This particular ECR recipe has nearly zero selectivity between GaAs and AlGaAs, important for creating flat vertical facets etched through the laser GRINSCH layer structure. The ECR can also be used to perform the transistor mesa etch, but the etch rate is too high to perform a gate recess etch without selectivity.

Despite its advantages, the ECR is difficult to control. Etch rates tend to vary, affecting the reproducibility of any etch process. Immediately prior to performing a critical etch, the ECR must be calibrated to ensure the best estimate of the etch rate being attained. Even following these precautions, there is a significant margin of error in the etch depth obtained. The incorporation of a laser reflectometer within the etching chamber, as shown in Figure 12.3, has allowed *in situ* etch depth control to be implemented,⁵⁰

eliminating the need for repetitive calibrations as well as the uncertainty of those measurements. The *in situ* reflectometer also eliminates the need for selective etching, since precise real-time indication of etch depth allows

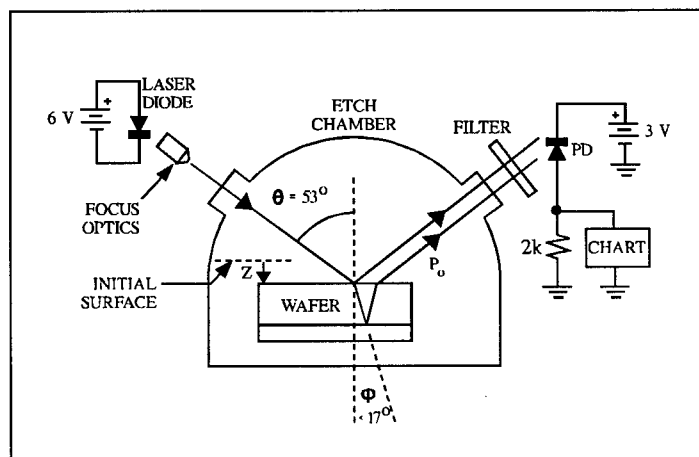


Figure 12.3: Laser Reflectometer Etch-Depth Monitor

accurate etch control despite any variations in etch rates or etching conditions.

The laser reflectometer indicates the presence of two distinct signals in the reflected beam.⁵⁰ The *primary* signal consists of the reflection of the incident beam off the exposed surface of the wafer. As the etch progresses through the heterostructure, the different refractive indices of the various layers result in a variation of the reflectance from the surface. As shown in Figure 12.4, the primary signal is manifested as the baseline, or DC level, which changes only at heterostructure interfaces. The GaAs layers, which have a higher refractive index than AlGaAs, are positioned higher in the recorded signal shown. The *secondary* signal consists of the interference of the primary signal with the beam which propagates through the first semiconductor layer and reflects off the nearest heterojunction. Absorption within the semiconductor influences the intensity of this propagated signal, as well as the amplitude of the resulting interference pattern at the detector. Beams reflecting off deeper interfaces are thus attenuated to a negligible level. The interference signal is clearly evident in Figure 12.4, which indicates absorption in the GaAs layers, but none in the AlGaAs layers.

Figure 12.4 correlates the reflectometer signal to the opto-electronic heterostructure. The actual MISFET layers are so thin that they are not identifiable within the resolution of this system.

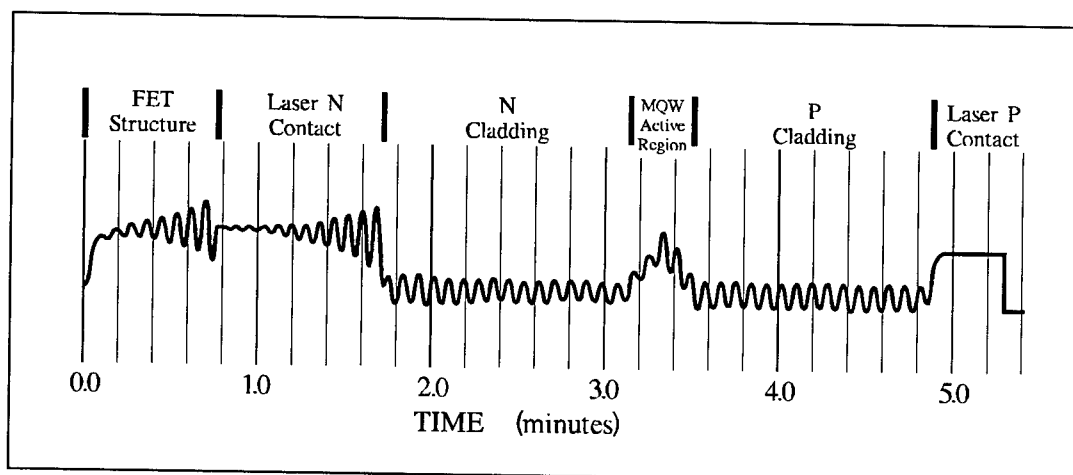


Figure 12.4: Sample Data from the ECR Laser Reflectometer

The section labeled “FET Structure” in the figure primarily indicates the GaAs buffer layer grown between the laser and FET layers. As this GaAs layer is etched thinner, absorption decreases and the secondary (interference) signal grows. The secondary signal disappears when the $\text{Al}_{0.6}\text{Ga}_{0.4}\text{As}$ “etch-stop” layer is removed, but again slowly grows as the GaAs top laser contact is etched. With the removal of the GaAs layers, the primary signal suddenly decreases, indicating a thick layer of AlGaAs with lower reflectance. The amplitude of the secondary signal does not vary significantly during the etching of the AlGaAs cladding, since there is negligible absorption in this layer at 670 nm. The multiple-quantum-well active region is clearly evident, centered between the two cladding layers. The graded-index confinement layers are manifested as a gradual rise and fall in the primary reflectance signal. The lower cladding region reflects a signal very similar to the upper one. As the deepest heterojunction is encountered by the plasma, the interference signal is lost, indicating that the bottom laser contact is exposed. No reflection is evident from the epitaxial / substrate interface, since both materials are pure GaAs (with the exception of the p-type dopants in the epitaxial layer, which do not significantly alter the refractive index).

After obtaining an optical reflectance “map” representative of the entire epitaxial heterostructure, it is not difficult to monitor the reflected signal during subsequent wafer processing to accurately control the etched depth to better than⁵⁰ 500 Å, which is half the width of the interference fringes generated by a 670-nm laser and the AlGaAs material system.

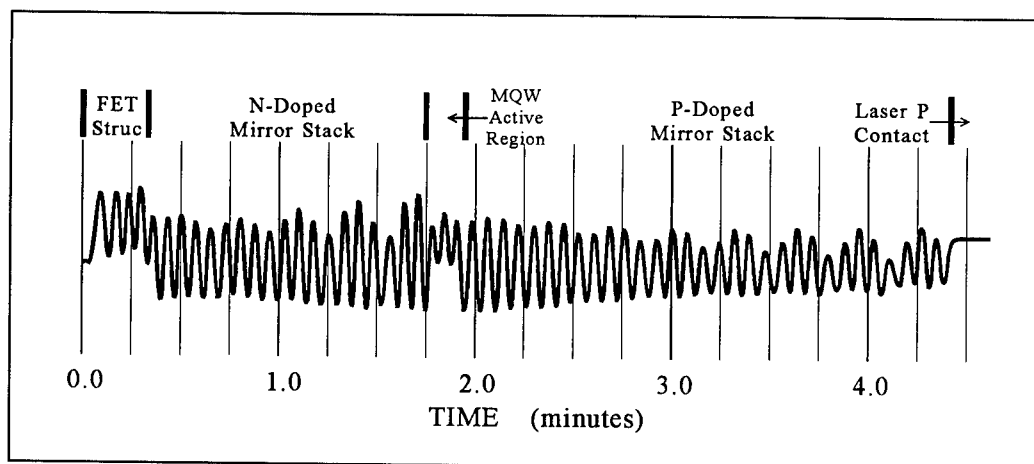


Figure 12.5: ECR Laser Reflectometer Signal Recorded While Etching VCSEL Material

This method has been applied to the dry etching (by ECR) of MQW lasers and optoelectronic integrated heterostructures, as well as vertical-cavity surface-emitting laser (VCSEL) heterostructures. The optical reflectance map for VCSEL material has a modulated primary signal, as shown in Figure 12.5, due to the presence of the quarter-wave mirror stacks epitaxially grown on both sides of the active region. Nevertheless, the MQW active region is identifiable between the two mirror stacks. The large amplitude of the interference fringes in the VCSEL map makes it a simple matter to control etched depth by counting peaks, a task which could easily be automated for computerized etch control in the manufacturing environment. Recently, this laser reflectometer technique has also been successfully applied to monitoring in real time the depth of *wet* etches in GaAs / AlGaAs heterostructures.

Another useful parameter indicated by the reflectometer signal is the magnitude of etch-induced surface roughness,⁵¹ as shown in Figure 12.6, which can be compared to Figure 12.4 to see the effects of roughness on both the primary and secondary signals. The secondary (interference) signal is reduced in amplitude by surface roughness, since the differences in path lengths tend to cancel the phase coherence across the width of the laser beam. The primary (surface reflectance) signal no longer indicates abrupt heterojunctions as sharp steps. Since the

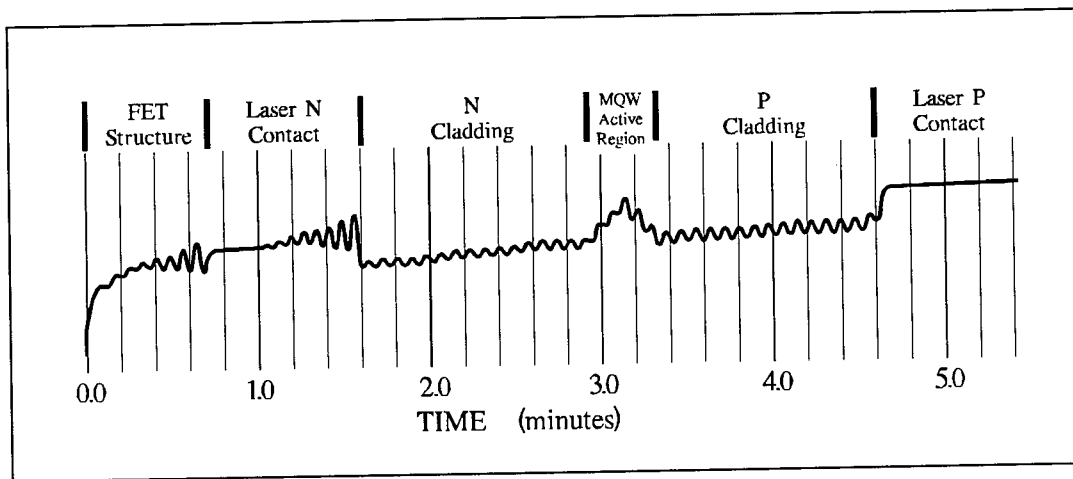


Figure 12.6: Surface Roughness Indications in the ECR Laser Reflectometer Signal

underlying material is *gradually* illuminated by an increasing portion of the laser beam as the etch progresses, the interface is indicated by a sloped and rounded step on the optical reflectance map.

In summary, reliable and reproducible etching techniques are essential to the fabrication of integrated circuits. They provide a means to delineate device boundaries (transistor mesas, laser ridges, and mirrors) and to establish contact with buried heterostructure layers. Both wet and dry etch mechanisms were explored in this project, in an attempt to develop a dependable selective etch process for gate recessing and mesa formation. The selective wet etch was shown to be incompatible with partially processed wafers containing metalized regions. The selective plasma etch induced such a degree of surface roughness, its ability to form an impervious etch barrier at the AlGaAs etch-stop layer was corrupted. Timed, non-selective RIE plasma etches were therefore used to form the transistor mesas for the two fabrication batches completed during this project. A laser reflectometer was also incorporated into an ECR plasma etching chamber, and was shown to provide excellent *in situ* monitoring of the total etch depth into a heterostructure. ECR etching is a favored technique for etching mesas and laser ridges, because of the minimal degree of induced ion bombardment damage, and the high quality of the orthogonally etched laser

mirrors. The ability to monitor the etch depth in real time eliminates the need to rely on selective etching methods.

Chapter 13: High Quality Gas Etching Using a Cyclotron Resonant Etcher (ECR)

High quality etched laser mirrors remain a priority for monolithic photonic device integration. While cleaved facets provide consistent, high quality in-plane laser mirrors, cleaves can only be made at the edges of the die, where the output light exits. Cleaves cannot be used for integrated laser mirrors for which the output light remains within the monolithic chip. In this letter, we report on the fabrication and characterization of laser mirrors in GaAs using an Electron Cyclotron Resonance (ECR) etcher. The ECR etcher^{1,2} offers several advantages over competing Chemically Assisted Ion Beam Etching (CAIBE)³ and Reactive Ion Etching (RIE)⁴ for fabricating etched mirrors including a higher etch rate, control over more adjustable parameters, and higher etch selectivity between GaAs and the etch mask.

The optical scattering and reflectivity of the laser mirrors are direct measures of the quality of the etch. Total Internal Reflection (TIR) mirrors are particularly suited for comparisons of various methods of etching. The reflectivity of these mirrors can be found by measuring

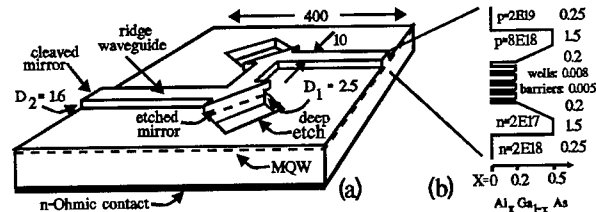


Figure 13.1: (a) A typical laser with two etched turning mirrors and two cleaved end mirrors. (b) The MQW laser heterostructure. The scale at the bottom indicates the ratio of Al to Ga and the numbers to the right give the thickness of each layer in μm .

the threshold current for lasers with multiple 90° turning mirrors.⁵ As shown in Figure 13.1, the lasers are fabricated on GaAs-AlGaAs 5-quantum-well heterostructure with shallow etches for the ridge waveguides and deep etches for the Total Internal Reflection (TIR) mirrors. The waveguides have a number $N=2j$ of TIR mirrors ($j = 1$ to 6) and two cleaved end mirrors. Although narrower lasers can be fabricated, the lasers used in this study are $10 \mu\text{m}$ wide in order to (1) reduce the distributed impedance across the $700 \mu\text{m}$ length of the laser, and (2) improve the optical coupling into the waveguide at the mirror. As shown in the figure, the mirrors extend slightly ($5 \mu\text{m}$) beyond the waveguide in order to reduce the scattering loss at the mirror edges; this scattering can occur when the optical mode strikes an imperfection such as the rounded edges produced during photolithography. Although the TIR mirrors are of interest in their own right, we show that the

reflectivity of these TIR mirrors are comparable to those obtained from other etchers in order to demonstrate that the ECR etcher is a viable alternative for the fabrication of opto-electronic circuits.

The lasers for this study are etched in a Plasma Quest Model 357 ECR etcher.¹ The ECR etcher has a low pressure chamber with a chuck to hold a wafer for etching. A microwave generator and a set of upper magnets excites and contains a plasma in reactive gasses above the wafer. A set of lower magnets focuses the ions near the wafer surface. A 13.566 MHz RF signal applied to the wafer chuck produces the self-bias potential that accelerates the ions toward the wafer. It is possible to adjust the gas pressure and flow rate, the plasma density, the focus and the accelerating potential independently. The etch parameters for the ECR etcher are optimized for smooth, vertical side walls.² Chlorine (Cl_2) and boron trichloride (BCl_3) are the etchants. The Cl_2 and BCl_3 gas flow rates are 16 and 4 sccm, respectively. The chamber pressure is 2 mTorr. The microwave forward power is 400 Watts. The RF forward power is 80 Watts. The upper and lower magnets on the etcher are set to 16 and 20 Amps respectively. A pressure of 10 Torr from a helium source pushes the rim of a 3-inch silicon wafer up against the cooling stage, set at 0 °C. An o-ring prevents the He back-pressure from escaping into the chamber. The masked wafer for etching (1 cm square) is mounted on top of the silicon wafer using resist. The silicon wafer is then place into the etcher through a load lock.

Since the mirrors and waveguides for etched-ridge lasers need to be perfectly aligned for optimum performance, it is preferable to use a variation of a One-Step Two-Level Etch (OSTLE)⁶ to form the shallow etches for the waveguides and the deep etches for the mirrors. The metal for the P-Ohmic contact is the first etch mask, which defines the ridge waveguides and the vertical mirrors. The metallization consists of 500 Å of titanium, 200 Å of platinum, 3000 Å of gold and 1500 Å of nickel, patterned by lift-off. The titanium layer insures adhesion to the GaAs cap of the laser heterostructure; the platinum serves as a diffusion barrier; the gold acts as both conductor and implant mask for an oxygen implant (performed after etching, for electrical isolation); and the nickel provides a high selectivity etch mask for etching GaAs/AlGaAs in the ECR etcher. The

second etch mask consists of 3 μm of photoresist. This mask defines the deep etch regions for the mirrors, with the photoresist openings extending up onto the nickel so that the exposed nickel edge defines the mirror surfaces. Photoresist burn is prevented by cooling the wafer to 0 °C during the ECR etch. It is highly desirable to have a masking material (e.g. photoresist) that can be removed without damaging the underlying nickel etch mask. It allows the lithography to define shallow-etched ridge regions and deep-etched mirror regions while the wafer still has a planar surface.

The surface of the etched mirrors cannot be made smoother than the edge of the nickel mask delineating the mirror etch. For this reason, minimizing the grain size of the metal for the P-Ohmic contact is important for obtaining high quality mirrors. The metals are deposited using an electron beam evaporator. Cooling the substrate to approximately 0 °C reduces the grain size from ~50 nm to ~5 nm and smoothes the edges of the etch mask. The improved quality of the edges is significant for an 850 nm laser with an effective wavelength (λ/n) in the semiconductor of ~240 nm.

Two ECR etches are performed as follows. The first etch is to the depth D_1 shown in Figure 13.1b; this is the difference between the etch depth required for the laser mirrors and the etch depth required to create ridge waveguides. After this etch, the photoresist is removed (while the wafer remains in the ECR etcher) using an oxygen plasma. The second etch forms the ridges on the waveguides and takes the etched mirrors to their final depth; it uses the same gasses and parameters as the first etch. This second etch is to the depth D_2 (refer to Figure 13.1b) which is approximately 100 nm above the quantum wells. Under these conditions, the nickel etches at 600 Å/min, the photoresist etches at 2000 Å/min, and the GaAs / AlGaAs heterostructure etches at 8600 Å /min. Typically both the mirrors and floors (surface of the etched region) are smooth. However, on occasion the mirror has a relatively smooth facet but a rough floor. We have found that the rough floors are a result of the etching conditions, problems with the development or removal of the photoresist mask and any slight sputtering of the metal on the waveguide and its subsequent re-deposition in the mirror recess. The perturbations can be smoothed out by dipping

the wafer momentarily in an acid etch. However, the floor is below the waveguiding region of the waveguide and it should not affect the optical mode.

The fabrication process is completed by lapping the wafer to a thickness of approximately 150 μm and then evaporating 100 \AA of Ni, 400 \AA of Ge and 1600 \AA of Au on the N-side. After alloying the contacts in a hydrogen atmosphere at $>350^\circ\text{C}$ for 1 minute, the wafer is cleaved into 400 μm wide strips, creating the two cleaved end facets of all the lasers. The sets of lasers are then bonded to copper heat sinks using electrically conductive epoxy. The N-Ohmic contact is common to all of the devices.

Following the work of Johnson et. al.⁵ which uses a logarithmic model for the gain in quantum well lasers,⁷ the reflectivity R_m of the etched mirrors can be calculated from knowledge of the reflection coefficient R for normal-incident mirrors, the length of the laser $L=700 \times 10^{-4} \text{ cm}$, and the modal gain coefficient^{5,7} $\Gamma G_0 = -136 \ln(R) \text{ cm}^{-1}$. Let $J_{th} = J_{th}(N)$ denote the threshold current density for a laser with N etched TIR mirrors, and define a normalized current density $J_m = J_{th} \exp[\ln(R)/L\Gamma G_0]$. Physically, J_m is the threshold current density of the laser without the output coupler loss.⁵ The slope $M = d(\ln J_m)/dN$ of a linear fit to the $\ln(J_m)$ versus N data yields the reflectivity $R_m = \exp(-ML\Gamma G_0)$. The value used for the modal gain coefficient ΓG_0 is obtained⁷ from a separate series of measurements on the threshold current of similar 10 μm wide lasers with lengths of 200 and 400 μm . These threshold currents are 825 and 687 A/cm^2 , respectively.

The threshold currents of the serpentine-shaped lasers are found from measurements of the emitted optical power P as a function of the laser bias current I (P - I curves). The lasers with the heat sinks are mounted in an electro-optic probe station. To insure even electrical pumping and help reduce the effects of distributed impedance, two probes are applied to the P-side of the lasers at approximately 200 μm from either cleaved facet. A positive-going sinusoidal pulse of 5 μsec duration is applied to the laser and the emitted optical power is detected by a fast 1 cm^2 detector. The data is displayed on a digital oscilloscope as the detector photocurrent versus the bias current to the laser; these curves correspond to the P - I curves since optical power is linearly related to the

detector photocurrent. The threshold currents are determined in the usual manner by extrapolating the straight-line portion of each P-I curve to the I axis and denoting the point of intersection as I_{th} . J_m is then calculated from each threshold current.

The experimental data appears in Figure 13.2 as a semilog plot of the normalized current density J_m versus the number of mirrors N . The points on the graph represent the results from 36 separate lasers that emit near 850 nm. These lasers are not pre-sorted to find the best ones so that the graph represents typical results.

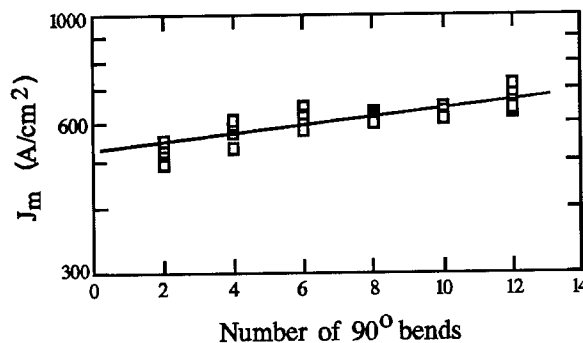


Figure 13.2: A semilog plot of the normalized threshold current as a function of the number of 90° bends within a 700 μm long laser.

The linear regression fit to the data yields the slope of $M=0.02$. Assuming a reflection coefficient of $R \approx 0.34$ for the guided TE waves at the cleaved facet, the average reflectivity for the TIR mirrors is then found to be $R_m = 81\%$. This value can be compared with example values of $R_m = 77\%$ obtained from a study of $10 \times 500 \mu\text{m}$ serpentine-shaped lasers etched in a Chemically Assisted Ion Beam Etcher (CAIBE),⁵ $R_m = 80\%$ for $40 \mu\text{m}$ wide waveguides made by Reactive Fast Atom Beam Etching (RFABE),⁸ and $R_m = 68\%$ from Reactive Ion Etched turning mirrors on $8 \mu\text{m}$ wide waveguides.⁴

In conclusion, we have fabricated GaAs-AlGaAs MQW ridge waveguided lasers with multiple numbers of TIR mirrors fabricated with an Electron Cyclotron Resonance (ECR) etcher. SEM micrographs show the improved quality of the reflecting surfaces which correspond to a TIR mirror reflectivity of better than 80%. The comparison with other multimode waveguides shows that the ECR etcher produces high quality etched-laser mirrors and etched ridge waveguides. In addition, it offers greater control over the etch parameters and it is ideal for etching opto-electronic components such as etched-ridge lasers with etched-mirror facets.

Chapter 14: Using a Laser Reflectometer as an In-Situ Monitor During a Gas Etch

Dry etching of semiconductor heterostructures is common for fabricating opto-electronic components¹ such as semiconductor lasers and field-effect transistors. However, it is difficult to accurately and repeatably etch to a specific depth. Several methods are available to achieve the desired etch profile. The most common method is to calibrate the time required to etch a specific depth into the material, using a sacrificial test sample with an identical material structure. However, the etch parameters must be tightly controlled for subsequent etches and the wafer structure must be known *a priori*. This knowledge cannot be guaranteed without extensive wafer testing since the thickness tolerance during wafer growth can be as high as 20%. In some cases, it is possible to use an optical or a mass spectrometer² to monitor the gas species in the etch-chamber as the etch progresses, determining etch depth by the sudden appearance of etch-products from a specific heterostructure layer of differing composition. Alternatively, thin etch-stop layers are sometimes added to the heterostructure, and the proper combination of reactant gasses is used to preferentially etch the heterostructure.^{3,4} The addition of etch-stop layers into the heterostructure, however, fixes the etch depth at specific values, eliminating the flexibility to optimize device performance.

We report on the use of a laser reflectometer as an in-situ monitor for Electron Cyclotron Resonance (ECR)

Etching. Several recent publications show its usefulness as a monitor during wet chemical⁵ and dry plasma^{6,7} etching. We apply a modified version of this technique to

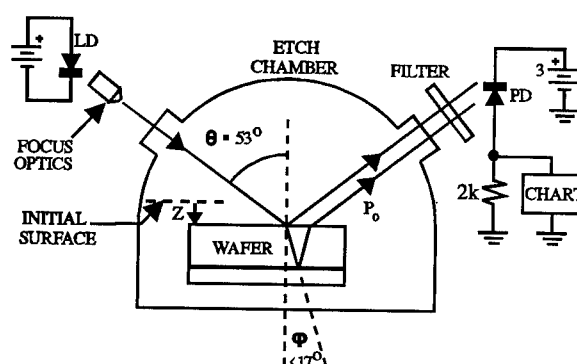


Figure 14.1: Diagram of the in-situ etch monitor showing the laser diode LD, photodetector PD, reflected signal P_o and the etch chamber. The depth etched from the initial surface is shown as z . The primary signal consists of the optical power reflected from the exposed surface and the secondary signal is caused by interference from a buried interface.

a GaAs-AlGaAs laser heterostructure (see Figure 14.1) to ascertain (i) the etch depth, (ii) the etch rate, (iii) the quality of the post-etch surface, and also to (iv) determine or verify the composition of a wafer without knowledge of its precise structure (i.e. "reverse engineering").

To utilize this method, one must correlate the optical power reflected from the $\text{Al}_x\text{Ga}_{1-x}\text{As}$ heterostructure with its composition. The aluminum mole fraction x and, hence, the index of refraction n varies with the depth z from the initial top surface (Figure 14.1). During the etch, $0.670\text{ }\mu\text{m}$ TE-polarized laser emission (2 mm diameter, 1 mW) is reflected from the wafer to a silicon photodetector as power P_o making an angle of 53° with respect to the surface normal. The primary detected signal consists of the optical power reflected from the surface of the wafer as it etches. A secondary detected signal consists of the interference between the light reflecting from the exposed surface and the buried heterostructure interfaces. The total detected power P_o is a superposition of the primary and secondary signals and constitutes a reflectivity-versus-depth map (shown in Figure 14.2) for the entire epitaxial structure. Once the map of the heterostructure is obtained, it is possible to stop the etch at any of the predetermined features, with a resolution better than $500\text{ }\text{\AA}$.

First, consider the primary signal. The refractive index of undoped $\text{Al}_x\text{Ga}_{1-x}\text{As}$ to within a few percent is given⁸⁻¹² by a form of the Sellmeier equation:

$$n = \left[A + \frac{B}{\lambda^2 - C} - D\lambda^2 \right]^{1/2} \quad (14.1)$$

where $A=13.5-15.4x+11.0x^2$, $B=0.690+3.60x-4.24x^2$, $C=0.154-0.476x+0.469x^2$, $D=1.84-8.18x+7.00x^2$. λ is the vacuum wavelength in the range of 0.564 to $1.033\text{ }\mu\text{m}$. Corrections to the index of refraction due to dielectric absorption and the conductivity of doped material are neglected. The power reflection coefficient R_E for TE-polarized light is given by

$$R_E = \left[\frac{\cos \theta - \sqrt{n^2 - \sin^2 \theta}}{\cos \theta + \sqrt{n^2 - \sin^2 \theta}} \right]^2 \quad (14.2)$$

where n is the index of the exposed surface (assuming the refractive index of the plasma is approximately equal to unity), and θ is the angle of incidence. The calculated values of $n = 3.87$, 3.49 and $R_E = 0.527$, 0.489 correspond to $x = 0$, 0.5 , respectively. A Primary Modulation Ratio (PMR) as a function of the aluminum concentration is defined here as the difference in reflectivity for GaAs ($x=0$) and $\text{Al}_x\text{Ga}_{1-x}\text{As}$, divided by the reflectivity for GaAs. We note that $\text{PMR}(0.5) = 7.2\%$. In addition to determining the etch depth, rate and quality, Equations 14.1-2 and the PMR are important for reverse engineering a wafer since, if the PMR is experimentally determined, then the mole-fraction x can be calculated from Equation 14.1.

The secondary interference signal is a more complicated phenomenon to calculate, due to (i) absorption, (ii) the contributions from Fabry-Perot modes⁶ between deeper layers and (iii) the regions of graded index. When etching through relatively thick epilayers (thousands of angstroms), it is this secondary signal that enables accurate depth control. The etch depth for adjacent interference fringes is approximately⁶

$$\Delta z = \lambda/2n. \quad (14.3)$$

For $\text{Al}_{0.5}\text{Ga}_{0.5}\text{As}$ cladding layers, Equation 14.3 yields $\Delta z = 0.1 \mu\text{m}$. A Secondary Modulation Ratio (SMR) is defined as the peak-to-peak power for the interference fringes divided by the average power for the fringes. The SMR is most related to the quality of the surface. The magnitude of the secondary signal is limited by the absorption coefficient of the various layers. The absorption length ($1/\alpha$) for GaAs at $0.670 \mu\text{m}$ is on the order of $0.5 \mu\text{m}$, but it is larger⁸ for $\text{Al}_x\text{Ga}_{1-x}\text{As}$. We use the visible $0.670 \mu\text{m}$ laser since (1) the alignment can be performed visually, (2) smaller wavelengths result in smaller Δz , and (3) the amplitude of the interference signal is smaller than the primary signal which simplifies the mapping procedure.

The technique is tested on an in-plane laser heterostructure. For this study, the semiconductor surface is prepared by first rinsing in acetone, methanol and isopropanol. A brief dip in dilute ammonium hydroxide removes surface oxides and the surface is dried with nitrogen. The etch is performed in a Plasma Quest 357 Electron Cyclotron Resonance (ECR) etcher. The etch rate is approximately 1 μm per minute with the parameters optimized for smooth, vertical side walls and the rate is essentially independent of the aluminum content of our wafers.¹ The Cl_2 and BCl_3 gas flow rates are 16 and 4 sccm, respectively, with a chamber pressure of 2 mTorr. The microwave forward power is 400 W. The RF forward power is 80 W with a self bias of approximately -100 V. The upper and lower magnets are set to 16 and 20 A, respectively. The wafer is maintained at 0 °C. An optical bandpass filter (FWHM = 10 nm) centered at 0.671 μm is inserted before the photodetector to help eliminate the quiescent signal due to the plasma emission.

Figure 14.2 shows the grower's specifications for the aluminum composition in the heterostructure and two strip-chart recordings for different surface conditions. The actual thickness of the layers may vary by $\pm 20\%$ from the grower's target profile. The first trace is the strip-chart recording for a sample with a high quality etched surface. The slow variations that occur on the time scale of minutes correspond to the primary signal, whereas the higher-frequency oscillations correspond to the secondary

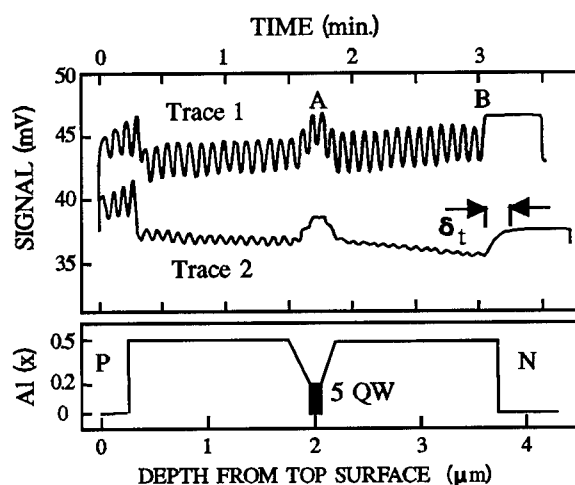


Figure 14.2: Trace 1 is the superposition of primary (envelope) and secondary (interference fringes) signals, as recorded by the strip chart recorder. The scaled heterostructure aluminum composition is shown for comparison. Trace 2 (displaced upward by 5 mV for display purposes) shows the effects of etch-induced surface roughness on the detected signals.

interference signal. The data recorded during the first 0.3 minutes show very distinct interference

fringes that result from reflections at the interface between the p-GaAs cap layer and the start of the $\text{Al}_{0.5}\text{Ga}_{0.5}\text{As}$ cladding. The SMR for this interference signal increases during the etch, since the remaining p-GaAs thickness L (and thus, the optical absorption αL) is decreasing. During the time period between 0.3 and 1.6 minutes, the secondary signal delineates the etching of the $\text{Al}_{0.5}\text{Ga}_{0.5}\text{As}$. The 14 fringes yield a measured thickness of $1.4\text{ }\mu\text{m}$ for the $\text{Al}_{0.5}\text{Ga}_{0.5}\text{As}$ layer according to Equation 14.3. The gradual rise and fall in the primary signal near 1.7 minutes (point A) indicates the surface reflection for the quantum wells and the graded-index region of the heterostructure. As the etch continues, the secondary signal corresponding to the lower cladding layer occurs between 1.8 and 3.1 minutes. The highly absorbing n-layer is reached at 3.1 minutes (point B). The etch stops at 3.5 minutes with a total etch depth, as determined by a surface profilometer, of $4.20 \pm 0.03\text{ }\mu\text{m}$. The average etch rate is $r_1 = 1.20\text{ }\mu\text{m/min}$. The observed PMR(0.5) of approximately 6.3% is in good agreement with the calculated ratio of 7.3%. As an example of reverse-engineering, these results indicate that the experimentally determined mole-fraction and thickness of the $\text{Al}_{0.5}\text{Ga}_{0.5}\text{As}$ cladding layers are smaller by 10.8% and 6.7%, respectively, from the specified values of 0.5 and $1.5\text{ }\mu\text{m}$. The observed SMR for the lower $\text{Al}_{0.5}\text{Ga}_{0.5}\text{As}$ layer is approximately 9 %.

As a result of obtaining the detailed map, the etch can be stopped on either the features represented by the primary signal or on any specific fringe of the secondary signal, since the fringe spacing is known. The map features have been verified by etching several separate test pieces, stopping the etch at the points A and B shown in Figure 14.2. Measurements of the etch depths taken with a surface profilometer yield the averaged values 2.01 ± 0.09 and $3.70 \pm 0.03\text{ }\mu\text{m}$, respectively, which are in good agreement with the grower's specified values of 1.98 and $3.73\text{ }\mu\text{m}$. The samples for point A are from different 2" wafers which explains the larger standard deviation. To stop an etch at other than an interface, the interference fringes of the secondary

signal can be counted. Both signals provide a possible resolution of approximately 500 Å (for the secondary signal, this is half the fringe width).

The second trace in Figure 14.2 is produced by a specimen from the same heterostructure as the first but with inferior post-etch surface quality as determined by visual inspection. The key observation is that the same heterostructure produces two quite different traces. It can be seen that the primary and secondary signals for trace 2 decrease during the course of the etch. In addition, the trace has a sloped feature of width $\delta_t \cong 0.23$ min. The apparent width of the n-GaAs / $\text{Al}_{0.5}\text{Ga}_{0.5}\text{As}$ interface is $\delta = r_2 \delta_t \cong 0.25$ μm since the etch rate is approximately $r_2 = 1.1$ $\mu\text{m}/\text{min}$.

A comparison of the two traces suggests that the quality of the etch can be ascertained from the modulation ratios. The apparent thickness of an interface, such as the n-GaAs / $\text{Al}_{0.5}\text{Ga}_{0.5}\text{As}$ interface, is given by the distance δ obtained from the map. We find that the product of δ with the SMR for the lower cladding is on the order of 30 Å for test pieces taken from the same wafer. In general, there are two explanations for such an inverse relationship between δ and SMR. First, the interface might not be abrupt, but may have actually been grown as a graded interface. The SMR for the lower cladding would be small, since the phase of the reflected signal would vary with depth and hence tend to average out the interference signal. The width δ corresponding to the sloped-map feature would equal the thickness of the graded interface. The second possibility is that the primary signal reflected from an abrupt interface such as at the n-layer is affected by the surface quality. Consider, for example, that the etch depth has some small variation across the surface of the wafer, due to etch-induced roughness or non-planarity. In this case, as the etch approaches the interface, the depth variation would cause the n-GaAs layer to be exposed over a portion of the surface but a thin $\text{Al}_{0.5}\text{Ga}_{0.5}\text{As}$ layer would remain over the rest. The index of refraction of the exposed surface would be an average over the two regions. As the etch progresses, the average index and, hence, the reflected power would rise to that for GaAs. Thus,

the time δ_t required for the surface to change from $\text{Al}_x\text{Ga}_{1-x}\text{As}$ to GaAs would yield a value for δ that is larger than the actual thickness of the interface. A rough or non-planar surface would produce a small SMR by averaging out the coherence between the surface-reflected and internally-reflected signals. It is the variation of the optical path length in the $\text{Al}_x\text{Ga}_{1-x}\text{As}$ layer (and not the variation in path length for the primary signal) that is responsible for this behavior. The next chapter will show that the second explanation is the correct one for the $\text{n-GaAs} / \text{Al}_{0.5}\text{Ga}_{0.5}\text{As}$ interface. The values of δ and SMR are related to (1) the surface quality prior to etching, and (2) the ability of the plasma to etch uniformly across the surface of the wafer without introducing surface roughness.

In conclusion, we present an accurate in-situ method of monitoring the etch rate, depth and surface quality for in-plane lasers during an ECR etch. The correlation between the composition profile of the heterostructure and the optical map produced by the reflectometer provides an etching accuracy better than 500 Å. The use of this in-situ monitor eliminates the need for calibrated etch rates and exact control over the etch parameters. In addition, this technique makes it possible to computer control the etches in commercial applications using statistical quality control methods.

Chapter 15: Etched-Surface Roughness Measurements From an In-Situ Laser Reflectometer

The quality of plasma etching on III-V semiconductors is important for opto-electronic devices. The quality of the etch is determined, in part, by the roughness of the post-etched surface. Surface perturbations are known to affect the loss in optical waveguides and lasers.¹ In addition, fluctuations in the etch depth, whether systematic (such as tilt) or random, make it difficult to electrically contact a thin layer within the heterostructure by evaporating metal films. Although recent publications²⁻⁵ discuss the use of laser reflectometers for monitoring the etch depth and etch rate during the plasma etching of laser heterostructure, the use of these devices for monitoring the surface roughness needs further exploration. Considerable attention has been given to the reflection of E-M waves from exposed rough surfaces.^{6,7} Such reflections constitute the primary reflectometer signal. However, we show that a secondary reflectometer signal consisting of the interference between laser light reflected from an exposed $\text{Al}_x\text{Ga}_{1-x}\text{As}$ ($x>0$) surface and a sharp $\text{Al}_x\text{Ga}_{1-x}\text{As}/\text{GaAs}$ interface within the heterostructure provides the most sensitive measure of the surface conditions.² Unlike the interferometric method we describe, mechanical surface profilometers cannot measure macroscopic variations such as surface tilt and curvature since the sharp buried heterostructure interface is not accessible to them as a reference level. In addition, the reflectometer features an adjustable area of observation that provides a means either to focus on a specific type of microstructure or to average roughness over large areas. In the discussion that follows, we provide a stochastic model to link the observed reflectometer signals with the surface roughness for a thin $\text{Al}_{0.5}\text{Ga}_{0.5}\text{As}$ layer grown on GaAs.²

15.A: Introduction

Surface roughness refers to a distribution $\rho(z)$ of surface heights⁶ z with respect to a flat reference level. We find for many etched samples that the distribution is composed of two separate, statistically-independent distributions. The first describes random,

normally distributed fluctuations, while the second describes systematic variations that occur over the scale of millimeters. The probability density functions are denoted ρ_r and ρ_s , respectively, and are normalized so that their integrals over all possible surface heights z are unity. A convolution integral relates the density functions by

$$\rho(z) = \int d\xi \rho_r(z - \xi) \rho_s(\xi).$$

(15.1)

We assume that $\langle z \rangle = 0$ for both distributions. The normally distributed fluctuations are random in the ideal sense that the height at two neighboring points on the surface need not be the same, regardless of their proximity. In practice, the normal distribution has a non-zero correlation length. Surface profilometers typically provide the *surface roughness number* $Ra = \langle |z| \rangle$. Ra is related to the standard deviation $\sigma = \sqrt{\langle z^2 \rangle}$ by $Ra = \sigma/k_\sigma$ where k_σ is $\sqrt{\pi/2}$, $\sqrt{4/3}$, and $\sqrt{2}$ for the normal, uniform and exponential distributions, respectively. The surface statistics are linked to the reflectometer signals by the effects of *coherence*, *angular gain* and *beam size*.

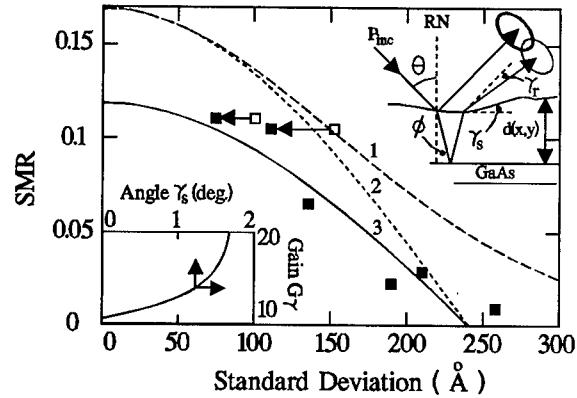


Figure 15.1: A plot of the Secondary Modulation Ratio (SMR) vs. the surface-height standard deviation σ . Curve 1 uses a normal distribution ρ_r for the surface heights. Curve 2 is a plot of the approximation $0.169\cos(\kappa\sigma)$ while curve 3 includes the overlap factor $V=0.7$. The data points are represented by the solid boxes. Upper Inset: Cross sectional view of a thin layer ($< 1 \mu\text{m}$) of $\text{Al}_{0.5}\text{Ga}_{0.5}\text{As}$ epitaxially grown on GaAs. The reflectometer laser signal reflects from the exposed rough surface as well as the buried heterostructure interface. RN is reference normal to the flat interface. The two circles schematically represent the images of the primary and refracted signals. Lower Inset: Plot of the angular gain $G_\gamma = \gamma_r/\gamma_s$ versus the surface angle γ_s .

15.B: Coherence Effects

First, the effects of *coherence* are described by the ratio of the reflected power P_{ref} to the incident power P_{inc} (refer to the upper inset to Figure 15.1). This transfer function is obtained by first summing the complex electric fields converging on the photodetector from each infinitesimal area of the surface and interface, and then calculating the total incident and reflected power from the Poynting Vector. The following discussion details the derivation.

There are two path lengths to consider. The first is the difference in path length for rays reflected from the various steps that approximate the continuous surface. The second path length is for the

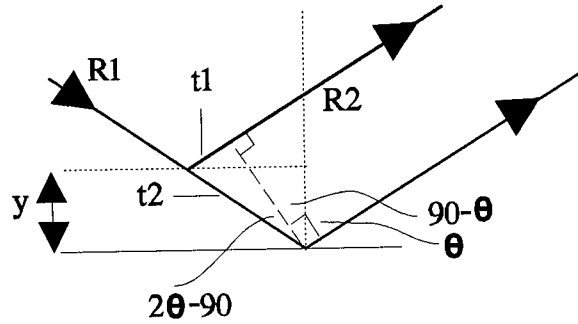


Figure 15.2: Difference in path lengths

refracted ray. The difference in path length for the surface reflected rays is $t_1 - t_2 = -2y \cos(\theta)$. This can be seen from Figure 15.2. Combine $t_2 = y / \cos \theta$ and with $t_1 = t_2 \sin(2\theta - 90)$ to get $t_1 = (y / \cos \theta) \sin(2\theta - 90)$. Subtract two expression to obtain $t_1 - t_2 = (-y / \cos \theta)(1 - \sin^2 \theta + \cos^2 \theta) = -2y \cos(\theta)$.

Let $R = R_1 + R_2$ is the total distance R_1 from the laser to the sample and the distance R_2 from the sample to the photodetector, but it does not include the path difference $t_1 - t_2$. Define the electric field per unit area as $\zeta = E_0 / A$ where A is the area of the beam on the sample. The field reaching the detector from the top surface is

$$E_s = r_s \int dA \cdot \zeta e^{ik(R - 2z \cos(\theta))} \quad (15.2)$$

and from the bottom surface is

$$E_i = r_i t_s^2 \beta \int dA \cdot \zeta e^{ik(R + 2nd(x))} \quad (15.3)$$

where the parameters r_s and r_i are the Fresnel reflection coefficients² for the top surface (0.699) and the buried interface (0.0516), respectively, and $t_s = (1 - r_s^2)^{1/2}$. For future reference, the

parameters θ , n , λ , k , β , are the angle of incidence (53°), the refractive index² of the $\text{Al}_{0.5}\text{Ga}_{0.5}\text{As}$ layer (3.49), the vacuum wavelength of the laser source (670 nm), the corresponding wavenumber $2\pi/\lambda$, and the material absorption $e^{-2\alpha\bar{d}}$ ($\cong 1$). α is the absorption coefficient for the exposed $\text{Al}_{0.5}\text{Ga}_{0.5}\text{As}$ layer and \bar{d} is the average thickness from the interface to the surface. Note that \bar{d} decreases as the etch progresses. The variation of the surface about its average height is described by $z = d(x,y) - \bar{d}$ where (x,y) is in a plane parallel to the flat interface. . Substitute $\zeta = E_0/A$ into each expression and note that the integrals over the area are averages. That is, for functions $f(z)$,

$$\langle f \rangle = \frac{1}{A} \int dA. f \quad (15.4)$$

is an average where z depends on the position of infinitesimal area dA .

This integral can be written in terms of a probability density function $\rho(z)$. For simplicity, consider the simple 1-dimensional case. Approximate the integral by a summation.

$$\langle f \rangle = \frac{1}{L} \int dx. f(x) \cong \frac{1}{L} \sum f(x_i) \Delta x \quad (15.5)$$

where, as usual, x_i is a point in the interval Δx . Rearrange the summation as follows. Let the set $\{z_1, z_2, \dots\}$ be the values assumed by $f(x)$ over the domain of length L . Let the set $\{N_1, N_2, \dots\}$ be the number of occurrences of each corresponding value z . The average can then be rewritten as

$$\langle f \rangle = \frac{1}{L} (N_1 z_1 + N_2 z_2 + \dots) \quad (15.6)$$

L can be written as $L = N \Delta x$ where $N = N_1 + N_2 + \dots$ is the total number of intervals Δx . Substituting into Eq. 15.6 and setting $\rho_1(z_i) = N_i/N$

$$\langle z \rangle = \sum \rho_1(z_i) z_i \rightarrow \int dz \rho(z) z \quad (15.7)$$

where $z = f(x)$. Equation 15.7 is extremely important since only the "number" of occurrences of a value z need be known to calculate the average and the exact functional form of $f(x)$ is

unimportant. Here, $f(x)$ is the shape of the surface written as a function. With the same distribution $\rho(z)$, the average of a function of the heights $g(z)$ has the average

$$\langle g(z) \rangle = \int dz \rho(z) g(z) \quad (15.8)$$

Combining equations 15.2 to 15.4,

$$E_{total} = E_s + E_i = r_s E_o e^{ikR} \langle e^{-2ikz \cos(\theta)} \rangle + r_i t_s^2 \beta E_o e^{ikR} e^{2iknd} \langle e^{2iknz} \rangle \quad (15.9)$$

Calculating the amplitude according to $P_{ref} \sim E_{total} E_{total}^*$ and $P_{inc} \sim E_{inc} E_{inc}^*$ yields the desired result

$$\frac{P_{ref}}{P_{inc}} = r_s^2 \left| \langle e^{-2jzk \cos \theta} \rangle \right|^2 + r_i^2 t_s^4 \beta^2 \left| \langle e^{-2jzkn} \rangle \right|^2 + A \cos(2knd) \quad (15.10)$$

where

$$A = 2r_s r_i t_s^2 \beta \operatorname{Re} \left[\langle e^{-2jzk \cos \theta} \rangle \langle e^{-2jzkn} \rangle^* \right] \quad (15.11)$$

The first term in Equation 15.10 corresponds to the primary surface-reflected signal while the last term corresponds to the secondary interference signal. The averages are over the ellipse-shaped area of the surface illuminated by the laser beam. With the values of the parameters given above, the second term in Equation 15.10 is negligible compared with the first one. Re in Equation 15.11 refers to the real part and j is $\sqrt{-1}$. Evidently, the following assumptions are made: (1) The surfaces are sufficiently smooth and the distance from the interface to the surface $d=d(x,y)$ is sufficiently small so that the refracted beam enters and leaves the $Al_{0.5}Ga_{0.5}As$ at approximately the same distance from the interface (thus the optical path length is approximately given by $2nd$). (2) The distance from the surface to the detector is large compared with the beam diameter. (3) The variation in the polarization of the light striking the detector due to surface roughness can be neglected. (4) The intensity of the incident beam is approximately uniformly distributed over its entire cross section. (5) Microstructure smaller than 1 or 2 μm can be ignored due to diffraction effects.⁸ (6) Multiple Fabry-Perot reflections between exposed surface and buried interface can be ignored, due to the small interfacial reflection coefficient r_i .

The coherence effects are embodied in the Secondary Modulation Ratio (SMR) which is the ratio of the peak-to-peak Fabry-Perot interference signal to its average value.² Taking the ratio of the 2A to the dominating primary signal in Equations 15.10 and 15.11 yields

$$SMR = C_f \operatorname{Re} \left[\frac{\langle e^{-2jzkn} \rangle}{\langle e^{-2jzk \cos \theta} \rangle} \right] \cong C_f \langle \cos(2knz) \rangle \quad (15.12)$$

where $C_f = 4r_i t_s^2 \beta / r_s \cong 0.169$. The SMR is proportional to $\langle \cos(2knz) \rangle$ since $\langle e^{-2jzkn} \rangle$ in Equations 2-4 is approximately equal⁹ to 1. Thus, the refracted beam provides the more sensitive measure of the surface roughness.

The reflectometer is useful for measuring surface quality since the SMR is relatively independent of the exact form of the probability density function in Equations 15.1 and 15.12. The approximate invariance of the SMR can be seen by integrating the first two terms of the Taylor expansion to obtain $\langle \cos(2knz) \rangle \cong \cos(2kn\sigma)$. The standard deviation in this *cosine* approximation is estimated directly from surface profilometer measurements. For independent distributions, the standard deviations are related by $\sigma^2 = \sigma_r^2 + \sigma_s^2$. A similar expression can be written for the Ra numbers. However, for this case, the resulting expression and the SMR both depend on the statistical distributions through the values of k_σ previously listed. The validity of the cosine approximation is shown in Figure 15.1, for example, which compares the plots of the SMR from the cosine approximation (curve 2) and from a normal distribution (curve 1).¹⁰

15.C: Angular Gain

The second effect on the SMR is the *angular gain* arising from the relation between the slope of the etched surface (angle γ_s) and the angle $\theta + \gamma_r$ that the refracted beam makes with respect to the reference normal RN (upper inset to Figure 15.1). The angular gain $G_\gamma = \gamma_r / \gamma_s$ is larger for angles ϕ closer to the critical angle (17°). The results from a Snell's Law calculation appear in the lower inset to Figure 15.1. Let $p_\gamma(\gamma_s)$ be the probability density for the angular variations of the surface.

Although ρ_γ describes the percentage of occurrence of a particular value of γ_s , it does not give the spatial distribution of γ_s . We assume that microstructures with a particular value of γ_s are uniformly distributed across the surface of the wafer. Thus, to each value of γ_s , there corresponds a circular area on the photodetector that is the image of the refracted signal. As suggested by the two overlapping circles in the upper inset to Figure 15.1, the image of the refracted signal is slightly displaced from the image of the dominant primary signal by γ_r .

Figure 15.3 shows a refracted beam displaced from the surface reflected beam by an angle γ_r . The images on the photodetector are displaced by the distance $L_1 \cong R \gamma_r$. If w is the width of the image then the length of overlap between the two images is given by $L_2 = w - L_1 = w - R \gamma_r$. The fractional overlap between the two images is then $L_2/w = 1 -$

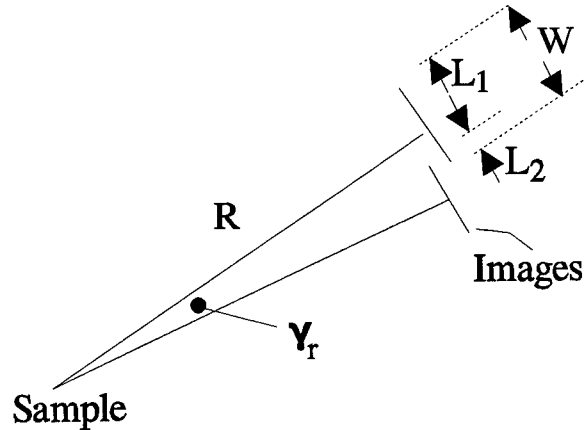


Figure 15.3: Geometry for overlapping images.

$|\gamma_r| R/w$ for $|\gamma_r| \leq w/R$ (where R is approximately 200 mm and w is approximately 3 mm at the detector. If microstructure on the surface of the sample all had the angle γ_s that produces the angle γ_r then the fractional overlap would be $1 - |\gamma_s| G_\gamma R/w$ where G_γ is the gain factor. However, only the fraction $d\gamma_s \rho_\gamma(\gamma_s)$ of the sample surface has the microstructure with the specific angle γ_s where $\rho_\gamma(\gamma_s)$ is the probability density and $d\gamma_s$ is an infinitesimal angle. The total overlap between the surface reflected images and the images from the refracted rays is given by

$$V = \int d\gamma_s \rho_\gamma(\gamma_s) \left[1 - |\gamma_s| G_\gamma \frac{R}{w} \right] \quad (15.13)$$

where $G_\gamma \sim 10$ from the lower inset to Figure 15.1. The factor V is the geometrical factor that must be multiplied into the SMR for the overlap. Evidently, the refracted beam will not overlap the

primary signal at all if the surface makes an angle $\gamma_s > 0.1^\circ$; for such a case, the secondary interference signal does not exist.

15.D: Size and Position Effects

The third effect on the SMR is related to the *size* and *position* of the illuminated area on a surface with systematic fluctuations. Substituting Equation 15.1 into 15.12, with the variable change $\eta = z - \xi$, expanding the term $\cos(\kappa\eta + \kappa\xi)$, and using the fact that $\rho_r(z)\sin\kappa z$ integrates to 0, the SMR can be written as

$$SMR = C_f \langle \cos\kappa z \rangle_r \langle \cos\kappa z \rangle_s \quad (15.14)$$

where the subscripts r and s refer to the random and systematic densities used to calculate the averages, C_f is the coefficient in Equation 15.12 and $\kappa = 2\pi/\lambda$. To continue, it must be noted that if the size of the illuminated area is decreased, then the variance $\sigma^2 = \langle z^2 \rangle_s$ of the systematic variation must also decrease. This requires that the density $\rho_s(\xi)$ approach the Dirac delta function $\delta(\xi)$ as $w \rightarrow 0$. Consequently, the SMR in Equation 15.14 approaches the maximum value $C_f \langle \cos\kappa z \rangle_r$. Therefore, reducing the illuminated area increases the SMR by eliminating the effects of systematic variations. For purely random fluctuations, the SMR is independent of the size of the illuminated area.

15.E: Experimental Results

The samples for this study are prepared and etched as in the previous chapter. The MOCVD-grown laser heterostructure is cleaved into 5×10 and 10×10 mm² pieces. A photoresist mask is placed across half the sample to protect part of the wafer from the etchants. During the etch, the signals from the reflectometer are digitally recorded. After the etch, the photoresist is removed by rinsing in solvents. The protected portion serves as a flat reference level for the surface profilometers.

The surface roughness is measured using two techniques. (1) A Tencor Instruments Alpha Step 200 surface profilometer is used to measure the random fluctuations by averaging 5 repeated scans over the same 400- μm length of etched surface. A total of ten averaged scans are taken in such a way that the end of one averaged scan coincides with the start of a subsequent one. The Alpha Step 200 can provide R_a numbers as low as 10 to 20 \AA . (2) The Alpha Step 200 is used to approximately measure the systematic fluctuations by scanning across the mask edge from the upper flat mesa (protected by the photoresist during etching) to the lower etched surface. These 400- μm scans are also averaged but they are laterally separated by approximately 200 μm . The results of method 1 and 2 are verified by an atomic force microscope scanning a $25 \times 25 \mu\text{m}^2$ etched-surface area and a Zygo interferometer measuring the surface height at 10^4 points in a 1 cm^2 area, respectively.

Figure 15.4A shows example scans obtained from the Alpha Step 200. For the "random" plot, each point represents the average surface height within a length of 3 μm . The square points in Figure 15.4A show an example of the systematic fluctuation. The

smaller samples are found to have etch depths that quadratically vary across the 5-mm width of the surface. The quadratic curve $z = (166.7 \pm 15\%) - (1.25 \times 10^{-4} \pm 15\%)x^2$ in the figure is a fit to the surface profile for several of the smaller samples. The wider samples show an increased etch rate within 1 to 2 mm of the edge. Figure 15.2B shows the probability density for both types of fluctuation. The density for the systematic fluctuation is calculated¹¹ from

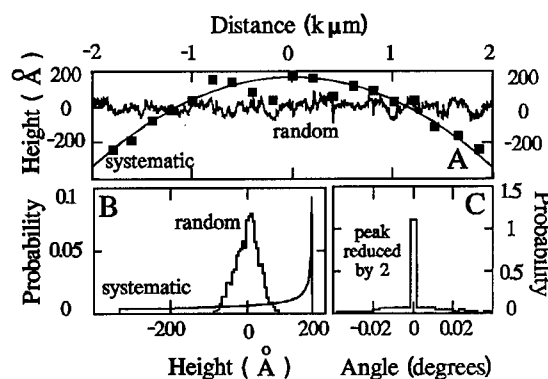


Figure 15.4: (a) An example plot of the random and systematic fluctuations as measured by an Alpha Step 200 for the etched samples. The quadratic curve is a best fit to the data from four samples (5 mm wide). (b) The probability density functions for the random and systematic distributions. (c) The probability density function for the distribution of surface angles γ_s .

$\rho_s = k_s \left| \frac{dx(z)}{dz} \right|$ where k_s is the normalization constant. Figure 15.4C shows the distribution of surface angles γ_s found by calculating the slope between adjacent points for the random distribution in Figure 15.4A. The distribution of angles and Equation 15.14 are used to calculate the overlap of $V \approx 0.7$ which leads to Curve 3 in Figure 15.1.

The data points for the SMR (measured with the reflectometer) are plotted in Figure 15.1 against the total standard deviation (measured by the Alpha Step 200). These empirical points verify the validity of curve 3. For the larger samples (open-box data points), the surface varies systematically with respect to the reference level only in the region near the edges of the wafer. Since the reflectometer beam samples only the center of the wafer, the systematic fluctuations can be ignored (i.e., $\sigma \rightarrow \sigma_r$, indicated by arrows in Figure 15.4). The data points again support Curve 3.

Chapter 16: Fabrication Methodology

One major emphasis of this effort was on the development of a fabrication process which enables the monolithic integration of GaAs electronics with optical sources and photodetectors. Each step of the overall process was characterized and optimized, so that working devices could be obtained despite the cascading effect of alignment errors and process tolerances throughout the eight-layer process. It should be noted that the combined fabrication of electronics with optics presents new challenges, in that the fabrication steps used to create one family of devices must not compromise the performance of the other. The most notable difficulty encountered during this research was the development of a reliable etching process both for defining the FET mesas and recessing the gate electrodes. Previous chapters contain a detailed description of these efforts. Certain other procedures, such as ohmic contact annealing, polyimide deposition, and the durability of dielectric films, presented minor difficulties which eventually resulted in process modifications and improvements. The fabrication process which produces integrated opto-electronic devices is thus continuously evolving.

All fabrication work was performed at the Cornell Nanofabrication Facility (CNF) at Cornell University in Ithaca, New York. This facility is set up for use not only by Engineering students from Cornell University, but also by outside researchers from other universities, the electronics industry, and government laboratories. The expansive array of semiconductor fabrication equipment and machinery, combined with the accessibility and flexibility offered by the user environment, makes this laboratory a mainstay in the research efforts of many semiconductor groups.

16.A: Layout Design and Mask Generation

The fabrication procedure begins with device and circuit layout, with the help of computer-aided design (CAD) software. The CNF has a cluster of color graphics workstations,

each running layout software which is used to draw the multilayer patterns that form optoelectronic devices. Different layers may represent, for example, areas to be coated with contact metals, areas to be covered by dielectric insulating films, or areas in which the semiconductor heterostructure is to be etched to a specific depth. During the layout design, it is imperative that subsequent fabrication processes are considered, such as lithographic focus and alignment limitations, machine tolerances, and process measuring techniques. The software encodes circuit patterns into the industry-standard GDS output file format, which is compatible with the lithography tools housed inside the cleanroom.

The geometric patterns drawn with CAD software are used to create lithographic masks which enable the transfer and size reduction of individual patterned layers onto the semiconductor wafer. Each photomask begins as a five-inch-square chrome-plated glass pane coated with photoresist. One CAD layer is projected onto each photomask as a series of tiny rectangular exposures, typically numbered in the thousands. Each flash is shaped by an aperture with variable size and rotation, controlled by the CAD data file. Following photographic developing and chrome etching, the photomask can transfer the entire patterned layer to a photoresist-coated semiconductor wafer in a single exposure.

16.B Wafer Cleaning

Prior to any patterning, heterostructure wafers are diced into 1.0-cm squares. This provides a reasonable chip size to handle, as well as a manageable financial loss if the chip should be damaged or destroyed during processing. Cleanliness is paramount during circuit fabrication. Compared to device dimensions of 1.0 μm and even smaller, hair follicles and dust particles are enormous, and wafer surfaces must be protected against contamination. The CNF facilities are housed in a Class-500 cleanroom, with complete circulation of the entire volume of filtered air every 3 minutes. Users are “togged” in a full cleanroom outfit, including boots,

jumpsuit, head covering, and face mask. Despite these precautions, the wafer surface inevitably attracts a certain amount of particulate matter, and therefore requires frequent cleaning. Typically, the wafer surface is sprayed consecutively with acetone, methanol, isopropanol, and deionized water. These solvents remove most organic contaminants, and the fluid force carries away most large dust particles. Each solvent in the above sequence is chosen for its ability to remove any residues from the previous solvent. Additionally, a final isopropanol rinse is conducted, because of its superior sheeting and drying action. Finally, the wafer surface is blown dry with a compressed-nitrogen stream to prevent spotting. Additional surface dehydration is performed prior to certain steps, by baking the chips in a convection oven at 120-150°C.

16.C: Photolithographic Image Reversal

Some metals, such as aluminum and tungsten, can be patterned by reactive-ion etching (RIE) after deposition. The most common metals used for contacting semiconductors, however, resist etching. In order to accurately reproduce the

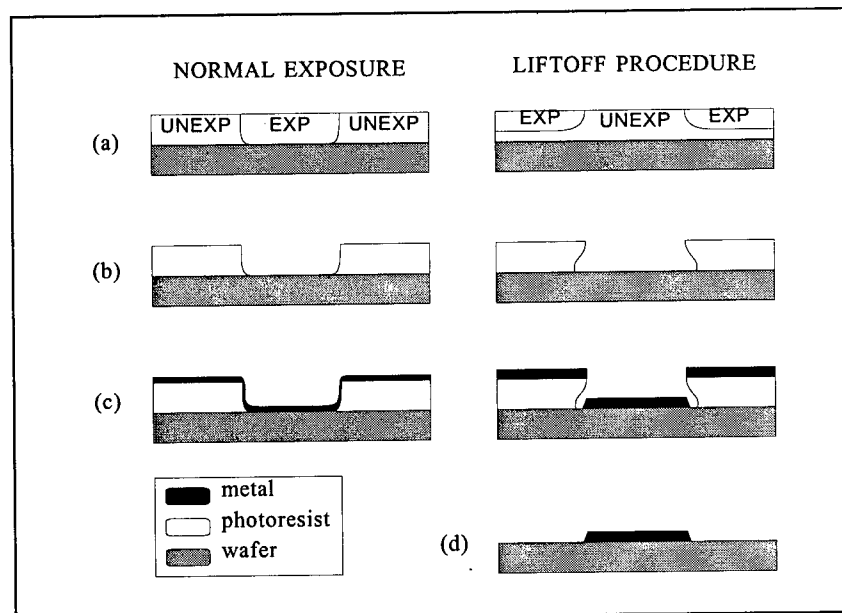


Figure 16.1: Photolithographic Liftoff Procedure: (a) patterned exposure of the photoresist film; (b) subsequent developing; (c) metalization; and (d) metal liftoff. EXP = exposed, UNEXP = unexposed

desired patterns in such metal layers, a photolithographic “liftoff” technique is used. For this procedure, the photoresist film is not fully exposed through its entire thickness. Prior to developing, the photoresist layer is subjected to an ammonia thermal diffusion step, which hardens the areas of exposed photoresist. A subsequent flood exposure over the entire wafer area, followed by development of the photoresist, results in the *negative* image of the original photomask exposure. The purpose of pursuing this lengthy lithographic exercise is that the resulting photoresist film has an *undercut* profile. In other words, the developed features in the photoresist are wider at the semiconductor surface than at the top surface of the photoresist. As shown in Figure 16.1, when a thin metal film is evaporated onto this patterned surface, the film is *discontinuous* at the edges of each patterned feature. Removal of the photoresist layer by solvent submersion simultaneously “lifts off” the overlying metal film, but metal deposited in the patterned areas remains adhered to the wafer surface. The undercut photoresist profile is essential for successful metal liftoff, since otherwise the deposited metal forms a continuous layer on normally-exposed photoresist.

16.D: Opto-Electronic Fabrication Sequence

The fabrication sequence developed for the monolithic integration of MISFETs with optical devices is based on previous success in fabricating lasers, photodetectors, and intra-cavity modulators in GaAs / AlGaAs heterostructures. An intense effort was expended, however, to modify the overall sequence for the simultaneous fabrication of transistors and lasers in physically separate layers within the heterostructure. Several major steps (not including the final metalization) of the resulting eight-layer fabrication process are diagrammed in Figure 16.2. A detailed process checklist is annotated during actual circuit fabrication, to record the completion of each process and annotate measurements, observations, and discrepancies.

Layer 1: FET Ohmic N-Type Contacts

The first layer to be imposed onto the heterostructure wafer is the pattern for the MISFET source and drain contacts (Figure 16.2a), which consists of a standard gold-germanium ohmic n-type metalization.¹¹⁰ This layer also creates permanent metal alignment marks on the wafer surface for consistent overlay accuracy of subsequent patterned layers. Prior to photoresist application, the wafer surface is treated with a dilute ammonium hydroxide solution, which removes surface oxide monolayers to promote better photoresist adhesion. Additionally, a thermal diffusion in hexamethyl disilazane (HMDS) can be performed, which helps drive off moisture from the wafer surface. Photoresist is then applied to the wafer surface and spun at a high speed to create a film with uniform thickness of $\sim 1.25\ \mu\text{m}$. The first photomask pattern is exposed, and the wafer is subjected to the image reversal process described above. The ohmic n-type metalization consists of an evaporated sequence of 150 Å nickel, which adheres well to the GaAs surface; 600 Å gold-germanium eutectic alloy (12% germanium by weight), which diffuses into the crystal during the annealing step to produce low contact resistance; 500 Å silver, which acts as a diffusion barrier for the topmost gold layer; and 1000 Å gold, which prevents corrosion of the metalization during subsequent processing. The metalization is patterned by liftoff of the photoresist, followed by an oxygen plasma “ashing” procedure which removes hardened photoresist residues. The gold-germanium contact is activated by heating the wafer to 420°C for 10 seconds in a rapid thermal anneal (RTA) furnace.¹¹¹

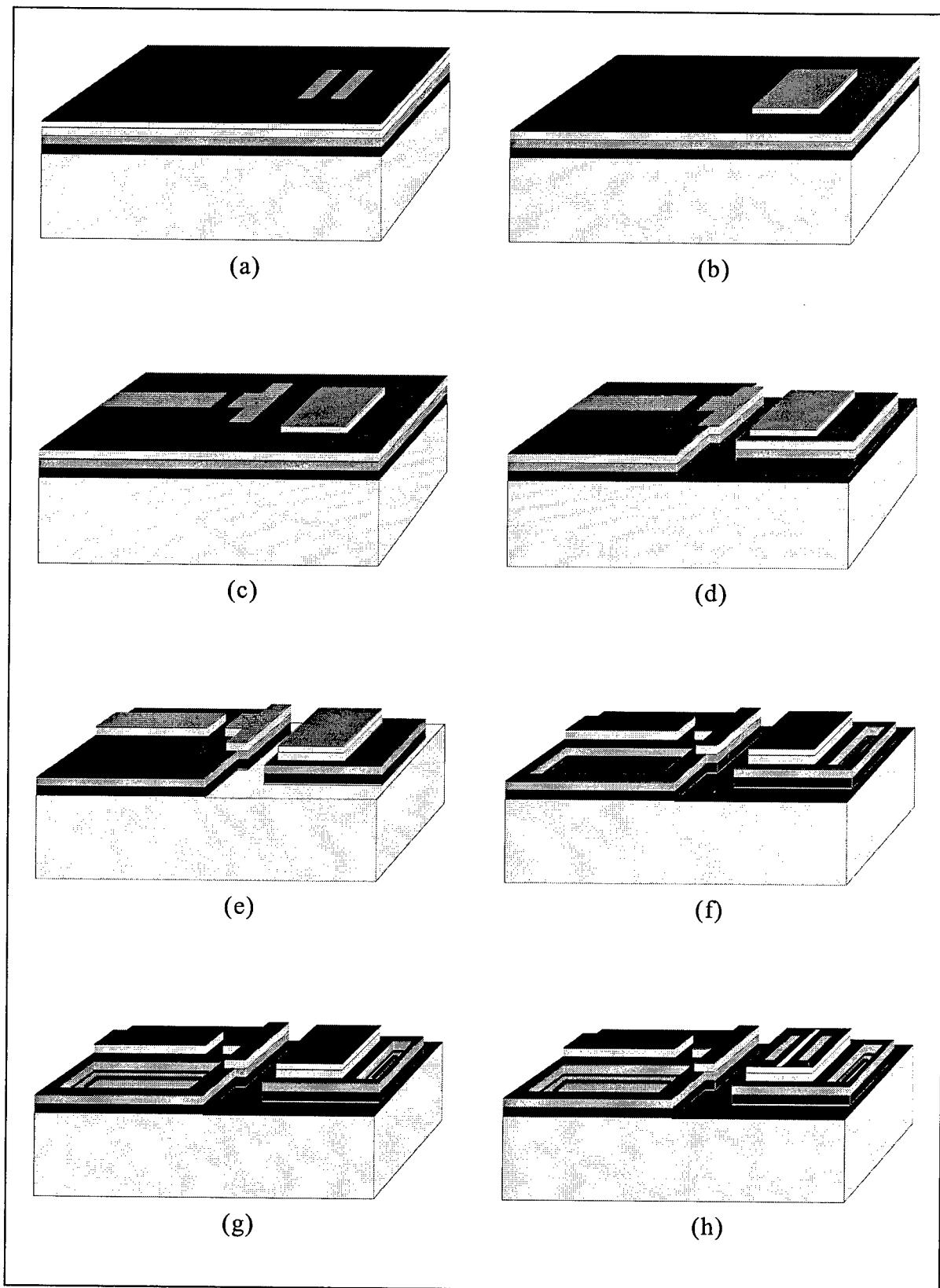


Figure 16.2: Diagram of the Integrated Opto-Electronic Fabrication Process. (a) FET metalization; (b) FET mesa etch; (c) laser n-contact metalization; (d) device isolation etch; (e) laser ridge etch; (f) wet etch and laser p-contact metalization; (g) polyimide via pattern; and (h) mesa via pattern. The final metalization step is not shown. Also not shown, for clarity, is the polyimide coating.

Layer 2: FET Mesa Etch

After solvent cleaning and surface dehydration, a dielectric film is deposited by plasma-enhanced chemical-vapor deposition (PECVD). This film is used to mask the FET mesa etch, and actually remains in place on top of the mesas throughout the remaining fabrication processes. Since this film is subjected to several plasma etches, heat treatments, and ion implantation during fabrication of the optical devices, the durability of the dielectric must be taken into consideration. A 4000 Å film of silicon-nitride is sufficient to protect the mesas during these processes. The FET mesa pattern is implemented by spinning a 2- μm -thick photoresist film over the dielectric layer, and exposing the second photomask. The pattern is subsequently transferred to the wafer by etching the Si_3N_4 film in a CF_4 plasma by RIE, after which the photoresist can be removed with a solvent rinse.

With the mesa pattern defined, the FET mesas are created (Figure 16.2b) by Electron Cyclotron Resonance (ECR) etching, using the laser reflectometer described in previous chapters to monitor the etch depth. The mesa etch removes the FET structure and GaAs buffer layers, and is stopped after removal of the $\text{Al}_{0.6}\text{Ga}_{0.4}\text{As}$ etch-stop layer (which is in fact not used as an “etch

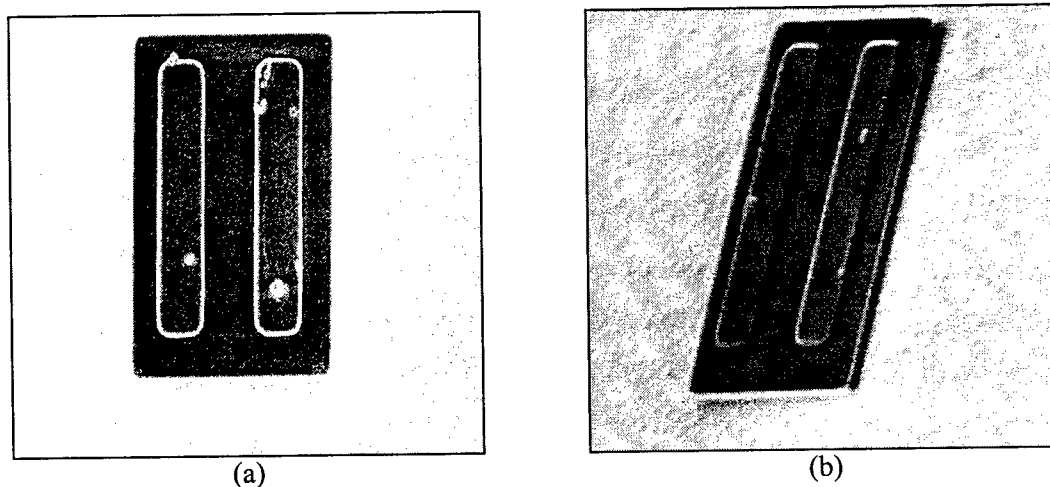


Figure 16.3: RIE-Etched FET Mesas. (a) top view, and (b) inclined view, of 6500-Å-tall mesas etched in BCl_3 / Ar by RIE. Mesas are covered with a 3100-Å SiO_2 mask.

stop” with the reflectometer etch method). This etch exposes the laser n-contact layer necessary for optical device fabrication. SEM micrographs of etched FET mesas are shown below. Figure 16.3a shows a top view, while Figure 16.3b shows a similar device at an inclination, for a better view of the mesa height. The roughness of the etched surface is a result of the RIE etch process used to fabricate this particular batch. The ECR etching technique does not cause this degree of roughness.

Layer 3: Laser Ohmic N-Type Contacts

The laser ohmic n-type contacts (Figure 16.2c) are placed using the same procedure as that for the FET sources and drains (Layer 1). The thicknesses of several layers are modified, however. The gold-germanium eutectic alloy is increased to 1200 Å for a deeper diffusion into the GaAs during contact annealing, and the top gold layer is increased to 3000 Å, to adequately shield the underlying waveguides during the oxygen-ion isolation implantation. A sacrificial layer of chrome (500 Å) is evaporated last, and is consumed during the laser ridge etch to prevent sputtering of the highly conducting gold top layer. Following the metalization and liftoff procedures, the laser n-type contacts are annealed in the same manner as the FET contacts above. The dielectric mesa mask protects the FET contacts from the effects of the rapid heat treatment.

Layer 4: Deep Isolation Etch

Ridge waveguides are formed with a two-step dry etch procedure. This process results in a shallow etch (to within 0.1 μm of the MQW active region) which defines the ridges for index-guided lasers, and a deeper etch (completely through the lower p-contact layer, into the semi-insulating substrate) which forms the laser mirrors and isolates the p-contact layers between devices. The two-step etch is performed in the ECR, again using the laser reflectometer etch monitor mentioned above.

The first etch is patterned with the Layer 4 photomask, developed in $\sim 1.75\text{-}\mu\text{m}$ -thick photoresist which masks each device so that an isolation trench is etched around its perimeter. Laser mirrors are masked with the n-type waveguide metal, rather than the photoresist film, to produce a better vertical profile. The desired depth for the first etch is the total distance through the remaining laser heterostructure, minus the depth to be etched by the subsequent, shallow waveguide etch (Figure 16.2d). In other words, the depth to be etched is the distance between the top of the graded-index confinement layers and the bottom of the p-type laser contact.

The photoresist mask is then removed with a solvent rinse, and a second ECR etch is performed. Besides creating the ridge waveguides defined by the laser contacts, this second etch extends the isolation trenches down through the deepest p-contact layer and into the substrate (Figure 16.2e). During this second etch, the FET mesas are protected by the dielectric mesa film.

Oxygen-Ion Isolation Implant

The deep isolation etch completely separates most devices electrically and optically. A deep etch, however, cannot be used between a main laser section and its associated intra-cavity modulator, as reflecting surfaces would be created within what is designed to be a single optical cavity. The deep p-contact layer must therefore be common to both elements, and a different means must be utilized to provide sufficient electrical isolation between the n-type contacts. The shallow ECR etch which creates the ridge waveguides removes the highly doped GaAs contact layer and most of the doped AlGaAs cladding between the laser and modulator; however, a sufficient conduction path still exists through the remaining cladding and MQW active region to degrade circuit performance.

A shallow oxygen-ion implant (10^{12} - 10^{13} ions/cm² at 60, 120, and 180 kV) is therefore used to increase the lateral resistivity between the laser and modulator, by inducing lattice

damage and creating deep traps. The implant voltages were selected, using the computer program TRIM,¹¹³ to produce a continuous ion penetration over the depth range 570 - 3700 Å, as shown in the table below. The resulting isolation implant has been shown¹⁰⁹ to raise the electrical resistance between the laser gain section and the intra-cavity modulator to 1.7 MΩ. (Prior to the implant, the resistance

was measured to be less than 1 kΩ.)

During this ion implantation, the dielectric mask protects the FET

Implant Energy	Longitudinal Range	Longitudinal Straggle
60 keV	1009 Å	435 Å
120 keV	1891 Å	719 Å
180 keV	2784 Å	922 Å

mesas from implant damage, while the n-contact metalization protects the ridge waveguides.

Layer 5: Laser Ohmic P-Type Contacts

Many compound semiconductor heterostructures are grown on a doped substrate, so that a single metalization over the entire backside of the wafer serves as a common ground electrode for all the devices. This significantly simplifies the fabrication complexity, as only one metalization needs to be patterned on the front of the wafer. More complex opto-electronic integrated circuits, however, require the ability to isolate both terminals of each device, so that isolated current paths can be implemented between devices. A semi-insulating substrate is required to electrically isolate the lower contacts of separate devices, and a fabrication method must be developed to allow front-side metalization of the deeply buried contact layer of each device. In this case, ohmic p-type contacts for the optical devices are formed by wet etching adjacent to the waveguides, down through the active region and lower cladding, to the p-contact layer, and then applying an ohmic metalization (Figure 16.2f).

The wet etch pattern is transferred into ~ 1.5-μm-thick photoresist, by exposing the Layer 5 photomask. A phosphoric acid / hydrogen peroxide etchant is used, because of its preferential etching of AlGaAs alloys over GaAs. Methanol is added to the etchant to improve

its "wetting" properties by reducing the surface tension of the fluid. The proximity of the etched areas to metal structures does not seem to have the same accelerating effect as with the citric acid selective etchant. The progress of the etch can therefore be accurately monitored with the *in situ* laser reflectometer technique.

Wet etching a compound semiconductor results in angled sidewalls along crystal planes, rather than the vertical sidewalls characteristic of plasma etching. Each etched pit will have two parallel sides with facets sloping into the pit, while the other two parallel sides exhibit angled undercut. This faceted topography actually facilitates later interconnect metalization of the deep-etched pits, by allowing a continuous metal layer to cover the downward slope, rather than gapping over an abrupt step. The sidewall phenomenon must be considered during the CAD pattern layout stage, however, to ensure proper metal coverage over the downward-sloping sides of the pit. This can be assured if the metal pattern overlaps any two adjacent sides of the pit.

The photoresist film used to pattern the wet etch is kept on the wafer to use for the metal liftoff. An undercut profile in the photoresist is not required in this case, since the wet etch itself undercuts the crystal beneath the photoresist edge. The ohmic p-type metalization consists of an evaporated sequence of 300 Å titanium, which adheres well to the GaAs surface; 200 Å platinum, which serves as a diffusion barrier for the overlying gold; and 1500 Å gold for good lateral conductivity of the metalization. Removal of the photoresist with a solvent rinse results in patterning of the metalization by liftoff. Because of the high p-type doping concentration in this layer, no dopant diffusion or annealing is necessary to achieve low contact resistance.

Layer 6: Polyimide Application and Vias

A layer of dielectric polyimide is applied to the wafer to smooth the vertical edges of the FET mesas and ridge waveguides. This layer facilitates later fabrication of metal interconnects between the FET mesas and the in-plane lasers, by ensuring that continuous metal traces can be

deposited without critical thinning over sharp edges. The polyimide also serves as an insulating dielectric, upon which large probe pads can be placed without interfering with the performance of underlying opto-electronic devices. A further benefit of applying a polyimide coating is the ability to incorporate insulated electrical crossovers in the circuit layout. Since the polyimide coating completely covers the wafer surface, however, "vias" must be etched back through the polyimide layer to allow penetration of the final metalization to each of the device contacts beneath the polyimide. The tops of the FET mesas must also be uncovered, to allow the gates to be patterned and deposited.

The Probimide® series of polyimides manufactured by the Ciba-Geigy Corporation can be applied in thicknesses covering the entire range from 0.35 μm - 20 μm . To ensure adequate filling of the isolation trenches and smoothing of the FET mesas, a thickness of 3-4 μm is typically selected. The polyimide

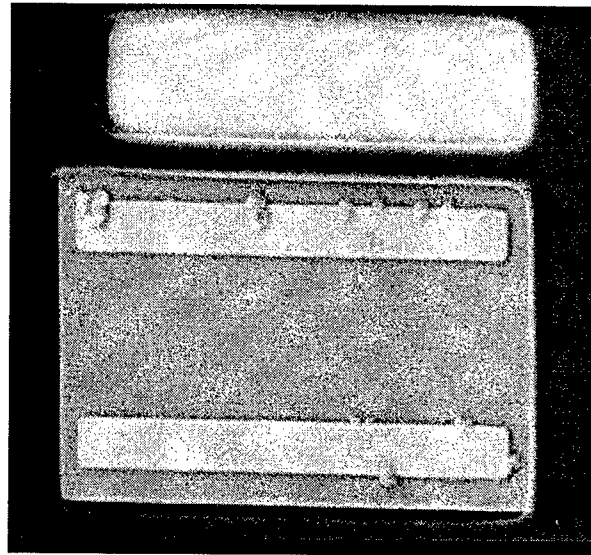


Figure 16.4: Polyimide Vias Etched at a FET Mesa

solution, preceded by a preparatory adhesion promoter, is applied to the wafer surface and spun at high speeds to achieve a uniform film thickness. The polyimide solution is fully cured by subjecting the wafer to a heat treatment cycle at 90°, 150°, and 240°C, over a one-hour period.

Since the polyimide film etches with only a 1:1 selectivity to a photoresist mask, a thin silicon dioxide layer ($\sim 1000 \text{ \AA}$) is deposited over the polyimide for patterning. The SiO_2 film remains over the polyimide to protect it during subsequent processing steps, such as oxygen

plasma “ashing”. The polyimide via pattern (Figure 16.2g) is transferred to the SiO_2 film by exposing the Layer 6 photomask in 1.25- μm -thick photoresist. The vias are then implemented in the polyimide layer by first etching the vias through the SiO_2 film, using a CF_4 plasma, then etching the polyimide with an O_2 / CF_4 plasma, both performed by RIE. The polyimide is subjected to a final 240°C cure to ensure sidewall hardening within the vias. An SEM micrograph of the polyimide coating and vias is shown in Figure 16.4. The smaller rectangle offset from the main mesa is for contacting an underlying layer for shielding of the transistor channel from stray electric fields. The roughened RIE-etched GaAs surface is visible at the floor of the offset via.

Layer 7: FET Mesa Vias

With the *laser* fabrication finished, attention is returned to completion of the FET fabrication. Although the polyimide layer has been removed over the tops of the mesas, the semiconductor surface and source/drain contacts still remain covered by the silicon-nitride mask deposited for Layer 2. Vias must be etched through

this dielectric layer for access to the source and drain contacts. The gate

electrodes are also defined by the Si_3N_4 vias (Figure 16.2h), since better lithographic resolution can be attained by etching through a thin dielectric film, rather than relying on the accuracy of the image reversal and metal liftoff procedures to define gate length.

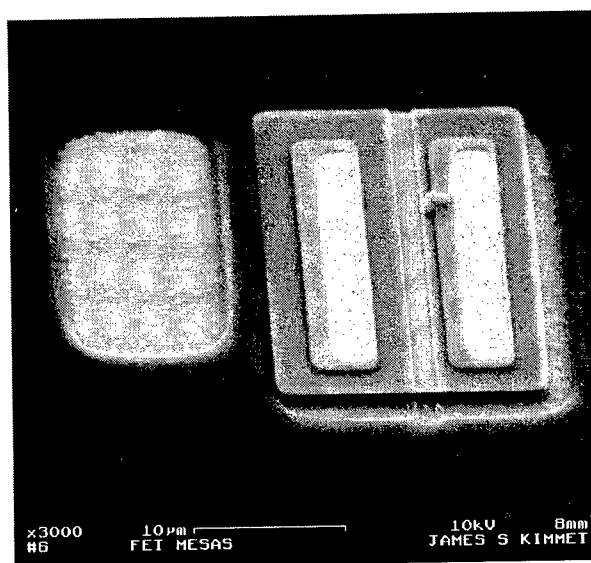


Figure 16.5: FET Vias Etched Through Dielectric Coating. The surrounding polyimide film has been eroded by the CF_4 etch.

The Layer 7 photomask is used to expose the mesa via pattern onto a 1.5- μm -thick photoresist film. The vias are then etched through the silicon nitride by RIE with a CF_4 plasma. The photoresist is removed with a solvent rinse, followed by an oxygen plasma ashing procedure. An SEM micrograph of the resulting mesa pattern is shown in Figure 16.5.

Layer 8: Top Metal Pads and FET Gate Metalization

For heterostructures with an *undoped* cap layer at the FET surface, fabrication can immediately proceed with patterning and metalization of Layer 8. Wafers with a highly-doped ohmic-contact cap, on the other hand, must first be subjected to an etch which removes this doped layer prior to gate electrode metalization. The phosphoric acid etch used above for Layer 5 can be used again to recess the gate vias through the GaAs cap, down to the AlGaAs gate barrier layer. Typically, the etchant is further diluted in deionized water to reduce its potency because of the thinness of the layer to be removed.

The Layer 8 metalization follows the same patterning, image reversal, and liftoff procedures used above for Layers 1 and 3. A different evaporated metal sequence is used, however, to achieve better Schottky contact characteristics in the gate electrodes. The metal sequence consists of 500 Å titanium for a high Schottky barrier, as well as good adhesion to the polyimide and GaAs; 3500 Å silver for good step coverage and high conductivity; and a top cap of 1000 Å gold, for corrosion resistance and wire bonding compatibility. Silver composes the majority of this metalization, because of its superior properties in covering steep vertical features.

Due to the thickness of this final metal layer, a thicker photoresist masking film ($\sim 3\text{ }\mu\text{m}$) is required to achieve the proper liftoff results. The thicker resist, however, cannot resolve small, submicron features because of the aspect ratio. By defining the contact area for the FET gate electrodes with the *silicon nitride* vias, as mentioned above, wider metal stripes can be

deposited for the gate electrodes, achieving better liftoff performance without sacrificing gate resolution. The thickness of the metalization results in a T-shaped vertical profile for the gate electrodes, as shown in Figure 16.6. This results in a large electrode cross-section for low RF impedance, whereas the actual "gate length" is defined by the length of the physical contact region between metal and semiconductor.

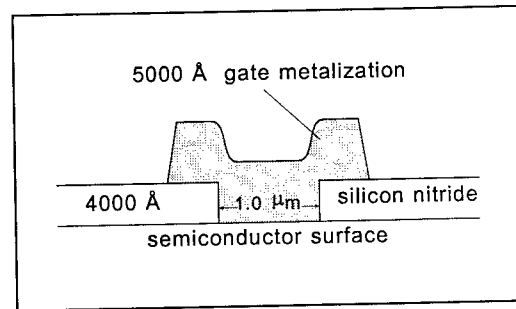


Figure 16.6. Cross-Sectional View of the Gate Electrode

16.E: Lapping, Cleaving, and Mounting

A completed FET device is shown in Figure 16.7. Prior to cleaving and mounting the wafers for opto-electronic characterization, the wafers are thinned by lapping down the backside of the substrate. Thinning the wafer facilitates the cleaving process and improves heat dissipation by bringing the devices closer to the heat sink. Lapping is achieved by mounting the wafer face-down onto a chuck with melted white wax. After cooling, the backside of the wafer is manually circulated on a glass plate covered with a 3- μm alumina slurry. As the thickness of the wafer is gradually reduced, progress is periodically monitored by measuring the reduction in wafer thickness with respect to the chuck. The wafer is reduced to a thickness of 4-10 mils (100-250 μm), after which it is removed from the chuck by melting the wax, and cleaned in organic

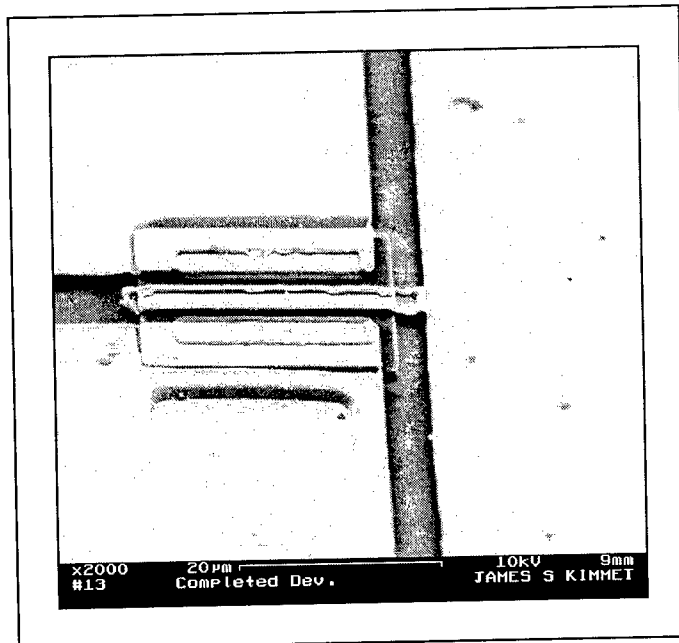


Figure 16.7: Completed 20 μm \times 1 μm FET Device

solvents.

The wafer may be scribed and cleaved to allow coupling of optical signals into or out of optical fibers. Cleaving is not necessary for laser operation, however, as most of the optical cavities are formed by ECR-etched vertical mirror facets. The wafer is typically mounted on a copper block prior to characterization, using electrically- and thermally-conductive silver epoxy. The copper block serves as a heat sink and ground plane during the opto-electronic testing of the integrated devices.

In summary, a comprehensive fabrication sequence has been developed to monolithically integrate GaAs MISFET electronics with GaAs / AlGaAs MQW lasers, photodetectors, and intra-cavity modulators. Etching techniques are extensively used as a means to isolate and delineate devices, as well as to contact buried heterostructure layers. The process begins with fabrication of the transistor mesas and alignment marks. During fabrication of the *optical* devices, the transistor mesas are protected by a dielectric thin film. This film is then patterned prior to the final metalization step, which simultaneously creates electrical device interconnects, large probing pads, and the Schottky gate electrodes for each transistor. The overall sequence has been designed to produce integrated circuits consisting of interconnected transistors and lasers, in a compatible process which does not compromise the performance of either type of component.

PART 3
SOFTWARE

Chapter 17: Software for the Wavelength Dependence of Light Reflected from Multiple Layers of GaAs-AlGaAs

This chapter contains the software for the wavelength dependence of light reflected from multiple layers of GaAs and AlGaAs. With simple modifications it can be used to determine the possible optical modes within a Vertical Cavity Surface Emitting Laser or used to etch GaAs-AlGaAs Heterostructure (refer to Chapter 18). The software is implemented on DOS machines but should have a pentium processor at minimum. No corrections to the listing are made and at present, several viewing features are not working. Unlike the software in Ch. 18, the listing here does not take into account absorption phenomena. IMPORTANT NOTE: A file called "parameter.rec" must be included in the default directory; this file can be empty on the first run.

```
' This program calculates the matrices required for dielectric stacks. The
' relevant matrices are found in G.R. Fowles, Intro to Optics, 2nd ed. See
' pp 97-98. For a single layer, the matrix has the form
' row 1, col 1 = A = cos(kL)      row 1, col 2 = B = (-i/n)sin(kL)
' row 2, col 1 = C = (-i n)sin(kL) row 2, col 2 = D = cos(kL)
' where k = 2*pi*n/wavelength and n = index of the layer. Let
' n0=index of left cap, Nt=index of right cap, denom = A*N0 + B*Nt + C + D*Nt
' then r = (A*N0 + B*Nt*N0 - C - DNt)/denom = reflectivity = Erefl/Eincid
' t = 2*N0 / denom = transmissivity = Etrans/Eincid
' note that t can be larger than 1 if N0 > n since the optical energy in N0
' is stored in both the polarization and in Eincid. Energy conservation
' requires E to increase in n. This is equivalent to the E boundary conditions.
' Below: Mr,Mi are the re and im matrices with the A,B,C,D coefficients above.
' X contains the aluminum mole fractions, T contains the layer thicknesses
' file.flag$ says whether or not to write data to file. Num.lay% is
' the number of layers in the stack. L.start etc are the start, stop and step
' wavelengths. Lay.in etc are the name of the input/output layers
' comp.in etc are the aluminum mole fraction of the input/output layers.
' file.number% is the extension for the data files. I.L etc are the wavelength
' al mole fraction, and index for the routine to separately calculate index
' for a specific layer. f$ and f2$ are for number formatting.
```

```
call read.N.table      ' read index of refract vs wavelength
num.lay%=18 : pi=4*atn(1) : file.number% = 1 : file.flag$ = "off"
L.start%=800 : L.stop%=900 : L.step% = 1
a$=date$ : lay.in$ = "Al(x)Ga(1-x)As" : lay.out$ = "air"
df.name$ = left$(a$,2) + mid$(a$,4,2) + right$(a$,2)
pf.name$ = "param" : g.type$ = "power" : graph.var$ = "reflected and transmitted"
I.L% = 850 : I.X = 0.5 : I.N = 3.307
f$ = "#.###" : f2$ = "####"
```

```
call dim.matrix(num.lay%)
```

```
main.menu:
```

```
cls
```

```
print "This program calculates the reflectivity of a dielectric mirror stack"
```

```
print "composed of alternating layers of Al(x)Ga(1-x)As. The left most end"
```

```

print "cap is assumed to be the input layer. The right end is the ouput."
print "Assume negligible absorption."
print
print "Number of layers: (" ; num.lay% ; ") excluding the two ends"
print "Composition X of layers excluding the end caps"
print "Thickness of each layer"
print "Specify end caps: " ; lay.in$ ; " X=" ; using f$ ; comp.in ;
    print "    output: " ; lay.out$ ; " X=" ; using f$ ; comp.out
print
print "Wavelength range (" ; using f2$ ; L.start% ; : print " " ; using f2$ ; L.stop% ; : print " )
    Step: " ; using f2$ ; L.step% ; : print " nm"
print "Graph type: " ; g.type$ ; " Variable: " ; graph.var$
print
print "Parameter file name: " ; pf.name$ + ".rec"
print "Data file name: " ; df.name$ + "." ; fnConvert$(file.number%) ; " File save is " ; file.flag$
print
print "Index of refraction for a specific wavelength and mole-fraction"
print "    wavelength: " ; using f2$ ; I.L% ; : print "    mole-fraction: " ; using f$ ; I.X ; :
    print "    index: " ;
print using f$ ; I.N
print
print "Run: calculate reflection coefficient vs. wavelength"
print "Quit"
print : print
input "Enter your choice: " , ch$ : ch$ = lcase$(ch$)

select case ch$
case "c"
    call get.comp( x() , num.lay% )
case "n"
    call num.layers(num.lay%)
    call erase.matrix
    call dim.matrix(num.lay%)
case "g"
    call graph.related(g.type$,graph.var$)
case "t"
    call get.thickness( T() , num.lay% )
case "p"
    call param.files
case "s"
    call specify.io(lay.in$, comp.in, lay.out$, comp.out)
case "i"
    call individual.index(I.L%,I.X,I.N)
case "d"
    call data.files(df.name$,file.number%,file.flag$)
case "w"
    call wavelength.range(L.start%,L.stop%,L.step%)
case "r"
screen 2 : cls

```

```

call label.graph(L.start%,L.stop%,L.step%)
call main.routine(num.lay%,L.start%,L.stop%,L.step%,df.name$,file.number%)
if file.flag$ = "on" then file.number% = file.number% + 1
screen 2,0
case "q"
system
case else
print chr$(7)
end select
goto main.menu
end

sub main.routine(num.lay%,L.start%,L.stop%,L.step%,df.name$,file.number%)
shared Mr(),Mi(),X(),T(), pi, file.flag$,g.type$,graph.var$
shared lay.in$,lay.out$,comp.in,comp.out
if file.flag$="on" then
ext$ = fnConvert$(file.number%)
file.number% = file.number% + 1
open "R" + df.name$ + "." + ext$ for output as #2
open "T" + df.name$ + "." + ext$ for output as #3
end if

for L% = L.start% to L.stop% step L.step%      ' L% is the wavelength
aba$ = inkey$
if aba$ <> "" then L% = L.stop% - L.step%
for row%=1 to 2 : for col%=1 to 2
Mr(1,row%,col%) = fnMatrixRe(row%,col%,L%,1)
Mi(1,row%,col%) = fnMatrixIm(row%,col%,L%,1)
next col% : next row%

if num.lay% = 1 then goto jump.point
for i% = 2 to num.lay%
for row% = 1 to 2 : for col% = 1 to 2
Mr(2,row%,col%) = fnMatrixRe(row%,Col%,L%,i%)
Mi(2,row%,col%) = fnMatrixIm(row%,Col%,L%,i%)
next col% : next row%

for row% = 1 to 2 : for col% = 1 to 2
Mr(3,row%,col%) = 0
Mi(3,row%,col%) = 0
next col% : next row%

' multiply matrices with complex entries
for row% = 1 to 2 : for col% = 1 to 2 : for temp% = 1 to 2
Mr(3,row%,col%)= Mr(3,row%,col%)+Mr(1,row%,temp%)*Mr(2,temp%,col%) -
Mi(1,row%,temp%)*Mi(2,temp%,col%)
Mi(3,row%,col%)= Mi(3,row%,col%)+Mr(1,row%,temp%)*Mi(2,temp%,col%) +
Mi(1,row%,temp%)*Mr(2,temp%,col%)
next temp% : next col% : next row%

```

```

for row% = 1 to 2 : for col% = 1 to 2
  Mr(1,row%,col%) = Mr(3,row%,col%)
  Mi(1,row%,col%) = Mi(3,row%,col%)
next col% : next row%
next i%

jump.point:
' calculate reflected component
n.zero = fnN(L%,0) : n.last = fnN(L%,num.lay%+1)

num.r.re = Mr(1,1,1)*n.zero + Mr(1,1,2)*n.zero*n.last - Mr(1,2,1) - Mr(1,2,2)*n.last
num.r.im = Mi(1,1,1)*n.zero + Mi(1,1,2)*n.zero*n.last - Mi(1,2,1) - Mi(1,2,2)*n.last
den.r.re = Mr(1,1,1)*n.zero + Mr(1,1,2)*n.zero*n.last + Mr(1,2,1) + Mr(1,2,2)*n.last
den.r.im = Mi(1,1,1)*n.zero + Mi(1,1,2)*n.zero*n.last + Mi(1,2,1) + Mi(1,2,2)*n.last

r.re = fnDivRectReal(num.r.re,num.r.im,den.r.re,den.r.im)
r.im = fnDivRectImag(num.r.re,num.r.im,den.r.re,den.r.im)

num.t.re = 2*n.zero
num.t.im = 0
den.t.re = den.r.re
den.t.im = den.r.im

t.re = fnDivRectReal(num.t.re,num.t.im,den.t.re,den.t.im)
t.im = fnDivRectImag(num.t.re,num.t.im,den.t.re,den.t.im)

' calculate amplitude and phase of reflectivity and transmissivity
r.amplit = fnR2Pa(r.re,r.im)
r.phase = fnR2Pt(r.re,r.im)
t.amplit = fnR2Pa(t.re,t.im)
t.phase = fnR2Pt(t.re,t.im)

if g.type$ = "power" then
  t.amplit = (n.last/n.zero)*t.amplit^2
  r.amplit = r.amplit^2
end if

select case graph.var$
case "reflected and transmitted"
case "reflected"
  t.amplit = 0
case "transmitted"
  r.amplit = 0
end select

call graph.amplitude((r.amplit),(t.amplit),L%,L.start%)
if file.flag$ = "on" then
  write #2, L%, L%,r.amplit, r.phase

```

```

write #3, L%, L%,t.amplit, T.phase
end if

next L%

loop1:
aa$=inkey$ : if aa$ = "" then loop1

close
end sub

sub graph.amplitude(y1,y2,L%,L.start%)
left.x% = 20 : right.x% = 619 : up.y% = 0 : down.y% = 190
x%=L%
' calculate vert and horiz scales
scale% = (down.y% - up.y%)/2
y1% = scale% * (2 - y1) : y2% = scale% * (2 - y2)      ' vertical scale
x% = x% - L.start% + left.x%                             ' horizontal scale
if x% = left.x% then
y1.old% = y1%
y2.old% = y2%
x.old% = left.x%
end if
line (x%,y1%) - (x.old%,y1.old%)
line (x%,y2%) - (x.old%,y2.old%)
y1.old% = y1% : y2.old% = y2% : x.old% = x%
end sub

sub label.graph(L.start%,L.stop%,L.step%)
shared g.type$
'Draw box and label axis
left.x% = 20 : right.x% = 619 : up.y% = 0 : down.y% = 190
locate 1,1 : print 2; : locate 24,1 : print 0;
locate 25,2 : print L.start%; : locate 25,74 : print L.start% + 600;
locate 25,33 : print "Wavelength (nm)";
locate 12,1 : print "R";
locate 2,69 : print g.type$ + " R";
ver.step% = (down.y%-up.y%)/10 : hor.step% = 100
line (right.x%,down.y%)-(left.x%,up.y%),,B
for i% = left.x% to right.x% step hor.step%
line (i%,down.y%-4)-(i%,down.y%): line (i%,up.y%+4)-(i%,up.y%)
next i%
for j% = up.y% to down.y% step ver.step%
line (left.x%+5,j%)-(left.x%,j%) : line (right.x%,j%)-(right.x%-5,j%)
next j%
end sub

sub graph.related(g.type$,graph.var$)
g.r.label:

```

```

cls
print "MENU OF GRAPH RELATED ITEMS"
print
print "... variables to plot: ";graph.var$;" ..."
print "Both reflected and transmitted"
print "Reflected component only"
print "Transmitted component only"
print
print "Definition of reflectivity: ";g.type$
print
print "Main menu"
print
input "Choice: ",ch$ : ch$ = lcase$(ch$)
select case ch$
case "d"
if g.type$ = "power" then
g.type$ = "field"
else
g.type$ = "power"
end if
case "b"
graph.var$ = "reflected and transmitted"
case "r"
graph.var$ = "reflected"
case "t"
graph.var$ = "transmitted"
case "m"
case else
print chr$(7)
end select
if ch$ <> "m" then g.r.label
end sub

```

```

def fnMatrixRe(row%,col%,L%,i%)
shared T()
select case row% * col%
case 1,4
fnMatrixRe = cos( T(i%) * fnK(L%,i%) )
case 2
fnMatrixRe = 0
end select
end def

```

'matrix for successive layers

```

def fnMatrixIm(row%,col%,L%,i%)
shared T()
select case row% * col%
case 1,4
fnMatrixIm = 0

```

'matrix for successive layers

```

case 2
select case col%
case 1
  fnMatrixIm = -1 * fnN(L%,i%) * sin( T(i%) * fnK(L%,i%) )
case 2
  fnMatrixIm = ( -1 / fnN(L%,i%) ) * sin ( T(i%) * fnK(L%,i%) )
end select
end select
end def

def fnK(L%,i%)
shared pi
fnK = 2*pi*fnN(L%,i%)/L%
end def

def fnN( L%,i% )                                ' index from interpolation routine
shared X(), num.lay%
shared lay.in$,lay.out$,comp.in,comp.out
select case i%
case 0
  if lay.in$="air" then
    fnN = 1
  else
    fnN = fnN.interpolate(L%,comp.in)
  end if
case <= num.lay%
  fnN = fnN.interpolate(L%,X(i%))
case > num.lay%
  if lay.out$ = "air" then
    fnN = 1
  else
    fnN = fnN.interpolate(L%,comp.out)
  end if
end select
end def

def fnN.interpolate(L%,X.comp)                  ' interp routine for index of refract
shared N.table
E = 1245/L%
row= E/0.2 - 1 : col = 1 + 10 * X.comp
row.base% = int(row) : row.fract = row - row.base%
col.base% = int(col) : col.fract = col - col.base%
if row.base% = 14 then
  row.base% = 13
  row.fract = 1
end if
if col.base% = 11 then
  col.base% = 10

```

```

col.fract = 1
end if
n.col1.dif = N.table(row.base%+1,col.base%) -N.table(row.base%,col.base%)
n.col2.dif = N.table(row.base%+1,col.base%+1)-N.table(row.base%,col.base%+1)
n1 = N.table(row.base%,col.base%) + row.fract * n.col1.dif
n2 = N.table(row.base%,col.base%+1) + row.fract * n.col2.dif
fnN.interpolate = n1 + col.fract * (n2 - n1)
end def

def FNconvert$(num.in%)                                     ' calculates data file extents
old.num% = 0 : a$ = ""
for i% = 1 to 3
new.num% = int(num.in% / 10^(3-i%))
a% = new.num% - 10 * old.num%
old.num% = new.num%
a$ = a$ + chr$(48 + a%)
next i%
FNconvert$ = a$
end def

def fnMultRectReal(Ax,Ay,Bx,By)
fnMultRectReal = Ax*Bx - Ay*By
end def

def fnMultRectImag(Ax,Ay,Bx,By)
fnMultRectImag = Ax*By + Ay*Bx
end def

def fnDivRectReal(Ax,Ay,Bx,By)
fnDivRectReal = (Ax*Bx + Ay*By) / (Bx^2 + By^2)
end def

def fnDivRectImag(Ax,Ay,Bx,By)
fnDivRectImag = (Ay*Bx - Ax*By) / (Bx^2 + By^2)
end def

def fnR2Pa(Cx,Cy)
fnR2Pa = sqr(Cx^2+Cy^2)
end def

def fnR2Pt(Cx,Cy)
shared pi
select case Cx
case = 0
select case Cy
case >0
fnR2Pt=pi
case <0
fnR2Pt=(3/2)*pi

```



```

    case =0
        fnR2Pt =0
    end select
case >0
    if Cy >= 0 then
        fnR2Pt=atn(Cy/Cx)
    else
        fnR2Pt= 2*pi + atn(Cy/Cx)
    end if
case <0
    fnR2Pt=pi+atn(Cy/Cx)
end select
end def

def fnP2Rx(a,t)
    fnP2Rx = a*cos(t)
end def

def fnP2Ry(a,t)
    fnP2Ry = a*sin(t)
end def

def fnMamp(A1,t1,A2,t2)
    fnMamp=A1*A2
end def

def fnMarg(A1,t1,A2,t2)
    shared pi
    sum.arg = t1 + t2
    if sum.arg >= 2*pi then sum.arg =sum.arg - 2*pi
    if sum.arg <=-2*pi then sum.arg =sum.arg + 2*pi
    fnMarg = sum.arg
end def

sub specify.io(lay.in$,comp.in$,lay.out$,comp.out)
io.menu:
cls
print "Light initially travels in the 'input end' and is then incident on"
print "the dielectric stack. The stack reflects some light back into the"
print "input end and transmits some light into the output end."
print
print "I  Input end: "; lay.in$
print "CI Composition of Input end: "; comp.in
print
print "O  Output end: "; lay.out$
print "CO Composition of output end: "; comp.out
print
print "Main menu"
print

```

```

input "Choice: ",ch$ : ch$ = lcase$(ch$)
select case ch$
case "i"
if lay.in$ = "air" then
lay.in$ = "Al(x)Ga(1-x)As"
else
lay.in$ = "air"
end if
case "o"
if lay.out$ = "air" then
lay.out$ = "Al(x)Ga(1-x)As"
else
lay.out$ = "air"
end if
case "ci"
Input "Enter mole fraction X of input layer: ", comp.in
case "co"
input "Enter mole fraction X of input layer: ", comp.out
case "m"
case else
print chr$(7)
end select
if ch$ <> "m" then goto io.menu
end sub

sub wavelength.range(L.start%,L.stop%,L.step%)
wave.menu:
cls
print
print "...wavelengths in nm..."
print
print "Start: ", L.start%
print "stoP: ", L.stop%
print "stEp: ", L.step%
print
print "Main menu"
print
input "Enter your choice: ", ch$ : ch$= lcase$(ch$)
select case ch$
case "s"
Input "New start wavelength: ", temp%
if temp% <> 0 then L.start% = temp%
case "p"
input "New stop wavelength: ", temp%
if temp% <> 0 then L.stop% = temp%
case "e"
input "New step between successive wavelengths: ",temp%
if temp% <> 0 then L.step% = temp%
case "m"

```

```

case else
  print chr$(7)
end select
if ch$ <> "m" then wave.menu
end sub

sub dim.matrix(num.lay%)
shared Mr(), Mi(), X(), T()
dim Mr(3,2,2) : dim Mi(3,2,2)          'real & imag matrices
dim x(0:num.lay%+1) : dim T(0:num.lay%+1) 'composition & thickness of layer
end sub

sub erase.matrix
shared Mr(),Mi(),X(),T()
erase Mr : erase Mi
erase X : erase T
end sub

sub individual.index(I.L%,I.X,I.N)
  II.menu:
  cls
  I.N = fnN.interpolate(I.L%,I.X)
  print "Calculates the index of refraction for a specific wavelength and mole"
  print "fraction of Al. The wavelength must be in the range 600 to 3000 nm."
  print
  print "Wavelength in nm: ";I.L%
  print "Mole-fraction X: ";I.X
  print
  print "... index: "; using "##.###"; I.N
  print
  print "Return to main menu"
  print
  input "Choice: ", ch$ : ch$ = lcase$(ch$)
  print
  print
  select case ch$
  case "w"
    input "Enter the new wavelength: ", temp%
    if temp% >= 600 and temp% <= 3000 then
      I.L% = temp%
    else
      print chr$(7)
    end if
  case "m"
    input "Enter the new mole-fraction X: ", temp
    if temp >= 0 and temp <= 1 then
      I.X = temp
    else
      print chr$(7)
    end if
  end select
end sub

```

```

    end if
case "r"
case else
    print chr$(7)
end select
if ch$ <> "r" then goto II.menu
end sub

sub data.files(df.name$,file.number%,file.flag$)
d.menu:
cls
print : print "Data file name: "; df.name$
print "Next file: "; file.number%
print "Enable/disable file saving. File saving is currently ";file.flag$
print "Main menu"
print : input "Enter your choice: ",ch$ : ch$ = lcase$(ch$)
select case ch$
case "e"
    if file.flag$="off" then
        file.flag$ = "on"
    else
        file.flag$ = "off"
    end if
case "d"
    Input "New file name: ", temp$
    if temp$ <> "" then df.name$ = temp$
case "n"
    input "Next file number: ",temp%
    if temp% <> 0 then file.number% = temp%
case "m"
case else
    print chr$(7)
end select
if ch$ <> "m" then d.menu
end sub

```

```

sub param.files
shared T(),X(),num.lay%,pf.name$,L.start%,L.stop%,L.step%
shared Lay.in$,comp.in$,lay.out$,comp.out$
loop.flag$ = "loop"
p.menu:
cls
print "PARAMETER FILE MENU"
print
print "Load file for parameters"
print "Save file"
print "Filename.REC: ",pf.name$+" .REC"
print
print "Main menu"

```

```

print : input "Choice: ",ch$ : ch$=lcase$(ch$)
Select case ch$
case "l"
  open pf.name$+".rec" for input as #1
  call erase.matrix
  input #1, num.lay%
  call dim.matrix(num.lay%)
  for i%=1 to num.lay% : input #1, T(i%) : next i%
  for i%=0 to num.lay%+1 : input #1, X(i%) : next i%
  input #1, L.start%, L.stop%, L.step%
  input #1, Lay.in$, comp.in$
  input #1, Lay.out$, comp.out$
  close #1
case "s"
  open pf.name$+".rec" for output as #1
  write #1, num.lay%
  for i%=1 to num.lay% : write #1, T(i%) : next i%
  for i%=0 to num.lay%+1 : write #1, X(i%) : next i%
  write #1, L.start%,L.stop%,L.step%
  write #1, Lay.in$,comp.in$
  write #1, Lay.out$,comp.out$
  close #1
case "f"
  cls : print "The present file name is "; pf.name$ : print
  input "Enter new name w/o extension: ", pf.name$
case "m"
  loop.flag$="no loop"
case else
  print chr$(7)
end select
if loop.flag$="loop" then goto p.menu
end sub

sub get.thickness( T(1), num.lay% )
label.t0:
cls
print "...thickness in nanometers..."
print
print "Input thickness of layers"
print "Edit specific layer"
print
print "Main Menu"
print
input "Choice: ",ch$ : ch$ = lcase$(ch$)
select case ch$
case "e"
  cls
  Input "Enter the layer number: ",edit.num%
  print : print "Layer ";edit.num%;" has thickness ";T(edit.num%)

```

```

print : print "New value: ",t.new%
if t.new% <> 0 then T(edit.num%)= t.new
case "i"
call thickness.entry(T(),num.lay%)
case "m"
case else
print chr$(7)
end select
if ch$ <> "m" then label.t0
end sub

sub thickness.entry(T(1),num.lay%)
return.flag$ = "off"
cls
print "THICKNESS DATA ENTRY: Layer 0 is the input layer"
print "... This routine can handle repeated layers: type 'start' after the"
print "initial layer of the group to be repeated; type 'stop' after the"
print "final layer in the group. When prompted, enter the number of"
print "ADDITIONAL copies to make."
print "...type 'quit' after a number to return to the menu..."
print
print "... Press return to retain the previous value..."
print
count%=0 : repeat.start% = 0 : repeat.stop% = 0
do while (count% < num.lay%) and (return.flag$ = "off")
count% = count% + 1
label.t1:
flag.t1$="off"
print "Layer "; count%; " ("; T(count%);") : ";
input "", T.new, repeat$ : repeat$=lcase$(repeat$)
if T.new <> 0 then T(count%)=T.new
select case repeat$
case "quit"
return.flag$ = "on"
case ""
case "start"
repeat.start% = count%
case "stop"
repeat.stop% = count%
if repeat.start% > repeat.stop% then
print chr$(7);"stop must be > start"
label.t1$ = "on"
end if
case else
print "Unexpected character encountered"
flag.t1$ = "on"
end select
if flag.t1$ = "on" then goto label.t1
if repeat$ = "stop" and return.flag$ = "off" then

```

```

label.t2:
flag.t2$ = "off"
input "Number of times to repeat the layers: ",n.rep%
if n.rep% < 0 then
print chr$(7)
flag.t2$ = "on"
end if
if flag.t2$ = "on" then label.t2
old.count% = count%
num.rep.lay% = repeat.stop% - repeat.start% + 1
for j% = 1 to n.rep%
for k% = 1 to num.rep.lay%
count% = count% + 1
big.entry% = (j% - 1) * i%
T(count%) = T(old.count% - num.rep.lay% + k%)
next k%
next j%
end if
loop
end sub

```

```

sub get.comp( x(1), num.lay% )
label.x0:
cls
print "COMPOSITION X of Al(x)Ga(1-x)As"
print
print "Input composition of layers"
print "Edit specific layer"
print
print "Main Menu"
print
input "Choice: ",ch$ : ch$ = lcase$(ch$)

select case ch$
case "e"
cls
Input "Enter the layer number: ",edit.num%
print : print "Layer ";edit.num%;" has Al mole-fraction X ";X(edit.num%)
print : input "New value: ",x.new%
if x.new% >= 0 and x.new% <= 1 then X(edit.num%)= X.new
case "i"
call composition.entry(X(),num.lay%)
case "m"
case else
print chr$(7)
end select
if ch$ <> "m" then label.x0
end sub

```

```

sub composition.entry(X(1),num.lay%)
return.flag$ = "off"
cls
print "COMPOSITION DATA ENTRY: Layer 0 is the 'input' layer."
print "... This routine can handle repeated layers: type 'start' after the"
print "initial layer of the group to be repeated; type 'stop' after the"
print "final layer in the group. When prompted, enter the number of"
print "ADDITIONAL copies to make."
print "... type 'quit' after the number to return to the main menu ..."
print
print "... Press return to retain the previous value ..."
print
count%=0 : repeat.start% = 0 : repeat.stop% = 0
do while count% < num.lay% and return.flag$ = "off"
count% = count% + 1
label.x1:
flag.x1$ = "off"
print "Layer "; count%; " ("; X(count%);") : ";
input "", X.new, repeat$
if x.new <> 0 then X(count%)=x.new
select case repeat$
case "quit"
return.flag$ = "on"
case ""
case "start"
repeat.start% = count%
case "stop"
repeat.stop% = count%
if repeat.start% > repeat.stop% then
print chr$(7); "stop must be > start"
flag.x1$ = "on"
end if
case else
print "Unexpected character encountered"
flag.x1$ = "on"
end select
if flag.x1$ = "on" then goto label.x1
if repeat$ = "stop" and return.flag$ = "off" then
label.x2:
flag.x2$ = "off"
input "Number of times to repeat the layers: ", n.rep%
if n.rep% < 0 then
print chr$(7)
flag.x2$ = "on"
end if
if flag.x2$ = "on" then label.x2
old.count% = count%
num.rep.lay% = repeat.stop% - repeat.start% + 1

```



```

for j% = 1 to n.rep%
  for k% = 1 to num.rep.lay%
    count% = count% + 1
    big.entry% = (j% - 1) * i%
    X(count%) = X(old.count% - num.rep.lay% + k%)
  next k%
next j%
end if
loop
end sub

sub num.layers(num.lay%)
cls
label.top:
print
print "There are ", num.lay%, " layers excluding the two ends"
print : input "Enter the new number: ", num.lay%
end sub

sub read.N.table
shared N.table()
dim n.table(10,11)
for i%=1 to 10 : for j%=1 to 11 : read N.table(i%,j%) : next j% : next i%
'==== REAL INDEX ====
' E=0.4 for x=0 to 1
  data 3.322,3.277,3.235,3.193,3.151,3.107,3.060,3.008,2.951,2.889,2.819
' E=0.6
  data 3.347,3.300,3.256,3.213,3.170,3.125,3.077,3.024,2.967,2.903,2.833
' E=0.8
  data 3.383,3.333,3.287,3.242,3.198,3.151,3.102,3.048,2.989,2.924,2.852
' E=1.000
  data 3.432,3.378,3.328,3.281,3.234,3.186,3.134,3.079,3.018,2.952,2.878
' E=1.200
  data 3.501,3.437,3.382,3.331,3.281,3.230,3.176,3.118,3.056,2.987,2.911
' E=1.400
  data 3.614,3.518,3.452,3.395,3.340,3.285,3.228,3.167,3.101,3.030,2.951
' E=1.600
  data 3.684,3.641,3.548,3.476,3.414,3.353,3.292,3.227,3.157,3.082,3.000
' E=1.800
  data 3.765,3.704,3.654,3.600,3.508,3.438,3.370,3.299,3.225,3.144,3.058
' E=2.000
  data 3.851,3.805,3.752,3.691,3.639,3.547,3.466,3.387,3.306,3.220,3.127
' E=2.200
  data 3.993,3.933,3.873,3.815,3.744,3.681,3.592,3.497,3.405,3.311,3.211
end sub

```

Chapter 18: Software for the Laser Reflectometer

This chapter contains software still under development but it gives excellent agreement with experiment for gas etches. It can be used for wet etches but the index of refraction of the etchant must be inserted. The software is similar to that in Chapter 17 except the complex index of refraction is included so as to account for absorption. This software can be easily modified to predict the possible modes within a Vertical Cavity Laser. To use the software for wet etches, the appropriate index of refraction must be included. **IMPORTANT NOTE:** A file called "parameter.rec" must be included in the default directory; this file can be empty on the first run.

```
' This program calculates the reflectivity vs etch depth for a wafer
' which is made up by layers of GaAs and AlGaAs. The relevant matrices are
' found in G.R. Fowles, Intro to Optics, 2nd ed. See
' pp 97-98. For a single layer, the matrix has the form
' row 1, col 1 = A = cos(kL)      row 1, col 2 = B = (-i/n)sin(kL)
' row 2, col 1 = C = (-i n)sin(kL) row 2, col 2 = D = cos(kL)
' where k = 2*pi*n/wavelength and n = index of the layer. Absorption is
' included by assuming that the index is of the form n=x+iy. Let
' n0=index of left cap, Nt=index of right cap, denom = A*N0 + B*Nt + C + D*Nt
' then r = (A*N0 + B*Nt*N0 - C - D*Nt)/denom = reflectivity = Erefl/Eincid
' t = 2*N0 / denom = transmissivity = Etrans/Eincid
' note that t can be larger than 1 if N0 > n since the optical energy in N0
' is stored in both the polarization and in Eincid. Energy conservation
' requires E to increase in n. This is equivalent to the E boundary conditions.
' Below: Mr,Mi are the re and im matrices with the A,B,C,D coefficients above.
' X contains the aluminum mole fractions, T contains the layer thicknesses
' file.flag$ says whether or not to write data to file. Num.lay% is
' the number of layers in the stack. Lay.in etc are the name of the input/output layers
' comp.in etc are the aluminum mole fraction of the input/output layers.
' file.number% is the extension for the data files. I.L etc are the wavelength
' al mole fraction, and index for the routine to separately calculate index
' for a specific layer. f$ and f2$ are for number formatting.
' --- version 1, M. A. Parker, A. Shapiro 1996
```

```
num.lay%=2 : pi=4*atn(1) : file.number% = 1 : file.flag$ = "off"
a$=date$ : lay.in$ = "air" : lay.out$ = "GaAs"
df.name$ = left$(a$,2) + mid$(a$,4,2) + right$(a$,2)
pf.name$ = "param" : g.type$ = "power" : graph.var$ = "reflected"
I.L% = 850 : I.X = 0.5 : I.N = 3.307
t.step% = 2 : L% = 670      ' L% is the wavelength
f$ = "#.##" : f2$ = "####"
version$="Version 1: M. A. Parker, A. Shapiro, Mar-Jul 1996"
```

```
call dim.matrix(num.lay%)
call read.N.table      'read real part of index of refract vs wavelength
call read.Y.table      'imaginary part of the index
call set.angle.0       'initialize transmitted angles - S()
```

```
cls
```

```

locate 5,1
print "This program calculates the reflectivity Al(x)Ga(1-x)As heterostructure"
print "as during either plasma or wet etches. The left most end cap is "
print "assumed to be the input layer. The right end is the ouput."
print : Print
Input "Press a key to continue ",ch$

main.menu:
cls
print "MAIN MENU: REFLECTANCE OF Al(x)Ga(1-x)As HETEROSTRUCTURE VS. ETCH
DEPTH"
print
print "Number of layers: (";num.lay%;") excluding the two ends"
print "Composition X of layers excluding the end caps"
print "Thickness of each layer"
print "Etch step: ";using f2$t.step%
print "Caps: specify end caps: input: ";lay.in$; : print " output: ";lay.out$
print
print "Wavelength ";using f2$L%; : print " nm"
print "Angle of incidence: "; ai%
print
print "Graph type: ";g.type$;" Variable: ";graph.var$
print "Starting depth: ";t.start%;" final depth: ";t.stop%
print
print "Parameter file name: "; pf.name$ + ".rec"
print "Data file name: "; df.name$ + "."; fnConvert$(file.number%);" File save is ";file.flag$
print
print "Index of refraction for a specific wavelength and mole-fraction"
print " wavelength: ";using f2$I.L%; : print " mole-fraction: "; using f$; I.X; : print "
index: ";
print using f$;I.N
print
print "Run: calculate reflection coefficient vs. etch depth"
print "Quit"
print
input "Enter your choice: ", ch$ : ch$ = lcase$(ch$)

select case ch$
case "ca"
call specify.io(lay.in$)
case "s"
call TotalDepth(T(), num.lay%, depth)
call zoom(depth, t.start%, t.stop%)
case "e"
call get.step(t.step%)
case "c"
call get.comp( x(), num.lay% )
case "n"
call num.layers(num.lay%)

```

```

call erase.matrix
call dim.matrix(num.lay%)
case "g"
call graph.related(g.type$,graph.var$)
case "t"
call get.thickness( T(), num.lay% )
call TotalDepth(T(), num.lay%, depth)
t.start% = 0 : t.stop% = depth
case "p"
call param.files
case "i"
call individual.index(I.L%,I.X,I.N)
case "d"
call data.files(df.name$,file.number%,file.flag$)
case "w"
call wavelength(L%)
case "a"
call get.trans.angle(L%,S(),num.lay%,ai%)
case "r"
screen 2 : cls
call label.graph
call main.routine(t.step%,num.lay%,L%,df.name$,file.number%)
if file.flag$ = "on" then file.number% = file.number% + 1
screen 2,0
case "q"
system
case else
print chr$(7)
end select
goto main.menu
end

```

```

sub main.routine(t.step%,num.lay%,L%,df.name$,file.number%)
shared Mr(),Mi(),X(),T(), pi, file.flag$,g.type$,graph.var$
shared lay.in$,lay.out$,comp.in,comp.out,t.start%,t.stop%,n.r,n.i
if file.flag$="on" then
ext$ = fnConvert$(file.number%)
file.number% = file.number% + 1
open "R" + df.name$ + "." + ext$ for output as #2
end if
z%=0:j%=1      'z-present etch depth, j-layer number

do until j%>num.lay%
first.time.flag% = 1
for t%=T(j%) to t.step% step -t.step%  ' t is thickness of top layer
aba$ = inkey$
if aba$ <> "" then goto loop1

if z%<t.start% then goto artloop  'zoom feature - allows to select

```

```

if z%>t.stop% then          'etch depth between t.start and t.stop
t%=t.step% : j%=num.lay%
end if

for row%=1 to 2 : for col%=1 to 2
Mr1(1,row%,col%) = fnMatrixReTop(t%,row%,col%,L%,j%) 'read in matrix for
Mi1(1,row%,col%) = fnMatrixImTop(t%,row%,col%,L%,j%) 'top layer - Mr1
next col% : next row%
if num.lay% = 1 or j%=num.lay% then
for row% = 1 to 2 : for col% = 1 to 2
Mr(1,row%,col%) = Mr1(1,row%,col%)
Mi(1,row%,col%) = Mi1(1,row%,col%)
next col% : next row%
goto jump.point
end if

if first.time.flag% = 1 or z%=t.start% then
first.time.flag% = 0
k%=j%+1
for row% = 1 to 2 : for col% = 1 to 2
Mr(0,row%,col%) = fnMatrixRe(row%,Col%,L%,k%)      'Mr(0 - second layer
Mi(0,row%,col%) = fnMatrixIm(row%,Col%,L%,k%)
next col% : next row%
if num.lay%=2 or j%=num.lay%-1 then goto loop3
for i% = k% to num.lay%
for row% = 1 to 2 : for col% = 1 to 2
Mr(2,row%,col%) = fnMatrixRe(row%,Col%,L%,i%+1)    'present bottom layer
Mi(2,row%,col%) = fnMatrixIm(row%,Col%,L%,i%+1)
next col% : next row%

for row% = 1 to 2 : for col% = 1 to 2
Mr(3,row%,col%) = 0
Mi(3,row%,col%) = 0
next col% : next row%

' multiply matrices with complex entries
for row% = 1 to 2 : for col% = 1 to 2 : for temp% = 1 to 2
Mr(3,row%,col%)= Mr(3,row%,col%)+Mr(0,row%,temp%)*Mr(2,temp%,col%) -
Mi(0,row%,temp%)*Mi(2,temp%,col%)
Mi(3,row%,col%)= Mi(3,row%,col%)+Mr(0,row%,temp%)*Mi(2,temp%,col%) +
Mi(0,row%,temp%)*Mr(2,temp%,col%)
next temp% : next col% : next row%

for row% = 1 to 2 : for col% = 1 to 2
Mr(0,row%,col%) = Mr(3,row%,col%)      'multiply all matrixes except for
Mi(0,row%,col%) = Mi(3,row%,col%)      'the top one and store in Mr(0,...
next col% : next row%
next i%
end if

```

```

loop3:
for row% = 1 to 2 : for col% = 1 to 2
  Mr(1,row%,col%) = 0          'store final result in Mr(1,...
  Mi(1,row%,col%) = 0
next col% : next row%

for row% = 1 to 2 : for col% = 1 to 2 : for temp% = 1 to 2
  Mr(1,row%,col%)= Mr(1,row%,col%)+Mr1(1,row%,temp%)*Mr(0,temp%,col%) -
  Mi1(1,row%,temp%)*Mi(0,temp%,col%)
  Mi(1,row%,col%)= Mi(1,row%,col%)+Mr1(1,row%,temp%)*Mi(0,temp%,col%) +
  Mi1(1,row%,temp%)*Mr(0,temp%,col%)
next temp% : next col% : next row%

jump.point:
' indexes for input and output layers - real
n.zero = fnN(L%,0) : n.r = fnN(L%,num.lay%+1) : n.i=-fnY(L%,num.lay%+1)
' calculate reflected component
num.r.re = Mr(1,1,1)*n.zero + Mr(1,1,2)*n.zero*n.r - Mi(1,1,2)*n.zero*n.i - Mr(1,2,1) -
Mr(1,2,2)*n.r+Mi(1,2,2)*n.i
num.r.im = Mi(1,1,1)*n.zero + Mi(1,1,2)*n.zero*n.r+Mr(1,1,2)*n.zero*n.i - Mi(1,2,1) -
Mi(1,2,2)*n.r-Mr(1,2,2)*n.i
den.r.re = Mr(1,1,1)*n.zero + Mr(1,1,2)*n.zero*n.r-Mi(1,1,2)*n.zero*n.i + Mr(1,2,1) +
Mr(1,2,2)*n.r-Mi(1,2,2)*n.i
den.r.im = Mi(1,1,1)*n.zero + Mi(1,1,2)*n.zero*n.r+Mr(1,1,2)*n.zero*n.i + Mi(1,2,1) +
Mi(1,2,2)*n.r+Mr(1,2,2)*n.i

r.re = fnDivRectReal(num.r.re,num.r.im,den.r.re,den.r.im)
r.im = fnDivRectImag(num.r.re,num.r.im,den.r.re,den.r.im)
num.t.re = 2*n.zero
num.t.im = 0
den.t.re = den.r.re
den.t.im = den.r.im
t.re = fnDivRectReal(num.t.re,num.t.im,den.t.re,den.t.im)
t.im = fnDivRectImag(num.t.re,num.t.im,den.t.re,den.t.im)
' calculate amplitude and phase of reflectivity and transmissivity
r.amplit = fnR2Pa(r.re,r.im)
r.phase = fnR2Pt(r.re,r.im)
transm = fnR2Pa(t.re,t.im)
t.phase = fnR2Pt(t.re,t.im)
if g.type$ = "power" then
  transm = (n.last/n.zero)*transm^2
  r.amplit = r.amplit^2
end if

select case graph.var$
case "reflected and transmitted"
case "reflected"
  transm = 0
case "transmitted"

```

```

    r.amplit = 0
  end select
  call graph.conc(j%,z%)
  call graph.amplitude((r.amplit),(transm),z%)
  if file.flag$ = "on" then
    write #2, z%, r.amplit
  end if
  artloop:
  z%=z%+t.step%
  next t%
  j%=j%+1
  loop
  loop1:
  aa$=inkey$ : if aa$ = "" then loop1
  close
end sub

sub specify.io(lay.in$)
io.menu:
cls
print "What material is in contact with the surface of the wafer?"
print
print "S: Switch between dry (air) and wet (water) etches. Present: "; lay.in$
print "Main menu"
print
input "Choice: ",ch$ : ch$=lcase$(ch$)
select case ch$
case "s"
  if lay.in$="air" then
    lay.in$="water"
  else
    lay.in$="air"
  end if
case "m"
case else
  print chr$(7)
end select
if ch$<>"m" then goto io.menu
end sub

sub zoom(depth, t.start%, t.stop%)          'define t.start and t.stop
cls
print
print "View entire etch from 0 to "; depth
print "Starting etch depth: "; t.start%
print "Final etch depth: "; t.stop%
print "Main menu"
print : print
input "Choice:",ch$ : ch$=lcase$(ch$)

```

```

select case ch$
case "v"
t.start%=0
t.stop%=depth
case "s"
print : print
Input "Enter starting depth: ",t.start%
case "f"
print : print
Input"Enter final depth: ", t.stop%
case "m"
case else
print chr$(7)
end select
end sub

sub graph.amplitude(y1,y2,z%)      'plot reflectivity vs depth
shared depth,t.stop%,t.start%
left.x% = 20 : right.x% = 619 : up.y% = 0 : down.y% = 190
x%=(600/(t.stop%-t.start%))*(z%-t.start%)+left.x%  'horizontal scale
' calculate vert and horiz scales
scale% = (down.y% - up.y%)/2
y1% = scale% * (2 - y1) : y2% = scale% * (2 - y2)    ' vertical scale
if x% = left.x% then
y1.old% = y1%
y2.old% = y2%
x.old% = left.x%
end if
line (x%,y1%) - (x.old%,y1.old%)
line (x%,y2%) - (x.old%,y2.old%)
y1.old% = y1% : y2.old% = y2% : x.old% = x%
end sub

sub graph.conc(j%,z%)             'plot aluminum mole fraction
shared X(),depth,t.stop%,t.start%
left.x% = 20 : right.x% = 619 : up.y% = 0 : down.y% = 190
x%=(600/(t.stop%-t.start%))*(z%-t.start%)+left.x%  'horizontal scal
scale% = (down.y% - up.y%)/2
y1% = scale% * (1-X(j%))        ' vertical scale
if x% = left.x% then
y1.old% = y1%
x.old% = left.x%
end if
line (x%,y1%) - (x.old%,y1.old%)
y1.old% = y1% : x.old% = x%
end sub

sub label.graph
shared g.type$, depth,t.stop%,t.start%

```



```

'Draw box and label axis
left.x% = 20 : right.x% = 619 : up.y% = 0 : down.y% = 190
Char.per.pix = 75/600
locate 1,1 : print 1; : locate 25,1 : print 0;
locate 12,1 : print 0; : locate 13,1 : print 1;
locate 18,1 : print "R";
locate 2,69 : print g.type$ + " R,T";
locate 6,1:print "X"
middle%=(down.y%-up.y%)/2
ver.step% = (down.y%-up.y%)/10 : hor.step% = 60
line (right.x%,down.y%)-(left.x%,up.y%),,B
line (left.x%,middle%)-(right.x%,middle%)
for i% = left.x% to right.x% step hor.step%
  line (i%,down.y%-4)-(i%,down.y%): line (i%,up.y%+4)-(i%,up.y%)
  line (i%,middle%-4)-(i%,middle%)
  axis.num = t.start%+(i%-20)*((t.stop%-t.start%)/600) 'no integer overflow so extra parens
  x.axis.pos% = 1+(i% - left.x%) * char.per.pix
  locate 25,x.axis.pos%
  print using "####"; axis.num;
next i%
for j% = up.y% to down.y% step ver.step%
  line (left.x%+5,j%)-(left.x%,j%) : line (right.x%,j%)-(right.x%-5,j%)
next j%
end sub

sub graph.related(g.type$,graph.var$)
g.r.label:
cls
print "MENU OF GRAPH RELATED ITEMS"
print
print "... variables to plot: ";graph.var$;" ..."
print "Both reflected and transmitted"
print "Reflected component only"
print "Transmitted component only"
print
print "Definition of reflectivity: ";g.type$
print
print "Main menu"
print
input "Choice: ",ch$ : ch$ = lcase$(ch$)
select case ch$
case "d"
  if g.type$ = "power" then
    g.type$ = "field"
  else
    g.type$ = "power"
  end if
case "b"
  graph.var$ = "reflected and transmitted"

```

```

case "r"
  graph.var$ = "reflected"
case "t"
  graph.var$ = "transmitted"
case "m"
case else
  print chr$(7)
end select
if ch$ <> "m" then g.r.label
end sub

```

```

def fnMatrixRe(row%,col%,L%,i%)                                'real matrix for successive layers
  shared T(),pi,S(),ai%
  n=fnN(L%,i%) : y=fnY(L%,i%) : k=cos(S(i%))*2*pi*T(i%)/L%      'index=n+i*y
  if row%=1 and col%=1 then
    fnMatrixRe = 0.5*cos(k*n)*(exp(k*y)+exp(-k*y))
  elseif row%=1 and col%=2 then
    fnMatrixRe = -0.5/(n^2+y^2)*(n*cos(k*n)*(exp(k*y)-exp(-k*y))-y*sin(k*n)*(exp(k*y)+exp(-
k*y)))
  elseif row%=2 and col%=1 then
    fnMatrixRe=-0.5*(n*cos(k*n)*(exp(k*y)-exp(-k*y))+y*sin(k*n)*(exp(k*y)+exp(-k*y)))
  elseif row%=2 and col%=2 then
    fnMatrixRe = 0.5*cos(k*n)*(exp(k*y)+exp(-k*y))
  end if
end def

```

```

def fnMatrixReTop(t%,row%,col%,L%,i%)                          'real matrix for successive
layers
  shared T(),pi,S(),ai%
  n=fnN(L%,i%) : y=fnY(L%,i%) : k=cos(S(i%))*2*pi*t%/L%      'index=n+i*y
  if row%=1 and col%=1 then
    fnMatrixReTop = 0.5*cos(k*n)*(exp(k*y)+exp(-k*y))
  elseif row%=1 and col%=2 then
    fnMatrixReTop = -0.5/(n^2+y^2)*(n*cos(k*n)*(exp(k*y)-exp(-k*y))-
y*sin(k*n)*(exp(k*y)+exp(-k*y)))
  elseif row%=2 and col%=1 then
    fnMatrixReTop=-0.5/cos(pi/180*ai%)*(n*cos(k*n)*(exp(k*y)-exp(-
k*y))+y*sin(k*n)*(exp(k*y)+exp(-k*y)))
  elseif row%=2 and col%=2 then
    fnMatrixReTop = 0.5/cos(pi/180*ai%)*cos(k*n)*(exp(k*y)+exp(-k*y))
  end if
end def

```

```

def fnMatrixIm(row%,col%,L%,i%)                                'imaginary matrix for successive layers
  shared T(),pi,S(),ai%
  n=fnN(L%,i%) : y=fnY(L%,i%) : k=cos(S(i%))*2*pi*T(i%)/L%
  if row%=1 and col%=1 then

```

```

    fnMatrixIm = 0.5*sin(k*n)*(exp(k*y)-exp(-k*y))
elseif row%=1 and col%=2 then
    fnMatrixIm = -0.5/(n^2+y^2)*(n*sin(k*n)*(exp(k*y)+exp(-k*y))+y*cos(k*n)*(exp(k*y)-exp(-k*y)))
elseif row%=2 and col%=1 then
    fnMatrixIm=-0.5*(n*sin(k*n)*(exp(k*y)+exp(-k*y))-y*cos(k*n)*(exp(k*y)-exp(-k*y)))
elseif row%=2 and col%=2 then
    fnMatrixIm = 0.5*sin(k*n)*(exp(k*y)-exp(-k*y))
end if
end def

```

```

def fnMatrixImTop(t%,row%,col%,L%,i%)                                'imaginary matrix for
successive layers
shared T(),pi,S(),ai%
n=fnN(L%,i%) : y=fnY(L%,i%) : k=cos(S(i%))*2*pi*t%/L%
if row%=1 and col%=1 then
    fnMatrixImTop = 0.5*sin(k*n)*(exp(k*y)-exp(-k*y))
elseif row%=1 and col%=2 then
    fnMatrixImTop = -0.5/(n^2+y^2)*(n*sin(k*n)*(exp(k*y)+exp(-k*y))+y*cos(k*n)*(exp(k*y)-exp(-k*y)))
elseif row%=2 and col%=1 then
    fnMatrixImTop=-0.5/cos(pi/180*ai%)*(n*sin(k*n)*(exp(k*y)+exp(-k*y))-y*cos(k*n)*(exp(k*y)-exp(-k*y)))
elseif row%=2 and col%=2 then
    fnMatrixImTop = 0.5/cos(pi/180*ai%)*sin(k*n)*(exp(k*y)-exp(-k*y))
end if
end def

```

```

sub Totaldepth( T(1), num.lay%, depth) 'calculates total depth
depth=0
for q%=1 to num.lay%
    depth=T(q%)+depth
next q%
end sub

```

```

def fnN( L%,i% )                                ' real index from interpolation routine
shared X(), num.lay%
shared lay.in$,lay.out$,comp.in
select case i%
case 0
    if lay.in$="air" then
        fnN = 1
    else
        fnN = 1.3
    end if
case <= num.lay%
    fnN = fnN.interpolate(L%,X(i%))
case > num.lay%
    fnN = fnN.interpolate(L%,0)

```

```

end select
end def

```

```

def fnY( L%,i% )                                ' imaginary index from interpolation routine
shared X(), num.lay%
shared lay.in$,lay.out$,comp.in
select case i%
case 0
  fnY = 0
case <= num.lay%
  fnY = -fnY.interpolate(L%,X(i%))
case > num.lay%
  fnY = -fnY.interpolate(L%,0)
end select
end def

```

```

def fnN.interpolate(L%,X.comp)                  ' interp routine for real index of refract
shared N.table
E = 1245/L%
row= E/0.2 - 1 : col = 1 + 10 * X.comp
row.base% = int(row) : row.fract = row - row.base%
col.base% = int(col) : col.fract = col - col.base%
if row.base% = 14 then
  row.base% = 13
  row.fract = 1
end if
if col.base% = 11 then
  col.base% = 10
  col.fract = 1
end if
n.col1.dif = N.table(row.base%+1,col.base%)-N.table(row.base%,col.base%)
n.col2.dif = N.table(row.base%+1,col.base%+1)-N.table(row.base%,col.base%+1)
n1 = N.table(row.base%,col.base%) + row.fract * n.col1.dif
n2 = N.table(row.base%,col.base%+1) + row.fract * n.col2.dif
fnN.interpolate = n1 + col.fract * (n2 - n1)
end def

```

```

def fnY.interpolate(L%,X.comp)                  ' interp routine for imaginary part of index of
refract
shared Y.table
E = 1245/L%
row= E/0.2 - 1 : col = 1 + 10 * X.comp
row.base% = int(row) : row.fract = row - row.base%
col.base% = int(col) : col.fract = col - col.base%
if row.base% = 14 then
  row.base% = 13
  row.fract = 1
end if
if col.base% = 11 then

```

```

col.base% = 10
col.fract = 1
end if
n.col1.dif = Y.table(row.base%+1,col.base%) -Y.table(row.base%,col.base%)
n.col2.dif = Y.table(row.base%+1,col.base%+1)-Y.table(row.base%,col.base%+1)
n1 = Y.table(row.base%,col.base%) + row.fract * n.col1.dif
n2 = Y.table(row.base%,col.base%+1) + row.fract * n.col2.dif
fnY.interpolate = n1 + col.fract * (n2 - n1)
end def

def FNconvert$(num.in%)
old.num% = 0 : a$ = ""
for i% = 1 to 3
new.num% = int(num.in% / 10^(3-i%))
a% = new.num% - 10 * old.num%
old.num% = new.num%
a$ = a$ + chr$(48 + a%)
next i%
FNconvert$ = a$
end def

def fnMultRectReal(Ax,Ay,Bx,By)
fnMultRectReal = Ax*Bx - Ay*By
end def

def fnMultRectImag(Ax,Ay,Bx,By)
fnMultRectImag = Ax*By + Ay*Bx
end def

def fnDivRectReal(Ax,Ay,Bx,By)
fnDivRectReal = (Ax*Bx + Ay*By) / (Bx^2 + By^2)
end def

def fnDivRectImag(Ax,Ay,Bx,By)
fnDivRectImag = (Ay*Bx - Ax*By) / (Bx^2 + By^2)
end def

def fnR2Pa(Cx,Cy)
fnR2Pa = sqr(Cx^2+Cy^2)
end def

def fnR2Pt(Cx,Cy)
shared pi
select case Cx
case = 0
select case Cy
case >0
fnR2Pt=pi
case <0

```

' calculates data file extens

```

    fnR2Pt=(3/2)*pi
case =0
    fnR2Pt =0
end select
case >0
if Cy >= 0 then
    fnR2Pt=atn(Cy/Cx)
else
    fnR2Pt= 2*pi + atn(Cy/Cx)
end if
case <0
    fnR2Pt=pi+atn(Cy/Cx)
end select
end def

```

```

def fnP2Rx(a,t)
fnP2Rx = a*cos(t)
end def

```

```

def fnP2Ry(a,t)
fnP2Ry = a*sin(t)
end def

```

```

def fnMamp(A1,t1,A2,t2)
fnMamp=A1*A2
end def

```

```

def fnMarg(A1,t1,A2,t2)
shared pi
sum.arg = t1 + t2
if sum.arg >= 2*pi then sum.arg =sum.arg - 2*pi
if sum.arg <=-2*pi then sum.arg =sum.arg + 2*pi
fnMarg = sum.arg
end def

```

```

sub get.step(t.step%)
cls
Input "Enter etch step in nm (must be integer): ",t.step%
end sub

```

```

sub wavelength(L%)
cls : print : print
input "Enter wavelength: ", L%
end sub

```

```

sub dim.matrix(num.lay%)
shared Mr1(), Mi1(), Mr(), Mi(), X(), T(),S()
dim Mr(3,2,2) : dim Mi(3,2,2)
dim Mr1(3,2,2) : dim Mi1(3,2,2)      'real & imag matrices

```

```

dim X(0:num.lay%+1) : dim T(0:num.lay%+1) 'composition & thickness of layer
dim S(0:num.lay%+1)
end sub

```

```

sub erase.matrix
shared Mr(),Mi(),X(),T(),S()
erase Mr : erase Mi
erase S : erase X : erase T
end sub

```

```

sub individual.index(I.L%,I.X,I.N)
II.menu:
cls
I.N = fnN.interpolate(I.L%,I.X)
print "Calculates the index of refraction for a specific wavelength and mole"
print "fraction of Al. The wavelength must be in the range 600 to 3000 nm."
print
print "Wavelength in nm: ";I.L%
print "Mole-fraction X: ";I.X
print
print "... index: "; using "##.###"; I.N
print
print "Return to main menu"
print
input "Choice: ", ch$ : ch$ = lcase$(ch$)
print
print
select case ch$
case "w"
input "Enter the new wavelength: ", temp%
if temp% >= 600 and temp% <= 3000 then
I.L% = temp%
else
print chr$(7)
end if
case "m"
input "Enter the new mole-fraction X: ", temp
if temp >= 0 and temp <= 1 then
I.X = temp
else
print chr$(7)
end if
case "r"
case else
print chr$(7)
end select
if ch$ <> "r" then goto II.menu
end sub

```

```

sub data.files(df.name$,file.number%,file.flag$)
d.menu:
cls
print "... data is saved in files as etch depth, reflectance ..."
print : print "Data file name: "; df.name$
print "Next file: "; file.number%
print "Enable/disable file saving. File saving is currently ";file.flag$
print "Main menu"
print : input "Enter your choice: ",ch$ : ch$ = lcase$(ch$)
select case ch$
case "e"
if file.flag$="off" then
file.flag$ = "on"
else
file.flag$ = "off"
end if
case "d"
Input "New file name: ", temp$
if temp$ <> "" then df.name$ = temp$
case "n"
input "Next file number: ",temp%
if temp% <> 0 then file.number% = temp%
case "m"
case else
print chr$(7)
end select
if ch$ <> "m" then d.menu
end sub

```

```

sub param.files
shared T(),X(),num.lay%,pf.name$
shared L%,t.step%,t.start%,t.stop%
loop.flag$ = "loop"
p.menu:
cls
print "PARAMETER FILE MENU"
print
print "Load file for parameters"
print "Save file"
print "Filename.REC: ",pf.name$+".REC"
print
print "Main menu"
print : input "Choice: ",ch$ : ch$=lcase$(ch$)
Select case ch$
case "1"
open pf.name$+".rec" for input as #1
call erase.matrix
input #1, L%
input #1, t.start%

```



```

input #1, t.stop%
input #1, t.step%
input #1, num.lay%
call dim.matrix(num.lay%)
for i%=1 to num.lay%+1 : input #1, S(i%) : next i%
for i%=1 to num.lay% : input #1, T(i%) : next i%
for i%=0 to num.lay%+1 : input #1, X(i%) : next i%
close #1
case "s"
open pf.name$+".rec" for output as #1
write #1, L%
write #1, t.start%
write #1, t.stop%
write #1, t.step%
write #1, num.lay%
for i%=1 to num.lay%+1 : write #1, S(i%) : next i%
for i%=1 to num.lay% : write #1, T(i%) : next i%
for i%=0 to num.lay%+1 : write #1, X(i%) : next i%
close #1
case "f"
cls : files "*.rec"
print "The present file name is "; pf.name$ : print
input "Enter new name w/o extension: ", pf.name$
case "m"
loop.flag$="no loop"
case else
print chr$(7)
end select
if loop.flag$="loop" then goto p.menu
end sub

sub get.trans.angle(L%,S(1),num.lay%,ai%)
shared pi
cls
input "Enter the angle of incidence in degrees: ",ai%
x=(fnN(L%,0)*sin(pi*ai%/180)/fnN(L%,1))
S(1)=atn((x^2/(1-x^2))^0.5)
for i%=2 to num.lay%+1
y=(fnN(L%,i%-1)*sin(S(i%-1))/fnN(L%,i%))
S(i%)=atn((y^2/(1-y^2))^0.5)
next i%
goto main.menu
end sub

sub set.angle.0
shared S()
for i%=0 to num.lay%+1
S(i%)=0
next i%

```

end sub

```
sub get.thickness( T(1), num.lay% )
label.t0:
cls
print "...thickness in nanometers..."
print
print "Input thickness of layers"
print "Edit specific layer"
print
print "Main Menu"
print
input "Choice: ",ch$ : ch$ = lcase$(ch$)
select case ch$
case "e"
cls
Input "Enter the layer number: ",edit.num%
print : print "Layer ";edit.num%;" has thickness ";T(edit.num%)
print : print "New value: ",t.new%
if t.new% <> 0 then T(edit.num%)= t.new
case "i"
call thickness.entry(T(),num.lay%)
case "m"
case else
print chr$(7)
end select
if ch$ <> "m" then label.t0
end sub
```

```
sub thickness.entry(T(1),num.lay%)
return.flag$ = "off"
cls
print "THICKNESS DATA ENTRY: Layer 0 is the input layer"
print "... This routine can handle repeated layers: type 'start' after the"
print "initial layer of the group to be repeated; type 'stop' after the"
print "final layer in the group. When prompted, enter the number of"
print "ADDITIONAL copies to make."
print "...type 'quit' after a number to return to the menu..."
print
print "... Press return to retain the previous value..."
print
print "... ALL VALUES IN NANOMETERS..."
PRINT
count%=0 : repeat.start% = 0 : repeat.stop% = 0
do while (count% < num.lay%) and (return.flag$ = "off")
count% = count% + 1
label.t1:
flag.t1$="off"
print "Layer "; count%; " ("; T(count%);") : ";
```

```

input "", T.new, repeat$ : repeat$=lcase$(repeat$)
if T.new <> 0 then T(count%)=T.new
select case repeat$
case "quit"
return.flag$ = "on"
case ""
case "start"
repeat.start% = count%
case "stop"
repeat.stop% = count%
if repeat.start% > repeat.stop% then
print chr$(7);"stop must be > start"
label.t1$ = "on"
end if
case else
print "Unexpected character encountered"
flag.t1$ = "on"
end select
if flag.t1$ = "on" then goto label.t1
if repeat$ = "stop" and return.flag$ = "off" then
label.t2:
flag.t2$ = "off"
input "Number of times to repeat the layers: ",n.rep%
if n.rep% < 0 then
print chr$(7)
flag.t2$ = "on"
end if
if flag.t2$ = "on" then label.t2
old.count% = count%
num.rep.lay% = repeat.stop% - repeat.start% + 1
for j% = 1 to n.rep%
for k% = 1 to num.rep.lay%
count% = count% + 1
big.entry% = (j% - 1) * i%
T(count%) = T(old.count% - num.rep.lay% + k%)
next k%
next j%
end if
loop
end sub

sub get.comp( x(1), num.lay% )
label.x0:
cls
print "COMPOSITION X of Al(x)Ga(1-x)As"
print
print "Input composition of layers"
print "Edit specific layer"
print

```

```

print "Main Menu"
print
input "Choice: ",ch$ : ch$ = lcase$(ch$)
select case ch$
case "e"
cls
Input "Enter the layer number: ",edit.num%
print : print "Layer ";edit.num%;" has A1 mole-fraction X ";X(edit.num%)
print : input "New value: ",x.new%
if x.new% >= 0 and x.new% <= 1 then X(edit.num%)= X.new
case "i"
call composition.entry(X(),num.lay%)
case "m"
case else
print chr$(7)
end select
if ch$ <> "m" then label.x0
end sub

```

```

sub composition.entry(X(1),num.lay%)
return.flag$ = "off"
cls
print "COMPOSITION DATA ENTRY: Layer 0 is the 'input' layer."
print "... This routine can handle repeated layers: type 'start' after the"
print "initial layer of the group to be repeated; type 'stop' after the"
print "final layer in the group. When prompted, enter the number of"
print "ADDITIONAL copies to make."
print "... type 'quit' after the number to return to the main menu ..."
print
print "... Press return to retain the previous value ..."
print
count%=0 : repeat.start% = 0 : repeat.stop% = 0
do while count% < num.lay% and return.flag$ = "off"
count% = count% + 1
label.x1:
flag.x1$ = "off"
print "Layer "; count%; " ("; X(count%);") : ";
input "", X.new, repeat$
if x.new <> 0 then X(count%)=x.new
select case repeat$
case "quit"
return.flag$ = "on"
case ""
case "start"
repeat.start% = count%
case "stop"
repeat.stop% = count%
if repeat.start% > repeat.stop% then
print chr$(7);"stop must be > start"

```

```

    flag.x1$ = "on"
  end if
case else
  print "Unexpected character encountered"
  flag.x1$ = "on"
end select
if flag.x1$ = "on" then goto label.x1
if repeat$ = "stop" and return.flag$ = "off" then
  label.x2:
  flag.x2$ = "off"
  input "Number of times to repeat the layers: ",n.rep%
  if n.rep% < 0 then
    print chr$(7)
    flag.x2$ = "on"
  end if
  if flag.x2$ = "on" then label.x2
  old.count% = count%
  num.rep.lay% = repeat.stop% - repeat.start% + 1
  for j% = 1 to n.rep%
    for k% = 1 to num.rep.lay%
      count% = count% + 1
      big.entry% = (j% - 1) * i%
      X(count%) = X(old.count% - num.rep.lay% + k%)
    next k%
  next j%
end if
loop
end sub

sub num.layers(num.lay%)
cls
label.top:
print
print "There are ", num.lay%, " layers excluding the two ends"
print : input "Enter the new number: ", num.lay%
end sub

sub read.N.table
shared N.table()
dim n.table(10,11)
for i%=1 to 10 : for j%=1 to 11 : read N.table(i%,j%) : next j% : next i%
'==== REAL INDEX ====
' E=0.4 for x=0 to 1
  data 3.322,3.277,3.235,3.193,3.151,3.107,3.060,3.008,2.951,2.889,2.819
' E=0.6
  data 3.347,3.300,3.256,3.213,3.170,3.125,3.077,3.024,2.967,2.903,2.833
' E=0.8
  data 3.383,3.333,3.287,3.242,3.198,3.151,3.102,3.048,2.989,2.924,2.852
' E=1.000

```

```

data 3.432,3.378,3.328,3.281,3.234,3.186,3.134,3.079,3.018,2.952,2.878
'E=1.200
data 3.501,3.437,3.382,3.331,3.281,3.230,3.176,3.118,3.056,2.987,2.911
'E=1.400
data 3.614,3.518,3.452,3.395,3.340,3.285,3.228,3.167,3.101,3.030,2.951
'E=1.600
data 3.684,3.641,3.548,3.476,3.414,3.353,3.292,3.227,3.157,3.082,3.000
'E=1.800
data 3.765,3.704,3.654,3.600,3.508,3.438,3.370,3.299,3.225,3.144,3.058
'E=2.000
data 3.851,3.805,3.752,3.691,3.639,3.547,3.466,3.387,3.306,3.220,3.127
'E=2.200
data 3.993,3.933,3.873,3.815,3.744,3.681,3.592,3.497,3.405,3.311,3.211
end sub

```

```

sub read.Y.table
shared Y.table()
dim Y.table(10,11)
for i%=1 to 10 : for j%=1 to 11 : read Y.table(i%,j%) : next j% : next i%
'==== Imaginary INDEX =====
'E=0.4 for x=0 to 1
data 0,0,0,0,0,0,0,0,0,0,0
'E=0.6
data 0,0,0,0,0,0,0,0,0,0,0
'E=0.8
data 0,0,0,0,0,0,0,0,0,0,0
'E=1.0
data 0,0,0,0,0,0,0,0,0,0,0
'E=1.2
data 0,0,0,0,0,0,0,0,0,0,0
'E=1.4
data 0,0,0,0,0,0,0,0,0,0,0
'E=1.6
data 0.097,0.050,0,0,0,0,0,0,0,0,0
'E=1.8
data 0.180,0.130,0.057,0,0,0,0,0,0,0,0
'E=2.0
data 0.260,0.206,0.145,0.111,0.075,0,0,0,0,0,0
'E=2.2
data 0.352,0.305,0.255,0.202,0.150,0.108,0.051,0.041,0,0,0
end sub

```

Chapter 19: Software for the Tencor Instruments Alpha Step 200

```
Start.prog:
cls
print "This program converts data from the alpha stepper to a format suitable"
print "for math cad. A large data file with data from a large number of scans"
print "can be converted to multiple files or one single file. The program"
print "assumes 400 micron scans with 1 point per micron. The data will be"
print "written in ANGSTROMS."
print
Print "Separate files can be extracted: "
print " extensions of .001 .002 ... will be assigned"
print "One large file can be made with an extension of DAT"
print : input "Single or Multiple files <s or m>? ", an$
an$ = lcase$(an$)
if an$ <> "s" and an$ <> "m" then start.prog
print
input "Enter input file EXT: ", ext.in$
input "Enter path and filename: ", file.name$
file.name.in$ = file.name$ + "." + ext.in$

'----- count the number of files -----
open file.name.in$ for input as #1
num.downloads% = 0

do until EOF(1)
input #1, data.line$
a$ = mid$(data.line$,5,5)
if a$ = "-----" then num.downloads% = num.downloads% + 1
loop
close #1
print : print "There will be "; num.downloads%;
select case an$
case "m"
print " separate files."
case "s"
print " scan in a single file."
end select
open file.name.in$ for input as #1
for file.num% = 1 to num.downloads%
select case an$
case "m"
file.out$ = file.name$ + "." + FNconvert$(file.num%)
print "Now writing "; file.out$
open file.out$ for output as #2
case "s"
if file.num% = 1 then
file.out$ = file.name$ + "." + "dat"
```

```

print "Now writing "; file.out$
open file.out$ for output as #2
end if
end select

for row%=1 to 13
input #1, data.line$
next row%

for row% = 0 to 39
input #1, data.line$
if row% = 0 then data.line$ = "0" + data.line$
data.length% = len(data.line$) - 9
data.line$ = right$(data.line$,data.length%)

for column%=1 to 10
data.value$ = left$(data.line$,7)
data.length% = data.length%-7
data.line$ = right$(data.line$,data.length%)
data.value% = 1000 * val(data.value$)
write #2, data.value%
next column%
next row%

input #1, a$, a$
if an$ = "m" then close #2
next file.num%

close
print : Print "Finished with "; num.downloads%;" scans."
print : input "Another file <y or n>? ", ans$
ans$=lcase$(ans$)
if ans$ = "y" then start.prog

end

def FNconvert$(num.in%)
old.num% = 0 : a$ = ""
for i% = 1 to 3
new.num% = int(num.in% / 10^(3-i%))
a% = new.num% - 10 * old.num%
old.num% = new.num%
a$ = a$ + chr$(48 + a%)
next i%
FNconvert$ = a$
end def

sub press.key
label1:

```



```
a$ = inkey$  
if a$ = "" then label1  
end sub
```

```
end
```

Chapter 20: Software for Complex Number Arithmetic

Some of the routines in this section are used in the software listed in Chapters 17 and 18. In addition, it is useful for small pocket sized DOS machines, such as the HP 200 LX palm-top computer.

```
dim A(2),B(2),C(2),M(2)
pi = 4*atn(1)
RD$="deg" : rd = 1
ND%=3 : f$="+#.###^"^^"
```

main.menu:

```
cls
print "X1 = (";using f$;A(1); : print ",";using f$;A(2); : print ")";
print " X2 = (";using f$;B(1); : print ",";using f$;B(2); : print ")"
print "Res= (";using f$;C(1); : print ",";using f$;C(2); : print ")";
print " Mem= (";using f$;M(1); : print ",";using f$;M(2); : print ")"
print
Print "1,2      Enter X1 or X2"
print "U ..... Units: Radians or degrees: "; rd$
print "P,R/1,2   Make Polar or Rectangular form for 1 or 2"
print "S12 ..... Switch X1 with X2"
print "SR/1,2,M   Switch results with X1, X2 or memory"
print "A ..... Add (X1,Y1)+(X2,Y2)"
print "S        Subtract (X1,Y1)-(X2,Y2)"
print "RM,D ..... Rectangular Multiply X1*X2 or Divide X1/X2"
print "PM,D      Polar Multiply X1*X2 or Divide X1/X2"
print "M/S,R/1,2,R Memory Store or Recall slot 1,2 or R"
print "N        Number of digits after the decimal point"
print
print "Q        Quit"
print : input "Choice: ",ch$ : ch$=lcase$(ch$)
```

select case ch\$

case "1"

cls

input "Enter X1: ",A(1)

input "Enter Y1: ",A(2)

case "2"

cls

input "Enter X2: ",B(1)

input "Enter Y2: ",B(2)

case "p1"

C(1)=fnR2Pa(A(1),A(2))

C(2)=fnR2Pt(A(1),A(2))

Case "r1"

C(1)=fnP2Rx(A(1),A(2))

C(2)=fnP2Ry(A(1),A(2))

```

case "p2"
  C(1)=fnR2Pa(B(1),B(2))
  C(2)=fnR2Pt(B(1),B(2))
Case "r2"
  C(1)=fnP2Rx(B(1),B(2))
  C(2)=fnP2Ry(B(1),B(2))
case "s12"
  temp1 = B(1) : B(1)=A(1) : A(1) = temp1
  temp2 = B(2) : B(2)=A(2) : A(2) = temp2
case "sr1"
  temp1 = c(1) : c(1)=a(1) : A(1) = temp1
  temp2 = c(2) : c(2)=a(2) : A(2) = temp2
case "sr2"
  temp1 = c(1) : c(1)=B(1) : B(1) = temp1
  temp2 = c(2) : c(2)=B(2) : B(2) = temp2
case "srm"
  temp1 = C(1) : C(1)=M(1) : M(1) = temp1
  temp2 = C(2) : C(2)=M(2) : M(2) = temp2
case "rm"
  C(1)=fnMultRectReal(A(1),A(2),B(1),B(2))
  C(2)=fnMultRectImag(A(1),A(2),B(1),B(2))
case "rd"
  c(1)=fnDivRectReal(A(1),A(2),B(1),B(2))
  c(2)=fnDivRectImag(A(1),A(2),B(1),B(2))
case "pm"
  c(1)=fnMamp(A(1),A(2),B(1),B(2))
  c(2)=fnMarg(A(1),A(2),B(1),B(2))
case "pd"
  c(1)=fnDamp(A(1),A(2),B(1),B(2))
  c(2)=fnDarg(A(1),A(2),B(1),B(2))
case "a"
  c(1)=A(1)+B(1)
  c(2)=A(2)+B(2)
case "s"
  c(1)=A(1)-B(1)
  c(2)=A(2)-B(2)
case "u"
  if RD$ = "deg" then
    RD$ = "rad"
    rd = 0
  else
    RD$="deg"
    rd=1
  end if
case "ms1"
  M(1) = A(1) : M(2) = A(2)
case "ms2"
  M(1) = B(1) : M(2) = B(2)
case "msr"

```

```

M(1) = C(1) : M(2) = C(2)
case "mr1"
  A(1) = M(1) : A(2) = M(2)
case "mr2"
  B(1) = M(1) : B(2) = M(2)
case "mrr"
  C(1) = M(1) : C(2) = M(2)
case "n"
  cls : input "Number of digits: ",ND%
  if ND% < 1 then Nd% = 1
  if ND% > 8 then ND% = 8
  f$ = fnDig$(ND%)
case "q"
  system
case else
  print chr$(7)
end select
goto main.menu
end

```

```

def fnDig$(ND%)
  temp$ = ""
  if ND% < 1 then ND% = 1
  for i% = 1 to ND%
    temp$ = temp$ + "#"
  next i%
  fnDig$ = "+#." + temp$ + "^^^^"
end def

```

```

def fnDamp(Ax,Ay,Bx,By)
  If Bx <> 0 then
    fnDamp = Ax/Bx
  else
    fnDamp=0
  print chr&(7)
  end if
end def

```

```

def fnDarg(Ax,Ay,Bx,By)
  shared pi,RD
  dif = (Ay-By) * (pi/180)^rd
  if dif >= 2*pi then dif = dif - 2*pi
  if dif <= -2*pi then dif = dif + 2*pi
  fnDarg = dif * (180/pi)^rd
end def

```

```

def fnMultRectReal(Ax,Ay,Bx,By)
  fnMultRectReal = Ax*Bx - Ay*By
end def

```

```

def fnMultRectImag(Ax,Ay,Bx,By)
  fnMultRectImag = Ax*By + Ay*Bx
end def

def fnDivRectReal(Ax,Ay,Bx,By)
  fnDivRectReal = (Ax*Bx + Ay*By) / (Bx^2 + By^2)
end def

def fnDivRectImag(Ax,Ay,Bx,By)
  fnDivRectImag = (Ay*Bx - Ax*By) / (Bx^2 + By^2)
end def

def fnR2Pa(Cx,Cy)
  fnR2Pa = sqrt(Cx^2+Cy^2)
end def

def fnR2Pt(Cx,Cy)
  shared pi,rd
  select case Cx
  case = 0
    select case Cy
    case >0
      fnR2Pt=pi * (180/pi)^rd
    case <0
      fnR2Pt=(3/2) * pi * (180/pi)^rd
    case =0
      fnR2Pt =0
    end select
  case >0
    if Cy >= 0 then
      fnR2Pt=(atn(Cy/Cx))*(180/pi)^rd
    else
      fnR2Pt= ( 2*pi + atn(Cy/Cx) ) * (180/pi)^rd
    end if
  case <0
    fnR2Pt= (pi+atn(Cy/Cx)) * (180/pi)^rd
  end select
end def

def fnP2Rx(a,t)
  shared rd, pi
  arg1 = t* (pi/180)^rd
  fnP2Rx = a*cos(arg1)
end def

def fnP2Ry(a,t)
  shared rd,pi
  arg1 = t * (pi/180)^rd

```

```
fnP2Ry = a*sin(arg1)
end def
```

```
def fnMamp(A1,t1,A2,t2)
  fnMamp=A1*A2
end def
```

```
def fnMarg(A1,t1,A2,t2)
  shared pi,rd
  sum.arg = (t1+t2)*(pi/180)^rd
  if sum.arg >= 2*pi then sum.arg=sum.arg-2*pi
  if sum.arg <= -2*pi then sum.arg=sum.arg+2*pi
  fnMarg= sum.arg * (180/pi)^rd
end def
```

Chapter 21: Software for an 8 Bit Analogue to Digital Converter

The software reads the A-D circuit and plots the data in real time. The A-D is the 8-bit chip from TI. The data is transferred through the parallel port on an IBM compatible computer.

```
call initial.conditions(sens%,offset,delta.t,filename$,num.files%,pb%)
key off

do
cls
print : print
print tab(12);"ANALOG TO DIGITAL CONVERTER AND DATA COLLECTION" : print
print tab (25); "NEXT FILE: "; filename$ : print : print
print tab(20);"Sensitivity (full scale): ";sens%
print tab(20);"Offset "; offset
print tab(20);"Interval in seconds: ";: print using "###.###";delta.t
print tab(20);"Push button active: "; : if pb%=1 then print "ON" else print "OFF"
print tab(20);"Test"
print tab(20);"Data"
print tab(20);"Quit"
print : print tab(15); "Enter first letter of your choice ..."
call push.key(ch$)

ch$=lcase$(ch$)

select case ch$
case "s" : call sens(sens%)
case "o" : call off.set(offset)
case "i" : call time.routine(delta.t)
case "d"
call collect.data(sens%,offset,delta.t,pb%,filename$,num.files%,ch$)
call file.name (filename$,num.files%)
case "t" : call collect.data(sens%,offset,delta.t,pb%,filename$,num.files%,ch$)
case "p" : call set.push.button(pb%)
case "q"
case else : print chr$(7)
end select

loop until (ch$ = "q")
end

sub file.name(filename$, num.files%)
incr num.files%
ext$ = str$(num.files%) : ext$ = mid$(ext$,2,3)
t.date$=date$
t.date$=left$(t.date$,2)+mid$(t.date$,4,2)+right$(t.date$,2)
filename$= "ad" + t.date$ + "." + ext$
end sub
```

```

sub initial.conditions(sens%,offset,delta.t,filename$,num.files%,pb%)
num.files% = 0
sens% = 100
offset = 0
delta.t = 0.5
call file.name(filename$,num.files%)
pb% = 1 'press red button to start and stop
screen 2
end sub

```

```

sub sens(sens%)
do
flag% = 0
cls
input "Enter full scale sensitivity (50, 100, 500): ",sens%
select case sens%
case 50,100,500
case else
print chr$(7)
flag% = 1
end select
loop until (flag% = 0)
end sub

```

```

sub off.set(offset)
do
flag% = 0
cls
Input "Offset in mV (0 to 1000): ",offset
if offset < 0 or offset > 1000 then print chr$(7) : flag% = 1
loop until (flag% = 0)
end sub

```

```

sub set.push.button(pb%)
incr pb%
pb% = pb% MOD 2
end sub

```

```

sub time.routine(delta.t)
do
flag%=0
cls
input "Number of seconds between samples (0.1 to 25): ",delta.t
if delta.t < 0.1 or delta.t > 25 then flag% = 1 : print chr$(7)
loop until (flag% = 0)
end sub

```

```

sub push.button
do

```



```

pb% = inp(889) and 16
loop until (pb% > 0)
end sub

```

```

sub button(pb.resp%)
pb.resp% = inp(889) and 16
end sub

```

```

sub push.key(a$)
do
a$ = inkey$
loop until ( a$ <> "" )
end sub

```

```

sub a2d(raw%)
for i% = 1 to 8
out 890,3 'chip enable, i/o=0
chp.data%(i%)=inp(889) and 32
out 890,2 'chip enable, i/o=1
next i%
raw%=0
for i%=1 to 8
raw% = raw% + (chp.data%(i%)/32) * 2^(8-i%)
next i%
end sub

```

```

sub screen.plot(x.pos%,raw%,first.pnt.flag%)
if first.pnt.flag% = 1 then
raw.old% = raw%
x.pos.old% = x.pos%
first.pnt.flag% = 0
end if

```

```

raw% = 200 * ( (255 - raw%)/255 ) 'y starts at top
incr x.pos%
if x.pos% = 640 then
cls
x.pos.old% = 0
x.pos% = (x.pos% MOD 640) + 1
end if
line (x.pos.old%,raw.old%) - (x.pos%,raw%)
raw.old% = raw% : x.pos.old% = x.pos%
end sub

```

```

sub collect.data(sens%,offset,delta.t,pb%,filename$,num.files%,ch$)
if ch$ = "d" then open "c:" + filename$ for output as #1
x.pos%=-1
gain% = 5000/sens%
delta.t% = 10 * delta.t

```

```

first.pnt.flag% = 1
cls
if pb% = 0 then
    print "Press any key to start and stop ... "
    call push.key(a$)
else
    print "Push red button to start and stop ... "
    call push.button
end if

cls
mtimer
initial.time& = 10 * timer      ' tenth sec. intervals

do
    data1.time& = 10 * timer      'tenth sec. intervals
    call a2d(raw%)
    data2.time& = 10 * timer
    start.time = (data1.time& - initial.time&)
    end.time = (data2.time& - initial.time&)
    mid.time = (start.time + end.time) / 2 : real.time = mid.time/10
    call screen.plot(x.pos%,(raw%),first.pnt.flag%)
    if ch$ = "d" then
        voltage = sens% * (raw% / 255) + offset / gain%
        write #1, real.time, voltage
    end if
    incr data2.time&, delta.t%
    do
        present.time& = 10 * timer
        loop until (present.time& >= data2.time&)

    call button(button.resp%) : a$ = inkey$
    loop until (button.resp% <> 0 or a$ <> "")

if ch$ = "d" then
    close #1
    open "c:" + filename$ for input as #1
    open "a:" + filename$ for output as #2

    do while ( not eof(1) )
        input #1, b, c
        print #2, using "#####.###"; b; : print #2, ", "; : print #2, using "#####.###"; c
        loop
    close
    kill "c:" + filename$
end if
call push.key(a$)
end sub

```

References for Chapter 2: Reviews of SEEDs, CELLS and DOES Smart Pixels

1. J. W. Goodman, F. J. Leonberger, S. L. Kung, R. A. Athale, "Optical Interconnects for VLSI Systems," *Proc. IEEE* 72, 850 (1984).
2. A. L. Lentine, D. A. B. Miller, "Evolution of the SEED Technology: Bistable Logic Gates to Optoelectronic Smart Pixels," *IEEE J. of Quantum Electronics*, 29, 655 (1993).
3. M. E. Prise, N. C. Croaft, R. E. Lamarche, M. M. Downs, S. J. Walker, L. A. D'Asaro, L. M. F. Chirovsky "Module for Optical Logic Circuits Using Symmetric Self Electro-Optic Effect Devices," *Appl. Opt.* 29, 2164 (1990).
4. G. D. Boyd, D. A. B. Miller, D. S. Chemla, S. L. McCall, A. C. Gossard, J. H. English, "Multiple Quantum Well Reflection Modulator," *Appl. Phys. Lett.* 17, 1119 (1987).
5. N. Peyghambarian, S. W. Koch, A. Mysyrowicz, *Introduction to Semiconductor Optics*, Prentice Hall (Englewood Cliffs, NJ) 1993, page 266.
6. D. A. B. Miller, D. S. Chemla, S. Schmitt-Rink, "Relation Between Electroabsorption in Bulk Semiconductors and in Quantum Wells: The Quantum-Confined Franz Keldysh Effect," *Phys. Rev. B* 33, 6976 (1986).
7. D. A. B. Miller, L. M. F. Chirovsky, T. Lentine, T. Woodward, R. McCormick, S. Hinton "FET-SEED Design Workshop," June 21, 1993. AT&T Bell Laboratories, 600 Mountain Ave., P. O. Box 636, Murray Hill, NJ 07974-0636.
8. E. A. De Souza, L. Carraresi, G. D. Boyd, D. A. B. Miller "Analog differential Self-Linearized Quantum-Well Self-Electro-Optic-Effect Modulator," *Opt. Lett.* 18, 974 (1993) and references therein.
9. L. A. D'Asaro, L. M. F. Chirovsky, E. J. Laskowski, S. S. Pei, T. K. Woodward, A. L. Lentine, R. E. Leibenguth, M. W. Focht, J. M. Freund, G. G. Guth, L. E. Smith, "Batch Fabrication and Operation of GaAs-Al_xGa_{1-x}As Field-Effect Transistor-Self-Electrooptic Effect Device (FET-SEED) Smart Pixel Arrays," *IEEE J. Quantum Electr.* 29, 670 (1993).
10. H. Hida, A. Okamoto, H. Toyoshima, K. Ohata, "An Investigation of i-AlGaAs/n-GaAs Doped-Channel MIS-like FET's (DMTs) -- Properties and Performance potentialities," *IEEE Trans. Electr. Dev.* ED-14, 1448 (1987).
11. H. C. Casey Jr., D. D. Sell, K. W. Wecht, "Concentration Dependence of the Absorption Coefficient for n- and p-type GaAs between 1.3 and 1.6 eV," *J. Appl. Phys.* 46, 250 (1975).
12. T. K. Woodward, A. L. Lentine, L. M. F. Chirovsky, S. S. Pei, J. M. Freund, L. A. D'Asaro, M. F. Focht, E. J. Laskowski, G. D. Guth, L. E. Smith, "Operating characteristics of GaAs/AlGaAs FET-SEED Smart Pixels" *IEEE International Electron Devices Meeting Technical Digest*, Dec 13-16, 1992, Page 92-655.
13. Photonics Research Incorporated, 325 Interlocken Pkwy., Building A, Broomfield, CO, 80021.
14. J. Cheng, P. Zhou, S. Z. Sun, S. Hersee, D. R. Myers, J. Zolper, G. A. Vawter, "Surface-Emitting Laser-Based Smart Pixels for Two-Dimensional Optical Logic and Reconfigurable Optical Interconnections," *IEEE J. Quantum Electr.* 29, 741 (1993).
15. P. A. Kiely, G. W. Taylor, D. P. Docter, P. R. Claisse, T. Vang, P. A. Evaldsson, S. K. Sargood, S. Daryanani, P. Cooke, K. F. Brown-Goebeler, "Demonstration of a smart pixel using DOES device technology," *IEE Proceedings-J*, Vol. 139, No. 3, 208 (1992).
16. G. W. Taylor, J. G. Simmons, A. Y. Cho, R. S. Mand, "A new double heterostructure optoelectronic switching device using molecular beam epitaxy," *J. Appl. Phys.* 59, 596 (1986).

17. G. W. Taylor, J. G. Simmons, "The bipolar inversion channel field effect transistor (BICFET) -- a new field effect solid state device: theory and structure," IEEE Trans. ED-32, No. 11, 2345 (1985).
18. M. A. Parker, P. D. Swanson, J. S. Kimmet, S. I. Libby, "Diode Laser Logic for Use as Smart Pixels for Optical Signal Processing," SPIE OELASE Optoelectronic Signal Processing for Phased-Array Antennas IV Conference Proceedings, Vol. 2155, P. 124 (1994).
19. G. J. Lasher, "Analysis of a Proposed Bistable Injection Laser," Sol. State Electr. 7, 707 (1964).
20. M. A. Parker, S. I. Libby, P. D. Swanson, "An Optical NOR Gate Based on GaAs- AlGaAs Heterostructure Lasers," IEEE C3I Conference, Utica, NY (June 1992).
21. W. J. Grande and C. L. Tang, "Semiconductor Laser Logic Gate Suitable for Monolithic Integration," Appl. Phys. Lett. 51, 1780 (1987).
22. C. L. Tang, A. Schremer, T. Fujita, "Bistability in Two-Mode Semiconductor Lasers Via Gain-Saturation," Appl. Phys. Lett. 51, 1392 (1987).
23. W. F. Kosonocky, U. S. Patent 3,431,437 (Mar. 4, 1969); filed May 25, 1964 .
24. J. L. Fitz, U. S. Patent 4,825,442 (Apr. 25, 1989); filed Apr. 19, 1988.
25. M. A. Parker, D. B. Shire, C. L. Tang, P. D. Swanson, R. J. Michalak, J. S. Kimmet, Vertical-cavity-surface-emitting Lasers with Optical GaIn Control (V-LOGIC), Patent Application in Mar. 1995.
26. M. A. Parker, P. D. Swanson, S. I. Libby, J. S. Kimmet, C. L. Tang, D. B. Shire, "Spontaneous Emission Filtered Laser Amplifiers," patent filed Dec. 1994.
27. D. B. Shire, M. A. Parker, C. L. Tang, P. D. Swanson, J. S. Kimmet, "Gain Control of Vertical Cavity Surface Emitting Lasers with Intra-cavity Coupled In-Plane Lasers," Accepted for publication in Appl. Phys. Lett. for Spring 1995.
28. D. A. B. Miller, "Novel Analogue Self-Electrooptic Effect Devices," IEEE J. Quantum Electr. 29, 678 (1993).
29. T. K. Woodward, "SEED Receivers and Transmitters," AT&T Bell Laboratories SEED Workshop June 1993.

References for Chapter 4: A Model for Optically Quenched Lasers

1. D. B. Shire, C. L. Tang, M. A. Parker, P. D. Swanson, J. S. Kimmet, Appl. Phys. Lett. 66, 1717 (1995).
2. D. B. Shire, C. L. Tang, Photon. Techn. Lett., Nov. 1996.
3. W. F. Kosonocky, R. H. Cornely, IEEE J. Quantum Electronics QE-6, 125 (1968).
4. D. F. G. Gallagher, Applied Optics 29, 4359 (1990).
5. H. Kawaguchi, Bistabilities and Nonlinearities in Laser Diodes, (Artech House , London, 1994).
6. Y. Ozeki and C. L. Tang, IEEE J. Quantum Electron. 27, 1160 (1991).
7. C. L. Tang, A. Schremer, F. Fujita, Appl. Phys. Lett. 51, 1392 (1978).
8. G. P. Agrawal, N. K. Dutta, Semiconductor Lasers, 2nd Ed., (Van Nostrand Reinhold, New York, 1993).
9. If the carrier density in each section can be approximated by the threshold value n_{thr} , then the constraint on the current density ($J_a=J_b=J$) is approximately equivalent to applying the same bias voltage to each section. This equivalence holds since an applied voltage appears as the difference in the hole and electron quasi-Fermi levels, which in turn fixes the carrier density. If each section has the same carrier density (approximately n_{thr} in this case), then the same voltage must be applied to each section.

10. M. Ueno, R. Lang, J. Appl. Phys. 58, 1689 (1985).
11. K. Y. Lau, in Quantum Well Lasers, edited by P. S. Zory, Jr., (Academic Press Inc., New York, 1993) Chap. 5.
12. Typical values are $J_{thr}=1E27$, $n_{thr}=1E18$, $n_o=5E17$, $g_o=1E-6$, $s=1E-9$, $b=1E-4$, $t_n=4$ ns, $t_g=2$ ps, $V=5 \times 0.04 \times 250$ mm³, $L=250$ mm, $l=860$ nm, $v_g=0.85E10$, $R=0.34$, $a=10$, $g_u=2E14$, $g=2E14$ (g is reduced from $4E14$ due to g_c), $g_c=2E14$ and $R \approx 0.34$ for edge emitting GaAs/AlGaAs lasers..
13. J. E. Bowers, B. R. Hemenway, A. H. Gnauck, D. P. Wilt, "High-Speed InGaAsP Constricted -Mesa Lasers," IEEE J. Quant. Electr. QE-22, pp. 833-843 (1986).

References for Chapter 5: V-LOGiC Devices

1. D. B. Shire, M. A. Parker, C. L. Tang, IEEE Photonics Techn. Lett. 8, pp. 188-190 (1996).
2. H. Uenohara, Y. Kawamura, H. Iwamura, K. Nonaka, H. Tsuda, and T. Kurokawa, Electron. Lett. 28, 1973 (1992).
3. H. Uenohara, Y. kawamura, H. Iwamura, K. Nonaka, H. Tsuda, T. Kurokawa, Electron. Lett. 29, 609 (1993).
4. W. J. Grande, J. E. Johnson, C. L. Tang, Appl. Phys. Lett. 57, 2537 (1990).
5. J. E. Johnson, W. J. Grande, C. L. Tang, Appl. Phys. Lett. 63, 3273 (1993).
6. Z. G. Pan, S. Jiang, M. Dagenais, R. A. Morgan, K. Kojima, M. T. Asom, R. E. Leibenguth, G. D. Guth, M. W. Focht, Appl. Phys. Lett. 63, 2999 (1993).
7. S. Jiang, Z. Pan, M. Dagenais, R. A. Morgan, and K. Kojima, IEEE Photonics Technol. Lett. PTL-6, 34 (1994).

References for Chapter 6: Diode Laser Logic

1. M. A. Parker, P. D. Swanson, S. I. Libby, J. S. Kimmet Patent Pending.
2. G. J. Lasher, "analysis of a Proposed Bistable Injection Laser," Sol. State Electr. 7, 707 (1964).
3. C. Harder, K. Y. Lau, A. Yariv, "Bistability and Pulsations in Semiconductor Lasers with Inhomogeneous Current Injection," IEEE J. Quant. Electr. QE-18, 1351 (1982).
4. P. D. Swanson, "Characteristics of Semiconductor Optical Waveguides Fabricated by Impurity Induced Layer Disordering," Ph.D. Dissertaion, University of Illinois, Urbana-Champaign, 1989.
5. C. M. Herzinger, P. D. Swanson, K. T. Tang, T. M. Cockerill, L. M. Miller, M. E. Givens, T. A. DeTemple, J. J. Coleman, J. P. Leburton, "Electroabsorption Properties of a Single GaAs Quantum Well," Phys. Rev. B 44, 13478 (1991).
6. W. Jung, Y. Kwon, "Nonlinear Quenching in a Monolithically Integrated Semiconductor Laser Logic Device," J. J. Appl. Phys. 28, L1242 (1989).
7. S. J. Pearton, M. P. Iannuzzi, C. L. Reynolds, L. Peticolas, "Formation of Thermally Stable High-Resistivity AlGaAs by Oxygen Implantation," Appl. Phys. Lett. 52, 395 (1988).
8. A. M. Fox, D. A. B. Miller, G. Livescu, J. E. Cunningham, W. Y. Jan, "Quantum Well Carrier Sweep Out: Relation to Electroabsorption and Exciton Saturation," IEEE J. Quant. Electr. 27, 2281 (1991).
9. W. J. Grande, J. E. Johnson, C. L. Tang, "Characterization of Etch Rate and Anisotropy in the Temperature-Controlled Chemically Assisted Ion Beam Etching of GaAs," J. Vac. Sci. Technol. B8, 1075 (1990).

References for Chapter 7: Coupled Waveguide Detectors

1. M. N. Zargar'yants, O. M. Gruding, N. B. Galkina, E. L. Gorelova, "High efficiency combined laser and photodetector in a monolithic integrated-optics module utilizing coupled waveguides," *Sov. J. Quantum Electronics* 15, 1342 (1985)
2. J. D. Soole, H. Schumacker, H. P. LeBlanc, R. Bhat, M. A. Koza, "Butt-coupled InGaAs metal-semiconductor-metal waveguide photodetector formed by selective area regrowth," *Appl. Phys. Lett.* 56, 1518 (1990).
3. K. Tada, J. Hashimoto, Y. Nakano, "Effects of Facet Reflection in a Monolithically Integrated Optical Device Consisting of a DFB Laser and an Amplifier/Modulator," *Integrated and Guided-Wave Optics*, Vol. 5, p. 219 (1988), Conference Edition by the Optical Society of America for the March 28-30 conference in Santa Fe, NM.
4. R. G. Hunsperger, "Integrated Optics: Theory and Technology, 3rd ed.," published by Springer-Verlag (New York) 1991.
5. A. V. Gershoig, O. M. Gruding, M. N. Zargaryants, M. A. Panchenko, "Optical characteristics of devices with coupled waveguides utilizing semiconductor heterostructures," *Sov. J. Quantum Electron.* 16, 1621 (1986).
6. Y. Suematsu, M. Yamada, K. Hayashi, "A Multi-Hetero-AlGaAs Laser with Integrated Twin Guide," *Proc. IEEE* 63, 208 (1975).
7. J. J. Liang, M. H. Leary, J. M. Ballantyne, "Monolithic Optoelectronics," *National Nanofabrication Facility Technical Abstracts for 1992-1993* page 43.
8. M. A. Parker, "SMART PIXELS," to be published in Jan. 1996 in the McGraw-Hill Handbook of Electronic Components as Chapter 9, section 4.

References for Chapter 8: Introduction to Opto-Electronic Technology

1. T.F. Bogart Jr., *Electronic Devices and Circuits*, Chapter 6, Merrill Publishing Co., Columbus OH, 1986.
2. T. Li, "Advances in Optical Fiber Communications: An Historical Perspective," *IEEE J. on Sel. Areas in Commun.*, SAC-1 (3), pp. 356-372, Apr 1983.
3. Y. Suematsu, "Long-Wavelength Optical Fiber Communication," *Proc. IEEE*, 71 (6), pp. 692-721, Jun 1983.
4. F. Bosch, G.M. Palmer, C.D. Sallada, C.B. Swan, "Compact 1.3- μ m Laser Transmitter for the SL Undersea Lightwave System," *J. Lightwave Technol.*, LT-2 (6), pp. 952-959, Dec 1984.
5. G.P. Agrawal, N.K. Dutta, *Semiconductor Lasers (2nd ed.)*, Chapter 1, Van Nostrand Reinhold (division of International Thomson Publishing, Inc.), New York NY, 1993.
6. E.M. Strzelecka, G.D. Robinson, M.G. Peters, F.H. Peters, L.A. Coldren, "Monolithic Integration of Vertical-Cavity Laser Diodes with Refractive GaAs Microlenses," *Electron. Lett.*, 31 (9), pp. 724-725, Apr 1995.
- * 7. S. Jiang, G.W. Taylor, *Optoelectronic Processors Implemented in the Inversion Channel Technology*, USAF Technical Report RL-TR-95-94, May 1995.
8. R.N. Ghosh, B. Griffing, J.M. Ballantyne, "Monolithic Integration of GaAs Light-Emitting Diodes and Si Metal-Oxide-Semiconductor Field-Effect Transistors," *Appl. Phys. Lett.*, 48 (5), pp. 370-371, Feb 1986.
9. S.K. Tewksbury, L.A. Hornak, "Can Optoelectronic and Silicon Chips be Monolithically Integrated?" *Laser Focus World*, 30 (5), pp. 151-156, May 1994.

*RL-TR-95-94, Distribution limited to U.S. Gov't agencies only.

10. V. Alberts, J.H. Neethling, A.W. Leitch, "Correlation Between Structural, Optical, and Electrical Properties of GaAs Grown on (001) Si," *J. Appl. Phys.*, **75** (11), pp. 7258-7265, Jun 1994.
11. J. Knall, L.T. Romano, D.K. Biegelsen, R.D. Bringans, H.C. Chui, J.S. Harris Jr., D.W. Treat, D.P. Bour, "The Use of Graded InGaAs Layers and Patterned Substrates to Remove Threading Dislocations from GaAs on Si," *J. Appl. Phys.*, **76** (5), pp. 2697-2702, Sep 1994.
12. R. Venkatasubramanian, M.L. Timmons, "Optoelectronic Properties of Eutectic-Metal-Bonded (EMB) GaAs-AlGaAs Structures on Si Substrates," *Solid-State Elect.*, **37** (11), pp. 1809-1815, Nov 1994.
13. X. Chen, D. Uttamchandani, C. Trager-Cowan, K.P. O'Donnell, "Luminescence from Porous Silicon," *Semicond. Sci. and Technol.*, **8** (1), pp. 92-96, Jan 1993.
14. R. Sabet-Dariani, N.S. McAlpine, D. Haneman, "Electroluminescence in Porous Silicon," *J. Appl. Phys.*, **75** (12), pp. 8008-8011, Jun 1994.
15. T. Ozaki, M. Araki, S. Yoshimura, H. Koyama, N. Koshida, "Photoelectronic Properties of Porous Silicon," *J. Appl. Phys.*, **76** (3), pp. 1986-1988, Aug 1994.
16. A. Bsiesy, J.C. Vial, F. Gaspard, R. Hérino, M. Ligeon, I. Mihalcescu, F. Muller, R. Romestain, "Light Emission From Porous Silicon Under Photo- and Electroexcitation," *J. Electrochem. Soc.*, **141** (11), pp. 3071-3076, Nov 1994.
17. E.D. Jungbluth, "All-Silicon Optoelectronic Structure in Development," *Solid State Technol.*, **38** (7), pp. 44-48, Jul 1995.
18. N. Bar-Chaim, S. Margalit, A. Yariv, I. Ury, "GaAs Integrated Optoelectronics," *IEEE Trans. Electron Dev.*, **ED-29** (9), pp. 1372-1381, Sep 1982.
19. A. Yariv, "The Beginning of Integrated Optoelectronic Circuits," *IEEE Trans. Electron Dev.*, **ED-31** (11), pp. 1656-1661, Nov 1984.
20. S.R. Forrest, "Monolithic Optoelectronic Integration: A New Component Technology for Lightwave Communications," *IEEE Trans. Electron Dev.*, **ED-32** (12), pp. 2640-2655, Dec 1985.
21. O. Wada, T. Sakurai, T. Nakagami, "Recent Progress in Optoelectronic Integrated Circuits (OEIC's)," *IEEE J. Quantum Electron.*, **QE-22** (6), pp. 805-821, Jun 1986.
22. M. Dagenais, R.F. Leheny, J. Crow, eds., *Integrated Optoelectronics*, Academic Press, San Diego CA, 1995.
23. S. Yamakoshi, T. Sanada, O. Wada, T. Fujii, T. Sakurai, "AlGaAs / GaAs Multiquantum-Well (MQW) Laser Applied to Monolithic Integration with FET Driver," *Electron. Lett.*, **19** (24), pp. 1020-1021, Nov 1983.
24. J. Shibata, I. Nakao, Y. Sasai, S. Kimura, N. Hase, H. Serizawa, "Monolithic Integration of an InGaAsP / InP Laser Diode with Heterojunction Bipolar Transistors," *Appl. Phys. Lett.*, **45** (3), pp. 191-193, Aug 1984.
25. M. Kuno, T. Sanada, H. Nobuhara, M. Makiuchi, T. Fujii, O. Wada, T. Sakurai, "Four-Channel AlGaAs / GaAs Optoelectronic Integrated Transmitter Array," *Appl. Phys. Lett.*, **49** (23), pp. 1575-1577, Dec 1986.
26. S.D. Offsey, P.J. Tasker, W.J. Schaff, L. Kapitan, J.R. Shealy, L.F. Eastman, "Vertical Integration of an In_{0.15}Ga_{0.85}As Modulation-Doped Field Effect Transistor and GaAs Laser Grown by Molecular Beam Epitaxy," *Electron. Lett.*, **26** (6), pp. 350-352, Mar 1990.
27. K.-Y. Liou, S. Chandrasekhar, A.G. Dentai, E.C. Burrows, G.J. Qua, C.H. Joyner, C.A. Burrus, "A 5 Gb/s Monolithically Integrated Lightwave Transmitter with 1.5 μ m Multiple Quantum Well Laser and HBT Driver Circuit," *IEEE Photon. Technol. Lett.*, **3** (10), pp. 928-930, Oct 1991.

28. A. Ketterson, J.-W. Seo, M. Tong, K. Nummala, D. Ballegeer, S.-M. Kang, K.Y. Cheng, I. Adesida, "A 10-GHz Bandwidth Pseudomorphic GaAs / InGaAs / AlGaAs MODFET-Based OEIC Receiver," *IEEE Trans. Electron Dev.*, **39** (11), pp. 2676-2677, Nov 1992.
29. W. Bronner, J. Hornung, K. Köhler, E. Olander, Z.-G. Wang, "Integration of a Quantum Well Laser with AlGaAs / GaAs - HEMT Electronics," *Mat. Res. Soc. Symp. Proc.*, **300** (III-V Electronic and Photonic Device Fabrication and Performance, San Francisco, Apr 1993), pp. 133-138, 1993.
30. W. Bronner, J. Hornung, K. Köhler, E. Olander, "Molecular Beam Epitaxy and Technology for the Monolithic Integration of Quantum Well Lasers and AlGaAs / GaAs / AlGaAs - HEMT Electronics," *Inst. Phys. Conf. Ser.*, **136** (Int. Symp. GaAs and Related Compounds, Freiburg, Aug/Sep 1993), pp. 461-466, 1994.
31. M.A. Parker, P.D. Swanson, J.S. Kimmet, S.I. Libby, "Diode Laser Logic for use as Smart Pixels for Optical Signal Processing," *SPIE Proceedings, Optoelectronic Signal Processing for Phased-Array Antennas IV*, **2155**, pp. 124-134, Jan 94.

References for Chapter 9: The Design of Monolithically Integrated FETs and Lasers

1. P.K.-L. Yu, P.-C. Chen, "GaAs Optoelectronic Device Technology," *Introduction to Semiconductor Technology: GaAs and Related Compounds*, (C.T. Wang, ed.), Chapter 9, John Wiley & Sons, New York NY, 1990.
2. M. Shur, *GaAs Devices and Circuits*, Plenum, New York NY, 1987.
3. M. Shur, "Modeling of GaAs and AlGaAs / GaAs Field Effect Transistors," *Introduction to Semiconductor Technology: GaAs and Related Compounds*, (C.T. Wang, ed.), Chapter 2, John Wiley & Sons, New York NY, 1990.
4. P.-C. Chao, M.S. Shur, R.C. Tiberio, K.H.G. Duh, P.M. Smith, J.M. Ballingall, P. Ho, A.A. Jabra, "DC and Microwave Characteristics of Sub-0.1- μ m Gate-Length Planar-Doped Pseudomorphic HEMT's," *IEEE Trans. Electron Dev.*, **36** (3), pp. 461-472, Mar 1989.
5. H. Hida, K. Ohata, Y. Suzuki, H. Toyoshima, "A New Low-Noise AlGaAs/GaAs 2DEG FET with a Surface Undoped Layer," *IEEE Trans. Electron Dev.*, **ED-33** (5), pp. 601-607, May 1986.
6. H. Hida, A. Okamoto, H. Toyoshima, K. Ohata, "A High-Current Drivability i-AlGaAs/n-GaAs Doped-Channel MIS-Like FET (DMT)," *IEEE Electron Dev. Lett.*, **EDL-7** (11), pp. 625-626, Nov 1986.
7. H. Hida, Y. Suzuki, F. Katano, H. Toyoshima, A. Okamoto, S. Kumashiro, "A 760 mS/mm N^+ Self-Aligned Enhancement Mode Doped-Channel MIS-Like FET (DMT)," *Tech. Dig.: IEDM 1986*, (Los Angeles CA, Dec 1986), pp. 759-762.
8. H. Hida, A. Okamoto, H. Toyoshima, K. Ohata, "An Investigation of i-AlGaAs/n-GaAs Doped-Channel MIS-Like FET's (DMT's) — Properties and Performance Potentialities," *IEEE Trans. Electron Dev.*, **ED-34** (7), pp. 1448-1455, Jul 1987.
9. H. Hida, H. Toyoshima, Y. Ogawa, "High-Speed Integrated Circuits Using i-AlGaAs/n-GaAs Doped-Channel Hetero-MISFET's (DMT's)," *IEEE Electron Dev. Lett.*, **EDL-8** (12), pp. 557-559, Dec 1987.
10. Y. Suzuki, H. Hida, T. Suzaki, S. Fujita, Y. Ogawa, A. Okamoto, T. Toda, T. Nozaki, "A 10-Gbit/s Laser Driver IC with i-AlGaAs/n-GaAs Doped-Channel Hetero-MISFETs (DMTs)," *11th Annual GaAs IC Symp.: Tech. Dig. 1989*, (San Diego CA, Oct 1989), pp. 129-132.
11. S.-S. Pei, N.J. Shah, "Heterostructure Field Effect Transistors," *Introduction to Semiconductor Technology: GaAs and Related Compounds*, (C.T. Wang, ed.), Chapter 3, John Wiley & Sons, New York NY, 1990.

12. M.C. Foisy, "A Physical Model for the Bias Dependence of the Modulation-Doped Field-Effect Transistor's High-Frequency Performance," PhD Dissertation, Cornell University, Ithaca NY, May 1990.
13. G. Duggan, "A Critical Review of Heterojunction Band Offsets", *J. Vac. Sci. Technol. B*, **3** (4), pp. 1224-1230, Jul 1985.
- 45.H.C. Casey Jr., M.B. Panish, *Heterostructure Lasers*, Academic Press, Orlando FL, 1978.
14. C. Weisbuch, B. Vinter, *Quantum Semiconductor Structures: Fundamentals and Applications*, Section 23, Academic Press, San Diego CA, 1991.
16. R.W.H. Engelmann, C.-L. Shieh, C. Shu, "Multiquantum Well Lasers: Threshold Considerations," *Quantum Well Lasers*, (P.S. Zory Jr., ed.), Chapter 3, Academic Press, San Diego CA, 1993.
17. S.W. Corzine, R.-H. Yan, L.A. Coldren, "Optical Gain in III-V Bulk and Quantum Well Semiconductors," *Quantum Well Lasers*, (P.S. Zory Jr., ed.), Chapter 1, Academic Press, San Diego CA, 1993.
18. P. Yeh, *Optical Waves in Layered Media*, Chapter 12, John Wiley & Sons, New York NY, 1988.
19. S. Adachi, "GaAs, AlAs, and $\text{Al}_x\text{Ga}_{1-x}\text{As}$: Material Parameters for Use in Research and Device Applications," *J. Appl. Phys.*, **58** (3), pp. R1-R29, Aug 1985.
20. L.A. D'Asaro, L.M.F. Chirovsky, E.J. Laskowski, S.-S. Pei, T.K. Woodward, A.L. Lentine, S.J. Pearton, L.E. Smith, "Batch Fabrication and Structure of Integrated GaAs - $\text{Al}_x\text{Ga}_{1-x}\text{As}$ Field-Effect Transistor - Self-Electro-Optic Effect Devices (FET-SEEDs)," *IEEE Electron Dev. Lett.*, **13** (10), pp. 528-531, Oct 1992.
21. L.A. D'Asaro, L.M.F. Chirovsky, E.J. Laskowski, S.S. Pei, T.K. Woodward, A.L. Lentine, R.E. Leibenguth, M.W. Focht, J.M. Freund, G.G. Guth, L.E. Smith, "Batch Fabrication and Operation of GaAs - $\text{Al}_x\text{Ga}_{1-x}\text{As}$ Field-Effect Transistor - Self-Electrooptic Effect Device (FET-SEED) Smart Pixel Arrays," *IEEE J. Quantum Electron.*, **29** (2), pp. 670-676, Feb 1993.
22. D.A.B. Miller, M.D. Feuer, T.Y. Chang, S.C. Shunk, J.E. Henry, D.J. Burrows, D.S. Chemla, "Field-Effect Transistor Self-Electrooptic Effect Device: Integrated Photodiode, Quantum Well Modulator and Transistor," *IEEE Photon. Tech. Lett.*, **1** (3), pp. 62-64, Mar 1989.
23. T.K. Woodward, L.M.F. Chirovsky, A.L. Lentine, L.A. D'Asaro, E.J. Laskowski, M. Focht, G. Guth, S.S. Pei, F. Ren, G.J. Przybylek, L.E. Smith, R.E. Leibenguth, M.T. Asom, R.F. Kopf, J.M. Kuo, "Operation of a Fully Integrated GaAs - $\text{Al}_x\text{Ga}_{1-x}\text{As}$ FET-SEED: A Basic Optically Addressed Integrated Circuit," *IEEE Photon. Tech. Lett.*, **4** (6), pp. 614-617, Jun 1992.
24. T.K. Woodward, A.L. Lentine, L.M.F. Chirovsky, S.S. Pei, J.M. Freund, L.A. D'Asaro, M.F. Focht, E.J. Laskowski, G.D. Guth, L.E. Smith, "Operating Characteristics of GaAs / AlGaAs FET-SEED Smart Pixels," *Tech. Dig.: IEDM 1992*, (San Francisco CA, Dec 1992), pp. 655-658.

References for Chapter 11: Amorphous Silicon Elements for Memory (ASEM)

1. M. Stutzmann, W. B. Jackson, C. C. Tsai, "Light-induced metastable defects in hydrogenated amorphous silicon: A systematic study," *Phys. Rev. B*, **32**, 23 (1985)
2. M. A. Parker, "Anisotropic drift mobility in hydrogenated amorphous silicon," PhD dissertation Syracuse University, 1988.

References for Chapter 12: Developing a Reliable Etch

1. M. Tong, D.G. Ballegeer, A. Ketterson, E.J. Roan, K.Y. Cheng, I. Adesida, "A Comparative Study of Wet and Dry Selective Etching Processes for GaAs / AlGaAs / InGaAs Pseudomorphic MODFETs," *J. Electron. Mater.*, **21** (1), pp. 9-15, Jan 1992.
2. R. Grundbacher, H. Chang, M. Hannan, I. Adesida, "Fabrication of Parallel Quantum Wires in GaAs / AlGaAs Heterostructures Using AlAs Etch Stop Layers," *J. Vac. Sci. Technol. B*, **11** (6), pp. 2254-2257, Nov 1993.
3. G.C. DeSalvo, W.F. Tseng, J. Comas, "Etch Rates and Selectivities of Citric Acid / Hydrogen Peroxide on GaAs, $\text{Al}_{0.3}\text{Ga}_{0.7}\text{As}$, $\text{In}_{0.2}\text{Ga}_{0.8}\text{As}$, $\text{In}_{0.53}\text{Ga}_{0.47}\text{As}$, $\text{In}_{0.52}\text{Al}_{0.48}\text{As}$, and InP," *J. Electrochem. Soc.*, **139** (3), pp. 831-835, Mar 1992.
4. J.J. LePore, "An Improved Technique for Selective Etching of GaAs and $\text{Ga}_{1-x}\text{Al}_x\text{As}$," *J. Appl. Phys.*, **51** (12), pp. 6441-6442, Dec 1980.
5. K. Kenefick, "Selective Etching Characteristics of Peroxide / Ammonium-Hydroxide Solutions for GaAs / $\text{Al}_{0.16}\text{Ga}_{0.84}\text{As}$," *J. Electrochem. Soc.*, **129** (10), pp. 2380-2382, Oct 1982.
6. A.J. Tang, K. Sadra, B.G. Streetman, "Selective Etching of $\text{Al}_x\text{Ga}_{1-x}\text{As}$ and $\text{In}(\text{Al}_x\text{Ga}_{1-x})\text{As}$ Alloys in Succinic Acid - Hydrogen Peroxide Solutions," *J. Electrochem. Soc.*, **140** (5), pp. L82-L83, May 1993.
7. S.A. Merritt, M. Dagenais, "Etch Characteristics of Succinic Acid / Ammonia / Hydrogen Peroxide versus Aluminum Mole Fraction in AlGaAs," *J. Electrochem. Soc.*, **140** (9), pp. L138-L139, Sep 1993.
8. M. Otsubo, T. Oda, H. Kumabe, H. Miki, "Preferential Etching of GaAs Through Photoresist Masks," *J. Electrochem. Soc.*, **123** (5), pp. 676-680, May 1976.
9. C. Juang, K.J. Kuhn, R.B. Darling, "Selective Etching of GaAs and $\text{Al}_{0.30}\text{Ga}_{0.70}\text{As}$ with Citric Acid / Hydrogen Peroxide Solutions," *J. Vac. Sci. Technol. B*, **8** (5), pp. 1122-1124, Sep 1990.
10. B.C. Schmukler, P.E. Brunemeier, W.R. Hitchens, B.D. Cantos, W.A. Striffler, D.H. Rosenblatt, R.D. Remba, "Highly Selective Citric Buffer Etch-Stop Process for the Manufacture of Very Uniform GaAs / AlGaAs FETs," *15th Annual GaAs IC Symp.: Tech. Dig. 1993*, (San Jose CA, Oct 1993), pp. 325-328.
11. B.-Y. Mao, J.A. Nielsen, R.A. Friedman, G.Y. Lee, "The Applications of Citric Acid / Hydrogen Peroxide Etching Solutions in the Processing of Pseudomorphic MODFETs," *J. Electrochem. Soc.*, **141** (4), pp. 1082-1085, Apr 1994.
12. V.M. Donnelly, D.L. Flamm, "Anisotropic Etching in Chlorine-Containing Plasmas," *Solid State Technol.*, **24** (4), pp. 161-166, Apr 1981.
13. K.L. Seaward, N.J. Moll, D.J. Coulman, W.F. Stickle, "An Analytical Study of Etch and Etch-Stop Reactions for GaAs on AlGaAs in CCl_2F_2 Plasma," *J. Appl. Phys.*, **61** (6), pp. 2358-2364, Mar 1987.
14. K.L. Seaward, N.J. Moll, W.F. Stickle, "The Role of Aluminum in Selective Reactive Ion Etching of GaAs on AlGaAs," *J. Vac. Sci. Technol. B*, **6** (6), pp. 1645-1649, Nov 1988.
15. S. Salimian, C.B. Cooper III, "Selective Dry Etching of GaAs Over AlGaAs in SF_6 / SiCl_4 Mixtures," *J. Vac. Sci. Technol. B*, **6** (6), pp. 1641-1644, Nov 1988.
16. K. Hikosaka, T. Mimura, K. Joshin, "Selective Dry Etching of AlGaAs - GaAs Heterojunction," *Jpn. J. Appl. Phys.*, **20** (11), pp. L847-L850, Nov 1981.
17. J. Vatus, J. Chevrier, P. Delescluse, J.-F. Rochette, "Highly Selective Reactive Ion Etching Applied to the Fabrication of Low-Noise AlGaAs GaAs FET's," *IEEE Trans. Electron Dev.*, **ED-33** (7), pp. 934-937, Jul 1986.

18. C.M. Knoedler, T.F. Kuech, "Selective GaAs / Al_xGa_{1-x}As Reactive Ion Etching Using CCl₂F₂," *J. Vac. Sci. Technol. B*, **4** (5), pp. 1233-1236, Sep 1986.
19. N.I. Cameron, G. Hopkins, I.G. Thayne, S.P. Beaumont, C.D.W. Wilkinson, M. Holland, A.H. Kean, C.R. Stanley, "Selective Reactive Ion Etching of GaAs / AlGaAs Metal-Semiconductor Field Effect Transistors," *J. Vac. Sci. Technol. B*, **9** (6), pp. 3538-3541, Nov 1991.
20. Y.K. Su, Y.Z. Juang, S.C. Shei, B.C. Fang, "A Study of Selective and Nonselective Reactive Ion Etching of GaAs / AlGaAs Materials," *Solid-State Electronics*, **36** (12), pp. 1779-1785, Dec 1993.
21. N.I. Cameron, S. Ferguson, M.R.S. Taylor, S.P. Beaumont, M. Holland, C. Tronche, M. Soulard, P.H. Ladbroke, "Selectively Dry Gate Recessed GaAs Metal-Semiconductor Field-Effect Transistors, High Electron Mobility Transistors, and Monolithic Microwave Integrated Circuits," *J. Vac. Sci. Technol. B*, **11** (6), pp. 2244-2248, Nov 1993.
22. L.E. Smith, "A Highly Selective, Chlorofluorocarbon-Free GaAs on AlGaAs Etch," *J. Electrochem. Soc.*, **140** (7), pp. 2116-2120, Jul 1993.
23. M.T. Mocella, "The CFC - Ozone Issue in Dry Etch Process Development," *Solid State Technol.*, **34** (4), pp. 63-64, Apr 1991.
24. W.H. Guggina, A.A. Ketterson, E. Andideh, J. Hughes, I. Adesida, S. Caracci, J. Kolodzey, "Characterization of GaAs / Al_xGa_{1-x}As Selective Reactive Ion Etching in SiCl₄ / SiF₄ Plasmas," *J. Vac. Sci. Technol. B*, **8** (6), pp. 1956-1959, Nov 1990.
25. S. Salimian, C.B. Cooper III, R. Norton, J. Bacon, "Reactive Ion Etch Process with Highly Controllable GaAs-to-AlGaAs Selectivity Using SF₆ and SiCl₄," *Appl. Phys. Lett.*, **51** (14), pp. 1083-1085, Oct 1987.
26. C.B. Cooper III, S. Salimian, H.F. MacMillan, "Use of Thin AlGaAs and InGaAs Stop-Etch Layers for Reactive Ion Etch Processing of III-V Compound Semiconductor Devices," *Appl. Phys. Lett.*, **51** (26), pp. 2225-2226, Dec 1987.
27. S.K. Murad, C.D.W. Wilkinson, S.P. Beaumont, "Selective and Nonselective RIE of GaAs and Al_xGa_{1-x}As in SiCl₄ Plasma," *Microelectron. Eng.*, **23** (1-4), pp. 357-360, Jan 1994.
28. T.E. Kazior, B.I. Patel, "Selective Gate Recessing of GaAs / AlGaAs / InGaAs Pseudomorphic HEMT Structures Using BCl₃ Plasmas," *Mat. Res. Soc. Symp. Proc.*, **240** (Advanced III-V Compound Semiconductor Growth, Processing and Devices, Boston, Dec 1991), pp. 329-334, 1992.
29. G. Franz, "Robust Reactive Ion Etching Processes for GaAs / AlGaAs / AlAs by Application of Statistical Concepts," *J. Electrochem. Soc.*, **140** (4), pp. 1147-1151, Apr 1993.
30. H. Takenaka, Y. Oishi, D. Ueda, "Dead-Time-Free Selective Dry Etching of GaAs / AlGaAs Using BCl₃ / CHF₃ Plasma," *J. Vac. Sci. Technol. B*, **12** (6), pp. 3107-3111, Nov 1994.
31. J.W. Wu, C.Y. Chang, E.Y. Chang, S.H. Chang, K.C. Lin, "Reactive Ion Etching of GaInP, GaAs, and AlGaAs," *J. Electrochem. Soc.*, **142** (4), pp. 1340-1343, Apr 1995.
32. R.E. Klinger, J.E. Greene, "Reactive Ion Etching of GaAs in CCl₂F₂," *Appl. Phys. Lett.*, **38** (8), pp. 620-622, Apr 1981.
33. R.E. Klinger, J.E. Greene, "Reactive Ion Etching of GaAs in CCl_{4-x}F_x (x = 0, 2, 4) and Mixed CCl_{4-x}F_x / Ar Discharges," *J. Appl. Phys.*, **54** (3), pp. 1595-1604, Mar 1983.
34. H. Tamura, H. Kurihara, "GaAs and GaAlAs Reactive Ion Etching in BCl₃ - Cl₂ Mixture," *Jpn. J. Appl. Phys.*, **23** (9), pp. L731-L733, Sep 1984.
35. K. Tokunaga, F.C. Redeker, D.A. Danner, D.W. Hess, "Comparison of Aluminum Etch Rates in Carbon Tetrachloride and Boron Trichloride Plasmas," *J. Electrochem. Soc.*, **128** (4), pp. 851-855, Apr 1981.

36. E.L. Hu, R.E. Howard, "Reactive-Ion Etching of GaAs and InP Using CCl_2F_2 / Ar / O_2 ," *Appl. Phys. Lett.*, **37** (11), pp. 1022-1024, Dec 1980.
37. C.M. Knoedler, L. Osterling, H. Shtrikman, "Reactive Ion Etching Damage to GaAs Layers with Etch Stops," *J. Vac. Sci. Technol. B*, **6** (5), pp. 1573-1576, Sep 1988.
38. H.F. Wong, D.L. Green, T.Y. Liu, D.G. Lishan, M. Bellis, E.L. Hu, P.M. Petroff, P.O. Holtz, J.L. Merz, "Investigation of Reactive Ion Etching Induced Damage in GaAs - AlGaAs Quantum Well Structures," *J. Vac. Sci. Technol. B*, **6** (6), pp. 1906-1910, Nov 1988.
39. D.G. Lishan, H.F. Wong, D.L. Green, E.L. Hu, J.L. Merz, D. Kirillov, "Dry Etch Induced Damage in GaAs Investigated Using Raman Scattering Spectroscopy," *J. Vac. Sci. Technol. B*, **7** (3), pp. 556-560, May 1989.
40. W. Beinstingl, R. Christanell, J. Smoliner, C. Wirner, E. Gornik, G. Weimann, W. Schlapp, "Electron Concentration and Mobility Loss in GaAs / GaAlAs Heterostructures Caused by Reactive Ion Etching," *Appl. Phys. Lett.*, **57** (2), pp. 177-179, Jul 1990.
41. S. Salimian, C. Yuen, C. Shih, C.B. Cooper III, "Damage Studies of Dry Etched GaAs Recessed Gates for Field Effect Transistors," *J. Vac. Sci. Technol. B*, **9** (1), pp. 114-119, Jan 1991.
42. W.H. Guggina, D.G. Ballegeer, I. Adesida, "Effects of Reactive Ion Etching on GaAs / AlGaAs Heterostructures," *Nuclear Instr. and Methods in Phys. Res.*, **B 59/60** (Part II), pp. 1011-1014, Jul 1991.
43. M. Joseph, F.E.G. Guimaraes, J. Kraus, F.-J. Tegude, "Characterization of Reactive Ion Etched AlGaAs / GaAs Heterostructures by Photoluminescence and Low Temperature Hall Measurements," *J. Vac. Sci. Technol. B*, **9** (3), pp. 1456-1460, May 1991.
44. D.G. Ballegeer, S. Agarwala, M. Tong, A.A. Ketterson, I. Adesida, J. Griffin, M. Spencer, "Selective Reactive Ion Etching Effects on GaAs / AlGaAs MODFETs," *Mat. Res. Soc. Symp. Proc.*, **240** (Advanced III-V Compound Semiconductor Growth, Processing and Devices, Boston, Dec 1991), pp. 335-340, 1992.
45. H.H. Sawin, "Challenges in Dry Etching: Uniformity, Selectivity, Pattern Dependencies, Damage, and Cleaning," *Microelectron. Eng.*, **23** (1-4), pp. 15-21, Jan 1994.
46. S.J. Pearton, U.K. Chakrabarti, W.S. Hobson, C. Constantine, D. Johnson, "Low Damage Dry Etching of III-V Compound Semiconductors Using Electron Cyclotron Resonance Discharges," *Nuclear Instr. and Methods in Phys. Res.*, **B 59/60** (Part II), pp. 1015-1018, Jul 1991.
47. S.J. Pearton, F. Ren, J.R. Lothian, T.R. Fullowan, R.F. Kopf, U.K. Chakrabarti, S.P. Hui, A.B. Emerson, S.S. Pei, "Electron Cyclotron Resonance Plasma Processing of GaAs - AlGaAs HEMT Structures," *Mat. Res. Soc. Symp. Proc.*, **240** (Advanced III-V Compound Semiconductor Growth, Processing and Devices, Boston, Dec 1991), pp. 293-300, 1992.
48. S.W. Pang, "A Comparison Between Dry Etching with an Electron Cyclotron Resonance Source and Reactive Ion Etching for GaAs and InP," *Mat. Res. Soc. Symp. Proc.*, **240** (Advanced III-V Compound Semiconductor Growth, Processing and Devices, Boston, Dec 1991), pp. 273-283, 1992.
49. P.D. Swanson, D.B. Shire, C.L. Tang, M.A. Parker, J.S. Kimmet, R.J. Michalak, "Electron-Cyclotron Resonance Etching of Mirrors for Ridge-Guided Lasers," *IEEE Photon. Technol. Lett.*, **7** (6), pp. 605-607, Jun 1995.
50. M.A. Parker, J.S. Kimmet, R.J. Michalak, H.S. Wang, D.B. Shire, C.L. Tang, J.P. Drumheller, "Accurate Electron-Cyclotron-Resonance Etching of Semiconductor Laser Heterostructures Using a Simple Laser Reflectometer," *IEEE Photon. Technol. Lett.*, **8** (6), pp. 818-820, Jun 1996.

51. M.A. Parker, R.J. Michalak, J.S. Kimmeth, A.R. Pirich, D.B. Shire, "Etched-Surface Roughness Measurements From an *In-Situ* Laser Reflectometer," *Appl. Phys. Lett.*, **69** (10), pp. 1-3, Sep 1996.
52. The Cornell Nanofabrication Facility (CNF) is sponsored by the National Science Foundation, and is the largest laboratory in the National Nanofabrication Users Network (NNUN). More information about the facility can be found at its World Wide Web site, <http://www.cnf.cornell.edu/>.
53. M.A. Parker, J.S. Kimmeth, S.I. Libby, P.D. Swanson, *GaAs Optical Circuits*, Chapter 4, USAF Technical Report RL-TR-94-103, Aug 1994.
54. D.C. Miller, "The Alloying of Gold and Gold Alloy Ohmic Contact Metallizations with Gallium Arsenide," *J. Electrochem. Soc.*, **127** (2), pp. 467-475, Feb 1980.
55. S.J. Pearton, F. Ren, A. Katz, T.R. Fullowan, C.R. Abernathy, W.S. Hobson, R.F. Kopf, "Rapid Isothermal Processing for Fabrication of GaAs-Based Electronic Devices," *IEEE Trans. Electron Dev.*, **39** (1), pp. 154-158, Jan 1992.
56. P.N. Favenec, "Semi-Insulating Layers of GaAs by Oxygen Implantation," *J. Appl. Phys.*, **47** (6), pp. 2532-2536, Jun 1976.
57. TRIM-92, an ion implant simulator, © IBM 1984-1992. For detailed theory on ion stopping powers, and an original program listing and description, see J.F. Ziegler, J.P. Biersack, U. Littmark, *The Stopping and Range of Ions in Solids*, Pergamon Press, New York NY, 1985. The latest versions incorporate chemical-compound targets, based on research described by J.F. Ziegler, J.M. Manoyan, "The Stopping of Ions in Compounds," *Nuclear Instr. and Methods in Phys. Res.*, **B 35** (3-4), pp. 215-228, Dec 1988.
59. T. Sanada, S. Yamakoshi, H. Hamaguchi, O. Wada, T. Fujii, T. Horimatsu, T. Sakurai, "Monolithic Integration of a Low Threshold Current Quantum Well Laser and a Driver Circuit on a GaAs Substrate," *Appl. Phys. Lett.*, **46** (3), pp. 226-228, Feb 1985.
60. M. Nakamura, N. Suzuki, T. Ozeki, "The Superiority of Optoelectronic Integration for High-Speed Laser Diode Modulation," *IEEE J. Quantum Electron.*, **QE-22** (6), pp. 822-826, Jun 1986.
61. S.W. Corzine, R.-H. Yan, L.A. Coldren, "Optical Gain in III-V Bulk and Quantum Well Semiconductors," *Quantum Well Lasers*, (P.S. Zory Jr., ed.), Chapter 1, Academic Press, San Diego CA, 1993.
62. P. Yeh, *Optical Waves in Layered Media*, Chapter 12, John Wiley & Sons, New York NY, 1988.

References for Chapter 13: High Quality Gas Etching Using an ECR

1. E. Hu, "Dry Etching," in *Gallium Arsenide Technology*, Vol. II, Ed. by D. K. Ferry, (Howard Sams and Co. Books, 1989) pp. 403-440.
2. G.L. Snider, A.M. Then, R.J. Soave, G.W. Tasker, "High aspect ratio dry etching for microchannel plates," *J. Vac. Sci. Technol. B* **12**, 3327 (1994).
3. W.J. Grande, J.E. Johnson, and C.L. Tang, "GaAs/AlGaAs photonic integrated circuits fabricated using chemically assisted ion beam etching," *Appl. Phys. Lett.* **57**, 2537 (1990).
4. P. Buchmann, H. Kaufmann, "GaAs Single-Mode Rib Waveguides with Reactive Ion-Etched Totally Reflecting Corner Mirrors," *J. Lightwave Technol.* **LT-3**, 785 (1985).
5. J. E. Johnson, C. L. Tang, "Precise determination of turning mirror loss using GaAs/AlGaAs lasers with up to ten 90° turns," *IEEE Photon. Technol. Lett.* **4**, 24 (1992).

6. W.J. Grande, W.D. Braddock, J.R. Shealy, C.L. Tang, "One-step two-level etching technique for monolithic integrated optics," *Appl. Phys. Lett.* **51**, 2189 (1987).
7. P. W. A. McIlroy, A. Kurobe, Y. Uematsu, "Analysis and application of theoretical gain curves to the design of multi-quantum-well lasers," *IEEE J. of Quantum Electr.* QE-21, 1958 (1985).
8. F. Shimokawa, H. Tanaka, R. Sawada, S. Hara, "Continuous-wave operation and mirror loss of a U-shaped GaAs/AlGaAs laser diode with two totally reflecting mirrors," *Appl. Phys. Lett.* **56**, 1617 (1990).

References for Chapter 14: Using a Laser Reflectometer as an In-Situ Etch Monitor

1. P. D. Swanson, D. B. Shire, C. L. Tang, M. A. Parker, J. S. Kimmet, R. J. Michalak, "Electron-Cyclotron Resonance Etching of Mirrors for Ridge-Guided Lasers," *IEEE Photonics Techn. Lett.* **7**, pp. 605-607, 1995.
2. R. E. Klinger, J. E. Greene, "Reactive ion etching of GaAs in $\text{CCl}_{4-x}\text{F}_x$ ($x = 0,2,4$) and mixed $\text{CCl}_{4-x}\text{F}_x/\text{Ar}$ discharges," *J. Appl. Phys.* **54**, pp. 1595-1604, 1983.
3. E. Yablonovitch, T. Gmitter, J. P. Harbison, R. Bhat, "Extreme selectivity in the lift-off of epitaxial GaAs films," *Appl. Phys. Lett.* **51**, pp. 2222-2224, 1987.
4. J. Vatus, J. Chevrier, P. Delescluse, J. F. Rochette, "Highly Selective Reactive Ion Etching Applied to the Fabrication of Low-Noise AlGaAs GaAs FET's," *IEEE Trans. Electr. Devices* ED-33, pp. 934-937, 1986.
5. T. Wipieljewski, K. J. Ebeling, "In Situ Controlled Wet Chemical Etching of Layered AlGaAs Structures with Interferometric Accuracy," *J. Electrochem. Soc.* **140**, pp. 2028-2033 (1993).
6. S. E. Hicks, W. Parkes, J. A. H. Wilkinson, C. D. W. Wilkinson, "Reflectance Modelling for In-Situ Dry Etch Monitoring of Bulk SiO_2 and III-V Multilayer Structures," *JVST B* nov-dec 1995.
7. L. H. Grober, M. Hong, J. P. Mannaerts, R. S. Freund, "Etch Rate and Thickness Measurements of Layered GaAs, AlAs and AlGaAs Structures Using a Laser Reflectance Technique," *Compound Semiconductor Epitaxy*, MRS Proceedings Vol. 340, C. W. Tu, L. A. Kolodziejewski, V. R. McCrary, Editors, Materials Research Society, Pittsburgh, PA, 1994, pp. 227-232.
8. R. G. Hunsperger, "Integrated Optics: Theory and Technology," 3rd Edition, New York, NY: Springer-Verlag, 1991, p. 60.
9. E. D. Palik, "Gallium Arsenide (GaAs)," *Handbook of Optical Constants of Solids*, E. D. Palik, Ed., New York, NY: Academic Press Inc., 1985, pp. 429-443.
10. E. D. Palik, O. J. Glembocki, K. Takarabe, "Aluminum Arsenide (AlAs)," *ibid.* pp. 489-499.
11. O. J. Glembocki, K. Takarabe, "Aluminum Gallium Arsenide ($\text{Al}_x\text{Ga}_{1-x}\text{As}$)," *ibid.* pp. 513-533.
12. K. I. Litvin, "Metal-Semiconductor-Metal Photodiodes with Applications in Monolithic Integrated Optical Receiver Circuits Capable of Detecting and Amplifying a Millimeter-Wave Modulation Signal Being Transmitted via an Optical Carrier," Ph.D. Dissertation (Cornell University, School of Electrical Engineering, Ithaca, NY, 14853), Aug. 1994, p. 75.

References for ch 15: Etched-Surface Roughness Measurements from a Laser Reflectometer

1. P. K. Tien, Appl. Optics 10, 2395-2413, 1971.
2. M. A. Parker, J. S. Kimmet, R. J. Michalak, H. S. Wang, D. B. Shire, C. L. Tang, J. Drumheller, Photonics Techn. Lett. 8, 818-820, 1996.
3. S. E. Hicks, W. Parkes, J. A. H. Wilkinson, C. D. W. Wilkinson, "Reflectance Modelling for In-Situ Dry Etch Monitoring of Bulk SiO₂ and III-V Multilayer Structures," J. Vac. Sci. Technol. B12, 3306-3310, 1994.
4. L. H. Grober, M. Hong, J. P. Mannaerts, R. S. Freund, "Etch Rate and Thickness Measurements of Layered GaAs, AlAs and AlGaAs Structures Using a Laser Reflectance Technique," Compound Semiconductor Epitaxy, MRS Proceedings Vol. 340, C. W. Tu, L. A. Kolodziejewski, V. R. McCrary, Editors, Materials Research Society, Pittsburgh, PA, 1994, pp. 227-232.
5. T. Wipiejewski, K. J. Ebeling, "In Situ Controlled Wet Chemical Etching of Layered AlGaAs Structures with Interferometric Accuracy," J. Electrochem. Soc. 140, 2028-2033, 1993.
6. J. A. DeSanto and G. S. Brown, "Analytical Techniques for Multiple Scattering From Rough Surfaces," Progress in Optics XXIII, ed. E. Wolf, North Holland, 1986, pp. 1-62 (and references therein).
7. S. K. Nayar, K. Ikeuchi, T. Kanade, "Surface Reflection: Physical and Geometrical Perspective," IEEE Transactions on Pattern Analysis and Machine Intelligence 13, 611-634, 1991.
8. The model uses geometric optics.
9. $\langle e^{-2jz\kappa\cos q} \rangle \approx 1$ compared with $\langle e^{-2jz\kappa n} \rangle$ for reasonable distributions since $\cos q$ (≈ 0.6) is relatively small compared with n (≈ 3.49). Also note that the reflectometer does not employ focusing optics which would otherwise ensure the interference assumed by the first term in Equation 2.
10. Curve 1 is the correct SMR plot for the sum of a large number of independent random variables by the Central Limit Theorem.
11. A. M. Mood, F. A. Grayhill, D. C. Boes, "Introduction to the Theory of Statistics," 3rd Ed., New York, NY: McGraw-Hill Co., 1974, p. 200.